INTERNATIONAL DOCTORAL SCHOOL OF THE USC

Emilio Xosé
Rodríguez Fernández

PhD Thesis

Portals to New Physics: tracing the hints of Long-Lived particles at the LHCb and CODEX-b experiments

Santiago de Compostela, 2025

Doctoral Programme in Nuclear and Particle Physics

ESCOLA DE DOUTORAMENTO
INTERNACIONAL DA USC

DOCTORAL THESIS

PORTALS TO NEW PHYSICS: TRACING THE HINTS OF LONG-LIVED PARTICLES AT THE LHCB AND CODEX-B EXPERIMENTS

Author

Emilio Xosé Rodríguez Fernández

Supervisor/s: Xabier Cid Vidal

Titus Mombächer

Tutor: Xabier Cid Vidal

PHD PROGRAMME IN NUCLEAR AND PARTICLE PHYSICS

SANTIAGO DE COMPOSTELA - 2025

The author declares that there are no conflicts of interest related to the research presented in this thesis.

USC
UNIVERSIDADE
DE SANTIAGO
DE COMPOSTELA

"Somewhere, something incredible is waiting to be known."

— Carl Sagan

"Science is the belief in the ignorance of experts."

— Richard P. Feynman

"Cuidado con la fiesta, que nos la quitan de los fuciños"

— Arsenio Iglesias

USC
UNIVERSIDADE DE SANTIAGO DE COMPOSTELA

Abstract

This thesis contributes to the search for Long-Lived Particles beyond the Standard Model in the LHCb and CODEX-b experiments. It presents an analysis of the rare B-meson decays into multi-muon final states predicted by non-minimal Composite Higgs models. Experimental data from LHCb corresponding to Run 2 are used to set limits in both the prompt and displaced regimes for B_s^0 and B^+ decay chains, with several reconstruction techniques explored to maximize the sensitivity reach. The work also describes contributions to the early development of the future CODEX-b detector, including the installation of the CODEX-β demonstrator during Run 3 and the creation of a fast-simulation framework.

USC
UNIVERSIDADE
DE SANTIAGO
DE COMPOSTELA

Resumen

Esta tesis contribuye a la búsqueda de Partículas de Larga Vida más allá del Modelo Estándar en los experimentos LHCb y CODEX-b. Se presenta un análisis de desintegraciones raras de mesones B en estados finales con múltiples muones, predichas por modelos de Higgs Compuesto no minimales. Se utilizan datos experimentales del detector LHCb durante Run 2 para establecer límites tanto en el régimen prompt como en el desplazado para las cadenas de desintegración de B_s^0 y B^+, explorando varias técnicas de reconstrucción para maximizar la sensitividad. El trabajo también describe contribuciones al desarrollo temprano del futuro detector CODEX-b, incluyendo la instalación del detector demostrador CODEX-β y la creación de un sistema de simulación rápida.

USC
UNIVERSIDADE DE SANTIAGO DE COMPOSTELA

Resumo

Esta tesis contribúe á busca de Partículas de Longa Vida alén do Modelo Estándar nos experimentos LHCb e CODEX-b. Preséntase unha análise de desintegracións raras de mesóns B en estados finais con múltiples muóns, preditas en modelos de Higgs Composto non minimáis. Empréganse datos experimentais do experimento LHCb durante Run 2 para establecer límites tanto no réxime Prompt como no desprazado para cadenas de desintegración de B_s^0 e B^+, explorando diferentes técnicas de reconstrucción para maximizar a sensitividade. O traballo tamén describe a contribución ao cedo desenvolvemento do futuro detector CODEX-b, incluíndo a instalación do detector demostrador CODEX-β e a creación dun sistema de simulación rápida.

USC
UNIVERSIDADE DE SANTIAGO DE COMPOSTELA

Acknowledgements

Non podo evitar emocionarme recordando o que supoñen estes últimos anos da miña vida; de grande esforzo, de invaluable aprendizaxe e de incribles compañías. Máis que o sabor que otorga unha victoria persoal, celebro a influencia que as seguintes persoas tiveron en min, formando parte indivisible desta tese.

En primeiro lugar, é obrigado decir grazas ás dúas persoas máis importantes desta etapa, Xabier e Titus, sen os cales nada tivera sido posible. Celebro a vosa compañía nos momentos bos, pero sobre todo nos máis duros. Grazas polo apoio incondicional e pola aprendizaxe que os dous me brindastes. Soamente podo aspirar, algún día, a alcanzar parte dos incribles físicos que sodes vós.

Dentro da gran familia que supuxo o IGFAE nos últimos anos, comezar por dar grazas ás persoas coas que máis preto teño traballado. Grazas a Carlos, porque sen ser directamente responsable da tese, sempre atopou tempo e forzas para axudarme. Grazas a Máximo por sempre intentar transmitirnos gran parte da súa sabiduría. Especial grazas a Miguel, por compartir o proceso de crecemento dentro da física, con todas as anécdotas que nos levamos das viaxes e dos momentos de oficina, que non son poucos. Pablo e María, que chegastes ben avanzada a tese, grazas porque desfrutei do relativo pouco tempo que compartimos e porque me levo moitas leccións pola vosa parte. Tamén grazas a Adrián, Alexandre e Saúl, por sempre sacar un oco cando a física se tornaba difícil. Grazas tamén a Marcos, porque sen a súa axuda non sabería tanto de informática como sei agora.

Aínda que non directamente, desfrutei da presenza que moitas persoas do IGFAE me brindaron. En primeiro lugar, Iván, co que considero que me une unha gran amizade que comezou nos tempos da Covacha, e evolucionou ate convertirse nunha persoa máis que indispensable. Grazas tamén a Cristina, Sara e Victoria, por todos os cafés que desfrutamos. Tamén grazas a todas as persoas coas que compartín tempo estes últimos anos, por cultivar un espazo de traballo inmellorable. Non querería esquecerme de Marina, por sempre estar disposta a axudarnos, por facernos sentir coma na casa e por sempre recibirnos cun gran sorriso.

Especial mención merece tamén Albert, que pese a atoparse nas miñas antípodas do coñecemento futbolístico, é unha persoa con quen compartín moito e sen a cal non concibiría o mundo da física de partículas. Una abraçada, amic!

Turning into English, I would like to acknowledge the people whose impact on this

USC DE COMPOSTELA

process is invaluable. First, thanks to María Ramos for guiding me through my first steps in the difficult theory of the field. Thanks, Dean for your invitation to Berkeley Lab, which has been, to date, one of the most important experiences in my life. If I know now something about LLPs, it is because of you. Thanks, Harry, for becoming a fundamental part of this thesis: for always being willing to help, to teach and for cultivating that family atmosphere that I consider was fundamental in our difficult moments of multi-tension. I would not like to forget people like Juliette (apart from agreeing to help in reviewing the manuscript, for the good treatment that you always gave me), Phil (for procuring everything we needed at every moment), Andrii (for his invaluable inputs into the analysis) and Thomas (for his help during the last years). I would also like to acknowledge all the people who have ever contributed their grain of sand to improve the quality of my research: Miguel Ramos, Giulio, Simon, Michael W., Vitalii and Tom Gorordo, among many others. My apologies in advance if I cannot cover now the full list of people.

Durante todos estes anos, disfrutei da compañía sen igual dun amplo grupo de xente que deixaron o seu grao de area na miña evolución. Por orde cronolóxica, grazas a todos os meus amigos de Monforte, cos cales teño compartido inquedanzas, alegrías e momentos vitais durante toda a miña vida. Gran influencia tamén tivo o meu dream team de físicos da USC: JD, Xoel, Sebas, Pablo e Juan, aos que despois se incorporaron incondicionais como Alicia e Alejandro; un grazas como unha catedral. Punto de inflexión supuxo, tamén, coñecer a toda a miña familia do Monte da Condesa, en especial a Tito, Dani, Ildara, Rocío, Sheiliña, Eva, Rachel e Manoliño, entre outros; persoas que aínda que estén lonxe, sempre serán consideradas como familia.

Non me quero esquecer do grupo de xente irrepetible que me atopei no CERN, cos cales disfrutei dos mellores momentos na última etapa da miña tese. Como non, Nuria, Manuel, Sergio, MariFer, Guillermo, Miguel e Andrea sempre estaredes na miña aliñación titular. Back into English, Felicia, another component of the CERN team, and the CODEX squad, Zarria, Eloi, Jake, Michael and Silviu. You all gave me something that I will never give up.

Antes de finalizar, quero que as últimas palabras vaian dirixidas á miña familia, porque se algo son hoxe en día é porque vos o fixestes posible. Primeiro grazas Mamá e Papá, por sempre apoiarme en todo o que me propuxen e por querernos a min e a María de forma infinita. Gracias María por ser a parte de fóra de min que creceu comigo. Non cho digo moito, pero estou moi orgulloso do que estás a conseguer. Gonzalo, grazas por formar parte da nosa familia durante este curto tempo; considérote un irmán máis. Grazass Tatá e Juanjo, por ser os segundos pais dos vosos tres sobriños favoritos. Flavia, grazas por medrar xunto a nós: sempre estaremos contigo, querémoste como unha irmá. Gracias Paco por toda a sabiduría que nos transmites e por ser a persoa máis divertida que coñezo: se o meu humor é como é, todos os créditos son teus. Tamén grazas a Elisa, porque aínda non véndonos moi a miúdo, sempre atopa tempo para demostrarme o seu cariño e a felicidade que sente ó vernos medrar. Non quero olvidarme, tampouco,

do resto da familia, que de igual forma contribuíu ao meu crecemento como persoa.

Por último, quero dar grazas á persoa que, pese a chegar recentemente á miña vida, é a responsable de que sorrira a miúdo durante a escritura desta tese, Laura. Grazas por ser como eres, por complementarme e por recordarme a miúdo o cariño que, ás veces, esquezo terme a min mesmo.

Sentido recordo, tamén, cara os meus avós Antonio, Fina, Julia e Paco, que dende cativo estiveron ao meu carón. Estou convencido de que por pequenas que sexan as mal chamadas victorias, celébranas como ninguén alá onde estean. Quérovos.

USC
UNIVERSIDADE DE SANTIAGO DE COMPOSTELA

Contents

1 Introduction: small parts that make a whole **2**

1.1 The Standard Model of Particle Physics 4

1.2 Deviations from the Standard Model 12

1.3 Long-Lived Particles 18

2 Hypothesis, Objectives and Methodology **29**

2.1 Hypothesis and Objectives 29

2.2 Methodology 30

3 Experimental Landscape and Detector Performance **31**

3.1 The Large Hadron Collider 31

3.2 The LHCb experiment 33

3.3 LHCb subsystems 35

3.4 LHCb Run 2 data-taking and Detector Upgrades 42

3.5 State of the Art in LLP searches 52

3.6 The CODEX-b experiment 58

4 Following the track of hierarchical sectors at LHCb **66**

4.1 Phenomenological Analysis 67

4.2 Decay time and Mass Maps 69

4.3 Expected Backgrounds 74

5 Multimuon Searches at LHCb **80**

5.1 Analysis strategy 80

5.2 Data and MC samples 82

5.3 Signal Selection 85

5.4 Simulation Corrections 98

5.5 BDT selection 102

5.6 Backgrounds 112

USC UNIVERSIDADE DE SANTIAGO DE COMPOSTELA

5.7 Normalization and Sensitivities . . . 121
5.8 Fit Model . . . 131
5.9 Systematic Uncertainties . . . 140
5.10 Results . . . 149

6 Installation of a demonstrator detector: CODEX-beta 156
6.1 RPC Assembly and Commissioning . . . 156
6.2 Mechanical integration and Service Routing . . . 161
6.3 Installation of CODEX-β . . . 164

7 Fast Simulation Framework for CODEX-b 168
7.1 Simulation Framework . . . 169
7.2 Results: ESPPU update . . . 171

8 Results and Discussion 175
8.1 Phenomenological analysis . . . 175
8.2 Multimuon searches at LHCb . . . 176
8.3 Installation of a demonstrator detector: CODEX-β . . . 176
8.4 Fast Simulation Framework for CODEX-b . . . 177

9 Conclusions 178

10 Resumo en Galego 180
10.1 Introducción . . . 180
10.2 Condicións Experimentais . . . 181
10.3 Estudo fenomenolóxico de pistas Multimuónicas en LHCb . . . 182
10.4 Análise experimental de Multimuóns en LHCb . . . 184
10.5 Instalación do demostrador CODEX-β . . . 186
10.6 Sistema de simulación rápida para CODEX-b . . . 187

USC UNIVERSIDADE DE SANTIAGO DE COMPOSTELA

1

Introduction: small parts that make a whole

Since the dawn of civilization, humanity has displayed an enduring curiosity toward the animal kingdom, a trait that eventually contributed to the emergence of a scientific worldview. Over time, the instinct for mere survival evolved into a drive for understanding, enabling humans to manipulate and reshape their environment according to deliberate intentions. As rational thought developed, the universe itself became the central object of human consciousness and inquiry.

The first attempts to explain the Universe date back to the foundation of Atomism by *Democritus* (century V b.C.) [1]. In this school of thought, it was proposed that the ultimate answer to the functioning of nature was found in its minimal structure, indivisible entities called atoms. However, it would not be until the 19th century that the true precursor of the Atomic Theory was born with the ideas of *John Dalton* [2]. In his theory, it is derived that chemical elements are formed by unique and indivisible entities (atoms) and that the differentiation between chemical species resides in the different nature of their structural elements. Later, two events of no lesser importance took place: first, the discovery of the electron by *J.J. Thomson* [3] and the proposal of his new atomic model, with electrons stuck to the atomic nucleus; and second, the experiment of *Ernest Rutherford* [4] which provided the first evidence of a positively charged atomic nucleus, with electrons orbiting around it.

Until that moment, the rules of Newtonian dynamics and classical Electromagnetism dominated in the explanation of all the natural effects previously observed, in virtue of a continuous and totally deterministic description. Nevertheless, several problems with no obvious explanation gave rise to a change of paradigm. First, the imposibility of explaining the black body radiation led to a preliminary explanation by *Max Planck* [5] in which the continuous notion of nature was exchanged by a discrete naturalness, assuming that the black body only could emit or absorb energy in terms of *quanta* of

USC DE COMPOSTELA

energy, giving birth to the first appearance of the quantum theory. This explanation was widely rejected until later on, in 1905, when *Albert Einstein* used the same principle to explain the Photoelectric Effect [6]. Second, the atomic model from Rutherford was not stable, in contrast to the apparent stability of the perceptible reality, which led to the development of new models that, incorporating the principles of the newly born Quantum Mechanics, managed to give a satisfactory prescription of the smallest scales of the Universe [7].

Within this field, the work of remarkable personalities like *Louis de Broglie*, with the wave-particle duality [8], *Werner Heisenberg*, with the uncertainty principle [9], or *Erwin Schrodinger*, with the new laws of the wave mechanics [10], laid the foundations for what would become today's quantum theory. Nevertheless, again, many questions remained unsolved, since the theory was only valid in low-energy scales. For example, Schrodinger's equation was unable to explain spontaneous photon emission in electrons without any applied magnetic field and failed when trying to describe the motion of photons, since it was inconsistent with the principles of Special Relativity, described by Albert Einstein back in 1905.

During the decade of the 1920s, the first attempt to combine Quantum Mechanics with the notions of Special Relativity was carried out to study the interactions between the electrons and photons, giving rise to the first quantization of a classical field: the electromagnetic field. This quantization consisted of the evolution from a continuous classical field to an ensemble of coupled harmonic oscillators that, due to Heisenberg's principle, had a non-zero zero-point energy. This result introduced a new paradigm in particle physics, since the idea of the classic static vacuum turned into a description in which even nothing contains something, questioning the very foundations of the human conception of the universe. Another breakthrough was the achievement of a wave function analogous to the Schrödinger equation: the Dirac Equation (derived by *Paul Dirac*) [11]. The new one predicted new equivalent states to the electron, but with negative energy and opposite charge, which was considered the first ever theoretical evidence of the existence of antiparticles. The experimental proof of such particles would come later in the decade of the 1930s, when *Carl David Anderson* observed them with the cloud chamber [12].

These aforementioned efforts, even with problems like the infinities inside the theories (which would be sorted out with the renormalization techniques in the decade of 1950) [13, 14], gave rise to the simultaneous description of three out of the four forces governing nature[1] [15, 16, 17] and to the classification of the fundamental constituents of reality according to the interactions to which they respond. This theory is currently known as the Standard Model of Particle Physics (SM)—a detailed introduction can be found in [18].

USC UNIVERSIDADE DE SANTIAGO DE COMPOSTELA

[1] Namely electromagnetism and weak nuclear force (unified inside the so-called electroweak unification) and the strong nuclear force

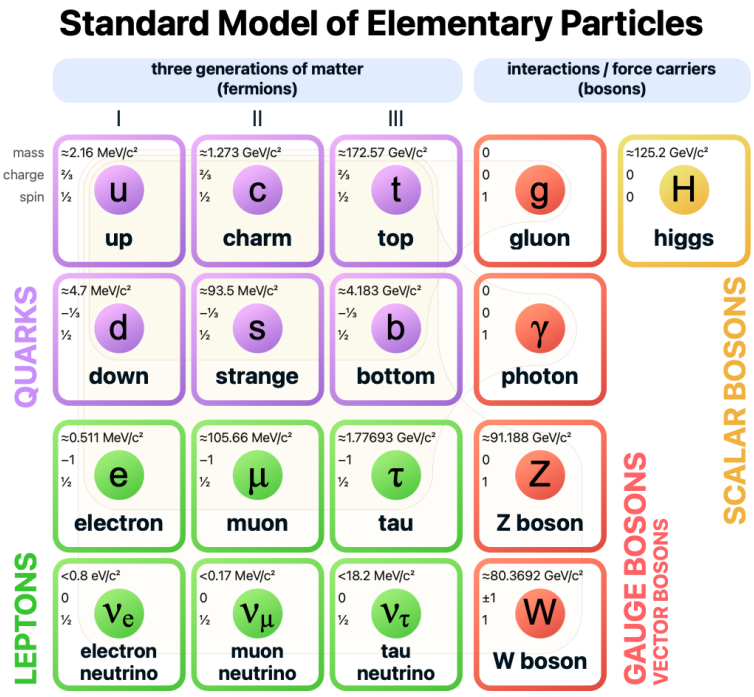


Figure 1.1: Representation of the different blocks that form the Standard Model of Particle Physics. Fermions, the fundamental blocks of matter, are composed of two other families: quarks, particles that experience the strong force, and leptons, the electroweak. Bosons, on the contrary, are the carriers of the fundamental interactions. Obtained from [20] under Creative Commons CC BY 3.0.

1.1 The Standard Model of Particle Physics

The Standard Model (SM), also known as *Glashow–Weinberg–Salam* model, is the most fundamental mathematical theory that describes nature at subatomic scales, namely the nature of the constituent blocks of matter and unequivocally the interactions existing among them. This theory is specifically a gauge theory[2] with a $U(1)\times SU(2)\times SU(3)$ symmetry group, which naturally accomodates the electroweak, under the $U(1)\times SU(2)$ group and the strong interaction, under the $SU(3)$ [19]. Interactions are derived from the Lagrangian invariance under local transformations belonging to the latter symmetry groups.

Fundamental particles are differentiated from their spin properties: on the one hand, fermions have half-integer spin, therefore satisfying the Fermi-Dirac statistic; and on the other hand, bosons (carriers of interactions) have integer spin and they obey the Bose-Einstein statistic.

Fermions are considered the fundamental blocks of matter, and at the same time, they can be split into two families according to their interactions: quarks, the fundamental particles that experience the strong force, and leptons, which experience the

[2] Quantum Field theory that contains one or certain degrees of freedom that, under a given transformation, do not modify the physical observables of the theory.

electroweak force. The first ones are characterized by fractional electric charges, being $Q = 2/3$ for u,c, and t quarks and $Q = -1/3$ for d,s, and b; building up the particles that form the atomic nucleus due to hadronic confinement. Leptons, however, are completely blind to the strong force and are split into 6 flavors, organized at the same time in doublets (e^-, ν_e), (μ^-, ν_μ) and (τ^-, ν_τ), i.e., irreducible representations of the SU(2) × U(1) group [21]. As can be observed in Figure 1.1, those fundamental matter blocks are organized in three different generations or mass scales:

- **First Generation:** u, d, e and ν_e are the lightest elements of the Standard Model.
- **Second Generation:** c, s, μ and ν_μ are almost-identical copies of the elements from the first generation, apart from non-negligible mass differences.
- **Third Generation:** t, b, τ and ν_τ the heaviest mass-wise copies of the other generations.

The latter ones are only accessible through high-energy particle colliders. It is worth highlighting that experimental evidence has rejected the existence of further generations [21].

Bosons, in the other column, are the carriers of the fundamental interactions, namely the photon (electromagnetic), gluons (strong force), and W/Z^0 bosons (weak force). Additionally, the Higgs boson, although it is not responsible for any force, is included as the quantum representation of the Higgs field, which governs the mechanism through which the remaining particles acquire mass. A priori, the graviton (hypothetical carrier of the gravitational force) should be included within this group, but until now, all the efforts to reconcile General Relativity and Quantum Mechanics have not prospered [22].

1.1.1 The Electroweak sector

The members of the Electroweak (EW) sector are irreducible components of the $SU(2)\times U(1)$ symmetry group [23]. Detailed analysis of the energy and angular observables on β transitions[3] have revealed that only left-handed fermion chiral states participate on such transitions. Historically, this group has been defined as the $SU(2)_L \times U(1)$ group, being correspondingly defined as the weak-isospin and the hyper-charge groups. Additionally, analysis of alternative processes like $\pi^- \rightarrow e^-\overline{\nu}_e$ or $\pi^- \rightarrow \mu^-\overline{\nu}_\mu$ has demonstrated the universality of the interaction strength [21].

For the $SU(2)_L \times U(1)$ symmetry, the covariant derivative can be expressed in the following way [24]:

[3] First observation through $^{60}\mathrm{Co} \rightarrow ^{60}\mathrm{Ni}^* + \mathrm{e}^-\overline{\nu}_\mathrm{e}$, carried by Wu and collaborators [21].

$$D_\mu = \partial_\mu - ig\sum_{i=1}^{3} W_\mu^i T_i - ig' B_\mu Y \tag{1.1}$$

where g and g' represent the coupling constants to $SU(2)_L$ and $U(1)$ respectively, the fields W_μ^i and B_μ are the carriers of the gauge interaction and the T_i[4] and Y are the generators of the non-abelian gauge groupe $SU(2)_L$ and the generator of the gauge group $U(1)$. Note that both groups are factorized as Y commutes with each T^i.

Usually, the latter covariant derivative is expressed in function of the generator $Q = T_3 + Y$ [25] (the generator of the usual electromagnetic group $U(1)_{em}$), the definition of the complex fields $W_\mu^\pm = \frac{W_\mu^1 \pm iW_\mu^2}{\sqrt{2}}$ with the rotation:

$$\begin{pmatrix} B_\mu \\ W_\mu^3 \end{pmatrix} = \begin{pmatrix} cos\theta_W & -sin\theta_W \\ sin\theta_W & cos\theta_W \end{pmatrix} \begin{pmatrix} A_\mu \\ Z_\mu \end{pmatrix} \tag{1.2}$$

where θ_W is the weak-mixing angle. This way, and with the reformulation of the coupling constants $g = \frac{e}{sin\theta_W}$ and $g' = \frac{e}{cos\theta_W}$:

$$D_\mu = \partial_\mu - i\frac{g}{\sqrt{2}}\left(W^+T^+ + W^-T^-\right) - ie\mathcal{Q}A_\mu - i\frac{g}{cos\theta_W}\left(T_3 - sin^2\theta_W\mathcal{Q}\right)Z_\mu \tag{1.3}$$

where $T^{+-} = T_1 \pm iT_2$ are ladder operators.

The Lagrangian for the Electroweak sector could be finally obtained by adding up the corresponding fermionic Dirac Lagrangian components and the gauge interaction term [23]:

$$\mathcal{L}_{EW} = \sum_\psi \overline{\psi_\mu} i\gamma^\mu D_\mu \psi_\mu - \frac{1}{4}W_a^{\mu\nu}W_{\mu\nu}^a - \frac{1}{4}B^{\mu\nu}B_{\mu\nu} \tag{1.4}$$

where the field strenghts have been included with the definitions $B_{\mu\nu} = \partial_\mu B_\nu - \partial_\nu B_\mu$ and $W_{\mu\nu} = \partial_\mu W_\nu - \partial_\nu W_\mu - ig[W_\mu, W_\nu]$; which represents the non-abelian structure of the $SU(2)$ group. The Lagrangian 1.4 (without mass terms) predicts the existence of the interactions captured in Figure 1.2. The gauge part involving the field derivatives also admits self-interaction between gauge mediators, predicting vertices up to four gauge mediators.

A key point inside the theory is represented by the Cabibbo hypothesis, which postulated a misalignment between the weak interaction eigenstates and the mass eigenstates in the quark sector [21]. The latter was born from experimental tensions which pointed towards a lepton flavour violation in superallowed nuclear transitions like $d \to ue^-\overline{\nu}_e$, showing a strength 5% smaller than the corresponding muonic decay. Other effects, like the difference observed between $K^- \to \mu^-\overline{\nu}_\mu$ and $\pi^- \to \mu^-\overline{\nu}_\mu$ de-

[4] The $SU(2)_L$ generators satisfy the conmutation relations $[T_i, T_j] = i\epsilon_{ijk}T_k$

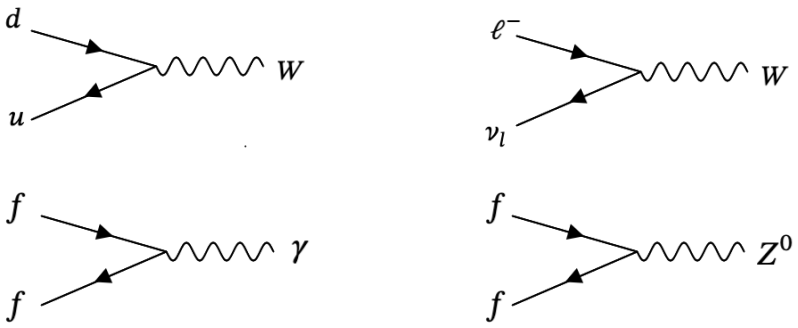


Figure 1.2: Charged (Up) and neutral (Down) current interaction vertices allowed by the electroweak lagrangian. For simplicity, only the first generation of quarks and leptons has been considered. Note, however, that this process is analogous for the rest of them.

cays [21], showing a difference of a factor 20, confirmed such a deviation. The unitary transformation connecting weak and mass eigenstates is formalized by the CKM matrix (Cabibbo–Kobayashi–Maskawa)

$$\begin{pmatrix} d' \\ s' \\ b' \end{pmatrix} = \begin{pmatrix} V_{ud} & V_{us} & V_{ub} \\ V_{cd} & V_{cs} & V_{cb} \\ V_{td} & V_{ts} & V_{tb} \end{pmatrix} \begin{pmatrix} d \\ s \\ b \end{pmatrix} \approx \begin{pmatrix} 1-\lambda^2/2 & \lambda & A\lambda^3(\rho - i\eta) \\ -\lambda & 1-\lambda^2/2 & A\lambda^2 \\ A\lambda^3(1-\rho-i\eta) & -A\lambda^2 & 1 \end{pmatrix} \begin{pmatrix} d \\ s \\ b \end{pmatrix} \tag{1.5}$$

where $\lambda \approx sen\theta_c = 0.225$ is expresed in function of the Cabbibo angle and A, ρ and η are the so-called Wolfenstein parameters [26]. The elements of the matrix are inevitably constrained by experiment, being one of the most important demands $\eta \neq 0$ to protect the quark sector against CP violation processes. The extraction of the CKM complex phases requires indirect probes, such as CP-violating observables. These have been studied extensively in neutral kaon and B-meson systems [26].

The unitarity of the CKM matrix triggers constraints among complex products of its elements, which can be represented as triangles. As can be seen in Figure 1.3, one of the most common representations makes use of the angles α, β and γ, which are related to the B_d^0 meson dynamics. Their experimental determination involves time-dependent analysis on CP-asymmetries of non-leptonic two-body decays, and the current values are [26]:

$$\alpha = \left(84.5^{+5.9}_{-5.2}\right)^\circ; \quad sin2\beta = 0.691 \pm 0.017; \quad \gamma = \left(73.5^{+4.2}_{-5.1}\right)^\circ; \tag{1.6}$$

1.1.2 The Strong sector

USC UNIVERSIDADE DE SANTIAGO

Classically, the infinitesimal (almost zero) distances between quarks in the protons and neutrons suggested the inclusion of a new quantum number to avoid the restrictions

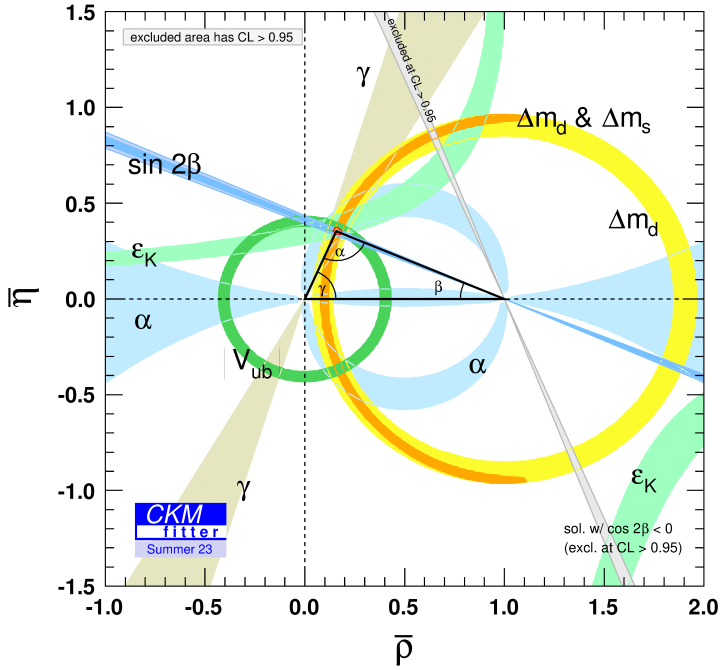


Figure 1.3: Global fit of the parameters of the CKM matrix in the $(\overline{\rho},\overline{\eta})$ plane. Obtained from [27].

imposed by Pauli's exclusion principle: the colour. Such an assumption provoked that colour states must manifest as colour's singlets, i.e., neutral combinations of colour states, therefore building a unitary symmetry group upon 3 different colors, namely: blue, green and red [21]. The possible colour combinations give rise to the two classic families of hadrons: baryons, composed of three different colour states, and mesons, formed by a colour–anticolour pair. Beyond the conventional mesons and baryons, QCD also allows for exotic multi-quark states such as tetraquarks and pentaquarks. The LHCb experiment [28] has played a key role in confirming these states. In 2019, LHCb reported a narrow pentaquark $P_c(4312)^+$ and resolved the previously observed $P_c(4450)^+$ into two distinct peaks $P_c(4440)^+$ and $P_c(4457)^+$ [29]. Theoretical analyses have interpreted these in terms of hadronic molecular configurations [30]. On the tetraquark side, the fully-charmed resonance $X(6900)$ observed by LHCb prompted systematic spectroscopic studies [31] and theoretical predictions of LHC production rates [32, 33]. Additionally, LHCb has observed a doubly charmed tetraquark T_{cc}^+, adding further evidence to the diversity of exotic hadrons [34].

The unitary matrices of the $SU(3)$ group can be written in the form $U = \exp\left[i\frac{\lambda^a}{2}\theta_a\right]$, where $\frac{\lambda^a}{2}$ $(a = 1, 2, ..., 8)$ are the so-called Gell-Man matrices, traceless and satisfying [23]:

USC UNIVERSIDADE DE SANTIAGO DE COMPOSTELA

$$\left[\frac{\lambda^a}{2}, \frac{\lambda^b}{2}\right] = if^{abc}\frac{\lambda^c}{2} \tag{1.7}$$

where f^{abc} are the (real and antisymmetric) $SU(3)$ structure constants.

Since there are 8 independent gauge parameters, 8 different gauge bosons are needed and, therefore, the following covariant derivative is built [23]:

$$D_\mu = \partial_\mu - ig_s \frac{\lambda^a}{2} G_a^\mu \tag{1.8}$$

Under an infinitesimal $SU(3)$ transformation, the quark and gauge fields transform according to the following expressions [23]:

$$q^{\alpha,*} = q^\alpha + i \left(\frac{\lambda^a}{2}\right)_{\alpha\beta} \delta\theta_a q^\beta \tag{1.9}$$

$$G_\alpha^{\mu,*} = G_a^\mu + \frac{1}{g_s}\partial^\mu \delta\theta_a - f^{abc}\delta\theta_b G_c^\mu \tag{1.10}$$

which ensures the Lagrangian is invariant under such transformations. Finally, introducing the gauge kinetic term through the corresponding field strengths:

$$G_a^{\mu\nu} = \partial^\mu G_a^\nu - \partial^\nu G_a^\mu + g_s f^{abc} G_b^\mu G_c^\nu \tag{1.11}$$

The Lagrangian of the theory lies [23]:

$$\begin{aligned}\mathcal{L}_{QCD} = &-\frac{1}{4}(\partial^\mu G_a^\nu - \partial^\nu G_a^\mu)(\partial_\mu G_a^\nu - \partial_\nu G_a^\mu) + \sum \overline{q}^\alpha (i\gamma_\mu \partial_\mu - m) q^\alpha \\ &+ g_s G_a^\mu \sum \overline{q}^\alpha \gamma_\mu \left(\frac{\lambda^a}{2}\right)_{\alpha\beta} q^\beta - \frac{g_s}{2} f^{abc}(\partial^\mu G_a^\nu - \partial^\nu G_a^\mu) G_\mu^b G_\nu^c \\ &- \frac{g_s^2}{4} f_{ade}^{abc} G_b^\mu G_c^\nu G_\mu^d G_\nu^e\end{aligned} \tag{1.12}$$

from which, again, clear self-interaction terms between the carriers (up to a four-interaction vertex) are noticeable, indicating a non-abelian structure.

Among its greatest achievements are the success in the prediction of the hadrons' inner structure, the jets' kinematics, and the most important one, the asymptotic freedom [21], observed after the decrease of the strong coupling constant at high energies. This phenomenon has been extensively investigated in a plethora of experiments, as shown in Figure 1.4. Hitherto, the most precise measurement has been reached by the ATLAS collaboration, achieving a total uncertainty of 1% using proton-proton data at an energy of 8 TeV [35].

1.1.3 The Higgs Mechanism

A new paradigm emerged in the decade of 1960 with the unification of the Electromagnetism and the Weak Nuclear Force under the umbrella of the Electroweak theory.

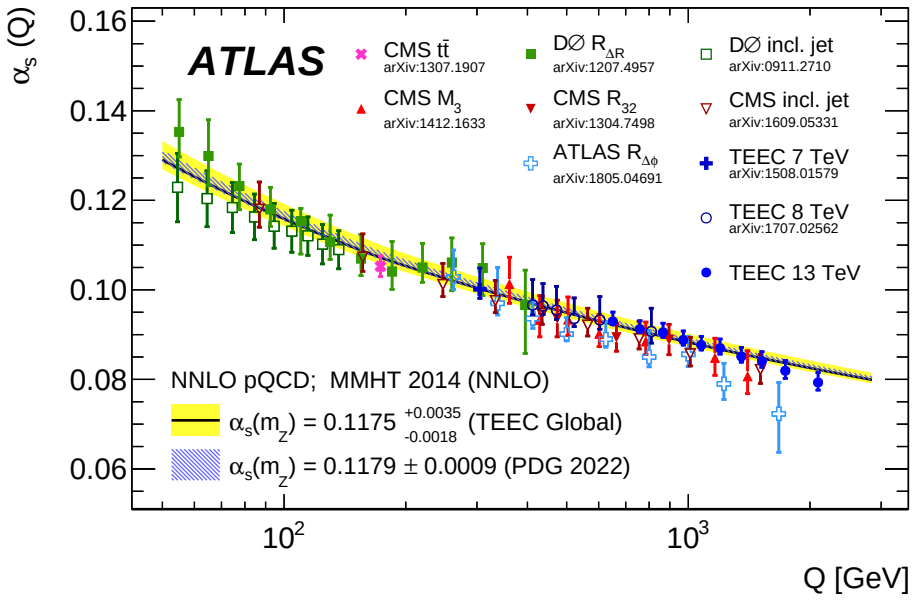


Figure 1.4: Strong Coupling Constant α_s comparison. Obtained from [36] under CC BY 4.0.

Despite its precision and mathematical elegance, the theory remained unable to explain the origin of the mass of the subatomic particles. Concretely, to preserve local gauge invariance, they should remain massless, contrary to what experiments were elucidating. This problem would finally be resolved with the inclusion of the so-called *Higgs-Englert-Brout Mechanism* [37, 38].

Such a mechanism is embedded in the local $SU(2) \times U(1)$ gauge symmetry of the Electroweak sector and, at first glance, it is responsible for generating the masses of the corresponding gauge bosons. The Higgs field, therefore, is represented by an isospin doublet with a neutral ϕ^0 and charged ϕ^+ complex fields [21]:

$$\phi = \begin{pmatrix} \phi^+ \\ \phi^0 \end{pmatrix} = \frac{1}{\sqrt{2}} \begin{pmatrix} \phi_1 + i\phi_2 \\ \phi_3 + i\phi_4 \end{pmatrix} \tag{1.13}$$

with four degrees of freedom, three corresponding to three Goldstone bosons (which will provide the longitudinal degrees of freedom to the W^+, W^- and Z^0 bosons) and an additional one for a massive scalar field representing the field excitations in the direction of the vacuum after the spontaneous symmetry breaking of such a field. In this regard, the Lagrangian of the doublet is defined as [21]:

$$\mathcal{L} = (\partial_\mu \phi)^\dagger (\partial_\mu \phi) - V(\phi) \tag{1.14}$$

USC UNIVERSIDADE DE COMPOSTELA

whereas the potential term lies:

$$V(\phi) = \mu^2 \phi^\dagger \phi + \lambda (\phi^\dagger \phi)^2 \tag{1.15}$$

which poses an infinite set of degenerate minima with $\mu^2 < 0$ satisfying:

$$\phi^\dagger\phi = \frac{1}{2}(\phi_1^2 + \phi_2^2 + \phi_3^2 + \phi_4^2) = \frac{v^2}{2} = -\frac{\mu^2}{2\lambda} \tag{1.16}$$

In the so-called unitary gauge, the complex field ϕ takes the form [21]:

$$\phi = \frac{1}{\sqrt{2}}\begin{pmatrix} 0 \\ v + h \end{pmatrix} \tag{1.17}$$

where h corresponds to the Higgs field. Applying the covariant derivative defined in 1.1 to the field ϕ, gauge bosons' mases can be directly obtained from the kinetic term [5] [25]:

$$\begin{aligned}(D_\mu\phi)^\dagger(D^\mu\phi) =& \frac{1}{2}(\partial^\mu h)(\partial_\mu h) + \frac{1}{8}g_W^2(W_\mu^{(1)} + iW_\mu^{(2)})(W^{\mu,(1)} + iW^{\mu,(2)})(v+h)^2 \\ &+\frac{1}{8}(g_W W_{\mu,(3)} - gB_\mu)(g_W W^{\mu,(3)} - gB^\mu)(v+h)^2\end{aligned} \tag{1.18}$$

where it can be seen that the gauge fields acquire a mass term through their interaction with the Higgs field. From there, the physical fields can be directly recovered. Firstly, considering $W^\pm = \frac{1}{\sqrt{2}}(W^{(1)} \mp iW^{(2)})$ [21], the mass and coupling term to the Higgs lies:

$$\mathcal{L}_W^{kin} = \frac{1}{4}g_W^2 v^2 W_\mu^+ W^{\mu,-} + \frac{1}{2}g_W^2 v W_\mu^+ W^{\mu,-} h + \frac{1}{4}g_W^2 W_\mu^+ W^{\mu,-} hh \tag{1.19}$$

expression from which the mass of the physical $W^\pm$ corresponds to $m_W = \frac{1}{2}g_W v$. Secondly, by diagonalizing the mass matrix, which mixes up the gauge fields:

$$\begin{pmatrix} A_\mu & Z_\mu \end{pmatrix} = \begin{pmatrix} 0 & 0 \\ 0 & g_W^2 + g'^2 \end{pmatrix}\begin{pmatrix} A^\mu \\ Z^\mu \end{pmatrix} \tag{1.20}$$

in which the physical fields are represented by the eigenvectors of the mass matrix [21]:

$$A_\mu = \frac{g' W_\mu^{(3)} + g_W B_\mu}{\sqrt{g_W^2 + g'^2}} \tag{1.21}$$

$$Z_\mu = \frac{g_W W_\mu^{(3)} - g' B_\mu}{\sqrt{g_W^2 + g'^2}} \tag{1.22}$$

The aforementioned architecture inside the $SU(2)$ group is also responsible for the generation of the fermionic masses. As the complex scalar fields of the Higgs are placed inside an $SU(2)$ doublet, infinitesimal transformations keep the product $\overline{\psi}_L\phi$ invariant

[5] For the Higgs doublet, the lower and neutral component has $I_3 = \frac{-1}{2}$, so the value of the weak hipercharge is $I = 2(Q - I_3) = 1$.

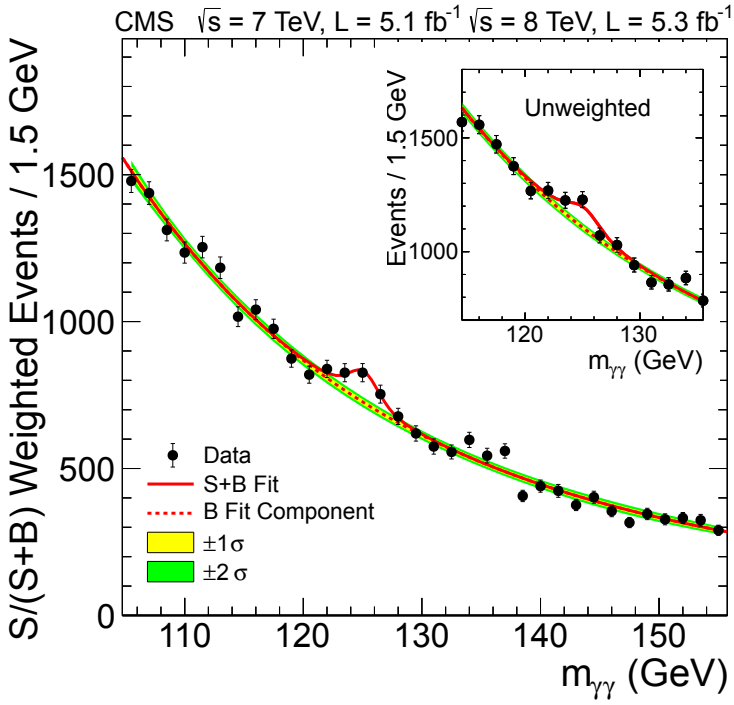


Figure 1.5: Higgs to diphoton searches at pp center-of-mass energy of 8TeV. Obtained from [39] under CC-BY-3.0.

[21, 25]. Additionally, as right-handed fermions are placed inside $SU(2)$ singlets, the total product $\overline{\psi}_L \phi \psi_R$ is by construction invariant under $SU(2) \times U(1)$ transformations. Accordingly, all fermionic mass terms can be generated from [21]:

$$\mathcal{L} = -g_f \left[\overline{\psi_L}\phi\psi_R + (\overline{\psi_L}\phi\psi_R)^\dagger\right] \quad \text{or} \quad \mathcal{L} = g_f \left[\overline{\psi_L}\phi_c\psi_R + (\overline{\psi_L}\phi_c\psi_R)^\dagger\right] \tag{1.23}$$

where the conjugate doublet is introduced as $\phi_c = -i\sigma_2\phi^*$.

The completion of the Standard Model puzzle started back at the Large Electron-Positron Collider (LEP) at CERN operations, with no evidence being recorded. Instead, lower and upper bounds were imposed on the mass of such a bosonic particle, namely $114 < m_H < 150\,\text{GeV}$ [40]. In 2012, the first experimental evidence was discovered by a simultaneous search carried by ATLAS and CMS collaborations [41, 39], at the Large Hadron Collider, in which a bosonic-type particle compatible with a Higgs boson was observed at $m_H = 125\,\text{GeV}$ (see Figure 1.5), achieving the "final" form of the Standard Model.

1.2 Deviations from the Standard Model

Since its full completion in 2012, the SM has established itself as the most accurate theoretical framework ever developed to describe the fundamental laws of nature. Despite its relatively short lifespan, it has withstood an extensive array of experimental

tests [42]. Among its most remarkable achievements are the explanation of the mass generation mechanism for fundamental particles, the precise description of all processes mediated by the fundamental interactions, and the extraordinarily accurate determination of constants such as the fine-structure constant, $\alpha^{-1} = 137.035999070(98)$ [43], measured with a precision of one part in a billion.

Nevertheless, the Standard Model cannot be considered the ultimate theory of nature. It is constructed ad hoc, relying on a set of free parameters and degrees of freedom that must be finely tuned to match experimental observations [44, 45]. As such, it is a purpose-built model. This intrinsic limitation suggests a lack of flexibility when it comes to explaining phenomena beyond its original scope [46]. Indeed, several open questions in contemporary physics seem to point precisely in this direction, namely the nature of Gravity (Section 1.2.1), Dark Matter (Section 1.2.2 or Higgs boson (Section 1.2.3), the origin of neutrino masses (Section 1.2.4) and the matter-antimatter problem of the Universe (Section 1.2.5); among others.

1.2.1 Gravity

Postulated by Isaac Newton in his work *Philosophiae naturalis principia mathematica* [47] and reformulated by Albert Einstein in the *General Relativity*[48], it is the unique fundamental force that is still not described by quantum field theory [49]. Different attempts have been made to include gravity in the Standard Model Lagrangian, none of them succeeding [50, 51]. A possible unification would require verifying the precepts of gauge invariance, through which the interaction would be described by an associated carrier, the graviton [52, 53]. Such a particle must verify it is massless, to account for the infinite scope of gravity, and possess spin 2, since gravitons must couple to the rank 2 stress-energy tensor, symmetric under a change of indices [54]. A priori, the major problem in reconciling both theories resides in the abrupt difference between the scales in which they are defined. On the one hand, the Standard Model is valid within the Electroweak scale, which is defined by the Vacuum Expectation Value of the Higgs' field $v \sim 246\,\text{GeV}$ [55]. On the other hand, hypothetical effects of Quantum Gravity would be expected to appear within the Planck scale, defined at $\sim 10^{19}$ GeV [56]. As the Standard Model is a field theory built upon a classic description of the space-time, quantum fluctuations at that scale would lead to an inevitable loss of predictability, meaning that any physical phenomena lack a valid definition [50]. In addition, the Lagrangian of the theory demands that any physical parameter must provide well-defined quantities, i.e., the theory must be renormalizable, and that is not the case of gravity [57]. In the denominated Kaluza-Klein picture [58, 59], the Einstein-Hilbert action under the weak field approximation $g_{\mu\nu} = \eta_{\mu\nu} + \frac{\kappa}{\sqrt{c}} h_{\mu\nu}$ (where the fluctuation $h_{\mu\nu}$ denotes the graviton's field)[6] becomes [60]:

USC UNIVERSIDADE DE SANTIAGO DE COMPOSTELA

[6] The constant κ is defined by $\kappa^2 = \frac{8\pi G}{c^3}$.

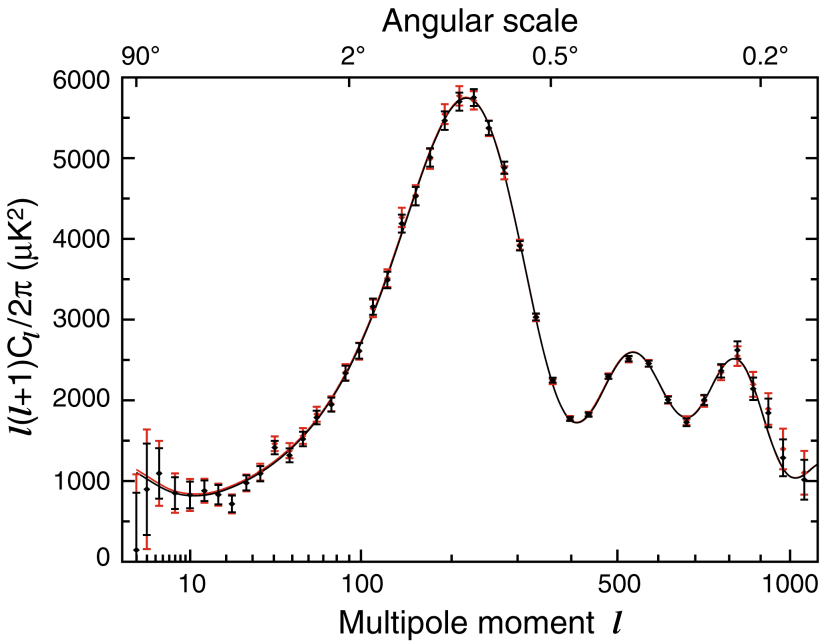


Figure 1.6: Estimates of the WMAP nine-year power spectrum along with best-fit model spectra; black – the C-1-weighted spectrum and corresponding model; red – the same for the MASTER spectrum and model. Obtained from [65].

$$S = \frac{c}{2\kappa^2}\int d^4x\sqrt{-g}R = \int d^4x\left[(\partial h)^2 + \kappa h(\partial h)^2 + \kappa^2 h^2(\partial h)^2 + \ ...\right] \tag{1.24}$$

which increases in powers of κ. There, the second-order terms are non-renormalizable, which indicates that at the Planck scale, NP must appear to recover the predictability of the theory.

1.2.2 Dark Matter

There is gravitational and cosmological evidence of a new species of matter, electrically neutral, that surpasses the abundance of ordinary matter in the Universe.

The first hints of this so-called dark matter date back to 1933, when Fritz Zwicky observed a discrepancy between the optical luminosity of the Coma Cluster and the mass inferred via the virial theorem, suggesting an incomplete understanding of the gravitational matter distribution in the cluster [61]. Decades later, in the 1970s, Vera Rubin confirmed the presence of a non-luminous component through the anomalous velocity profiles of stars in spiral galaxies [62], extending well beyond the visible matter. Additional supporting evidence has come from gravitational lensing caused by invisible mass concentrations, the unusual light distribution in the Bullet Cluster [63], and the Lyman-Alpha Forest radiation [64], which traces the large-scale distribution of dark matter.

As a relic from the Big Bang, dark matter may have coexisted with baryonic matter during a period when creation and annihilation processes were in thermal equilibrium, governed by rates exceeding the expansion of the Universe. Within this primordial plasma, photons experienced acoustic oscillations[7] [66], which—after decoupling—gave rise to the temperature anisotropies observed in the Cosmic Microwave Background (CMB) [67], shown in Figure 1.6. Detailed analyses of the angular power spectrum have demonstrated the necessity of dark matter to account for features such as enhanced odd acoustic peaks, which originate from gravitational potential wells that do not couple to the photon-baryon plasma. Cosmological models, such as the ΛCDM framework [68, 69], estimate the current relic densities as $\Omega_{\mathrm{DM}} \sim 0.26$ for dark matter and $\Omega_b \sim 0.045$ for baryonic matter [70].

Although the true nature of dark matter remains unknown, several candidates have been proposed. Among the most studied are: modifications of gravity, weakly interacting massive particles (WIMPs)[8], and primordial black holes [71].

1.2.3 Higgs Nature

Although the Higgs boson is a cornerstone of the Standard Model, several fundamental questions about its nature and role remain open. As discussed in Section 1.1.3, the Higgs mechanism postulates a complex scalar doublet whose spontaneous symmetry breaking endows the particles of the theory with mass. However, this process becomes significantly more intricate in various SM extensions.

In certain supersymmetric scenarios, such as the Two-Higgs-Doublet Model (2HDM) [72], the Higgs sector consists of two scalar doublets, yielding eight degrees of freedom. Three of these become the longitudinal components of the $W^{\pm}$ and Z^0 bosons, while the remaining five manifest as physical scalar particles: two neutral CP-even scalars (h and H^0), one neutral CP-odd scalar (A^0), and two charged scalars ($H^{\pm}$)[9]. Within this framework, the two doublets acquire different vacuum expectation values, leading to modified Yukawa couplings. As a result, deviations in Higgs–fermion interactions might be expected. To date, however, no significant discrepancies with SM predictions have been observed.

Another conceptual challenge that questions the understanding of the Higgs sector is the long-standing Hierarchy Problem [73]. While the SM accommodates large mass hierarchies between quarks and leptons under radiative corrections, this stability does not extend to the Higgs boson. In the Higgs mechanism, the parameter μ^2 (introduced with a negative sign in Eq. 1.15 to trigger electroweak symmetry breaking) is highly sensitive to quantum corrections, even at the one-loop level [74]:

[7] Caused by compression and rarefaction processes resulting from the equilibrium between gravitational collapse in potential wells and photon pressure.

[8] Predicted by theories such as Supersymmetry.

[9] In supersymmetric models, the h boson can be light and resemble the Standard Model Higgs boson, while H^0, A^0, and $H^{\pm}$ can be significantly heavier.

$$\mu^2 = \mu_0^2 - \frac{3y_t^2}{8\pi^2}\Lambda^2 + \frac{3\lambda}{8\pi^2}\Lambda^2 + \frac{9\alpha_w^2 + 3\alpha'}{16\pi}\lambda^2 + \dots \tag{1.25}$$

where Λ is the ultraviolet cut-off scale. At high energies, such a quadratic divergence should make the mass of the Higgs unusually large, contrary to what experiment dictates. This fact, known as the naturalness problem, would suggest some kind of fine-tuning that finely cancels radiative loop contributions, thus stabilizing the Higgs mass, an unnatural and highly tuned scenario. Supersymmetry offers a compelling resolution [75]: for each Standard Model particle, there exists a super-partner with spin differing by half a unit, forming two classes: sfermions (bosonic super-partners of fermions) and gauginos/higgsinos (fermionic super-partners of gauge and Higgs bosons). These super-partners contribute to loop corrections with opposite sign to those of their SM counterparts, resulting in a natural cancellation that protects the Higgs mass from divergent corrections. Of special interest for this thesis is the formulation of the Composite Higgs (CH) models, which address the hierarchy (and naturalness) problem by considering the Higgs as a low-energy bound state of a new strongly interacting sector [76]. As will be reviewed in Section 1.3.1, low-energy signatures in the form of LLPs decaying muonically might be expected, which could be investigated in the LHCb detector.

The future strategy to experimentally determine the underlying nature of the Higgs boson relies, in the short-to-medium term, on precision measurements primarily conducted at the LHC and its high-luminosity upgrade (HL-LHC). In the long term, the so-called Higgs factories take the lead in mass production of Higgses and precision studies. A Higgs factory represents a particle accelerator (fundamentally e^+e^- or $\mu^+\mu^-$ for the clean final-state production) whose conditions allow for its operation at the center-of-mass energy close to the ZH resonance [77]. Prominent proposals include linear colliders such as the International Linear Collider (ILC) [78] and the Compact Linear Collider (CLIC) [79], as well as circular colliders like the Future Circular Collider (FCC-ee) [80] or the Circular Electron Positron Collider (CEPC) [81].

1.2.4 Neutrino masses

At the beginning of the 21$^{\text{th}}$ century, the Superkamiokande and SNO experiments [82, 83] reported the first evidence of solar neutrino oscillations, which confirmed that neutrinos have mass. The origin of this mass, however, must have a different origin from the Standard Higgs mechanism.

USC DE SANTIAGO

If neutrinos are described by a Dirac field, a $SU_L(2) \times U(1)$ invariant Yukawa interaction can enter the full Standard Model Lagrangian (before and after the spontaneous symmetry breaking) [84]:

$$\mathcal{L}^{\nu} = -\sqrt{2}\sum_{l_1,l_2}\overline{\psi}_{l_1,L}Y^{\nu}_{l_1,l_2}\nu_{l_2,R}\phi^{c} \ + \text{h.c.} = -\sum_{l_1,l_2}\overline{\nu}_{l_1,L}Y_{l_1,l_2}\nu_{l_2,R}(v+h) \ + \text{h.c.} \qquad (1.26)$$

where Y is a dimensionless complex matrix.

After diagonalizing the matrix Y, the mass terms for all the neutrino generations turn $m_i = y_i v$. Taking into account the existing constraints in the mass for the heaviest neutrino mass [84], the associated Yukawa coupling must satisfy:

$$2 \cdot 10^{-13} \leq y_3 \leq 10^{-12} \qquad (1.27)$$

which is orders of magnitude smaller than the other Yukawa couplings in the third generations, namely $y_t \approx 7 \cdot 10^{-1}$, $y_b \approx 2 \cdot 10^{-2}$ and $y_\tau \approx 7 \cdot 10^{-3}$. This big hierarchy between the members of the family, added to the fact that right-handed neutrinos are needed to generate the corresponding mass terms, indicates that the generation mechanism could be beyond the scope of the SM.

A widespread mass generation process is represented by the Weinberg see-saw mechanism, which makes use of the fact that neutrinos are Majorana particles [84]. In this manner, SM would interact with heavy Beyond the Standard-Model (BSM) particles at a scale $\Lambda \gg v$ and, back at the Electroweak scale, those fields are integrated out and they induce a nonrenormalizable interaction responsible for such a mass generation.

The search for NP in the neutrino sector seems to be leaning towards the search for neutrinoless double-beta emissions, which would confirm that they are Majorana particles. Up to date, several experiments have been trying to observe those transitions in decays such as ${}^{76}_{32}\text{Ge} \rightarrow {}^{76}_{34}\text{Se} + 2e^-$ [85] and ${}^{136}_{54}\text{Xe} \rightarrow {}^{136}_{56}\text{Ba} + 2e^-$ [86], quoting the most stringent limits $\tau^{0\nu\beta\beta}_{1/2} > 10^{25}$ years.

1.2.5 Matter-Antimatter asymmetry

One of the great achievements of the Standard Model resides in the explanation of why Baryonic and Leptonic numbers are conserved. However, the sensible experience (both at small and cosmological scales) indicates a matter dominance over antimatter, which is known as *Matter-Antimatter asymmetry*.

In the early Universe, baryonic and antibaryonic matter would remain in thermal equilibrium, in processes of creation and consequent annihilation [87]. As the Universe expanded, when the temperature fell below the expansion rate, particles and antiparticles were not able to recombine and the apparent imbalance was created. The conditions over which such an imbalance was created were summarized in the Sakharov conditions [88]: a net difference between baryons and antibaryons at thermal equilibrium, the existence of C and CP violation and a departure from thermal equilibrium. To date, no theory containing the aforementioned requirements has been successful

enough.

In the SM, CP violation can be accommodated in the weak interactions of quarks and leptons through the irreducible complex phases in the CKM matrix, but it is not sufficient to explain the matter–antimatter asymmetry of the Universe. To date, CP violation has been firmly established in the quark sector: first in the neutral kaon and B-meson systems [89, 90, 91], and more recently in the charm sector through the observation of direct CP violation in $D^0 \to K^-K^+$ and $D^0 \to \pi^-\pi^+$ decays by the LHCb collaboration [92]. A further milestone was reached with the first observation of CP violation in the baryon sector, namely in $\Lambda_b^0 \to pK^-\pi^+\pi^-$ decays by LHCb, reporting an asymmetry of $(2.45 \pm 0.46 \pm 0.10)\%$ with a significance of 5.2σ [93]. This result is particularly important because it extends the study of CP violation beyond mesons to heavy baryons, opening a novel domain for testing the CKM mechanism and probing possible new-physics contributions.

It has been suggested that CP violation in the lepton sector during the early moments of the Universe could account for the current asymmetry [94], even though experimental data have not yet pointed in either direction or the possibility of other mechanisms.

1.3 Long-Lived Particles

A wide range of theoretical proposals aimed at addressing the tensions in the SM naturally predict the existence of Long-Lived Particles (LLPs). These are defined as any particle that traverses a macroscopic distance before decaying. Given the excellent sensitivity that may be achievable with the LHC detectors, together with the potentially large production cross sections and the large amount of data expected at the High-Luminosity LHC, LLPs have become a key component of the LHC experimental program in the near term [95].

Historically, the discoveries of the muon (1936) [96] and the kaon (1947) [97] marked a paradigm shift, as they were the first particles that did not fit the particle physics model of the time. Both were identified through their unexpectedly long lifetimes and distinct signatures in cloud chambers [98]. With the advent of particle accelerators, the focus of experimental techniques broadened: higher collision energies and luminosities demanded detectors with excellent spatial, momentum, and energy resolution, enabling precision spectroscopy and the direct discovery of heavy particles such as the W and Z bosons, the top quark, and eventually the Higgs boson [98]. Nonetheless, the capability to resolve decay vertices and measure lifetimes has remained a cornerstone of experimental particle physics — from strange and charm spectroscopy to b-tagging and time-dependent analyses such as $B^0 - \overline{B^0}$ oscillations, both at LEP [99, 100] and at the Tevatron [101, 102]. Throughout these developments, there has always been a strong interplay between direct discoveries and indirect observations, as exemplified by the experimental confirmation of the weak neutral current [103], which paved the way

for the subsequent detection of the Z^0 boson.

Following these historical precedents, exotic long-lived particles (LLPs) have long been regarded as a promising discovery channel for physics beyond the Standard Model (BSM) [95]. In the pre-LHC and early LHC eras, the theoretical landscape was shaped by the paradigm at the time, Supersymmetry, able to generate LLPs in association with high-p_T photons, jets, or leptons—a feature that made them experimentally accessible with the trigger and reconstruction strategies available before Run 1 of the LHC. More elusive signatures, lower in energy (such as neutral, low-mass, or low-momentum LLPs) remained largely unexplored at that time, partly due to technical limitations and partly because theoretical priors favored heavier spectra. From an experimental standpoint, early LLP searches were constrained by high trigger thresholds and by reconstruction algorithms optimized for prompt, high-p_T objects originating from the primary vertex. Particles decaying at large displacements or producing low-energy visible signatures were often missed or rejected by standard quality criteria, and the understanding of the associated backgrounds was still limited. As knowledge of detector performance, trigger flexibility, and background characterization improved, the theoretical and experimental focus broadened substantially, opening the door to a new generation of LLP searches beyond the traditional landscape [98].

As the LHC program matured, two important theoretical and experimental shifts took place. On the one hand, the physics community became increasingly aware of the subtleties involved in designing and recasting LLP searches, allowing improvements in trigger, reconstruction and analysis techniques [104]. On the other hand, ATLAS, CMS, and LHCb rose to the challenge, delivering a diverse set of innovative searches for LLPs, thanks to the hermeticity and precise tracking capabilities of ATLAS and CMS, complemented by the superb vertexing performance of LHCb in the forward regime [105, 106, 107].

Today, the LLP program constitutes a major component of the LHC experimental agenda. Methods that were once niche, including displaced tracking, ionization energy loss, and timing-based observables, have become central tools in the search for new physics with displaced signatures [108].

From a morphological perspective, the underlying mechanisms responsible for the generation of LLPs should be fundamentally invariant [109], irrespective of whether they appear in the spectrum of the SM or from extensions beyond it. In general, any long-lived particle must fulfil at least one of the following conditions: i) the decay occurs through a heavy, off-shell particle; ii) the decay is subject to a severe phase-space suppression, or iii) the width is suppressed by a small dimensionless parameter associated with an approximate symmetry [98]. Under those conditions, the decay width of a long-lived particle would result in:

USC UNIVERSIDADE DE SANTIAGO DE COMPOSTELA

$$\Gamma \sim \frac{\epsilon^2}{(8\pi)^{k-1}} \frac{m^n}{M^{n-1}} \tag{1.28}$$

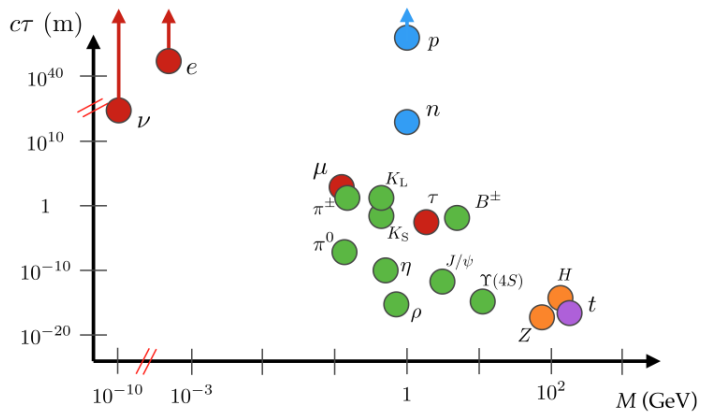


Figure 1.7: Decay length versus mass scale of the particles building the SM. Obtained from [95] under CC BY 3.0.

where ε is the suppression parameter, k the multiplicity of the final state, m the mass of the decaying particle, M the mass of the intermediate state and n an odd, positive integer that is derived through the symmetries of the theory. In the SM, the latter principles apply, shaping its vast landscape of lifetimes (displayed in Figure 1.7) in the following manner:

- **Proton stability:** Due to the accidental baryon-number symmetry in the SM.
- **Muon lifetime:** The small coupling to a large dimensionful scale arises because of the high mass of the W boson.
- **Neutron:** The small phase-space available in the decay to proton and leptons results in $\tau \sim 15$ min outside of the atomic nucleus.
- **Higgs boson:** Although non-macroscopically long-lived, the small bottom Yukawa coupling $y_b \sim 0.02$ that dominates the SM Higgs decay makes it travel an average of a proton diameter before decaying.
- **b-quark:** Phase space suppression, approximate flavour symmetry and large dimensionful scale.

Despite the relatively close nature between LLPs in the SM and in BSM theories, the discovery of exotic LLPs presents experimental challenges stemming from their production and detection [109], both correlated.

On the production side, two main sources can be differentiated: intensity frontier experiments, focusing on the generation of high rates of low-energy LLPs generated through intense beams; and energy frontier experiments, prioritizing the energy scale they allow to reach [109]. The first can be customized to search for low-mass hidden sectors with very low background sources [109, 95]. However, if the mass of the LLP increases ($\sim$ GeV, TeV), as well as higher-dimensional operators that are suppressed

by a high scale are responsible for the LLP lifetime, then intensity frontier experiments are surpassed by the energy frontier ones [109]. Of shared interest to both production modes is the limits that Big Bang Nucleosynthesis (BBN) imposes on the lifetimes of these exotic particles. If it could be produced, such a particle would have had to have been created at the primordial plasma and be in thermal equilibrium with other species, so the observed elemental abundances would limit its morphological properties [109, 95, 98]. Usually, BBN reports bounds of $\tau < 0.1 - 10^4$ s, depending on the dominant decay modes and its onset [98].

On the experimental side, exotic LLPs might have very different signatures than SM LLPs. On the one hand, if the LLP has charge or colour content, it might be detected directly with current detector technology, giving rise to unusual ionization and propagation events [109]. On the other hand, two possibilities arise: if the LLP is neutral, it might be detected through scattering off a shielded detector target if it has significant SM interactions [109] or, if contrary, it is too feebly-interacting, the detection completely relies on observing its final decay products, if any. The latter might arise as delayed signals in the detector, which could comprise calorimeter deposits without associated tracks, displaced vertices in the innermost detectors or disappearing tracks [95]. Presumably, in this last case, the most important experimental drawback is to allocate the observed LLP candidate within the available timescale of a full triggered event [95].

A priori, the vast amount of theoretical and experimental prospects to observe exotic LLPs introduces certain assumptions on the production mechanisms. Under such a consideration, in the next section, an overview of the theoretical priors that concern the research of this thesis are provided. Later in the Section 3.5, a description of the state of the art regarding the different experimental possibilities aimed at observing LLPs will be made.

1.3.1 LLPs in Composite Higgs Models

The foundations of the Composite Higgs (CH) paradigm, as discussed in Section 1.2.3, rest on the hierarchy and naturalness problems. The former refers to the large gap between the electroweak scale and the fundamental scales (Planck or GUT), while the latter refers to the apparent fine-tuning required to stabilize the Higgs mass. Both issues could be addressed if, under this hypothesis, the Higgs doublet were not elementary but rather a bound state of strongly-coupled constituents at a scale $f > v$, in close analogy with standard QCD.

This framework builds upon the implications of the Goldstone theorem [110], which states that in a relativistic quantum field theory every spontaneously broken continuous global symmetry gives rise to a massless scalar particle, one for each broken generator. If $\mathcal{G}$ denotes the global symmetry of the composite sector[10] and $\mathcal{H} \subset \mathcal{G}$ the preserved

[10]Note that $\mathcal{G}$ must be large enough to contain both one Higgs doublet in the coset and the elec-

subgroup, the Lie algebra can be decomposed into the unbroken generators T^a ($a = 1, \ldots, \dim(\mathcal{H})$) and the broken ones $\hat{T}^{\hat{a}}$ ($\hat{a} = 1, \ldots, \dim(\mathcal{G}/\mathcal{H})$). Acting on a vacuum configuration $\vec{F}$, one finds [76]:

$$T^a \vec{F} = 0, \qquad \hat{T}^{\hat{a}} \vec{F} \neq 0$$

The field Φ, which parametrizes the coset $\mathcal{G}/\mathcal{H}$, can then be written in terms of oscillations along the broken directions:

$$\Phi = e^{i\theta^{\hat{a}}\hat{T}^{\hat{a}}} \vec{F} \tag{1.29}$$

where the $\theta^{\hat{a}}$ are the associated NGBs. Once $\mathcal{G}$ is explicitly broken, these acquire a potential and become pseudo–Nambu–Goldstone bosons (pNGBs) [111]. In particular, the Higgs field is identified with one of them, developing a vacuum expectation value that triggers EW symmetry breaking.

The notion of vacuum misalignment quantifies the deviation between the spontaneous symmetry breaking scale f and the EW scale v, through the relation [76]:

$$\sin^2\langle\theta\rangle = \frac{v^2}{f^2} \tag{1.30}$$

For fixed v, in the limit $f \to \infty$ the composite sector decouples from the low-energy spectrum, leaving the Higgs boson alone as in the SM.

Potential SM departures hidden in the Higgs sector motivate the case in which the CH framework is not minimal, with additional pNGBs arising in the theory depending on the coset choice [112]. In the special case in which the coset is chosen to be $SO(7)/SO(6)$, the low-energy scalar sector would consist of a Higgs field and two real scalars, a_1 and a_2, which are singlets under the SM gauge group [112]. In virtue of the Callan-Coleman-Wess-Zumino (CCWZ) construction [113], any field transforming under $\mathcal{G}$ is connected through the coset 1.29 to the directions of the pNGB's which, in analogy to QCD, triggers a coupling between a vector boson (transforms linearly in $\mathcal{G}$) and the new singlets under the SM.

One of the most notable effects of this model is the protection a symmetry under $\mathcal{G}$ brings to the Higgs boson, effectively forbidding the direct Yukawa couplings of the fermions [111]. Following the partial compositeness paradigm [114], if fermions are partially composite, the standard fermions couple to operators of the strong sector and, after EW symmetry breaking, effective Yukawa couplings arise and mass terms are generated. In this manner, third-generation fermions (t or b) couple strongly to the composite sector, whereas the lightest ones remain more standard [115].

One potential signature of the CH models at low energies (to which LHCb might be really sensitive) is featured by intermediate scalars would be produced in $b \to s l^+ l^-$

troweak gauge group, identified with $SU(2)_L \times U(1)_Y$.

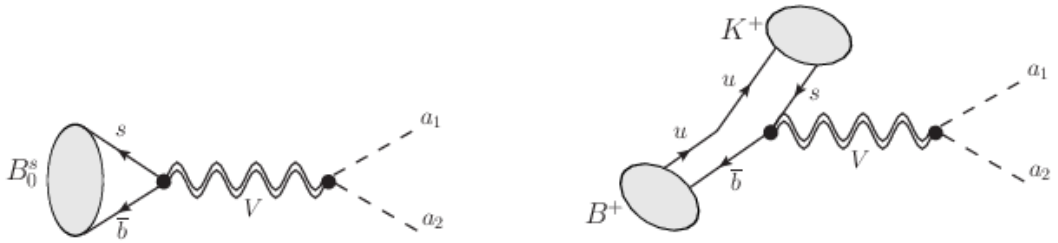


Figure 1.8: Diagramatic sketch of the decays taking place within the hierarchical framework. Obtained from [116] under CC BY 4.0.

transitions through a heavy (~ 1 TeV) flavour-violating vector boson [116]. A key point of the theory is that, under certain conditions, the appearance of Long-Lived particles in the spectrum of the theory. If additionally, the model results in non-minimal, three-body decays into intermediate scalars would dominate the spectrum and 4μ modes would be suppressed in favour of 6μ multiplicity [116]. The Lagrangian would lie as:

$$\begin{aligned}\mathcal{L} = &\left[\frac{g_{sb}g_{12}}{m_V^2}\left(\bar{b}_L\gamma^\mu s_L\right)\left(a_1 \overleftrightarrow{\partial}_\mu a_2\right) + ig_1 y^l a_1 \bar{l}\gamma_5 l + g_2 y^l a_2 \bar{l} l + \text{h.c.}\right] \\ &- \frac{m_1^2}{2}a_1^2 - \frac{m_2^2}{2}a_2^2 - m_{12}a_2 a_1^2\end{aligned} \tag{1.31}$$

where b and s denote the SM bottom and strange left-handed quarks, g_{sb} the coupling of V to third generation quarks, g_{12} the coupling to the scalars[11] and y^l the effective Yukawa coupling of the l lepton. Without loss of generality, a_2 is considered more massive than a_1 henceforth. Note that the effective coupling of the theory is both suppressed by mass powers and the CKM factors that relate the coupling between V and the quarks in the unbroken phase. In Figure 1.8, the tree-level interactions included in the Lagrangian 1.31 are displayed.

The nature of both scalars is collected in the second and third term of the Lagrangian 1.31, through which they couple to SM fermions with a Higgs-like strength $\sim g_{1,2}y_l a_{1,2} l^+ l^-$. Again, with the spirit of partial compositeness, it might be considered that the lightest pNGB is muonphilic, whereas the decay of the heaviest one would depend on the mass relations between scalars [116].

$$\Gamma(a_2 \to l^+ l^-) = \frac{g_2^2 y_l^2}{8\pi}\left[1 - \frac{4m_l^2}{m_2^2}\right]^{\frac{3}{2}} m_2 \tag{1.32}$$

$$\Gamma(a_2 \to a_1 a_1) = \frac{m_{12}^2}{8\pi m_2}\left[1 - \frac{4m_1^2}{m_2^2}\right]^{\frac{1}{2}} \tag{1.33}$$

where it can be seen clearly the kinematic threshold $m_2 = 2m_1$ under which the decay $a_2 \to a_1 a_1$ vanishes in favour of purely muonphilic decays.

[11] It is predicted to be $\mathcal{O}(1)$ due to strong dynamics.

Note that, if $m_2 < 2m_1$, the process $a_2 \to a_1\mu^+\mu^-$ would also be allowed, triggering a decay through both on-shell and off-shell a_1 particles. This scenario, which would need $g_1 \gtrsim 100g_2$, is highly discarded cause it would lead to vanishing experimental signatures (widths smaller than 10 MeV and lifetimes below 10 fs), and it is itself Yukawa suppressed [116].

The full mass phase space of the model is finally determined by the relations between the B_s^0/B^+ and the scalar particles. Two main areas could be proven: the one corresponding to $m_B > m_1 + m_2$, namely decays of the form $B_s^0 \to a_1a_2$, and the one to $m_B > m_1 + m_2 + m_K$, triggering $B^+ \to a_1a_2K^+$. Each of the areas is, at the same time, split into two due to the hierarchical relations between scalars. Note that both neutral and charged modes are essential for accessing to the full phase space: whereas the width $\Gamma(B_s^0 \to a_1a_2)$ grows with m_2 (and therefore reaching the highest supression power), $\Gamma(B^+ \to K^+a_1a_2)$ is kinematically suppressed for high $m_{1,2}$ values.



Figure 1.9: Low muon multiplicity decays, where $m_2 < 2m_1$.

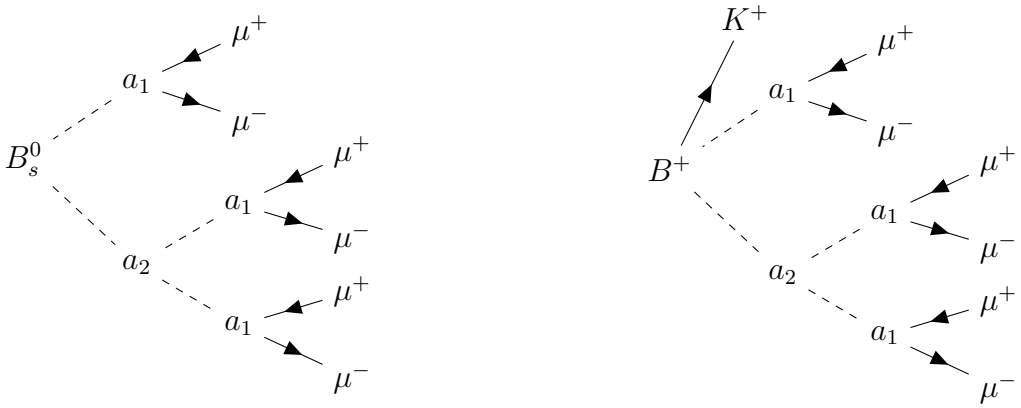


Figure 1.10: High muon multiplicity decays, where $m_2 > 2m_1$.

All in all, the four very rare modes (with branching fractions below 10^{-8}) to which LHCb will show a competitive sensitivity are the decays displayed in Figure 1.9 and 1.10. To date, LHCb capabilities have already been used in the search for very similar topologies. First, in the study of New Physics decays $B_s^0 \to a(\mu^+\mu^-)a(\mu^+\mu^-)$ with $m_a = 1$ GeV and $t_a = 1$ ps giving $\mathcal{B}(B_s^0 \to a(\mu^+\mu^-)a(\mu^+\mu^-)) < 6.4 \cdot 10^{-10}$ at 95% confidence level [117]. Second, a search for low-mass dimuon resonances [118], which

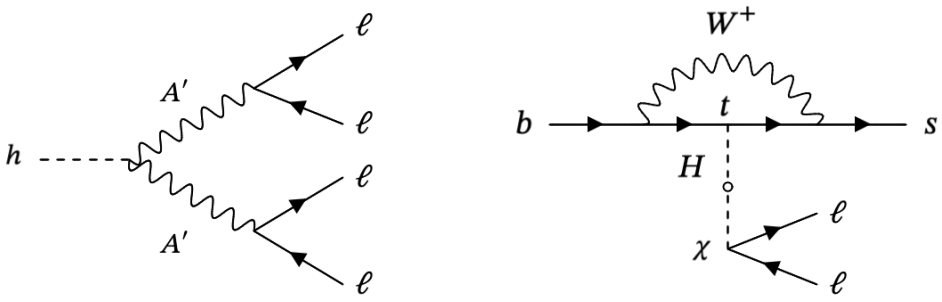


Figure 1.11: Possible portals to the Standard Model triggering Long-Lived Particles: Abelian Hidden Sector (left) and Dark Higgs (right).

is sensitive to this model, is conducted in the fiducial region in which high transverse-displaced vertices are requested.

Apart from the great motivation that this model represents in the experimental field, it also contains certain implications that could explain different tensions found with the standard model to date. First, in the regime where $g_1 \ll g_2 \sim \mathcal{O}(1)$ the CP-even scalar with $m_2 \sim 1$ GeV might provide an explanation to the $(g-2)_\mu$ anomaly within 2σ [115]. Although not a tension anymore, flavour-violating vector bosons at the TeV were highly considerated within literature for being "a priori" able to solve anomalies observed in the branching fractions, angular distributions and lepton universality tests of $B^{0(+)} \to K^{*(+)} l^+ l^-$ decays [115]. Those tensions were experimentally rejected by the re-analysis of LHCb data corresponding to Run 1 and Run 2 data [119].

1.3.2 Portals for Long-Lived Particles

Complete models, as the CH framework presented in Section 1.3.1, directly address open problems in the SM and can naturally contain LLPs in their spectrum. On the other hand, minimal models are simplified extensions containing a single new state, neutral under the SM gauge group [120, 121, 95], that interacts with the SM sector through a limited set of lowest-dimension effective operators consistent with SM gauge symmetries, also known as portals. Although such minimal models have less direct theoretical motivation, they provide clean benchmarks for experimental searches [122]. It has, therefore, a major role in the definition of the physics case for the CODEX-b detector.

The classification is organized according to the spin and quantum numbers of the new neutral particle, namely a scalar (S), pseudo-scalar (a), a fermion (N), or a vector (A') particle.

The first minimal extension of the SM can be obtained by introducing a new **Abelian Hidden Sector** [123, 124] with its own gauge symmetry $U(1)_X$ and its corresponding vector boson A', commonly referred to as the Dark Photon. This new sector could interact with the SM sector through two renormalizable portals [125]:

- The gauge portal via kinetic mixing of the new field tensor and the SM hypercharge $\sim \epsilon B_{\mu\nu} X^{\mu\nu}$, where ϵ is the mixing parameter.
- The scalar portal, corresponding to the coupling of the SM Higgs doublet and the Higgs of the new sector $\sim |\Phi_{SM}|^2 |\Phi_X|^2$.

In the low-energy theory, if the new Higgs is heavier than the SM Higgs, the Lagrangian of the theory contains the terms [120]:

$$\mathcal{L} \supset F_{\mu\nu} F'^{\mu\nu}, \; h A'_\mu A'^\mu \tag{1.34}$$

where the first term represents the kinetic mixing operator (from which takes place the decay of the A') and the second represents the $h \to A'A'$ decay.

Despite the lack of a theoretically preferred mass range, light dark photons remain of high phenomenological interest for two main reasons: first, B factories, fixed-target, and beam-dump experiments have not yet probed masses above the $\mathcal{O}(10\,\text{GeV})$ scale; and second, sub-GeV dark photons still provide a clean benchmark for exploring physics beyond the Standard Model, even though the previous tension with the muon anomalous magnetic moment has largely been resolved [126]. Theoretical uncertainties—especially in hadronic vacuum polarization—remain under active investigation [127], and future measurements may further refine constraints on new physics.

The most minimal extension of the SM consists of adding a single, real scalar field S which is invariant under the SM symmetry group. The renormalizable elements entering the Lagrangian in the so-called **Scalar Higgs Portal** are [120, 128]:

$$\mathcal{L} \supset A_S S^2 H^\dagger H + \frac{\lambda}{2} S^2 H^\dagger H \tag{1.35}$$

where the parameter A_S can be changed for the mixing angle between the physical Higgs and the S, controlling the lifetime of the latter and the rate through B decays. As a consequence, the new light scalar inherits all the couplings of the SM Higgs. The parameter λ represents the production of S from the Higgs.

Phenomenologically, for small values of the mixing angle, the particle S could be produced through an LLP intermediate state in $b \to s l^+ l^-$ transitions. The LHCb detector has recently been able to show a competitive sensitivity to such a process [129], whose topology can be observed in Figure 1.11 (right). Likewise, the $\sim 3\sigma$ deviation observed in the $B^+ \to K^+ \nu\nu$ decay in Belle II could be explained through the Higgs portal if the new scalar verifies $m_K < m_X < m_B$ [130].

Heavy-Neutral Leptons (HNLs) may interact with the SM sector via the lepton Yukawa portal mediated by the marginal operator $\overline{L}_\alpha \tilde{H} N$ or through higher-dimensional operators in simplified NP models [120].

In general, the HNLs act as sterile neutrinos (they remain uncharged under the SM gauge groups) and they can have an associated Majorana mass term [131, 132]. The

corresponding part of the Lagrangian of a theory featuring such particles would read as [132]:

$$\mathcal{L} \supset \left(\frac{m_N}{2} \overline{N} N + \sum_\alpha y_\alpha \overline{L}_\alpha H N + \text{h.c.} \right) \tag{1.36}$$

where N represents a right-handed neutrino field, m_N the mass of N (in fact, a Majorana mass term) and α the corresponding flavour of the $\overline{L}_\alpha$ lepton doublet. When H settles on a vacuum expectation value, neutrinos just acquire Dirac mass terms of the form [132]:

$$\mathcal{L} \supset -\frac{1}{2} \left[\overline{\nu}_L m_D N + \overline{N} m_D \nu_R + \overline{N} m_N N \right] \tag{1.37}$$

where $m_D = y_\alpha v/\sqrt{2}$. Introducing a unitary transformation into the system in which the mass matrix is diagonal, one finds that the neutrino masses are suppressed by the scale of the HNL [132]:

$$m_\nu = \frac{m_D^2}{m_N} \tag{1.38}$$

Such an extension of the neutrino sector implies that flavour eigenstates generally contain some fraction of the heavy component due to the mixing $U_{\alpha N} = y_\alpha v/\sqrt{2} m_N$ [120, 131, 132]:

$$\nu_\alpha = \sum_{i=1}^{3} U_{\alpha i} \nu_i + U_{\alpha N} N \tag{1.39}$$

which would make HNLs participate in every process in which active neutrinos appear. The suppression existing in the mixing would, therefore, make HNLs a promising candidate for LLPs.

Fixed-target and kaon experiments such as NA62 have set stringent bounds on the mixing with electron and muon neutrinos in the sub-GeV region [133]. At the GeV scale, Belle and Belle II have imposed limits in B-meson and τ decays, improving limits especially for mixing with ν_τ [134, 135]. At higher masses, LHCb has exploited displaced-vertex signatures in B decays to constrain the mixing with ν_μ [136], while ATLAS and CMS have probed HNLs produced in W decays up to the electroweak scale [137, 138]. Despite these efforts, a sizeable open parameter space remains.

Finally, **Axion-like Particles (ALPs)** are pseudo-scalar particles which, when associated with the breaking of approximate Peccei-Quinn-like symmetries, tend to be light [139, 120]. At low energies, the interaction with the SM is carried through dimension-five operators suppressed by a large scale f_a, which make them natural LLP candidates [120]. The effective Lagrangian consists of terms with the following form

USC UNIVERSIDADE DE COMPOSTELA

[120]:

$$\mathcal{L} \supset \partial_\mu a \overline{\psi} \gamma_\mu \gamma_5 \psi, \; a G_{\mu\nu} \tilde{G}^{\mu\nu}, \; a W_{\mu\nu} \tilde{W}^{\mu\nu}, \; a B_{\mu\nu} \tilde{B}^{\mu\nu} \tag{1.40}$$

Depending on which coupling dominates, different ALP portals to the SM are defined [120]:

- **Photonic portal:** originating from the couplings $aW_{\mu\nu}\tilde{W}^{\mu\nu}$ and $aB_{\mu\nu}\tilde{B}^{\mu\nu}$, which induce effective interactions between the ALP and photons. For certain relations among the coefficients, the $a \to \gamma\gamma$ coupling can be suppressed, giving rise to "photophobic" scenarios.
- **Fermionic portal:** described by derivative interactions of the form $\partial_\mu a \, \bar{\psi}\gamma^\mu\gamma_5\psi$, leading to ALP decays into leptonic or hadronic pairs. Such couplings are particularly relevant in the context of flavor physics.
- **Gluonic portal:** associated with the operator $aG_{\mu\nu}\tilde{G}^{\mu\nu}$, which enables ALP production via QCD processes and typically leads to hadronic decay channels.

Experimental searches for ALPs have covered a wide range of masses and couplings. At high energies, above $\sim$ 10 GeV, LHCb has probed ALPs decaying into photon pairs in proton-proton collisions [140]. Fixed-target experiments such as NA64 have constrained the ALP-photon coupling for masses in the MeV range [141]. Forward experiments like FASER have searched for ALPs produced in LHC collisions decaying into photons or leptons, covering the 0.1–10 GeV mass window [142]. In addition, ATLAS and CMS dominate the higher-mass $\sim$ 10–1000 GeV ALPs through exotic Higgs decays, diphoton resonances, and other high-energy channels [143, 138]. Despite this broad coverage, significant regions remain unexplored. In particular, the intermediate mass range of 0.1–5 GeV, with small couplings leading to long-lived ALPs, is only weakly constrained and represents the most promising target for future searches [122, 95].

USC UNIVERSIDADE DE SANTIAGO DE COMPOSTELA

2

Hypothesis, Objectives and Methodology

2.1 Hypothesis and Objectives

The general hypothesis of this work can be divided into two complementary components. First, the LHCb detector is suitable for studying the low-energy signatures of composite Higgs models, owing to the presence of LLPs predicted in the theoretical spectrum. Second, this work explores the feasibility of the future CODEX-b detector for detecting such signatures. Throughout all the work, specific objectives are reached by three different streams, namely simulation, data analysis and hardware developments.

The first specific goal is to evaluate the sensitivity of the LHCb detector to non-Minimal CH Models and, in particular, to identify the regions of the parameter space that could give rise to long-lived particles (LLPs) in their spectrum through a phenomenological analysis. This study serves as a guideline for the subsequent analysis of LHCb Run 2 experimental data in the search for such long-lived states. It represents the first experimental search aimed at the direct observation of these states.

The vast amount of possible LLP signatures entails that, apart from searches in the existing experimental facilities, complementary experimental approaches must be considered. These efforts include the execution of the CODEX-b experiment, a detector placed transverse to the LHC beam at the LHCb experimental cavern. Planned for the Run 5 of the LHC, a reduced proof-of-concept demonstrator denoted CODEX-β is about to start operations during Run 3 with the main goals of: i) the testing of the suitability of the Resistive Plate Chambers (RPCs) as the core of the tracking design, ii) the demonstration of control over the SM backgrounds and iii) the inclusion of CODEX-β in the data acquisition and trigger system of LHCb. The main goal of such a line within the thesis is to actively participate in the assembly, installation and com-

USC
DE SANTIAGO

missioning of the demonstrator detector. In addition, a fast-simulation framework that should be the seed of a complete CODEX-b simulation system is developed and tested in the case study of evaluating future locations and geometries of the full detector.

2.2 Methodology

In order to reach the aforementioned objectives, the following methodology is followed:

First, a phenomenological analysis is performed to characterize the most important features of the signal modes, comprising an extensive study of the parameter space and determination of the optimal points to be studied with LHCb experimental data. Concretely, the 4μ channels $B_s^0 \to \mu^+\mu^-\mu^+\mu^-$ and $B^+ \to \mu^+\mu^-\mu^+\mu^-K^+$, and the high-multiplicity 6μ modes $B_s^0 \to \mu^+\mu^-\mu^+\mu^-\mu^+\mu^-$ and $B^+ \to \mu^+\mu^-\mu^+\mu^-\mu^+\mu^-K^+$ are studied. The characteristic topologies of the model also lead to the assessment of different reconstruction methods in the detector, most of them motivated by the aim of increasing the sensitivity reach at high lifetimes. Such a study drives the consequent official simulation development with the LHCb software (more details in Section 3.4.3.

With the phenomenological study in hand, the experimental analysis of LHCb Run 2 data exploits as much as possible its final results. For such a purpose, dedicated reconstruction categories are used to build physical candidates, and correspondingly signal selections are applied to ensure a high background rejection while keeping an optimal signal efficiency. The selection comprises a detailed study of topological variables to select the signal and a multivariate selection to separate the signal and the combinatorial background. The sensitivity reach of the selection is also studied, and the effect of human decisions is incorporated as a source of systematic uncertainties in each case. After analysing possible peaking background sources in the signal window, a bump hunt at the B meson mass is performed. Two possibilities arise: in case results are compatible with the absence of signal, upper limits in the Branching ratio of the decays are set, but if contrary, a measurement of the corresponding Branching ratio is performed.

As previously mentioned, the installation and commissioning of the CODEX-β demonstrator is procured. The roadmap includes building and testing the corresponding RPCs, the installation of the gas and electrical services, final structure assembly and including the data-acquisition modules.

Finally, a fast-simulation framework for the design and optimization of the future CODEX-b experiment is developed. For that, the benchmarks $H^0 \to A^0A^0 \to 2e^+2e^-$ and $B \to X_s\varphi$ are simulated, and a set of selections and tracking conditions is imposed. As a result, a realistic comparison can be made among designs, being able to compare the sensitivity reach with other general-purpose and dedicated experiments. This effort constitutes a seed for a complete simulation framework in the short-term run.

USC UNIVERSIDADE DE SANTIAGO DE COMPOSTELA

3

Experimental Landscape and Detector Performance

This chapter provides an overview of the experimental landscape relevant for the studies carried out in this thesis, which focuses on the experimental determination of LLPs with the LHCb and CODEX-b detectors. It begins with a description of the Large Hadron Collider (LHC) and its operational parameters during Run 2 in Section 3.1, followed by an introduction to the LHCb experiment, including its detector subsystems, the general detector performance during Run 2 (trigger, tracking and simulation, among others) in Section 3.2. The chapter then reviews, in Section 3.5, the state of the art of the global experimental efforts devoted to LLP searches, providing the context for the proposal of the CODEX-b detector, which is discussed in detail in Section 3.6.

3.1 The Large Hadron Collider

The conclusion of the so-called SM puzzle has historically driven the development of increasingly powerful accelerators. At the end of the 20th century, a 27km-ring electron-positron collider, the Large Electron Positron Collider (LEP), initiated its journey, acting as a $W^{\pm}$ and Z^0 boson factory with which to perform precision measurements and setting the most stringent limits to date on the Higgs boson mass [144]. On the other side of the Atlantic Ocean, the Tevatron, a proton-proton 6.3 km-ring accelerator, made a remarkable contribution to the SM after observing the top quark in the D0 experiment [145]. Although both experiments were able to reach unprecedented center-of-mass energies, 209 GeV and 1 TeV respectively, the last piece, the Higgs boson, was still out of reach.

USC UNIVERSIDADE DE SANTIAGO

The need for a powerful accelerator led to the construction of the Large Hadron Collider (LHC). It was successfully commissioned in 2010 for proton-proton collisions with 7 TeV centre-of-mass energy [147], reaching 13.6 TeV in Run 3 after several upgrades

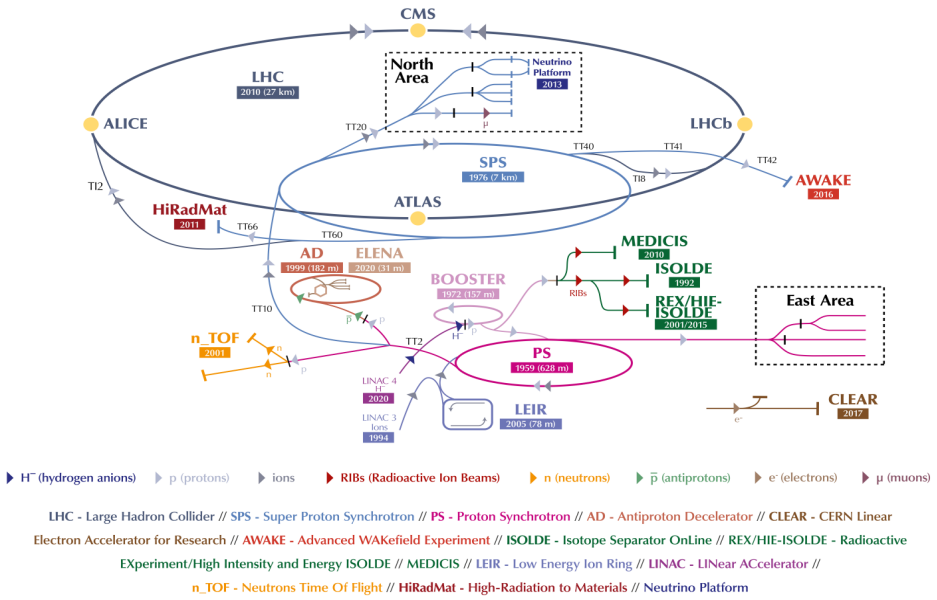


Figure 3.1: CERN accelerator complex, comprising pre-accelerator stages and experimental facilities. Obtained from [146].

[148]. The most remarkable milestone reached by the accelerator was the discovery of a fundamental particle compatible with the Higgs boson [149, 150], completing the puzzle of the subatomic interactions included within the SM.

Behind the LHC, a complex injector chain is responsible for accelerating proton bunches according to the machinery's demands. The constituents, displayed in Figure 3.1, are the Linac2[1], the Proton Synchrotron Booster (PB), the Proton Synchrotron (PS) and the Super Proton Synchrotron (SPS). The specifications of each one are the following:

- **Linac2:** It receives hydrogen atoms and accelerates the resulting beam at 50 MeV. It consists of a Duoplasmatron (ionizes hydrogen atoms and accelerates the resulting proton beams), a Radio Frequency Quadrupole with output energy of 750 keV and a three-tank drift tube [151, 152].

- **Proton Booster:** four rings stacked on top of each other with one-quarter of the length of the PS. This structure ensures a sequential extraction of the protons (it avoids space-charge issues) at an energy of 1.4 GeV [153, 154].

- **Proton Synchrotron:** It accelerates the proton bunch to 14 GeV for SPS physics beams or to 26 GeV for LHC beams [153].

- **Super Proton Synchrotron:** It accelerates proton beams up to an energy of 450 GeV. Once the proton bunches reach their target energy, they are conducted into the final acceleration stage [155, 154].

[1]It has been replaced by Linac4 during the Long-Shutdown 2.

The LHC is composed of two concentric rings in which protons are injected and obligated to circulate in opposite senses. Throughout the ring, each bunch of protons meet 1232 NbTi superconducting dipole magnets, cooled down to 1.9 K and allowing magnetic fields up to 8.33 T[2][156, 157]. The nominal operation point is located at a radiofrecuency[3] of 400 MHz, spacing bunches 25 ns in a complete fill, and the estimated number protons per bunch scales up to $\sim 1 \cdot 10^{11}$. [157]

Once the nominal point is reached, protons are set to collide at four different intersections between the rings, the so-called Interaction Points, where both general- and specific-purpose experiments are located. Among them, ATLAS and CMS are the largest general-purpose detectors, designed to investigate a wide range of physics phenomena, such as the discovery of the Higgs boson in 2012 [149, 150], the measurement of different production rates (like W, WW, WZ or W+jets, among others), the precise measurement of the SM parameters or searches of BSM physics, like supersymmetry or extra dimensions. LHCb, by contrast, is a detector originally designed for b- and c-flavour physics, which nowadays allows to perform generic hadron studies, QCD and EW precission studies and also ion physics; although it has demonstrated reasonable flexibility in probing NP models [28]. Finally, operating at lower luminosity, ALICE is oriented toward heavy-ion collision physics, making it a powerful instrument to study the quark–gluon plasma [158]. Each detector's unique geometry and instrumentation (ATLAS and CMS with nearly full azimuthal coverage and multi-layered tracking, calorimetry, and muon systems; LHCb with a forward spectrometer optimized for heavy-flavor and precision measurements; and ALICE with central tracking and specialized detectors for heavy-ion collisions) ensures that, collectively, the LHC experiments provide a near-4π comprehensive picture of fundamental interactions under extreme conditions.

In particular, the experimental work presented in this thesis exploits the unique capabilities of the LHCb detector. Its forward geometry, excellent tracking performance, and precise particle identification provide a distinctive advantage, making LHCb especially well-suited for searches of LLPs.

3.2 The LHCb experiment

The LHCb experiment is a single-arm spectrometer with a forward angular coverage from 10 mrad to 300 (250) mrad in the bending (non-bending) plane [159, 160]. Its design was originally conceived for heavy flavour physics and, specifically, for the study of the CP violation, rare decays of beauty and charm hadrons, and indirectly, search for evidence of New Physics in those sectors. It is the unique LHC experiment fully instrumentalized in the forward pseudorapidity range $2 < \eta < 5$, which ensures the

[2]The LHC also contains decades of quadrupole magnets, whose objective is to focalize the bunch around the propagation axis.

[3]Eight superconducting radiofrequency cavities are placed in Interaction Point 4 for acceleration purposes.

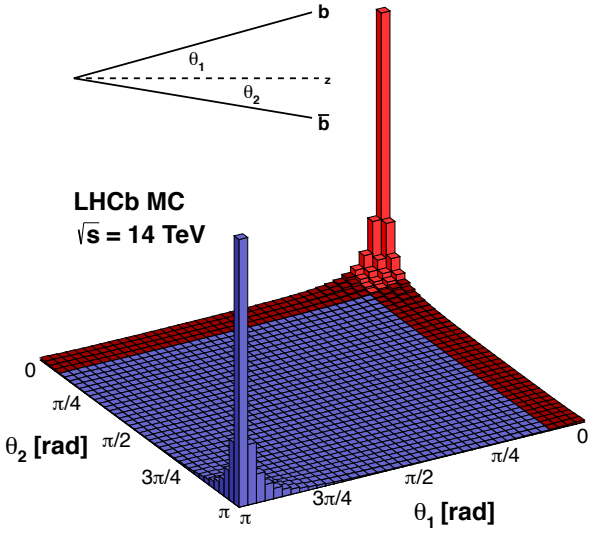


Figure 3.2: Simulation of individual polar distribution for a pair $b\bar{b}$ at $\sqrt{s} = 14$ TeV. Obtained from [164].

good reconstruction of particles with large longitudinal boost [161, 162]. LHCb has been installed in the Interaction Point 8 of the LHC, previously used by the DELPHI experiment [163] during LEP operations. A schematic view of the LHCb detector can be observed in Figure 3.3.

The LHCb detector is colloquially defined as a b-meson factory, with an estimated $b\bar{b}$ cross section of $500\mu b$ at an energy of 14 TeV [160, 165]. In comparison to other LHC experiments, the LHCb configuration ensures its execution at a lower instantaneous luminosity of $\mathcal{L} \sim 2 \cdot 10^{32}\,\mathrm{cm}^{-1}\mathrm{s}^{-1}$ [160] [4], which ensures events are dominated by a single pp interaction per crossing bunch [165]. At the operational energy 14 TeV, the creation of $b\bar{b}$ pairs happens mainly through gluon-gluon fusion, and because of angular momentum conservation, each component of the pair hadronizes in opposite directions, namely the backward and forward directions. This process is displayed in Figure 3.2, in which the number of $b/\bar{b}$ processes is histogrammed against the polar components of each member of the pair. In numbers, LHCb geometry is optimized to retain 24% of $b\bar{b}$ created pairs [165, 166].

The LHC nominal data-taking periods are organized in Runs, ranging over several years, during which the major detectors do not undergo any extensive upgrade and with previously scheduled technical stops of a couple of months. So far, LHCb has accomplished two complete runs, namely Run 1 and Run 2. In the first, LHCb collected data corresponding to an integrated luminosity of $3\,\mathrm{fb}^{-1}$ during the years 2011 and 2012, at a maximum center-of-mass energy of 7 TeV and 8 TeV, respectively [167].

[4] At this luminosity performance, LHCb can generate the order of 10^{12} $b\bar{b}$ pairs in a canonical 1 year data taking period [160, 165].

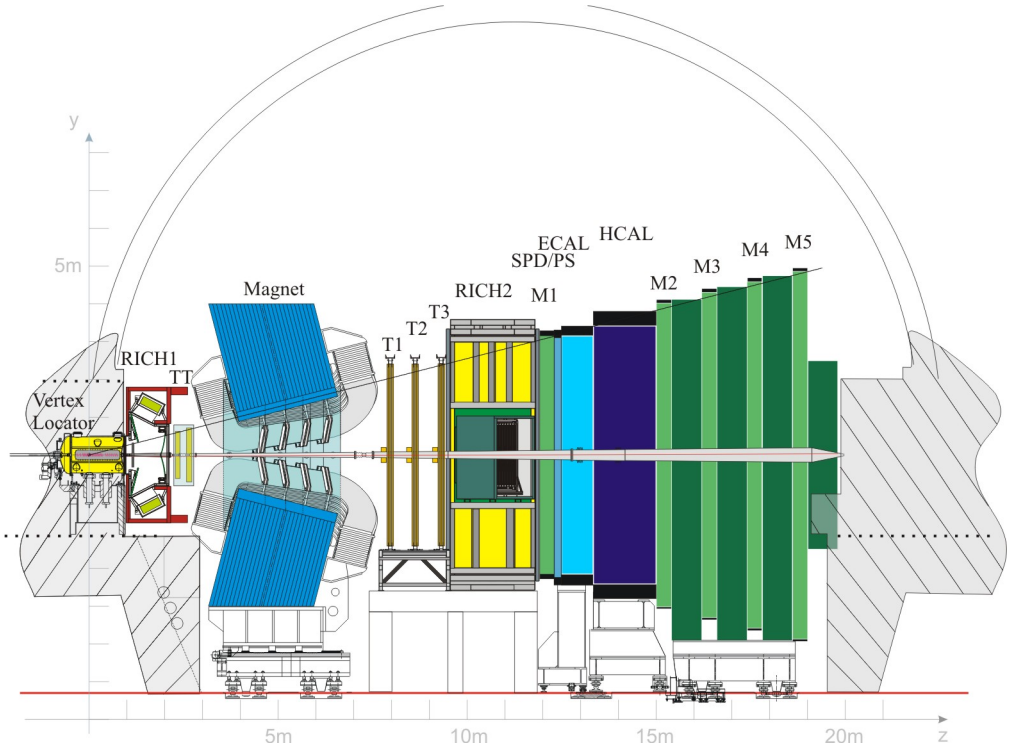


Figure 3.3: View of the LHCb detector. The propagation axis is chosen across the z-axis, whereas the height is oriented towards the y coordinate. Subdetectors are displayed in colours. Obtained from [170] under CC BY-SA 3.0.

The second Run ranged from 2015 to 2018, achieving an integrated luminosity of $5.1\,\mathrm{fb}^{-1}$, after which the full detector underwent the denoted Upgrade-1, with the focus of upgrading all the subdetectors to run with a higher center-of-mass energy and with a higher pileup [168, 169].

The ultimate LHCb performance relies on the detector subsystems, each one specializes in a specific function, whether in terms of reconstruction, particle identification, or luminosity measurements. A comprehensive list describing each subsystem can be found in the next section [160].

3.3 LHCb subsystems

The LHCb detector is divided into different subsystems, each with a specific objective in terms of its role in physics measurements. A description of the detector components (schematically displayed in Figure 3.3) is given for the period 2016-2018.

3.3.1 Vertex Locator-VELO

USC UNIVERSIDADE DE SANTIAGO

The Vertex Locator (VELO) [171, 172] is the principal tracking instrument of the LHCb detector, and its geometry provides the necessary conditions to perform b and c physics successfully.

The VELO (and consequently the full detector) is connected to the LHC machine through the beam pipe, a 19m-long vacuum tube with conical shape through which primary and secondary particles fly. Beryllium was chosen as the material of the first 12 m[5] of the beam pipe due to its transparency quality, whereas the rest is stainless steel, because of its mechanical and vacuum properties [173]. The width of the tube ranges from 50 mm close to the LHCb interaction point to 380 mm in the most forward part of the detector.

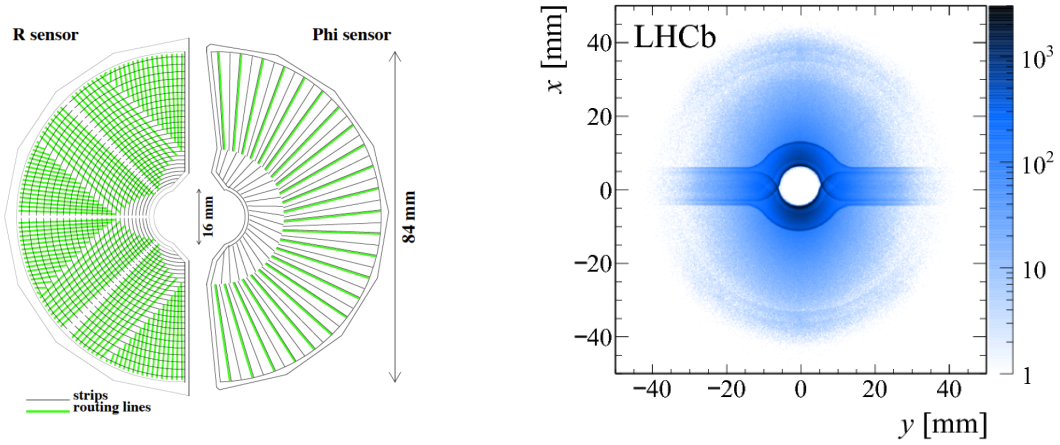
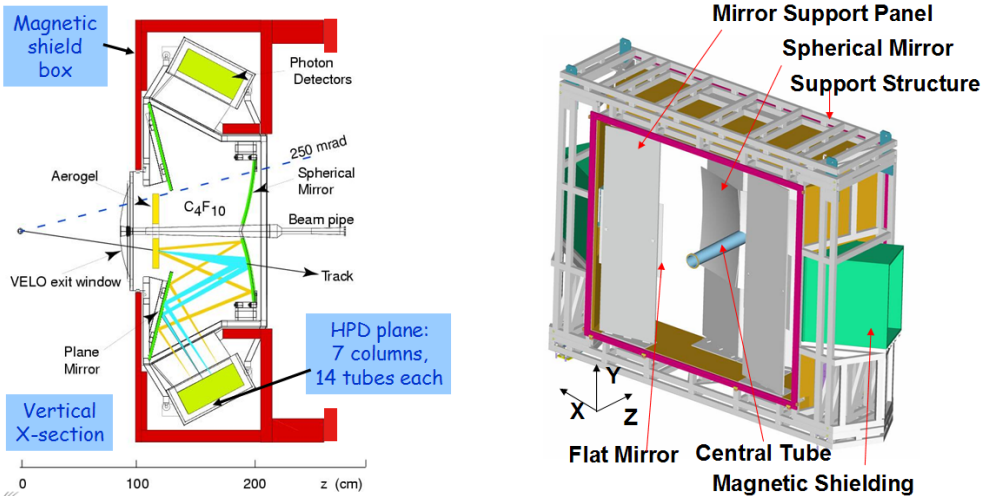


Figure 3.4: Front view of a schematic representation of the distribution of silicon pixels in the VELO (left) and material interaction reconstruction with secondary hadronic interactions. Obtained from [172] and [174] under CC BY 3.0 and CC BY 4.0, respectively.

In Run 2, the VELO consisted of 2 mechanically mounted halves that closed around the beam pipe at 8 mm from the beam axis. Both halves had 21 stations (modules of silicon sensors) to record the hit position of every charged particle flying through the VELO. The full setup was embedded in a vacuum chamber because of the extreme radiation and temperature conditions in the vicinity of the pp collision point [175]. Two types of sensors, mounted back-to-back, are used to provide a measurement of the r coordinate with respect to the beam axis (circular strips) and the ϕ coordinate (straight strips), as shown in Figure 3.4 left. Sensors are isolated from the vacuum by an aluminium RF foil with a thickness of 0.5 mm [175]. This component is shown in Figure 3.4, together with the reconstruction of charged-particle secondary vertices in the yx plane. It represents an important background source for LLP analyses, as inelastic interactions with the material may mimic the signatures of displaced decay products.

The Run 2 VELO achieved outstanding resolution, with typical single-hit precision between 4 and 10 μm, and primary vertex resolutions of about 13 μm transversely and 78 μm longitudinally. It also provided excellent transverse impact parameter resolution, around 35 μm for tracks with $p_T > 1$ GeV, enabling precise separation of primary and secondary vertices—crucial for studying heavy-hadron decays [172].

[5]Where the critical zone in terms of product density is located.



(a) Schematic view of RICH1 detector. (b) RICH2 detector.

Figure 3.5: RICH1 and RICH2 detector schematics. Obtained from [176] and [177] under CC BY 4.0 and CC-BY-3.0, respectively.

3.3.2 Ring-Imaging Cherenkov detectors (RICH)

The first identification of charged particles is carried out through two RICH detectors, located upstream of the dipole magnet and in the downstream direction. Both detectors are used synchronously to separate particle species across the full momentum coverage of the LHCb detector [178, 176]. Such identification constitutes a critical procedure for the correct development of flavor physics.

RICH detectors operate by using Cherenkov radiation, which is characteristic of any charged particle moving at a speed higher than the speed of light in a certain environment. When this happens, the emission of photons occurs through a conical wavefront, whose opening angle is proportional to the ratio of the two speeds, namely $cos\theta \sim \frac{c}{v}$. In both RICH detectors, the focusing of the Cherenkov light is accomplished using a combination of spherical and flat mirrors to reflect the image out of the spectrometer acceptance [178]. A schematic view of RICH 1 and RICH 2 subdetectors can be seen in Figure 3.5.

The upstream detector, RICH 1, makes use of aerogel and C_4F_{14} radiators. As it is closer to the VELO, this detector has a wide acceptance covering the full LHCb acceptance, ranging from ± 25 mrad to ± 300 mrad (horizontal) and ± 25 mrad (vertical). It has access to the low momentum region, covering from $\sim 1-60$ GeV. Figure 3.6 shows the Cherenkov angle as a function of momentum for different particle species [176].

On the contrary, the RICH 2 detector has a limited angular acceptance, from ± 15 mrad to ± 100 mrad (vertical) and ± 120 mrad (horizontal), and thus is dedicated to higher momentum production (15 GeV to $\sim$ 100 GeV) [176].

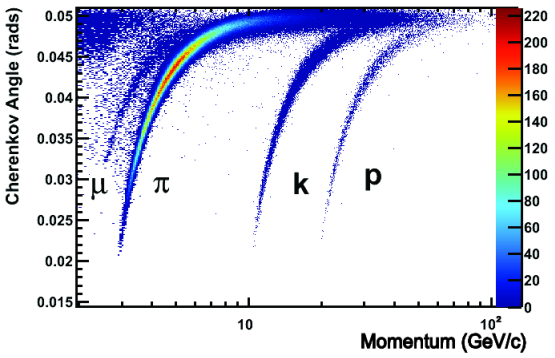


Figure 3.6: Reconstructed Cherenkov angle as a function of track momentum in the C4F10 radiator. Obtained from [176] under CC BY 3.0.

3.3.3 Tracking stations

The main LHCb tracking system comprises two modules located directly upstream and downstream of the dipole magnet, the Tracker Turicensis (TT), and three tracking stations, which comprise the Inner Tracker (IT) and the Outer Tracker (OT) [179]. During Run 2, the full system was essential for flavour physics analyses, providing the precise spatial resolution and tracking needed to reconstruct secondary vertices from the decays of heavy-flavour hadrons, enabling accurate measurements of lifetimes, impact parameters, and decay topologies. The full tracking system is responsible for the measurement of the tracks' momentum through the curvature in the direction caused by the action of the magnet.

The TT stations upstream of the magnet and the IT consists of micro-strip silicon technology, able to provide a relatively high single-hit efficiency ($\sim 50\ \mu$m) in conditions of extremely-high hit occupancies [180]. Together, they form the so-called Silicon tracker, and cover a total area of $12.2\ \text{m}^2$ and possess $\sim$ 270k readout channels. A schematic view of the Inner Tracker can be found in Figure 3.7.

On the other hand, the OT (see Figure 3.7) is a gaseous drift-time detector using a mixture of Argon (70%) and CO_2 (30%) and it is subjected to a less stringent hit occupancy due to its distance with the beam axis [182, 183]. It possesses a drift time below 50 ns and a drift coordinate resolution of 200 μm.

3.3.4 Dipole Magnet

A dipole magnetic field with a free aperture of ± 300 mrad vertically and ± 250 mrad allows momentum measurement for charged particles in nearby tracking stations with a precision of 0.4% for momenta up to 200 GeV [185]. The nominal working point is located at 4 mT for tracks originated near the primary interaction point.

Due to technical downsides, the original magnet design evolved to a warm magnet, operating at environmental temperature, with pole faces shaped to follow the detector

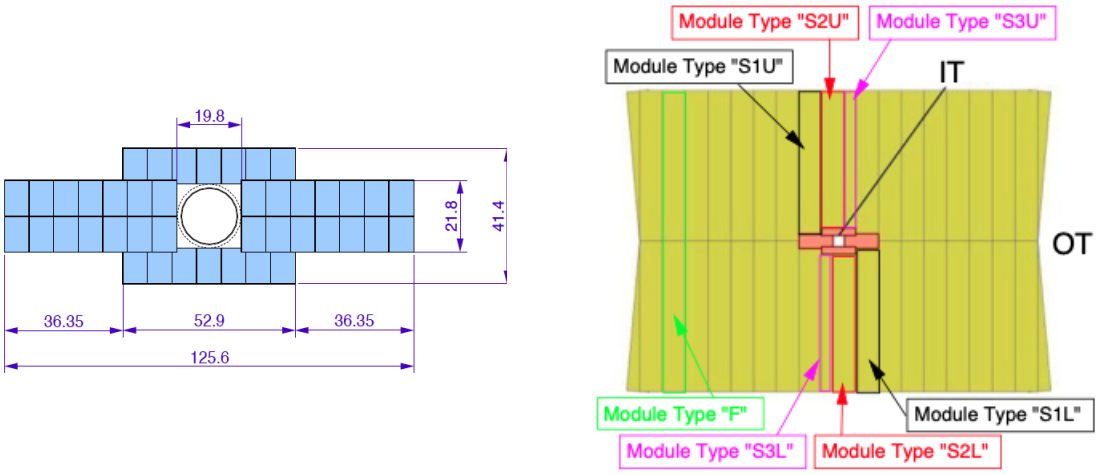


Figure 3.7: Inner and Outer tracker schematics. Obtained from [180] and [181] under CC-BY-3.0 and CC-BY-4.0, respectively.

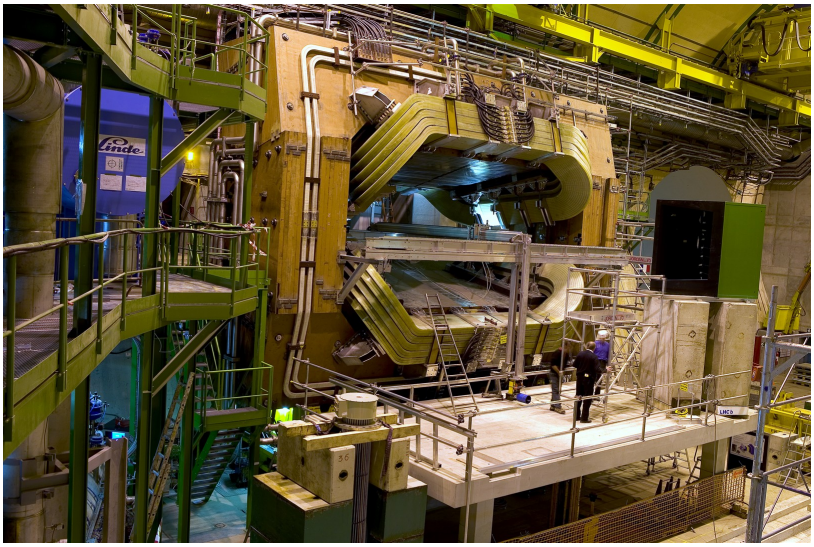


Figure 3.8: Front view of the LHCb dipole magnet. Obtained from [184] under CC-BY-4.0.

USC UNIVERSIDADE DE SANTIAGO DE COMPOSTELA

angular acceptance. Magnetic coils are made from Aluminium for reliability reasons and to reduce energy consumption, with 2 to 4 A/mm2 the current needs, and they are assembled from 15 individual mono-layer pancakes. Each coil consists of a 50×50 mm^2 cross-section, with a bore purely dedicated to cooling with water. A front view of the magnet in the opening window is displayed in Figure 3.8.

Apart from momentum measurements, the magnet also plays a key role in CP violation measurements and in the systematic evaluation of the detector, a reason for which it changes the polarity periodically across data-taking periods. The configurations are labeled as MagUp (positive y) and MagDown (negative y).

3.3.5 Calorimeter system

The calorimeter system is responsible for a fast and correct separation between electrons, photons and hadrons, for which access to the energy deposition and its position is needed. In the LHCb detector, the calorimeter system consists of an electromagnetic calorimeter (ECAL) followed by a hadronic (HCAL) calorimeter. In Run 2, they were responsible for selecting transverse energy candidates for the first level trigger (L0) [186, 159] (Section 3.4.1). The full calorimeter system is divided into four modules, depending on the physics purpose: a scintillator pad detector (SPD), a pre-shower detector (PS), the ECAL, and the HCAL [187, 188].

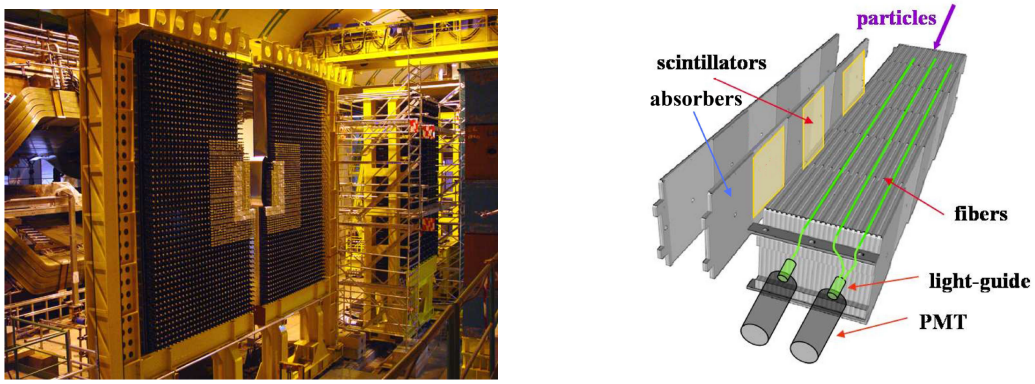


Figure 3.9: Rear view of the hadron calorimeter (left) and schematic of the internal cell structure (right). Obtained from [28] and [187] under CC-BY-3.0 and CC BY 4.0, respectively.

The SPD/PS consists of a 15 mm lead converter of 2.5 radiation length that is sandwiched in between two almost identical planes of rectangular scintillator pads of high granularity. The objective of this module is to veto an important background component of, first, charged pions and, second, high-energy π^0's that could dramatically affect the L0 electron trigger [188].

The ECAL is made up of scintillator/lead structure, making up to 25 radiation lengths to fully contain showers from high-energy photons [189]. The nominal energy resolution is:

$$\sigma_E/E = \frac{10\%}{E} \oplus 1\% \tag{3.1}$$

with E in GeV units. Such a resolution has a clear impact in B physics, resulting in a mass precision of 65 MeV in $B \to K^*\gamma$ penguin decays with a high-p_T photon or 75 MeV in $B \to \rho\pi$ decays, with 8% pion mass resolution [165]. A rear view of the ECAL is displayed in Figure 3.9 left.

Finally, the HCAL is a sampling device made from iron and scintillating tiles (schema in Figure 3.9 right) that run parallel to the beam axis, reaching a thickness of 5.6 radiation lengths. Overall, energy deposit resolution is smaller for the HCAL, resulting in:

$$\sigma_E/E = \frac{(69 \pm 5)\%}{\sqrt{E}} \oplus (9 \pm 2)\% \tag{3.2}$$

where E is again measured in GeV [186, 187].

All parts of the calorimeter system contain photomultiplier cells whose scintillation light is transmitted to a Photo- Multiplier (PMT) by wavelength-shifting (WLS) fibres, which allows a decision to be taken within the 4 μs after the interaction, at a bunch crossing rate of 40 MHz [186]. All components, at the same time, are subdivided into three regions, each one increasing the granularity of cells as the distance to the beam pipe decreases.

3.3.6 Muon system

In LHCb, muon identification and characterization play a crucial role in studies of CP asymmetries and oscillation measurements [190], as well as in models predicting LLP signatures, as will be discussed later. Owing to their large penetration capability and relatively long lifetime (2.2 μs), muons can be experimentally characterized in regions far from the interaction point, where other charged particles are typically absorbed or decay before reaching. This results in very clean and distinctive detector signatures.

The muon system is composed of five stations (M1-M5) placed along the beam axis, M1 being placed before the calorimeter system ($\sim$ 12 from the interaction point) and M2-M5 after the latter one (from 15 to 19 m – see Figure 3.10). The downstream chambers are interleaved with iron absorbers 80 cm thick, ensuring that only muons reach the outer detector layers. The goal of stations M1-M3 is the determination of the propagation direction and the transverse momentum of the muon candidate, whereas M4 and M5 have a limited spatial resolution and are optimized for the identification of penetrating particles.

Each muon station is divided into four regions, R1 to R4. The segmentation sizes scale in the ratio 1:2:4:8, with granularity increasing as the distance to the beam pipe gets smaller, ensuring a flux and channel occupancy roughly the same between them (a representation can be found in Figure 3.10). Geometrically-wise, the inner and outer

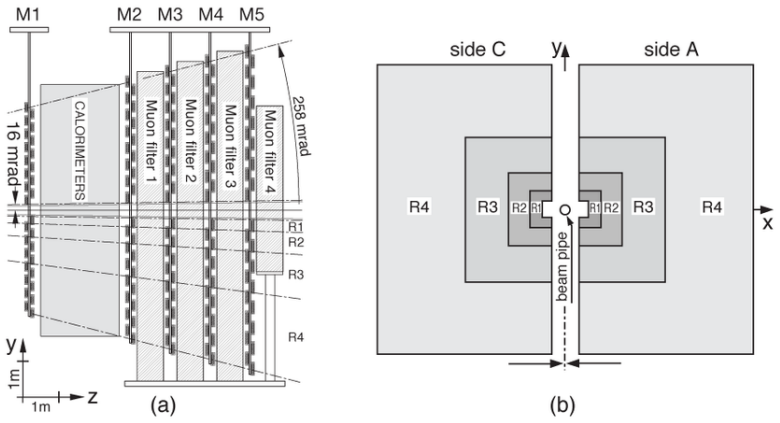


Figure 3.10: Side and front schematics of the LHCb muon stations. Obtained from [191] under CC BY 4.0.

angular acceptances of the muon system are 20 (16) mrad and 306 (258) mrad in the bending (non-bending) plane, resulting in a 20% acceptance for muons from inclusive b-semileptonic decays.

The muon system chambers are equipped with multi-wire proportional chambers [192] operating with a non-flammable gas mixture of Ar in 40%, and CO_2 and CF_4 in variable concentrations. The nominal timing resolution is around 5 ns for a gas gap with a wire plane of 2mm spacing, symmetrically placed in a 5 mm gas gap.

Muon identification is particularly relevant for analyses involving final states with multimuon decays, as is the case in the analysis presented in this thesis in Section 5. Such signatures are among the cleanest experimental channels, as muons can be efficiently triggered, reconstructed, and identified even in busy hadronic environments [190, 192]. Their relatively low backgrounds, combined with excellent momentum resolution and vertexing capabilities, make multi-muon searches a powerful tool to explore such very rare decays and LLP signatures.

In this context, the LHCb muon system plays a decisive role. Its fine granularity and large angular acceptance allow not only for high-efficiency muon identification, but also for the rejection of backgrounds from charged hadrons misidentified as muons [192, 193]. Moreover, the system is designed to provide precise timing information, ensuring robust performance for displaced muons originating far from the primary vertex. These features are essential to extend the physics reach of LHCb towards processes with tiny branching fractions or unconventional topologies that would remain undetected without a performant muon system [190].

3.4 LHCb Run 2 data-taking and Detector Upgrades

USC DE SANTIAGO

In 2015, after the Long Shutdown 1, the LHC started the Run 2 with an increased center-of-mass energy of 13 TeV. This year was fully dedicated to establishing an operation energy of 6.5 TeV per beam with standard 25 ns bunch spacing and to

prepare for substantial luminosity production during the rest of the Run [194].

Year	$\sqrt{s}$ [TeV]	$\mathcal{L}$ [cm^{-2}s^{-1}]	$\mathcal{L}^{\text{Int}}$ [fb^{-1}]	Pile Up
2016	13	$1.4 \cdot 10^{34}$	40	$\sim$ 25-30
2017	13	$2.0 \cdot 10^{34}$	50	$\sim$ 40
2018	13	$2.1 \cdot 10^{34}$	66	$\sim$ 45-50

Table 3.1: Breakdown of Operation LHC parameters throughout the full Run 2 period.

Across the duration of the Run (2015-2018), the LHC operated by keeping the center-of-mass energy of the collisions. Year 2016 marked a significant increase in the instantaneous luminosity[6], being on June 26th, with an optimization of the accelerator settings and luminosity injectors, when the LHC reached its design luminosity of $1 \cdot 10^{34}$ cm^{-2}s^{-1} [195]. In the following years, operational improvements allowed successive increases in the bunch occupancy and in the number of proton bunches per fill (reaching the target of 2460 at the end of the Run), which contributed positively to the time invested in physics purposes on the detectors. As a result (see Figure 3.11 left), the amount of data obtained in each year far exceeded that obtained in Run 1, marking a record for the efficiency of LHC operation in its short but intense history. For specific details on the parameter landscape of the Run, see Table 3.1.

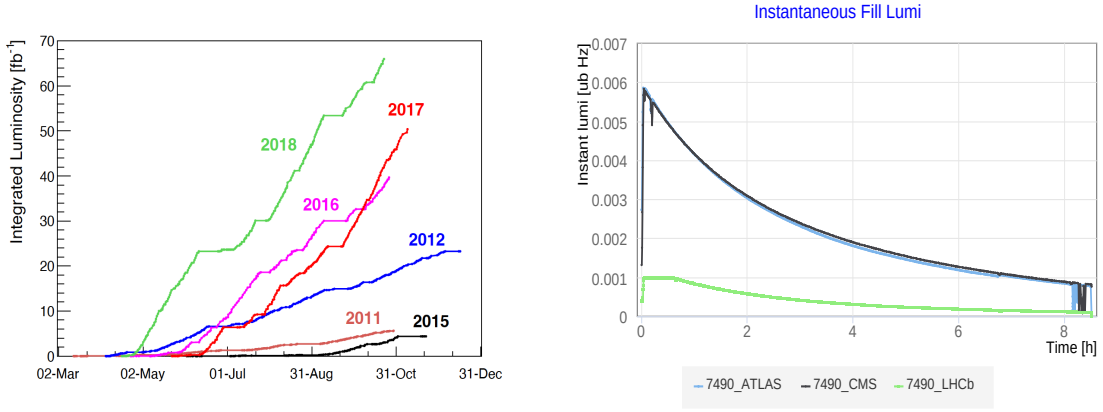


Figure 3.11: Left: Breakdown of Integrated Luminosities for Run 1 and 2. Right: Comparison between Instantaneous Luminosity for ATLAS, CMS and LHCb in a proton fill during Run 2, across operation time. Obtained from [194] under CC-BY-NC-ND-4.0 and [196], respectively.

At LHCb, the luminosity conditions are softened compared to the ATLAS and CMS detectors in order to fulfill tracking requirements. In numbers, the squeeze parameter β^* was set to $\sim 3m$ during the whole duration of Run 2, a defocusing of the beam which led to an average pile-up of 1.5 and finally to an instantaneous Luminosity of $4 \cdot 10^{32}$ cm^{-2}s^{-1}. The effect can be observed in Figure 3.11 right, which highlights the fact that the instantaneous Luminosity remains constant for LHCb during the course

[6]Number of effective pp interactions per time unit.

of the fill, allowing to preserve a uniform detector occupancy and stable data-taking conditions throughout the run.

The Run 2 configuration of LHCb resulted in a substantial gain in physics reach with respect to Run 1. The increase in center-of-mass energy from 8 TeV to 13 TeV led to a 60% rise in the production cross-sections of heavy-flavor quark pairs. Within the LHCb acceptance, this resulted in [197, 198, 199]:

$$\begin{aligned} \sigma_{b\bar{b}} &= 154.3 \pm 1.5(\text{stat}) \pm 14.3(\text{syst})\ \mu\text{b} \\ \sigma_{c\bar{c}} &= 2840 \pm 3(\text{stat}) \pm 170(\text{syst}) \pm 150(\text{frag})\ \mu\text{b} \end{aligned} \tag{3.3}$$

Given the low pile-up environment and LHCb's forward geometry, a large fraction of selected collisions contain at least one $b\bar{b}$ or $c\bar{c}$ pair. This heavy-flavor dominance in the recorded data significantly boosts the experiment's sensitivity to rare decays and CP violation, even under softened luminosity conditions.

3.4.1 Trigger System and Data Saving

In Run 2, the LHCb trigger system was fully redesigned to perform offline event reconstruction at the trigger stage, highly increasing selection efficiencies for charm and strange hadron decays, and to achieve a high-quality alignment and calibration within the trigger, allowing for inclusion of final signal selection [200, 201, 202]. The fundamental goal of the trigger system is to reduce the LHC bunch-crossing rate of 40 MHz to 12.5 kHz, which allows a full event reconstruction, a key point where the richness of LHCb physics' data lies. In Figure 3.12, the different blocks that build up the trigger system can be observed.

The first stage of the trigger is denominated Level 0 trigger, a $4\mu s$-latency hardware filter which reduces the incoming 40 MHz to a more manageable rate of roughly 1 MHz, sending the surviving info to the High-Level Trigger 1 [203]. The L0 level trigger is divided, at the same time, into two complementary algorithms: the L0 Hadron and L0Muon trigger.

The L0 Hadron trigger collects the energy depositions in the SPD, PS, ECAL and HCAL, and triggers a decision based on the total transverse energy deposited in clusters of 2 x 2 cells in the calorimeters, defined as:

$$\mathrm{E_T} = \sum_{\mathrm{i}=1}^{4} \mathrm{E_i} \cdot \sin\theta_{\mathrm{i}} \tag{3.4}$$

where $\mathrm{E_i}$ is the energy deposition in cell i and $\sin\theta_{\mathrm{i}}$ the angle subtended between the z-axis and a line from the cell center to the pp interaction vertex. Additionally, information from the SPD is used to identify hadron, photon and electron candidates, as well as for imposing a limit on the total number of recorded hits to discard events with extreme multiplicity.

USC UNIVERSIDADE DE SANTIAGO DE COMPOSTELA

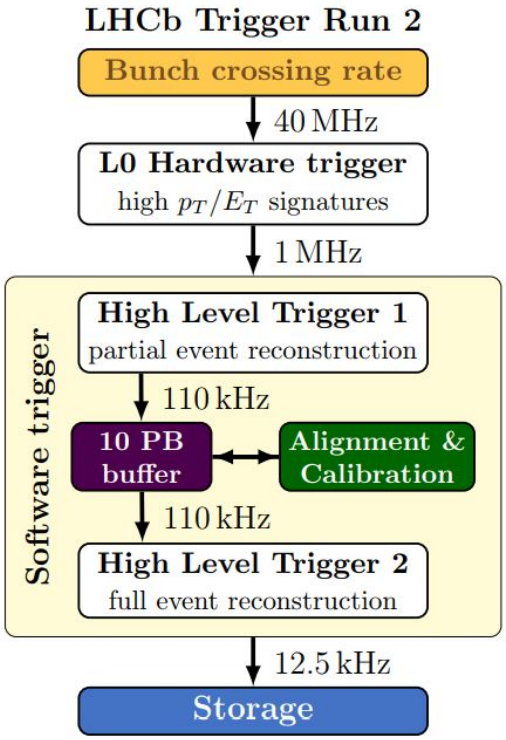


Figure 3.12: LHCb trigger system breakdown. Obtained from [200] under CC BY 4.0.

The L0 Muon trigger searches for straight lines in the muon stations, and computes the track p_T from the bending experienced after the magnet, assuming production in the primary vertex. The trigger decision is broken, at the same time, into two lines called L0Muon and L0Dimuon. The first operates by triggering events whose maximum p_T track verifies $p_T > 6$ GeV whereas the second one asks for the product of the largest and second largest p_T values to verify $p_{T,1} \times p_{T,2} > (1.6)^2$ GeV^2. Correspondingly, the SPD veto is totally removed in the high-p_T Muon line, to avoid biases in efficiency determination in electroweak production analyses, and loosened for L0DimuonLine as the acceptance rate is far below respect of other lines [200].

Events selected by L0 are sent to the High Level Trigger, an online algorithm which runs in the Event Filter Farm[7] [200]. The online trigger output is divided into around 20 trigger lines for HLT1 and 500 for HLT2.

At HLT1, a preliminary reconstruction is made by targeting charged particles traversing the full LHCb tracking system with a $p_T > 500$ MeV. At this stage, a precise reconstruction of the primary vertex is also performed with the information from the VELO standalone. The HLT1 output, at a rate of ~ 100 kHz, is saved in a buffer, and thanks to the computing resources in Run 2, they are used for alignment and calibration purposes in the detector [200, 204]. The major calibration tasks include the alignment of tracking stations (VELO, Muon and Outer Tracker), orientation of primary and secondary mirrors or gas refractive-index calibration (RICH) or π^0 rejection

[7] In Run 2, it was instrumentalized with 27000 physical cores, with a total disk buffer of 10 PT.

calibration (ECAL).

Finally, at HLT2, full event reconstruction and particle identification are performed using information from all subdetectors. Signal selections at this stage are split into physics alleys, each one focusing on a concrete physics case. Each selection can be inclusive, if it targets general topologies, or exclusive, if it looks for exclusive final states. All in all, 40% of the output rate is dedicated to inclusive topological lines, another 40% to exclusive c-hadron decays and the rest is divided among dimuon, electroweak physics, exotica and exclusive trigger lines [200].

Stage	**Line**	**Decision**
L0	MuonDecision	TOS
HLT1	TrackMuonDecision DiMuonLowMassDecision	TOS
HLT2	TopoMu{2,3,4}BodyDecision Topo{2,3,4}BodyDecision TopoMuMu{2,3,4}BodyDecision	TOS

Table 3.2: Summary of trigger selection. All candidates must be identified as TOS by at least one trigger line at each stage.

At every stage, each trigger decision is labeled according to the condition that caused the event to fire. Two possibilities exist: TOS (Triggered On Signal), when the signal object under study is itself responsible for firing the trigger; and TIS (Triggered Independently of Signal), when the trigger is fired due to other parts of the event, independently of the signal. The latter, apart from contributing to the overall signal efficiency, also allows for the definition of signal-independent control samples. Complementarily, the TISTOS category indicates events that were fired with both TIS and TOS decisions [203].

The surviving event rate ($\sim$ 12.5 kHz) is finally sent to permanent storage. In Run 2, an additional offline selection was applied to further filter and optimize the reconstructed data: the Stripping selection. This stage comprises a large set of selection lines, each designed to select specific signal topologies or control samples. Events passing a given line are grouped into Streams, which categorize the data according to the physics domain (e.g., charm, beauty, electroweak, or calibration), allowing for efficient access and storage optimization [205]. The full legacy datasets remain stored in tape, allowing for development of new physics selections or improving the performance of the existing ones.

For completeness, and linking to the experimental analysis of Multimuon tracks that will be developed in Section 5, the corresponding set of trigger selections can be found in Table 3.2. All candidates are subject to the same trigger requirements, which ensure the (partial) cancellation of systematic uncertainties associated with trigger line selections. This selection exploits the conditions for good identification of individual

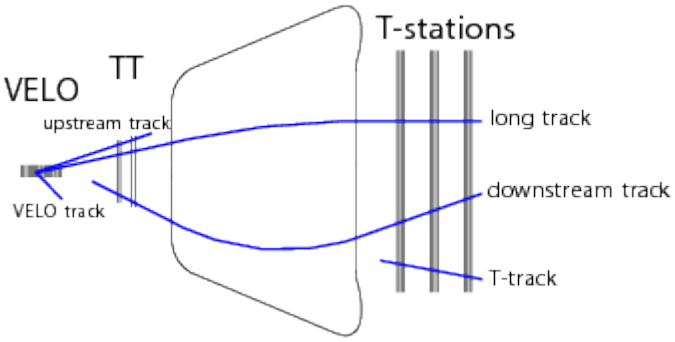


Figure 3.13: Different track reconstruction in LHCb: Long tracks, Upstream tracks, Downstream tracks and T-Tracks are displayed. Obtained from [204] under CC BY 3.0.

muons as well as the characteristic topology of multimuon events.

3.4.2 Track reconstruction and Particle Identification

Decay	Prompt	Long	Downstream
$B^+ \to 4\mu K^+$	B4muX	B24muXLongLived	B24muXDown
$B_s^0 \to 4\mu$	B2MuMuMuMu	B2MuMuMuMuDimuonAndJpsi	Incl2mu2muDown
$B^+ \to 6\mu K^+$	B26muX	B26muXLongLivedLine	B26muXDown B26muXDownDown
$B_s^0 \to 6\mu$	B26m	InclDet6mu3bodyLongLived	InclDet6mu3bodyDown InclDet6mu3bodyDownDown

Table 3.3: Summary of dedicated stripping lines used to select signal modes. In reconstruction categories, Long encloses LL and LLL samples and Downstream LD, LLD and LDD.

In LHCb, due to its forward geometry, track reconstruction focuses on the determination of particle trajectories through the association of hits in different tracking layers along the detector. The execution is performed in two stages, namely Pattern Recognition and Kalman Filter [206, 204], producing different tracks according to their nature (Figure 3.13):

- **VELO tracks:** Association of hits in the VELO stations. They provide information about the particle trajectory [204].
- **Long Tracks:** usual and most reliable track type in LHCb, with the highest momentum resolution (about 0.5% for particles below 20 GeV, rising to about 0.8% for particles around 100 GeV) [201] and vertexing capabilities (dominated by the VELO). They have hits associated with all the tracking systems [207].
- **Upstream Tracks:** Represent the association of hits between the VELO stations and the TT stations. Mainly composed of low-momentum tracks ($p_T \leq 1$ GeV) which are bent out due to the magnet action [201].

USC UNIVERSIDADE DE SANTIAGO DE COMPOSTELA

- **Downstream Tracks:** Association of hits in TT tracker and T-stations. Their momentum resolution is significantly degraded (typically at the level of several percent, depending on the kinematics and decay topology) and no direct vertex reconstruction can be performed [201, 207]. Characteristic of particles decaying outside the VELO acceptance.

- **T-Tracks:** Association of hits in the T-stations standalone, typically produced by secondary interactions [207].

- **Ghost tracks:** None of the latter. They correspond to fake tracks due to the incorrect matching of hits throughout the detector stations [208].

As previously highlighted, partial track reconstruction starts at HLT1 by looking for tracks with $p_T > 500$ MeV[8]. First, hits in the VELO are combined and a simplified Kalman filter is used to fit and return the best fit parameters, information which is later used for the determination of the Primary Vertex. Afterwards, the resulting track is extrapolated with a straight line into the TT, where at least 3 hits are searched in a small region around the extrapolation. The resulting tracks allow for a relative momentum resolution of about 20%, which is sufficient to discard tracks with transverse momentum below roughly 1 GeV, as they are strongly deflected by the magnetic field and rarely correspond to physics objects of interest [201]. Finally, in a window determined by the maximum magnet bending for particles of $p_T > 500$ MeV, hits are looked for in the IT and OT, performing a full Kalman filter to perform the reconstruction. At HLT1, only loose muon identification requirements are put on tracks with $p > 3$ GeV, and they can be found in Table 3.4. There, the number of hits required for a hypothetical muon candidate is given according to a kinematic range, defined by the expected bending of muons after the magnet [204].

p [GeV]	Muon Stations
$3 < p < 6$	M2+M3
$6 < p < 10$	M2+M3+(M4 or M5)
$p > 10$	M2+M3+M4+M5

Table 3.4: IsMuon identification requirements at HLT1.

At HLT2, a full event reconstruction is performed, mainly with the general reconstruction of all charged and neutral particles, using the full information of the subdetectors, including particle identification criteria [200, 209].

On the tracking side, trajectories produced by HLT1 are reconsidered without momentum restrictions, and the same steps are followed. Next, a neural network is used

[8]Such a threshold is not a physical limitation of the detector, but an algorithmic choice driven by time-window constraints and the need to limit the rate of low-momentum tracks processed online. No explicit beam-spot constraint is applied at this stage; it is instead introduced later during vertex fitting to refine the determination of the primary vertex position.

to distinguish fake tracks, random combinations of hits or mismatches between track segments[9] [210]. Finally, clone tracks[10] are removed, keeping the track with more hits in total. As a result, the purest Long and Down tracks are achieved, with 12 μm IP resolution for high-momentum tracks or 45 fs [200, 207].

Particle identification criteria are mainly evaluated with the RICH detector by measuring the opening Cherenkov angle under a corresponding mass hypothesis (Figure 3.5). The latter information is complemented with information from the calorimeter system, oriented to the catalog of electromagnetic particles, like electrons, photons and neutral pions; and the muon stations. As a result, powerful single observables are reached in terms of particle identification:

- The $\text{DLL}_{X\pi}$, which stands for the log-likelihood difference between the hypothesis of a particle species X and pions.
- The `ProbNNX` variable, an output of dedicated neural networks trained with simulation with input from detector components and tracking information [200, 204].

This last point is critical since simulation is not always able to faithfully reproduce real conditions in the detector, which highlights the need for calibration samples. In Run 2, the selection of control samples was introduced in the HLT2 stage, being the calibration performed with the tag-and-probe method over clean and well-known decays [203]. The calibration is usually performed in bins of kinematic variables like the p_T or η to preserve cleanliness as far as systematics are concerned.

3.4.3 MC Simulation

Precise simulation frameworks are needed to understand experimental conditions and detector performances, as well as to reproduce physics phenomena to interpret experimental results [211]. In LHCb, the simulation framework is Gauss, which comprises the event generator (PYTHIA or MadGraph, among others) and the tracking of particles through matter (Geant) [212]. Additionally, Gauss is intrinsically connected to Boole [212], an application that translates the propagated MC particles into the digital response from the tracking elements.

Since its inclusion, the simulation framework has evolved drastically to adjust to the different experimental conditions of the detector throughout the Runs. Among the improvements introduced are: the inclusion of new models to predict the parton evolution in the primary interaction, the inclusion of new generator conditions to adapt the process to new physics scenarios, and the improvement of the detector descriptions. Those changes are usually included in different simulation versions, namely SimX,Y, where

[9] Its input variables are the χ^2 of the Kalman filter, the χ^2 values of the fits for track segments, the number of hits in each tracking station and the p_T of the track.

[10] They share a significant amount of hits in each subdetector.

X denotes the version (which implements major changes such as the geometry description and experimental conditions) and Y the subversion (comprising improvements or corrections, like small changes on the detector description and physics case).

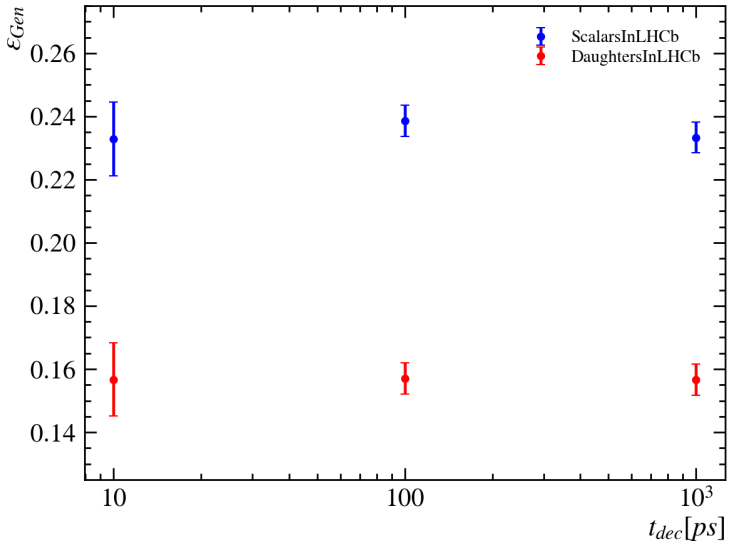


Figure 3.14: Comparison between the generation efficiencies for a set of a_1 lifetimes in $B_s^0 \to (a_1 \to \mu^+\mu^-)a_2(\mu^+\mu^-)$ decays.

In the specific case of Multimuon searches, Pythia is used with a pure phase-space approach to generate a set of decays in the mass and lifetime spectrum of the intermediate scalars. Concretely, a range of lifetimes are chosen for the a_1 scalar (the LLP) to effectively cover the acceptance of the LHCb detector, whereas a_2 always decays promptly.

In the event generation, scalar particles are required to be produced within an angular range of $10 < a_\theta < 400$ mrad, corresponding to the geometrical acceptance of the LHCb detector. This ensures that most of their decay products fall inside the detector and can be efficiently reconstructed. In LHCb simulations, it is common to apply the so-called `DaughtersInLHCb` requirement, which checks whether all final-state particles would traverse the LHCb acceptance if they were produced at the PV. However, in the case of displaced decays this assumption is not valid: Particles originating away from the PV can still enter the detector even with larger polar angles. To illustrate this effect, Figure 3.14 compares the geometric acceptance obtained using the standard `DaughtersInLHCb` condition over simulation produced with different scalar lifetimes. Such a Figure shows that applying the standard condition underestimates the reconstruction efficiency for decays occurring far from the PV, as these produce tracks at larger θ that remain within the detector acceptance.

Finally, of special importance in simulation is the Truth-Matching technique. In a typical simulation pipeline, the events of interest are first generated, then propagated through the detector, and subsequently digitized. During digitization, additional physical processes known to occur in the detector (such as electronic noise, spill-over from

previous bunch crossings, or interactions from unrelated minimum-bias events) are overlaid in order to reproduce the realistic detector environment. The resulting signals are then reconstructed using the same algorithms and procedures as for real data. At the reconstruction stage, the final-state particles can be associated with the original MC particles that produced the majority of the detector hits or clusters. This matching provides the so-called `trueID` and related truth information, which are essential for performance studies and have a strong impact on the outcome of the analysis.

3.4.4 LHCb upgrades

The consecutive improvements that the LHC machine is planned to undergo aim at extending the machine lifetime beyond the nominal running period, until the early 2040s [213, 214]. In such a period, the LHC is conceived to improve its machine configuration to increment the scope of the physics case, first by increasing the center-of-mass energy collision from 13 TeV to 13.6 TeV and the peaking instantaneous luminosity of $\mathcal{L} \sim 2 \cdot 10^{34}\text{cm}^{-2}\text{s}^{-1}$ for Run 3 (2022-2026) [215], and second to increase the baseline luminosity to $\mathcal{L} \sim 5 - 7.5 \cdot 10^{34}\text{cm}^{-2}\text{s}^{-1}$, 5 times bigger than the baseline design [214]. In terms of adapting the LHCb for the new conditions, two major upgrade projects are planned, namely **Upgrade I** and **Upgrade II**, which might boost the LHCb performance to LLP searches.

In the **Upgrade I**, important improvements happen to tracking and reconstruction. In hardware, LHCb replaces the current silicon microstrip sensors of the Vertex Locator (VELO) with pixel sensors, which enables it to withstand conditions of higher-track multiplicity and improve resolution, and reduces the distance to the beam pipe from 8.4 mm to 5.1 mm [209, 215]. Additionally, the amount of material traversed by a particle before the first hit is being reduced, leading to a better suppression of material interaction backgrounds. On the other hand, an improved silicon-microstrip upstream tracker (UT) also increases the reconstruction power of LLPs decaying outside the VELO [216]. On the trigger side, the hardware-based L0 trigger is removed and the HLT1 level fully runs on a GPU farm. The gain in computing power with improved tracking capabilities boosts the possibility of reconstructing displaced tracks with subdetectors located downstream to the VELO, as is the case with Downstream tracks (reconstructed with no associated hits in the VELO) and T-Tracks (exclusively with hits from the SciFi sub-detector).

In Upgrade II, the even increased Luminosity and occupancy conditions require that the detector's performance must be equal to or greater than that of Upgrade I. The inclusion of timing information in the VELO ($\sim$ 50 ps per hit) and the TORCH detector enables a 4D tracking for vertex identification on extreme pile-up conditions [214]. Additionally, the decrease in the amount of detector budget comes with the increase in the granularity of tracking detectors, boosting the reconstruction capabilities of displaced vertices and the veto of material interaction events.

USC DE SANTIAGO

3.5 State of the Art in LLP searches

The definition of an LLP (any particle that travels a macroscopic distance before decaying) is broad enough that virtually all high-energy experiments can be sensitive to at least some classes of LLP models. At the LHC, general-purpose detectors such as ATLAS and CMS, as well as forward detectors like LHCb, have all demonstrated sensitivity to LLPs across various production mechanisms and lifetimes. However, as the LLP lifetime increases, the probability of decay within the detector drops, leading to a significant loss of sensitivity in the long-lifetime regime. This limitation has motivated the development of dedicated experiments designed to be located far from the interaction points, providing enhanced reach for ultra-long-lived scenarios and complementing the capabilities of the main LHC detectors.

This section aims to provide an overview of several key experimental proposals —both upgrades to existing detectors and entirely new dedicated experiments— that are designed to enhance the experimental sensitivity to LLPs. While not exhaustive, this selection highlights representative approaches that address different regions of LLP parameter space. The description of the experimental landscape is organized as follows: Section 3.5.1 describes existing collider experiments, Section 3.5.2 forward experiments, Section 3.5.3 transverse experiments, Section 3.5.4 experiments and in Section 3.5.5 experiments that do not fit in the latter categories, broadening the sensitivity landscape to estable or metaestable exotic particles that might carry fractional electric charge or magnetic monopoles.

3.5.1 Collider Experiments

ATLAS and CMS

Characterized for completely involving the proton-proton collision point and for being optimized for high transverse-momentum tracks and prompt signatures, they are general-purpose detectors placed at the Interaction Points 1 and 5 of the LHC, respectively. While not initially designed for LLPs detection, both collaborations have implemented dedicated strategies to search for displaced vertices, disappearing tracks, and delayed signals.

Several LLP searches have already been performed in ATLAS and CMS, setting competitive bounds on a wide variety of BSM models such as gauge-mediated SUSY breaking, dark photons, and hidden valleys [217, 218, 219, 106]. It is expected that both detectors take around 3000 fb^{-1} of integrated Luminosity during the High-Luminosity phase of the LHC, which can be also utilized for LLP searches.

The increase in luminosity comes at the price of increasing the pileup, and both detectors are undergoing upgrades that will significantly increase the sensitivity to LLPs; see, for example, studies demonstrating the gain in sensitivity of CMS with the Mini-

mum Ionizing Particles Timing Detector (MTD) [220, 221] and the High-Granularity Calorimeter [222]. One critical aspect is the installation of improved inner tracking detectors, with higher granularity and greater resolutions, whose layouts will allow for improved tracking efficiencies at large displacements and less strict disappearing-track conditions [216] [11].

Additionally, both experiments will upgrade the calorimeter systems: on CMS, new readout electronics will improve the timing resolution of photons with $p_T > 25$ GeV to 30 ps and the increased granularity of the calorimeter system will increase sensitivity to showers that do not point to the primary vertex and delayed signals [95]; whereas ATLAS will upgrade the readout of the Electromagnetic and Hadronic Calorimeters [216].

Finally, both detectors will install very precise Minimum-Ionizing Particle timing detectors, which are motivated by the need to exploit the time dimension of the beam spot to discern individual vertices and enable accurate track-to-vertex association in an environment of high density [216].

Trigger-wise improvements have been recently included in the Upgrade plan of both detectors, and they focus on redesigning the trigger and data acquisition systems, providing them with tracking abilities for their hardware-based triggers. In CMS, the tracker design will include a series of double-layers which will enable global-event track-stub tracking down to $p_T > 2$ GeV and a L1 track trigger running at ~ 40 MHz [223]. On the ATLAS side, its hardware-based tracking system will perform a fast track-finding through pattern recognition, which might allow for an improved analysis of tracks associated with displaced decays [95, 216].

Belle II

Belle II is a 4π coverage detector located at the SuperKEKB high-luminosity collider at KEK (Japan). Similarly to LHCb, Belle II is a B-factory, and operates by recording e^+e^- collision data at 10.6 GeV [224], which special interest in sensitive $b \to q\bar{q}s$ and charmless $b \to q\bar{q}d(u)$, semileptonic $b \to s\nu\overline{\nu}$ and $b \to s\tau^+\tau^-$ decays [216]. The detector comprises several sub-detectors disposed cylindrically around the beam pipe and a polar structure for the asymmetric distributions of final state particles, namely: the vertex detector, central drift chamber, electromagnetic calorimeter, and displaced tracking detectors for K-long and muon observations. It is expected that Belle II records 50 ab^{-1} by 2025, after the planned upgrades.

In comparison with LHC detectors, Belle II poses several advantages that favour a specific type of searches. On the one hand, the low final-state multiplicity and the absence of event pile-up result in cleaner searches, enhancing the trigger capabilities for studying Long-Lived Particles [216]. On the other hand, the known nature of the

[11] It is thought, however, that the improvement might negatively affect some scenarios. The trackers will allocate a few bits of digital information to charge depositions, worsening the resolution of ionization measurements.

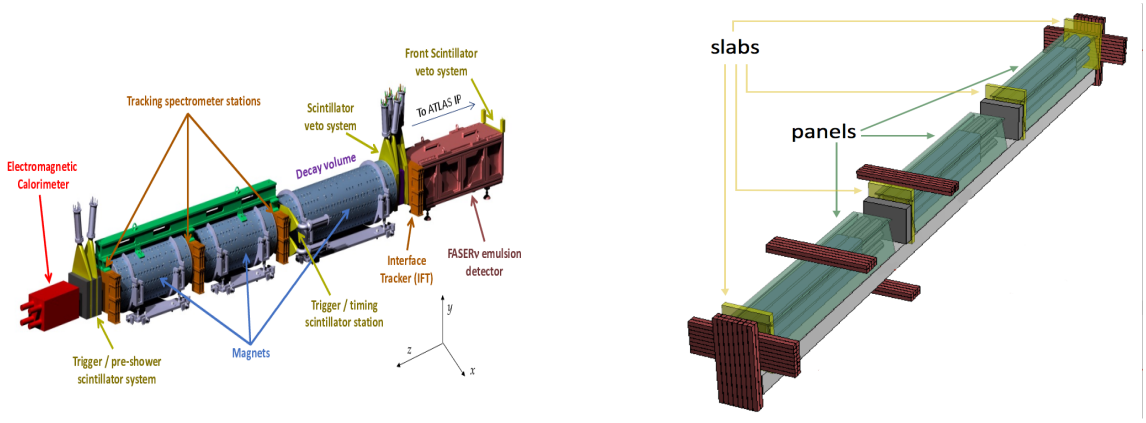


Figure 3.15: Detector schematics for forward experiments: FASER (left) and milliQan (right). Obtained from [228] and [229] both under CC BY 4.0.

initial state plus the detector hermeticity makes it possible to perform full-inclusive searches and a broad search of particles with little or no signature in the detector, irrespective of the lifetimes [216]. Concretely, Belle II would have a better sensitivity than ATLAS and CMS for light particles, and also than LHCb for final states involving hadrons plus missing particles or photons.

Belle II, although not implicitly built for dedicated LLP searches, has already proved its sensitivity to several scenarios. One of them is the Inelastic Dark Matter scenario via $e^+e^- \to \gamma A' \to \gamma\chi_1\chi_2$, in which transitions between mass states are mediated by a dark photon if the mass is higher than the sum of the daughters [225]. Belle II has also shown sensitivity to Dark Scalar portals through B meson penguin decays coupling to internal top quarks in processes like $B^+ \to K^+S$; in the limit of low mixing angles ($\theta \approx 10^{-5}$), a region consistent with the thermal relics [226]. Highlight, likewise, the analysis of a Dark Higgs boson produced in association with inelastic dark matter in events with at least one displaced vertex and missing energy, reporting the most sensitive bounds in the range $\sim 0.1 - 10$ GeV [227].

3.5.2 Forward Experiments

Forward Experiments are characterized by their optimization for observing neutral or charged particles that are produced collinearly (and usually with high pseudorapidity) with respect to the beam axis.

The experiment **FASER** [230] is one of the most remarkable experiments with such a nature, and it is designed to search for light and very weakly-interacting new particles produced in the LHC proton-proton collisions [95]. It is located 480 meters away from the ATLAS interaction point, on the beam collision axis line-of-sight, subtending an angular acceptance of $|\theta| < 0.21$ mrad [228]. The detector comprises (from the forward direction) a front scintillator veto system,an emulsion detector, an interface tracker, the scintillator veto station, the decay volume, the timin scintillator station, the tracking spectrometer, a pre-shower scintillator system and an electromagnetic

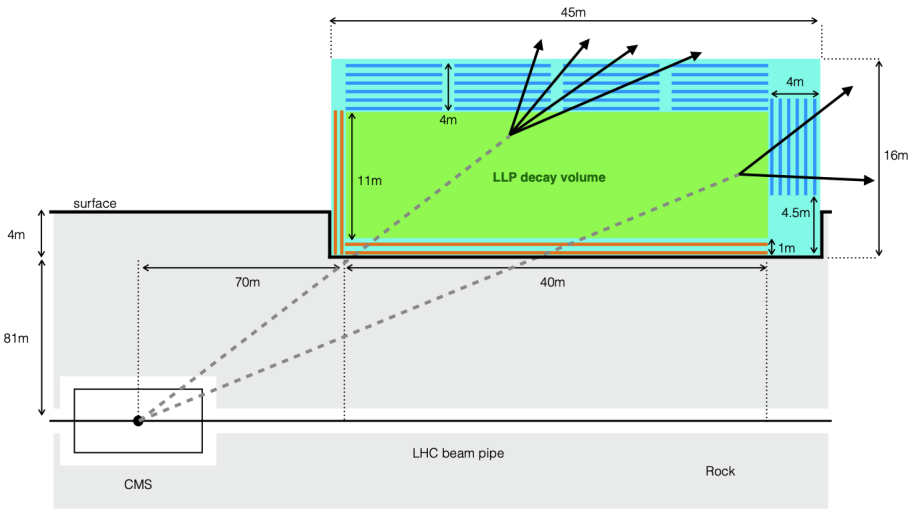


Figure 3.16: Design idea and experimental setup for MATHUSLA proposal. Obtained from [232] under CC BY 4.0.

calorimeter, along with three 0.57 T dipole magnets, one surrounding the decay volume and the other two embedded in the tracking spectrometer [228]. The aforementioned experimental setup makes it sensitive to neutral Long-Lived particles, highlighting above all sub-GeV dark photons and neutrinos, becoming the first-ever experiment to present a direct observation of collider neutrinos.

A similar forward facility, but oriented to the study of millicharged particles[12] is the **FORMOSA** [231] experiment[13], aiming for observing their energy deposition in a very-dense scintillator material. The experiment inherits part of the design idea of milliQan (Section 3.5.5), and adapts it for its installation 500 m downstream from ATLAS interaction point [231], comprising a 1 m $\times$ 1 m $\times$4 m array consisting of 4 layers of 400 scintillator bars. The future projections for FORMOSA show a sensitivity $10^{-4} \rightarrow 10^{-5}$ $\mathcal{Q}$/e (long lifetime) but higher restricted in the mass range with 0.1 $-$ 10 GeV.

3.5.3 Transverse experiments

Tracking experiment proposals usually comprise big fiducial detectors, comprising any kind of tracking technology, which stand far from the proton-proton collision points with a special focus on a very precise vertexing determination of displaced decays-in-flight for LLPs escaping the geometry of general-purpose detectors.

MATHUSLA [233] is a proposed surface detector to be located near the CMS experiment, and whose focus is the precise determination of LLPs with lifetimes up

[12] Hyphotetical particles with a fractional electric charge which appear in Dark Sector theories with kinetic mixing with Standard Model photons. They can be Long-Lived through the action of approximate symmetries.

[13] A low-scale demonstrator for FORMOSA has been installed during Run 3, in the Year-End Technical Stop 2023-2024.

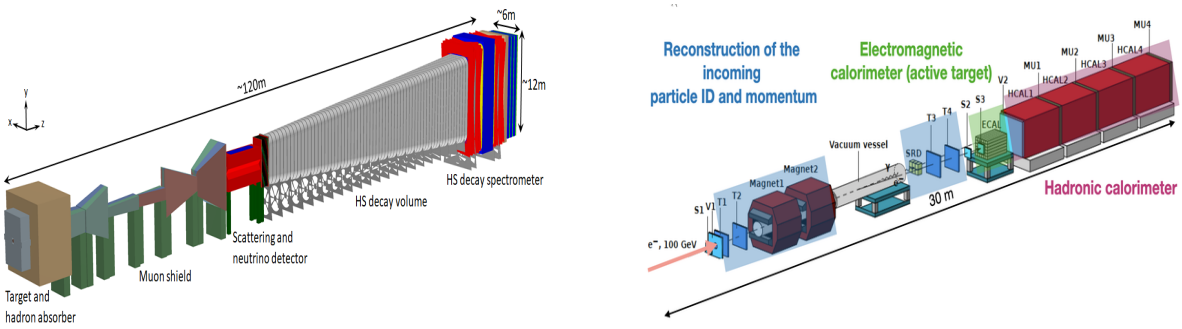


Figure 3.17: Experimental setup of SHiP (left) and NA64 (right) experiments. Obtained from [235] and [236] under CC BY 4.0.

to 0.1 s, limit imposed by Big-Bang Nucleosynthesis [98]. The updated baseline design, known as MATHUSLA40, features a modular decay volume of approximately $40 \times 40 \times 11$ m^3, situated about 70 m from the interaction point and shielded by 100 m of rock to suppress backgrounds [233]. Its detection system relies on multiple layers of plastic scintillators providing nanosecond-level timing and centimetric spatial resolution, enabling the reconstruction of displaced vertices from LLP decays in a large, low-background fiducial volume. This configuration would offer nearly background-free sensitivity to LLPs with masses up to $\mathcal{O}(100$ GeV), particularly for hadronic or dileptonic decay modes [232].

The **ANUBIS** detector has been proposed as an additional tracking system to be installed in the service shaft of the ATLAS cavern. Its baseline design instruments about 15,000 m^3 with RPC stations mounted on the shaft walls, providing a fiducial volume extending up to $\sim$ 80 m from the primary vertex. This configuration would yield sensitivity to long-lived particles with lifetimes in the range $0 < c\tau < 10^6$ m and masses above $\sim$ 1 GeV [234]. ANUBIS is expected to operate with nearly background-free conditions, though its geometric acceptance is partially limited by the ATLAS detector itself, corresponding to a veto of about 10 radiation lengths. Additionally, its inclusion in the ATLAS trigger would allow the simultaneous study of LLPs and massive prompt resonances such as the Z, W or Higgs bosons.

The detector **CODEX-b** is another example of a transverse LLP detector. It constitutes a fundamental part of the present thesis, and it is reviewed in detail in Section 3.6.

3.5.4 Beam-Dump Experiments

Beam Dump experiments are characterized by a particle beam which is directed into a block made up of a dense material in order to induce interactions between hypothetical Hidden-Sector particles at the time of absorbing possible background sources, typically hadronic cascades. Afterwards, the signal is conducted to a background-free environment, where the relevant tests are performed with the corresponding instrumentation.

The **SHiP** experiment [235] has been proposed as a general-purpose intensity-

frontier facility operating in beam-dump mode at the CERN SPS accelerator to search for feebly-interacting GeV-scale particles and to perform neutrino and flavour physics. The setup (schema in Figure 3.17 left) consists of a high-density proton target, followed by a hadron stopper and magnetic-deflection muon shield, an Scattering and Neutrino Detector (to search for scattering of light dark matter and neutrino physics) and finally a Hidden Sector (HS) Decay Spectrometer, designed to reconstruct the decay vertex of a HS particle, measure its invariant mass and provide particle identification of the decay products in an environment of extremely low background [235]. SHiP, above all, will show a very competitive sensitivity to Heavy-Neutral-Lepton models, covering the parameter space below the B mass down to the ultimate see-saw limit.

Complementarily, the **NA64** detector [141, 236] was also installed at the CERN SPS accelerator, designed as a hermetic general-purpose detector to search for Dark Sector physics in missing energy events from electron/positron, hadrons and muon scattering off nuclei. The experimental setup (Figure 3.17 right) consists of a magnet spectrometer made of tracking stations downstream and after the bending magnets for reconstructing charged-particle trajectories, a Synchrotron Radiation detector, an Electromagnetic calorimeter and, finally, four layers of muon stations introduced in between four hadronic calorimeters [236]. So far, NA64 has set the world's strongest limits on invisible dark photons using electron beams, and has recently begun probing the parameter space relevant to the muon $(g-2)$ anomaly with muon beams [141].

3.5.5 Other experiments

In contrast to detectors optimized for displaced decays, experiments such as **milliQan** [229] and **MoEDAL** [237] are designed to identify stable or non-decaying exotic particles through their distinctive ionization signatures. They extend the LHC's sensitivity to weakly or highly charged states, probing sectors of parameter space complementary to those accessible with traditional LLP searches.

The milliqan detector has been installed in an underground tunnel access 33 m away from the CMS experiment, shielded with 17 m of rock to suppress hadronic backgrounds. The proposal, based on a 1 m x 1 m x 3 m [229] scintillator plus photomultiplier Tube (PMT) array, aims to determine millicharges down to $10^{-3}e$ [238] with an estimated energy loss of 10^{-6} lower than that of an e-charged particle. The milliQan detector has already reached sensitivities down to $10^{-3} \rightarrow 10^{-4}$ for masses in the range $0.1 - 10\,\mathrm{GeV}\mathcal{Q}/\mathrm{e}$ (short lifetime).

The MoEDAL detector, installed around the LHCb interaction region at Point 8, consists of an array of passive Nuclear Track Detectors (NTDs) housed in aluminium frames covering up to 25 m^2 on the walls and ceiling of the VELO cavern [237]. Each stack, made of nine alternating layers of CR39, Makrofol, and Lexan plastic, records the passage of highly ionizing particles such as magnetic monopoles. Recent results based on the full Run 2 dataset found no evidence of monopole production, setting the

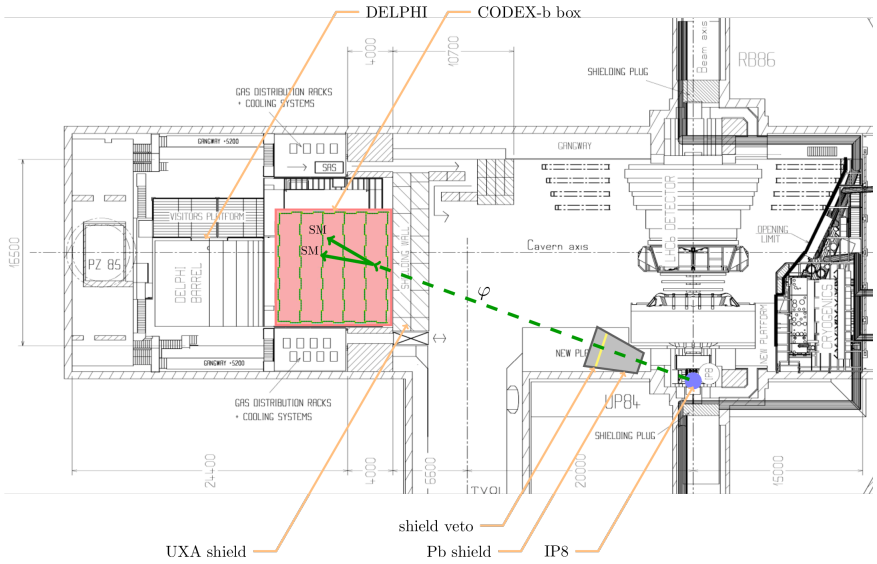


Figure 3.18: Baseline CODEX-b detector proposal at the LHCb experimental cavern. The cubic volume is located at $x = [26, 36]$ m, $y = [-7, 3]$ m and $z = [5, 15]$ m. Obtained from [241] under CC BY 4.0.

most stringent direct limits to date on magnetic charges up to $5g_D$[14] and masses up to $\sim$3.5 TeV [239].

3.6 The CODEX-b experiment

The strategy for installing detectors dedicated to LLPs arises from the balance between building new detectors (with the technological and logistical challenges this entails) and making use of spaces adjacent to the main detectors to enhance the search for new physics. The CODEX-b experiment is a proposed tracking detector designed to occupy a cubic volume of $10 \times 10 \times 10\text{m}^3$ and located 25 m from the pp interaction point of the LHCb detector. Although the luminosity at LHCb is lower than that of ATLAS or CMS, its transverse geometry and potentially favorable background conditions would enable a reach in new physics that complements or even surpasses that of the other LHC experiments [240].

The baseline configuration for CODEX-b consists of a cubic fiducial volume located behind a 3m-thick concrete wall which divides the experimental cavern into two sections (see Figure 3.18). This location, corresponding to the pseudorapidity range $0.13 < \eta < 0.54$, makes CODEX-b specially suitable for heavy-mediator physics (exotic Higgs decays or scalar portals), for exotic decays-in-flight of B meson products or even fermion and gluon-coupled ALPS [240]. Technical issues associated with the detector's geometry and the available space in the cavern sparkes debate about its final shape and location. Consequently, a rapid simulation framework is designed to evaluate different

[14]The Dirac magnetic charge, the minimum quantized unit of magnetic charge allowed according to the Dirac quantization condition. Its value is $g_D \approx 68.5e$.

proposals against certain physics benchmarks. More details are provided in Section 7.

While transversality brings a unique opportunity for new physics analysis, the baseline location provides CODEX-b with a series of advantages which are imperative to note:

- Relatively big space between the primary interaction and the CODEX-b volume, which might be used to include vetos in terms of background control. One important goal is to achieve an almost-zero background environment.
- Proximity to LHCb ($\sim$ four bunch-crossing times for relativistic particles) makes integration into the LHCb trigger system feasible, allowing partial reconstruction of LLP decays and access to the underlying event [240]. In fact, the characteristics of the LHCb trigger mean that event readout is limited by High-Level Trigger performance rather than latency
- Reduced costs, not only in terms of civil engineering, but also by leveraging existing infrastructure such as high and low voltage lines, gas distribution, and other services needed for assembly and operation.

CODEX-b aims to begin operation in 2036, coinciding with the start of Run 5. The target integrated luminosity for physics is about 300 fb^{-1}. In the shorter term, a smaller prototype, CODEX-β (Section 3.6.4), will take data during the final stage of Run 3 as a proof-of-concept demonstrator.

3.6.1 Baseline Design

The core drivers for an LLP detector are the geometric acceptance and the ability to reconstruct displaced events. Additionally, proper control over potential background sources must be demonstrated so that any observed event can be reliably associated with new physics (NP).

At first instance, the CODEX-b design is oriented towards the optimization of the number of possible decay vertices in the fiducial volume. With the numbers of the proposal (Figure 3.18), the estimated acceptance efficiency locates roughly at 1%, which might bring for example a maximum 2σ exclusion for a Higgs decay to dark photons of 10^{-4}, assuming an integrated luminosity of 300 fb^{-1} [240].

In terms of tracking, CODEX-b must keep the highest possible tracking capabilities while accommodating the largest possible number of topologies that could trigger LLPs. As vertexing resolutions depend on the distance between the vertex and the first measured point on the decay product trajectories, five equally spaced tracking layers are included inside the cube. Additionally, the six outer cube faces are also instrumentalized to avoid leaks of charged products coming from soft LLP decays [240].

USC UNIVERSIDADE DE SANTIAGO DE COMPOSTELA

The tracking technology in the CODEX proposal includes the use of fast-gaseous detectors such as Resistive Plate Chambers (RPCs), which have already proven their

sensitivity under challenging instantaneous luminosity conditions, as in the ATLAS barrel region [242]. Each detection layer is implemented as an RPC triplet (section 3.6.2), enabling improved spatial and temporal resolution for precise track reconstruction, efficient suppression of spurious signals via triple-coincidence logic, and local track fitting capabilities largely independent of the global detector alignment.

The (almost) free background environment is reached by the conjunction of passive and active elements. As shown in Figure 3.18, CODEX-b is positioned behind a 3 m concrete wall and an additional Pb shield effectively covering the angular range subtended by the detector, corresponding to a nuclear interaction length of 32λ [120]. This amount of passive shielding is sufficient to suppress the primary flux, dominated by neutrons and K_L^0 mesons[15]. However, such a large amount of material can itself become a source of secondary neutral LLP-like particles, produced by muons or neutrinos traversing the shield and therefore invisible to the detector [120]. To mitigate this, an active shield veto (highlighted in yellow in Figure 3.18), based on scintillator material (still to be defined), will tag these secondary products and correlate them with their corresponding parent particles.

Similar to the veto shield, the original design includes several elements that can be used as active veto elements as well. First, the inclusion of RPC triplets operating in coincidence allows for the suppression (via dedicated triggers) of co-scattering processes in the detector or cosmic ray products that survive in the cavern. Second, the association of CODEX-b events at LHCb would allow for the elimination of events unrelated to the underlying event.

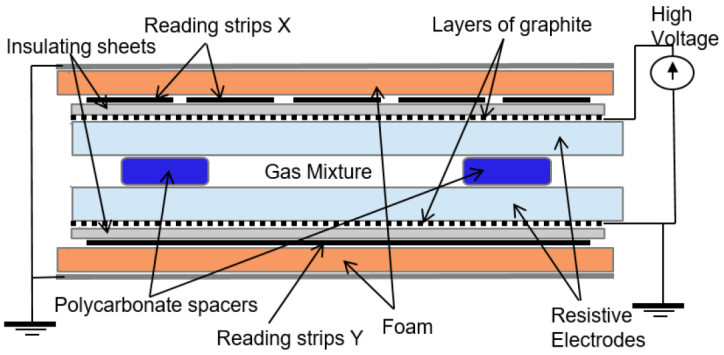


Figure 3.19: Sketch of a ATLAS BIS78 RPC module. Obtained from [241] under CC BY 4.0.

3.6.2 Tracking technology

The RPC tracking technology provides an excellent timing and spatial resolution, even with the lack of magnetic fields for momentum measurements. Additionally, their high-

[15]Roughly 10^{14} neutrons and K_L^0 are produced in 300 fb^{-1}.

rate capabilities and their excellent signal-to-noise ratio turn them into a flexible and reliable technology, excellent for LLP detection scenarios.

The type of RPC chosen comes from the ATLAS phase II design, called BIS78 [242]. Its main features include a spatial resolution of 1mm, a timing resolution of 350 ps and a rate capability of several kHz/cm^2, which represents a clear gain over its predecessors [242, 243]. A schematic representation of an RPC element can be seen in Figure 3.19.

The operational principle of an RPC is based on a highly resistive gas gap (mono-gap) subjected to a large potential difference (approximately 15 kV), operating via electron avalanches triggered by small charge depositions. The gas volume, enclosed by resistive electrodes made of bakelite, is coated on both sides with conductive graphite layers, which help to evenly distribute the applied potential across the electrodes. This entire assembly is then sandwiched between insulating sheets that provide electrostatic insulation while being sufficiently thick and dielectric to allow capacitive transmission of the avalanche signal. On top of this, strip panels made of conductive material are placed above a thermally insulating foam, which serves to read out the induced electronic signals. Typically, orthogonal strip patterns are included on both sides of the detector, enabling the precise measurement of X and Y coordinates.

Following the same technical principles for ATLAS and CMS RPC systems, the gas chosen for operational purposes is a mixture of 94.7% R-134a (1,1,1,2 tetrafluoro-ethane), 5% isobutane and 0.3% SF6 (sulfur hexafluoride) [241]. This gas is contained in a 1 mm gas gap, working at the environment temperature and pressure. A recycling and circulation system is needed to keep the gas moving, as well as a humidification system to remove possible impurities from the mixture during runtime.

Improvements in the BIS78 RPC have been mainly oriented towards the optimization of the chamber structure as a Faraday cage and the reduction of the average charge per count, which allows for an increase of the rate capability while operating the detector at fixed current [243]. Consequently, more sensitive front-end electronics are developed to detect and transmit very small signals, of the order of hundreds of μV. Fundamental readout module encloses: a preamplifier with Silicon Bipolar Junction Transistor technology, a Silicon-Germanium Hetero Junction bipolar Transistor for high-rate environments and a Low-Voltage Differential Signaling transmision unit [243].

3.6.3 Physics Reach

Qualitatively, the decay of an LLP is produced according to an exponential law with characteristic $c\tau\beta\gamma$ in the laboratory rest frame. Assuming a constant boost and an isotropic production, the geometric efficiency is determined from the probability of decaying in a detector volume:

USC UNIVERSIDADE DE SANTIAGO DE COMPOSTELA

$$\varepsilon_{Geo} = \int \frac{e^{-r/c\tau\beta\gamma}}{c\tau\beta\gamma} \frac{dV}{4\pi r^2} \tag{3.5}$$

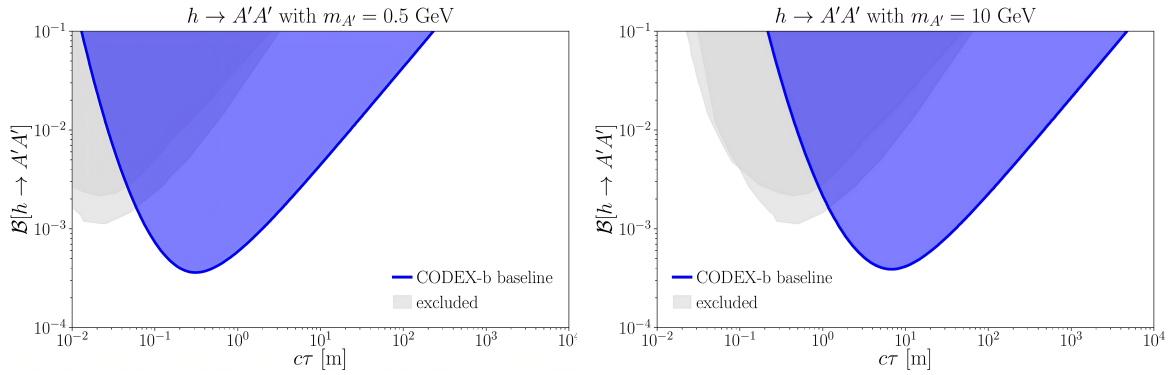


Figure 3.20: CODEX-b reach to Dark Photon signatures through a Kinetic mixing portal. Obtained from [139] under CC BY 4.0.

where r is the radial distance[16] from the interaction point, and dV is the infinitesimal element of volume, determined by the detector angular coverage $\delta\Omega$ and the depth d. Under such assumptions, three regimes are recognized:

- **Short lifetime regime:** The distance of the volume element with respect to the IP is bigger than the lab frame LLP displacement $r \gg c\tau\beta\gamma$:

$$\varepsilon_{Geo} \approx e^{-r/c\tau\beta\gamma}\frac{\delta\Omega}{4\pi} \tag{3.6}$$

- **Peaking regime:** The LLP displacement coincides with the location of the active volume $r \sim c\tau\beta\gamma$:

$$\varepsilon_{Geo} \approx e^{-1}\frac{d\delta\Omega}{4\pi r} \tag{3.7}$$

- **Long lifetime regime:** The characteristic displacement of the LLP overcomes the location of the detector volume $r \ll c\tau\beta\gamma$:

$$\varepsilon_{Geo} \approx \frac{d\delta\Omega}{4\pi c\tau\beta\gamma} \tag{3.8}$$

These analytical regimes directly translate into the qualitative structure of the usual exclusion plots in the $(\mathcal{B}, c\tau)$ plane. In the short-lifetime regime, the exponential suppression of the geometric acceptance (3.6) results in rapidly decreasing sensitivity at lifetimes much shorter than the detector's distance to the interaction point. Around the peaking regime (3.7), where the characteristic decay length matches the detector location, the search achieves its maximal reach; this defines the central plateau or "bump" of the exclusion contour. Finally, in the long-lifetime regime (3.8), the acceptance scales inversely with $c\tau$, producing the familiar $1/c\tau$-like falloff of the exclusion limit at high lifetimes. Together, these features create the characteristic triangular or wedge-shaped sensitivity regions commonly observed in LLP searches.

[16] For the discussion, spherical symmetry is assumed without loss of generality.

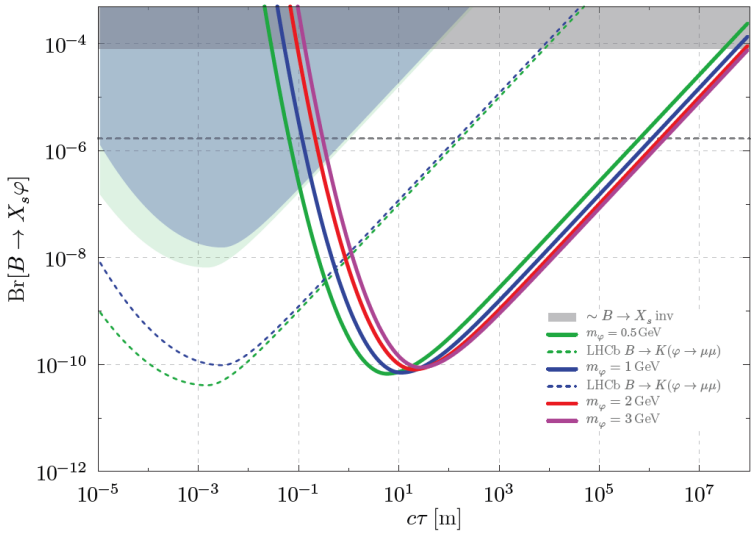


Figure 3.21: CODEX-b reach to exotic B decays. Obtained from [240] under CC BY 4.0.

As discussed in Section 1.3.2, the reach of CODEX-b to new physics spreads across different channels and topologies, like exotic Higgs Decays, $b \to s\phi$ transition in B meson decays, heavy neutral leptons, or even ALPs [122]. Overall, this detector is highly competitive in low-mass LLP tracks (< 10 GeV), where, for example, the backgrounds for ATLAS and CMS are competitive, and in relatively short-lived LLPs, surpassing contributions from other LLP detectors such as MATHUSLA in this range.

The main CODEX-b physics benchmarks [95, 240] arise from the Kinetic and Higgs mixing portal:

- The kinetic mixing between a Dark Photon and the SM U(1) hypercharge group might be responsible for processes such as $H^0 \to A'^\mu A'^\mu$, where the A'^μ decays mainly to electrons. The physics reach of CODEX to this channel is displayed in Figure 3.20, where a comparison to the ATLAS search for 1 and 2 displaced vertices (shadow areas) and to a rescaling of the expected MATHUSLA reach is performed.

- Higgs mixing would provide, through the coupling of a scalar particle φ, decays of the form $B \to K\varphi(\mu^+\mu^-)$ which are dominated by flavour-changing neutral current processes. The sensitivity reach of CODEX is shown in Figure 3.21, where also the one from LHCb (being solid the current reach and dashed the rescaled one to 300 fb^{-1}) to $B \to K\varphi$ (green) and $B \to K^*\varphi$ (blue). Additionally, the exclusion from precision measurements of $B \to K^{(*)} + \mathrm{inv}$ is also included.

USC UNIVERSIDADE DE SANTIAGO DE COMPOSTELA

Complementarily, ALPs and HNLs complete the physics landmark. The first could be copiously produced in LHC proton-proton collisions if they are coupled to quarks and gluons, and if they have a sizable non-invisible decay could be detected with

the CODEX-b nominal design if their angular distribution is enough collimated. The second, given the large $b\bar{b}$ and $c\bar{c}$ cross-sections that might be reached in LHCb, could be abundantly produced in processes such as $c \to slN$ and $b \to clN$ (N being the HNL state), and subsequently dominated by decays to multiple charged particles. Further discussions and sensitivity prospects can be found in [120, 95, 122].

Aside from its discovery potential, CODEX-b can also perform measurements of the LLP velocity from topological information [244]. This is possible provided the LLP originates from the primary pp interaction, so that reconstruction of its decay vertex enables a precise determination of the propagation vector. Under specific assumptions about the production mechanism [240], mass measurements are also feasible. For two-body decays, knowing the LLP flight vector allows the daughter momenta p_i to be Lorentz-transformed into the mother's rest frame, where they become back-to-back. In this configuration, the LLP velocity can be extracted from [244]:

$$\beta_{\mathrm{LLP}} = \frac{\beta_1 \beta_2 \sin(\theta_1 + \theta_2)}{\beta_1 \sin\theta_1 + \beta_2 \sin\theta_2} \tag{3.9}$$

where β_i and θ_i are the boost and reconstructed angle of daughter i, respectively. For highly relativistic daughters, one may safely approximate $\beta_i = 1$ without loss of generality.

For multi-track decays, Eq. 3.9 no longer applies. The LLP velocity can still be estimated if its parent is spin-0, or (more generally) if it is produced depolarized along the longitudinal direction, with negligible CP-violating effects. In this case, the momenta of the decay products in the LLP rest frame are, on average, front-to-back symmetric, allowing the event-by-event solution of:

$$\hat{p}_{\mathrm{LLP}} \cdot \sum_i \hat{p}_i(\beta_{\mathrm{LLP}}) = 0 \tag{3.10}$$

The determination of the LLP boost, within experimental uncertainties, can be used to identify the bunch crossing in which the particle was produced. Even with limited statistics, this information enables kinematic studies of other objects from the same collision and can set constraints to help discriminate between different production mechanisms.

3.6.4 A demonstrator: CODEX-β

A prototype, CODEX-β, is planned for operation during the final stage of Run 3 as a proof-of-concept demonstrator for the full CODEX-b detector. This project, which has covered a long period within the completion of this thesis, is discussed in depth in the Section 6.

As its successor, the geometry of CODEX-β consists of a 2m-side cube, with instrumented exterior faces and an inner tracking station. The main objectives of CODEX-β



Figure 3.22: CODEX-β demonstrator after the installation of the support structure and all the fourteen modules assembled to it.

are [245]:

- Validate preliminary background estimates for the full detector by reconstructing SM background events and benchmarking a full simulation against the LHCb detector and cavern environment.
- Demonstrate seamless integration of the detector readout with LHCb's data acquisition system.
- Assess the performance of RPCs as the baseline tracking technology, in terms of spatial granularity, hermeticity, and timing resolution.
- Validate the feasibility of the modular mechanical support structure and its scalability to the full CODEX-b design.

The demonstrator is being installed in the nominal location foreseen for the full detector (the D1 barracks, see Figure 3.18). Unlike the final configuration, the Pb veto and veto shield will be absent, leaving only the 7λ concrete wall that separates the detector volume from the LHCb interaction region. The absence of the veto will increase the event rate observed by CODEX-β. Among the most promising signatures are K_L^0 mesons, which can regenerate into K_S^0 upon interacting with the radiation wall and subsequently reaching the detector's fiducial volume. Measuring the K_S^0 lifetime in this setup will serve both as a test of the detector's sensitivity and as a powerful calibration tool.

USC UNIVERSIDADE DE SANTIAGO DE COMPOSTELA

4

Following the track of hierarchical sectors at LHCb

The good muon identification capabilities for relatively soft momentum tracks and the precise vertex resolution make the LHCb experiment an excellent choice to look for displaced multi-muon signatures from B-meson decays (see Section 1.3.1). Such final states have been previously studied at LHCb, mainly in the context of flavour-changing neutral currents (FCNC), leading to current world-best results for the very rare decays [117]:

$$\begin{aligned} \mathcal{B}(B_s^0 \to \mu^+\mu^-\mu^+\mu^-) &< 8.6 \cdot 10^{-10} \\ \mathcal{B}(B_s^0 \to a(\mu^+\mu^-)a(\mu^+\mu^-)) &< 5.8 \cdot 10^{-10} \end{aligned} \tag{4.1}$$

where in the second block a prompt 1 GeV is considered. Both limits were computed at 95% CL with 9 fb^{-1}, the combined Run 1 and Run 2 dataset.

In the present work, an analysis of the Multimuon hierarchical model [116] is presented, relaxing the assumption of a short-lived exotic sector. As a first approximation, a phenomenological study is proposed to evaluate the sensitivity of LHCb and CODEX-b detectors regarding the topology of the decays from Figure 1.9 and 1.10. After scanning the decay chains in the $m_{a_1}, m_{a_2}, t_{a_1}$ parameter space, a set of representative benchmark points is selected for an experimental analysis using pp collision data recorded during Run 2.

Beyond the possible enhancement of the branching ratio in displaced scenarios, two additional aspects drive the motivation for this study: (i) assessing the potential efficiency gain from reconstructing tracks solely in downstream subsystems for highly displaced decays, and (ii) exploring whether, within the considered model, the 4μ final states are suppressed in favour of 6μ multiplicities.

USC
DE SANTIAGO
DE COMPOSTELA

This study is performed by a team of four researchers. The contribution of this thesis corresponds to the generation and analysis of the events yielding the sensitivity reach for the experimental signatures with the LHCb and CODEX-b experiments.

At the time this study was published, the tension in the R_K parameter reported by LHCb had not yet been disproved [246]. The analysis explored the parameter space that could account for such an anomaly, which later measurements have largely resolved.

4.1 Phenomenological Analysis

Following the motivations outlined in previous sections, the following exclusive decay modes are studied:

1. $B_s^0 \to a_1(a_2 \to a_1 a_1) \to 3\mu^+ 3\mu^-$ and $B^+ \to a_1(a_2 \to a_1 a_1) K^+ \to 3\mu^+ 3\mu^- K^+$,
2. $B_s^0 \to a_1 a_2 \to 2\mu^+ 2\mu^-$ and $B^+ \to a_1 a_2 K^+ \to 2\mu^+ 2\mu^- K^+$,

that correspond to the main decay modes of the scalar particles in the regimes $m_2 > 2m_1$ and $m_2 < 2m_1$, respectively. While a_2 is taken as a prompt resonance, a range of lifetimes for a_1 is considered.

As a reference channel, the decay $B_s^0 \to a_1 a_1 \to 2\mu^+ 2\mu^-$ is used, whose sensitivity is taken from the recently published search [117]. In that analysis, the LHCb experiment looked for a peak at the B_s^0 mass in the invariant four-muon mass, requiring that the two dimuon pairs have a reconstructed mass compatible with each other within the mass resolution.

An analysis of the different decay signatures is performed with simulation samples generated by PYTHIA 8.305 [247]. Signal B mesons are generated from $b\bar{b}$ events and decayed in many different (m_1, m_2, τ_1) configurations using a flat phase space model. Adding the momentum dependence in the meson form factors leads to negligible effects on the sensitivity (differences of around 1% were obtained). Background processes from pp-collisions involving $b\bar{b}$-events and non-diffractive QCD processes are studied with PYTHIA simulation. No attempt is made to simulate detector resolution effects, which are accounted for through normalising to the published search. Similar to the published search [117], the expected background is low, and therefore, the mass resolution is also considered to make a negligible impact.

To investigate the best possible reach, an inclusive and an exclusive reconstruction approach are compared. The exclusive approach requires a reconstruction and selection of all final states and vertices of the exclusive decays, while the inclusive approach requires only the reconstruction of four muons and at least two dimuon vertices inside the detector volume. When considering the CODEX-b experiment, an exclusive reconstruction is found infeasible because of the large transverse displacement of $> 26\,\mathrm{m}$, and the inclusive reconstruction is relaxed by requiring at least one dimuon vertex to

USC UNIVERSIDAD DE SANTIAGO

be inside the CODEX-b detector volume. In the analysis of recorded LHCb data, the discriminating feature would be a clear peak at the B mass in the case of the exclusive reconstruction, making use of the fact that all a_1 candidates in the selection have a similar mass [116]. In the inclusive reconstruction, the discriminating feature would be a bump in the reconstructed 4μ mass where the flight direction of both dimuon candidates points to the same vertex. A clear signature in the CODEX-b detector would already be given by the existence of a vertex inside the volume.

For LHCb events, the following requirement must hold:

- Each track must have an angle $10 < \theta < 400\,\text{mrad}$ to fall within the LHCb acceptance.
- Each track must ensure $p_T > 250\,\text{MeV}$ to ensure good tracking quality and reconstruction efficiency[1].
- Muon tracks with $p > 2.5\,\text{GeV}$ for correct identification purposes. Note that muons with lower momentum will hardly pass through the shields of the muon stations, and thus limiting a correctly muon identification (Table 3.4).

whereas the different track types are then defined according to the position of the reconstructed $a_1 \to \mu^+\mu^-$ decay vertex: inside the VELO (Long tracks), between the VELO and the UT (Downstream tracks), or before the SciFi tracker (T-tracks). In Table 4.1, a comprehensive overview can be found [248, 249, 120]. Likewise, reconstruction efficiency for each kind of track is included with penalty factors, which are included in Table 4.1, and estimated according to Refs. [204, 207, 250]. These factors do not contain efficiency losses due to material interactions, which are expected to be less than $\approx 10\,\%$ per track and should cancel out with respect to the reference channel in the inclusive searches. As the CODEX-b experiment is still in planning, no penalty factor is associated with the reconstruction of tracks. However, the low occupancy of the detector would suggest a near-perfect reconstruction efficiency, thus rendering tracking an irrelevant limitation for the analysis [240].

In terms of homogenizing the signal selection and the control mode, apart from vertex reconstruction and vertex displacement, L0 trigger requirements are set for Run 1 and Run 2 projections. These rely on requiring at least one muon with $p_T > 1.76\,\text{GeV}$ or at least one combination of two muons with $p_{T,1} \times p_{T,2} > (1.6\,\text{GeV})^2$, which results in a total efficiency of $\varepsilon_{\text{ref}} = 8.4\,\%$. The effective removal of the hardware-based trigger for Run 3 onwards would allow for an increase in the efficiency of roughly a 20%. The total efficiency is approximately 10 times larger than the efficiencies found in the published search. The discrepancy can be explained by additional vertexing and vertex displacement requirements, which cannot be simulated with the chosen

[1]Note that LHCb can reconstruct particles with transverse momentum down to 100 MeV, but a cut in $p_T > 250$ MeV is usually chosen to suppress poorly reconstructed or low-quality tracks

Track Type	x [m]	y [m]	ρ [m]	z [m]	Penalty Tracking Factor
Long	—	—	$[0, 0.03]$	$[0, 0.5]$	0.98
Downstream	$[-0.75, 0.75]$	$[-0.65, 0.65]$	—	$[0.6, 2.3]$	0.89
T-Track	$[-3.15, 3.15]$	$[-2.35, 2.35]$	—	$[2.3, 7.6]$	0.70
CODEX-b	$[26, 36]$	$[-7, 3]$	—	$[5, 15]$	1.00

Table 4.1: Different track types at the LHCb and CODEX-b experiments that are studied in this work: corresponding geometrical requirements and track reconstruction efficiencies. For CODEX-b, no penalty for the track reconstruction can be estimated yet.

simplistic approach. However, these requirements are likely unavoidable in any data analysis of the studied decays, and therefore, this factor is considered irreducible.

Under the assumption that a similar low background can be achieved with similar vertexing efficiencies as in the reference search, the expected upper limit for each scenario can be obtained as

$$\mathcal{B}_{\text{sig}} = \mathcal{B}_{\text{ref}} \times \frac{\varepsilon_{\text{ref}}}{\varepsilon_{\text{sig}}} \times \frac{N_{\text{ref}}^{b\bar{b}}}{N_{\text{sig}}^{b\bar{b}}} \frac{f_s}{f_{s,u}}, \tag{4.2}$$

where $\mathcal{B}_{\text{ref}}$ is the expected upper limit of the published analysis, ε_{ref} and ε_{sig} are the efficiencies of the signal and reference modes as determined in this work and $N_{\text{ref,sig}}^{b\bar{b}}$ are the effective B-hadron yields, obtained by multiplying the integrated luminosity of each data set with the corresponding $\sigma(pp \to b\bar{b}X)$ cross section [251, 252, 253]. The hadronization fractions of the B_s^0 (~ 0.1) and the B^+ mesons (~ 0.4) [254] are labeled as $f_{s,u}$. The integrated luminosities of the LHCb data sets are taken as $1\,\text{fb}^{-1}$ at 7 TeV for the 2011 part of Run 1; $2\,\text{fb}^{-1}$ at 8 TeV for the 2012 part of Run 1; and $6\,\text{fb}^{-1}$ at 13 TeV for Run 2. After Run 3, Run 4 and Run 5, respectively, $23\,\text{fb}^{-1}$, $50\,\text{fb}^{-1}$ and $250\,\text{fb}^{-1}$ are expected to be collected at a center-of-mass energy of 14 TeV. To obtain the b-quark production cross section at $\sqrt{s} = 14$ TeV, the cross section measured at 13 TeV is rescaled by a factor of 14/13. Thus, $N_{\text{ref}}^{b\bar{b}} = 3.9 \times 10^{12}$ is assumed. The linear scaling of the expected upper limit with luminosity in equation 4.2 is only valid under the assumption of very low background, which is discussed in detail in Section 4.3.

4.2 Decay time and Mass Maps

Signal decay samples, as defined in 2, are produced from generator-level B_s^0 and B^+ mesons. The subsequent decays into the required final-state phase space are simulated using the `TGenPhaseSpace` class [255], which performs the full kinematic decomposition of an n-body decay while enforcing exact energy–momentum conservation. Given the reconstructed production vertex of the parent B meson, its flight direction, and the

four-momentum of an intermediate particle a_i, the decay vertex of a_i is computed as

$$x_i = x_{i,0} + t\frac{p_i}{m} \tag{4.3}$$

where $x_{i,0}$ is the parent decay vertex, p_i the three-momentum vector of a_i, m its invariant mass, and t its proper decay time. The latter is generated using the inverse transform sampling method [256], drawing from an exponential probability density with mean lifetime τ_i.

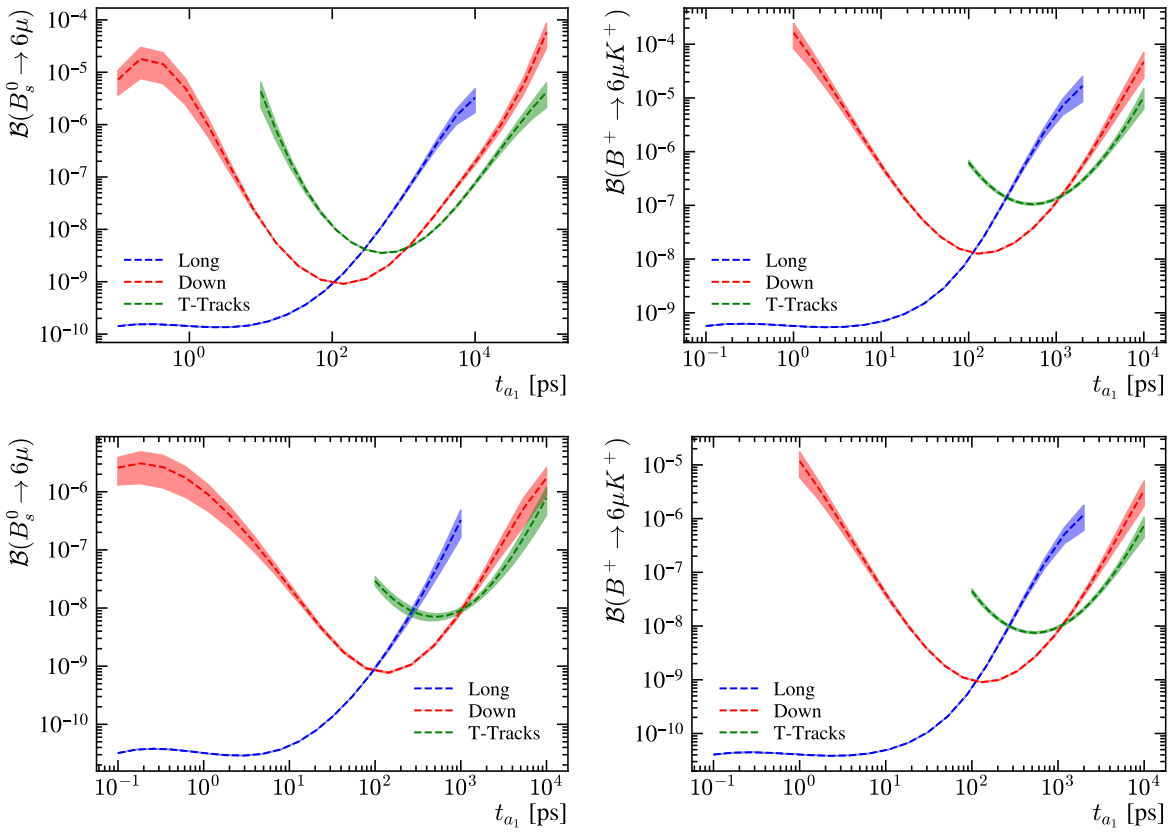


Figure 4.1: The expected upper limits on the $B_s^0 \to 3\mu^+3\mu^-$ and $B^+ \to K^+3\mu^+3\mu^-$ branching fractions that can be derived from the exclusive searches proposed in this work, for different lifetimes of the a_1 particle. In the upper (bottom) panels, the detector configuration after Run 3 (Run 5) is assumed. The benchmark masses were fixed to $(m_1, m_2) = (1.0, 2.5)$ GeV.

For the sensitivity maps across lifetimes, a mass point is chosen for each 4μ or 6μ scenario and a set of 10,000 decays is generated in eleven equidistant bins of lifetime in the range $(0, 10^7)$ ps. The efficiency is supposed to follow a binomial distribution, being the associated value and uncertainty computed following [46]. Finally, having computed exclusion reach from Equation 4.2, a spline interpolation [257] is performed in between lifetime seed points and the results are displayed over different track categories.

The resulting expected upper limits in branching fraction for the individual decay modes are shown in Figures 4.1 and 4.2. For the exclusive searches, by the end of Run

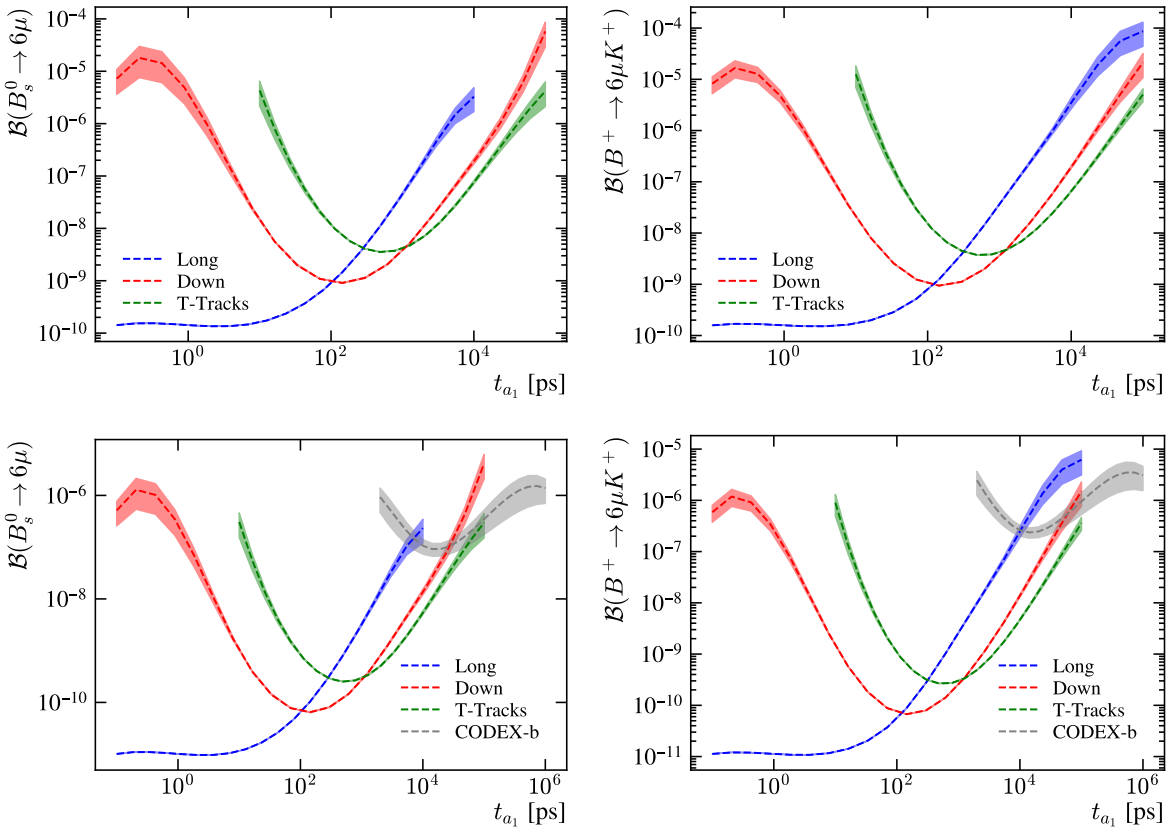


Figure 4.2: Same as in Figure 4.1, but requiring only four muons in the final state. Also included are the projected bounds for the CODEX-b experiment, requiring the presence of only one muon pair inside the acceptance.

5, quite high sensitivities down to the level of $\mathcal{O}(10^{-11} - 10^{-10})$ can be reached over a lifetime range up to 100 ps if all particles are reconstructed as long tracks. Even by the end of Run 3, sensitivities of $\mathcal{O}(10^{-10} - 10^{-9})$ can already be achieved. If all muons are reconstructed as downstream tracks, sensitivities down to $\mathcal{O}(10^{-10} - 10^{-9})$ can be reached in a lifetime range between 10 ps and 1 ns. The consideration of all muons being reconstructed as T-Tracks would allow to reach a moderate increase in efficiency (a factor of ≈ 3) and thus improve the expected sensitivity for lifetimes between 1 and 100 ns for the final states discussed in this work. For these searches, extra sensitivities might be gained in overlap regions when mixed track types are considered: e.g, in the case of $B_s^0 \to 3\mu^+ 3\mu^-$, if two dimuon pairs are reconstructed as downstream tracks and the other two muons as T-Tracks.

While not being selective to the final state and thus not as fit to distinguish between models, only reconstructing four muons instead of the full exclusive final states can improve the search sensitivity by about an order of magnitude. Reconstructing dimuon vertices in the CODEX-b experiment could improve the sensitivity to decays at very large lifetimes between 100 ns and 1 μs, allowing to test branching fractions of $\mathcal{O}(10^{-7} - 10^{-6})$ by the end of Run 5. Therefore, a good complementarity could be achieved between the LHCb and CODEX-b experiments in the large lifetime regime.

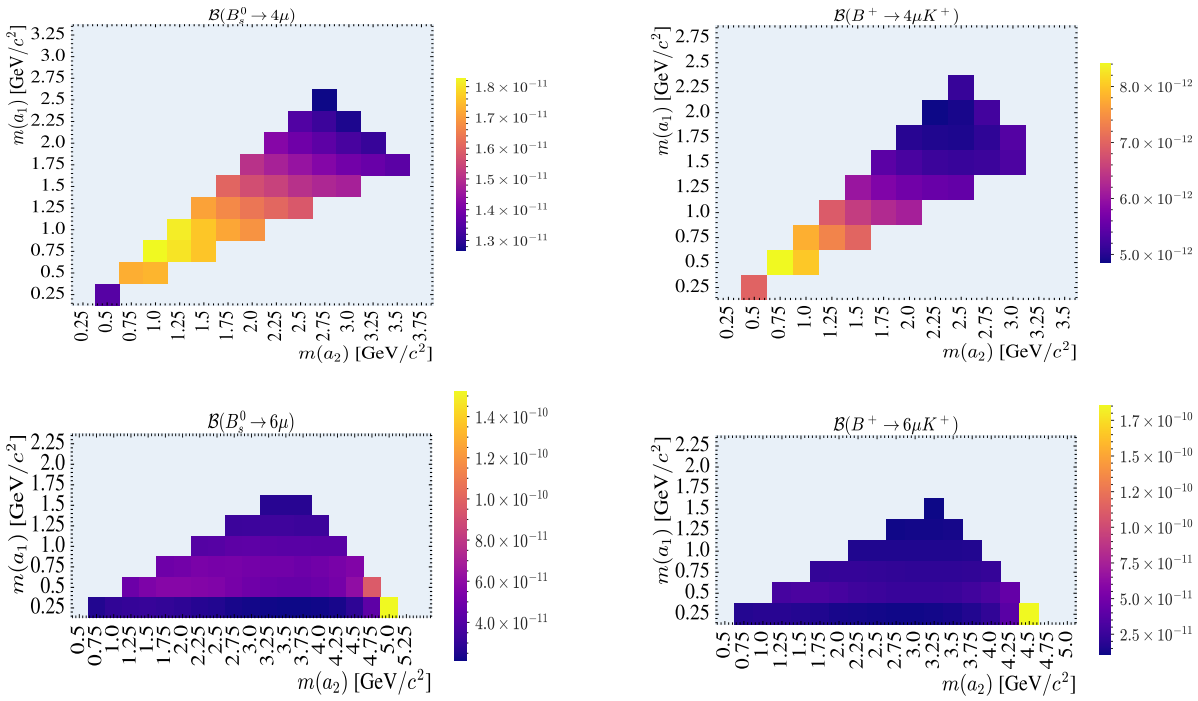


Figure 4.3: Mass-dependent expected limits at Run 5 on the branching fractions of (top left)$B_s^0 \to 2\mu^+2\mu^-$, (top right) $B^+ \to K^+2\mu^+2\mu^-$, (bottom left) $B_s^0 \to 3\mu^+3\mu^-$ and (bottom right) $B^+ \to K^+3\mu^+3\mu^-$ for a lifetime of the long-lived scalar of 1 ps.

The mass limits are determined for a given lifetime hypothesis, with the sensitivity reach evaluated within the phase-space regions defined by the final-state multiplicity: the space bounded by $m_2 < 2m_1$ for 4μ modes and $m_2 > 2m_1$ for 6μ modes. An inclusive 4μ approach is chosen for such a purpose. In Figures 4.3, 4.4 and 4.5 mass-dependent expected upper limit distributions for 1 ps, 100 ps and 1 ns are shown.

A clear structure can be observed. Larger efficiencies (and correspondingly smaller expected limits) are observed for high and low m_1 values. This structure is caused by the requirements on the transverse momentum of the muons. Products of heavy particle decays have a larger spread of transverse momenta than those of light particles. In the limit of low m_1, each pair of muons is produced collinearly and their transverse momentum is defined by the heavy ancestor, ultimately the B-meson. For high m_1, the a_1 scalars themselves are heavy and thus a source of larger muon p_T. At high a_1 lifetimes, the efficiency increases continuously with increasing m_1 as the geometrical requirement of the detector components becomes more important. The higher m_1, the less its boost away from the direction of the B; thus, the fraction of scalars (and consequently muons) that can be reconstructed inside the LHCb acceptance increases.

Another important effect that might be observed in all the mass maps 4.3, 4.4 and 4.5 is the homogeneity in the behaviour of the branching ratio as the multiplicity of the final state increases. This effect is inherited from the fact that the higher the multiplicity, the smaller the phase space available for the decays, and therefore, the kinematic differences tend to become minimal. This multiplicity also has a clear effect

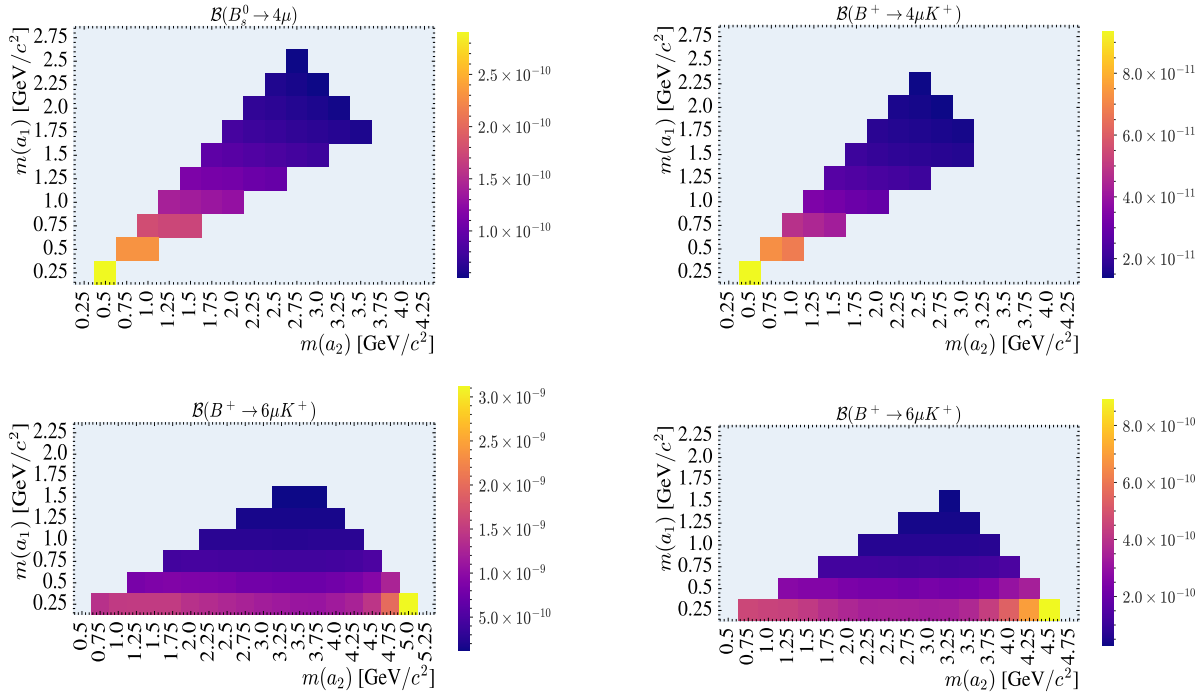


Figure 4.4: Mass-dependent expected limits at Run 5 on the branching fractions of (top left)$B_s^0 \to 2\mu^+2\mu^-$, (top right) $B^+ \to K^+2\mu^+2\mu^-$, (bottom left) $B_s^0 \to 3\mu^+3\mu^-$ and (bottom right) $B^+ \to K^+3\mu^+3\mu^-$ for a lifetime of the long-lived scalar of 100 ps. All decays are reconstructed inclusively with Downstream tracks.

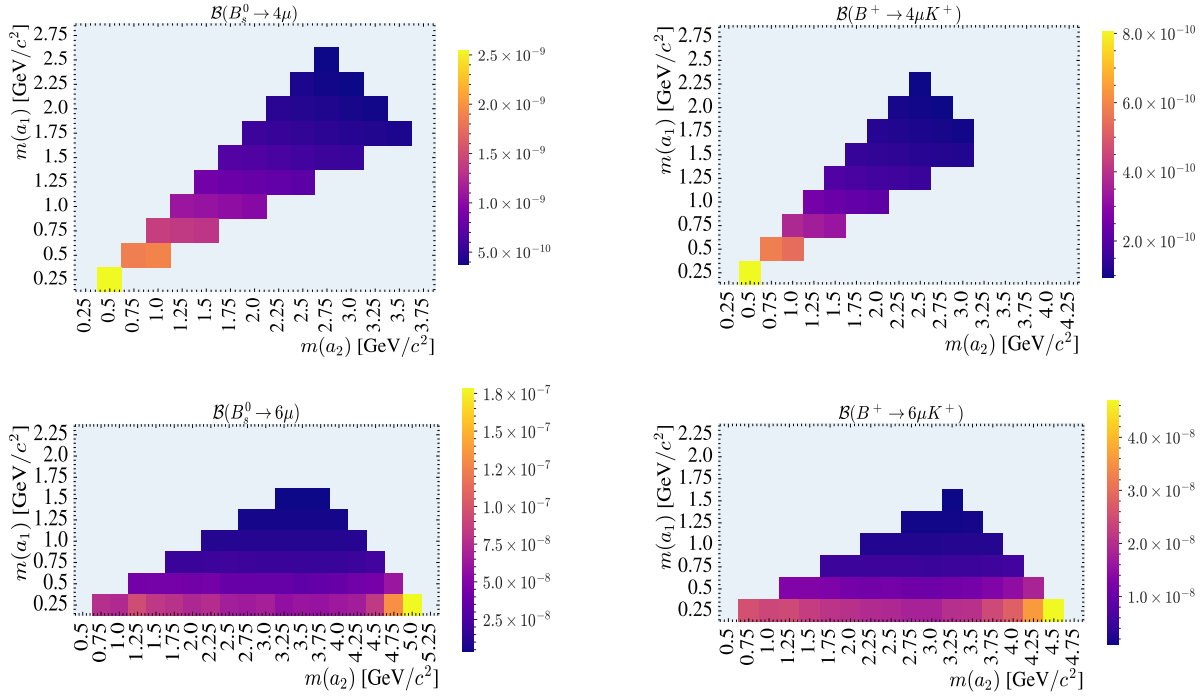


Figure 4.5: Mass-dependent expected limits at Run 5 on the branching fractions of (top left)$B_s^0 \to 2\mu^+2\mu^-$, (top right) $B^+ \to K^+2\mu^+2\mu^-$, (bottom left) $B_s^0 \to 3\mu^+3\mu^-$ and (bottom right) $B^+ \to K^+3\mu^+3\mu^-$ for a lifetime of the long-lived scalar of 1 ns. All decays are reconstructed inclusively with T-Tracks.

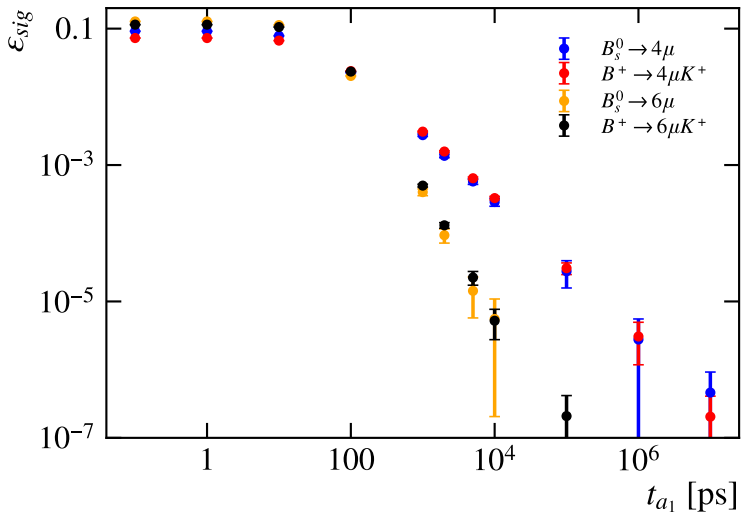


Figure 4.6: Signal efficiencies across lifetimes for each of the decay chains. All decays are reconstructed by being compatible with the Long tracks hypothesis.

on the extent of decay times in the corresponding decays. The decay length depends strongly on the boost that the parent particle can provide to the daughters (in this case, the scalars), which is reduced as more particles participate in the disintegration of the B meson. As a result (Figure 4.6) modes with 6μ multiplicity exhibit greater deterioration in reconstruction efficiency at high lifetimes. It is therefore noted that the use of alternative reconstruction strategies does not provide such powerful results in these modes compared to 4μ modes, with differences up to several orders of magnitude.

4.3 Expected Backgrounds

For the proposed searches with the LHCb experiment, several sources of background have to be considered. A dominant contribution typically arises from random track combinations. As demonstrated in the recently published LHCb search for four muon final states, it is possible to effectively remove these backgrounds with vertexing and muon identification requirements. If that is true for the four-muon final state, the same will hold for the decays with even more muons in the final state. Additionally, the behaviour of possible (dominantly combinatorial) background processes is studied with inclusive $pp \to b\bar{b}X$ and non-diffractive QCD simulation, which is reconstructed with the decay chain $B_s^0 \to a_1 a_2 \to 2\mu^+ 2\mu^-$. The same requirements (including muon identification, taking into account the misidentification efficiencies presented in Refs. [258, 201]) as discussed earlier are applied, imposing additionally the B candidate mass to lie between 4.5 and 6 GeV and a distance of closest approach (DOCA) between the scalars and each dimuon pair forming a vertex to be < 1 mm. It is found that $> 99\,\%$ of the background events (mainly random track combinations) are compatible with vertices originating inside the VELO. Only $< 1\,\%$ of the background processes have

at least one dimuon candidate decaying downstream of the VELO. Thus, if the background processes inside the VELO can be controlled, the ones outside the VELO can be suppressed even better.

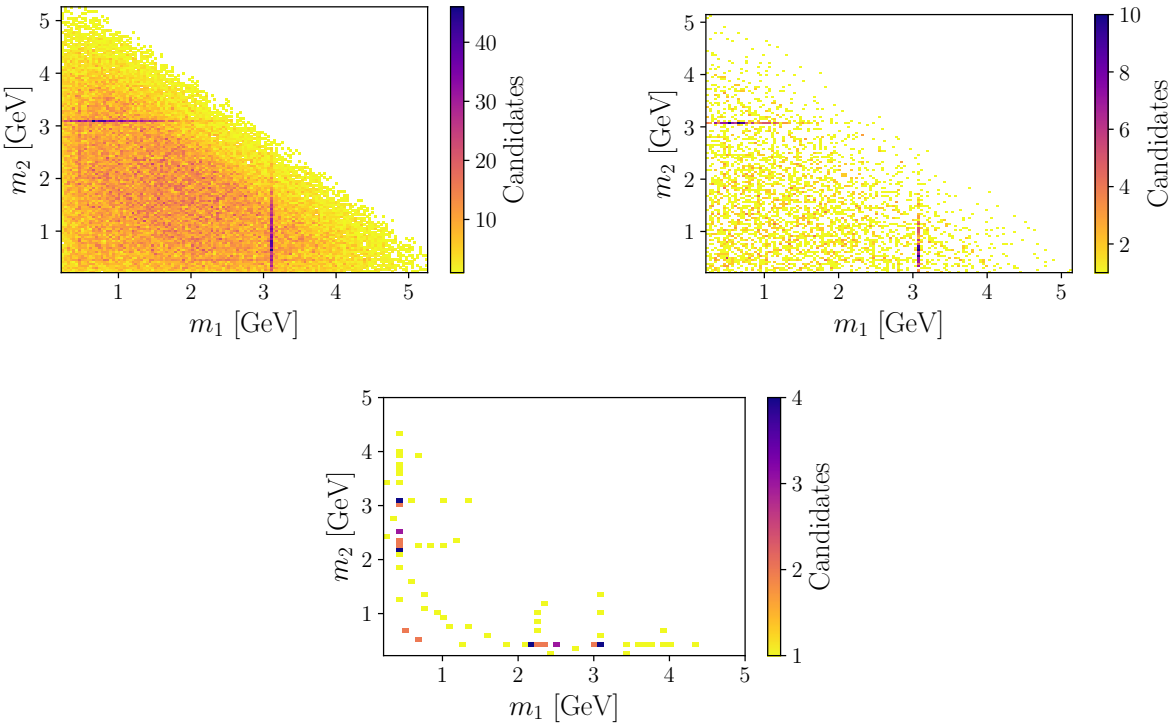


Figure 4.7: Dimuon mass distributions in simulated $pp \to b\bar{b}\mathrm{X}$ events reconstructed as $B_s^0 \to a_1 a_2 \to 2\mu^+ 2\mu^-$. In the left panel, only the requirements discussed in Section 4.1 are applied. In the central panel, strong vertex requirements are applied. In the right panel, it is required instead that one of the dimuon systems has a significant flight distance.

However, there can be particle decays with intermediate dimuon or dipion resonances that might mimic the signal processes. These are dominantly real dimuon resonances like $J/\psi(1S)$, $\Psi(2S)$ and $\phi(1020)$, as well as $K_S^0 \to \pi^+\pi^-$ decays where the pions are misidentified as muons. Although the latter are strongly suppressed by the muon identification requirements, they are so abundant that they can still fake a dimuon signal. The relevant processes can either come directly from a B-meson, such as $B_s^0 \to J/\psi\phi$ and $B_s^0 \to J/\psi K_S^0$, or be randomly combined. Explicit B decays like the above-mentioned have to be vetoed; however, they constitute only a very small fraction of the phase space. For random combinations of the dimuon resonant processes, again making strict vertexing requirements and imposing a significant lifetime for one of the dimuons will allow to successfully erase those backgrounds similarly to backgrounds from random muon combinations, as demonstrated in Figure 4.7. Despite the muon identification requirements, clear contributions from $J/\psi(1S)$ and K_S^0 resonances persist. The former can be removed by requiring a significant distance (in this case 50 mm) between the reconstructed B vertex and one scalar vertex. The latter can be removed, requiring a good vertex between the two scalars and each dimuon candidate, simulated by DOCA <

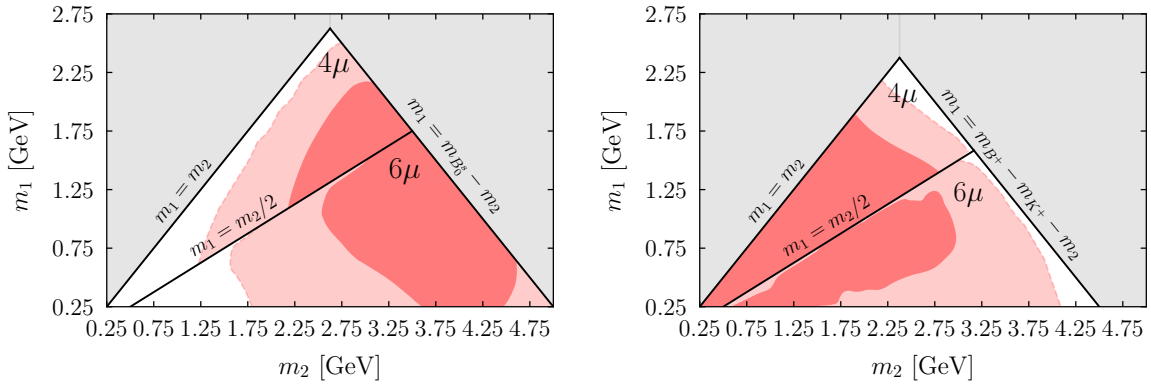


Figure 4.8: Sensitivity projections of LHCb to the hierarchical phase space with the use of Downstream Tracks. Projections for Run3 and Run5 are displayed. The following values are considered: $g_{sb} = 0.01$, $g_{12} = 1.5$, $m_V = 3$ TeV and $t_{a_1} = 100$ ps.

0.1 mm. This is effective, since the K_S^0 particles do not tend to be produced in the same vertex.

Additional backgrounds might come from $J/\psi \to 2\mu^+2\mu^-$ decays [259], which can be vetoed efficiently for the search for the low-lifetime configurations and will be negligible as soon as a significant lifetime for at least one of the dimuon candidates is required.

The exclusive study of the six muon final states will not suffer from the previous limitations, allowing for the avoidance of any veto, as no SM process can be misidentified as the signal with rates close to the reachable sensitivities (e.g. decays like $B_s^0 \to J/\psi\phi\phi$ have branching fractions of the order of 10^{-13} [260]).

Finally, important backgrounds mimicking long-lived signals can come from charged-particle interactions with the detector material. No attempt is made to simulate these backgrounds. However, the detector geometry is well known and data-driven tools [261] have been developed to efficiently suppress material interaction processes for data already collected with the LHCb detector, which will be transferable to future detector modifications.

CODEX-b is considered a background-free experiment, as discussed in Section 7. This results in the fact that any dimuon vertex registered in the CODEX-b volume can be considered as signal.

Altogether, these arguments show that a search with negligible background can be performed, validating the use of Equation 4.2.

4.3.1 Model Interpretation

In Figure 4.8, the reach for the proposed analysis to the hierarchical light sector, comprising both the short- and long-lived singlets, is represented in the (m_1, m_2) plane. The lightest scalar lifetime is fixed to $\tau_1 = 100$ ps in this example. As can be seen, the central area of the phase space could be tested in either of the two channels, B_s^0 or B^+, for multiple muons. On the other hand, these have a complementary role in probing

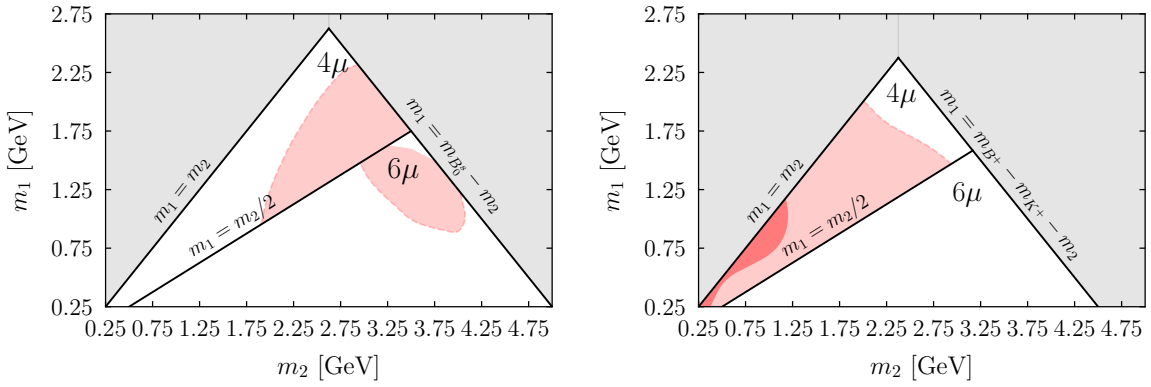


Figure 4.9: Sensitivity projections of LHCb to the hierarchical phase space with the use of Downstream Tracks. Projections for Run3 and Run5 are displayed. The following values are considered: $g_{sb} = 0.01$, $g_{12} = 1.5$, $m_V = 3$ TeV and $t_{a_1} = 100$ ps.

the borders of the phase space. Due to the higher production rate of B^+ mesons, the analysis applied to the channel $B^+ \to K^+ 3\mu^+ 3\mu^-$ could lead to the strongest limits, being able to probe the parameter space where $m_1 \sim m_2$ that is left unconstrained by the two-body decay of the B. Along m_2, the efficiencies are essentially constant, allowing to understand straightforwardly the behaviour along the horizontal lines of the plots. Since $\Gamma(B_s^0 \to a_1 a_2)$ grows with the scalar masses (Equation 1.32), the potential exclusion region is found for large m_2. On the other hand, the three-body decay $B^+ \to K^+ a_1 a_2$ is kinematically suppressed for large $m_{1,2}$, which explains the opposite behaviour of the panels in Figure 4.8.

The constraints in Figure 4.8 were obtained assuming the reconstruction of downstream tracks. Had long tracks been used instead for the assumed lifetime of a_1, limits at Run 5 in the kinematic region $m_2 > 2m_1$ would be comparable to the Run 3 exclusion area in the left panel. Moreover, the corresponding region in the right panel would remain completely unproven. This clearly shows the benefit of introducing new trigger strategies with alternative tracking approaches for probing the non-minimal scalar sectors.

For even larger scalar lifetimes, analyses making use of T-Tracks could lead to the strongest limits on the model parameter space, as represented in Figure 4.9. Assuming the same model parameters as in that figure, a downstream track-based analysis would be insensitive to the entire kinematic region where $m_2 > 2m_1$.

Another remark must be made regarding the potential solution to the $(g-2)_\mu$ anomaly in this setup. The parameter space compatible with such a solution was probed in a recent analysis by LHCb focused on final states with four prompt muons, assuming only one scalar of 1 GeV as intermediate state. However, if a light a_2 explains this anomaly while decaying mostly into a long-lived scalar, such parameter space could only be probed at future LHC Runs using the reconstruction of tracks only in subsystems of the LHCb detector.

USC UNIVERSIDADE DE SANTIAGO

Next, the constraints on the heavy resonance mediating the B decays into the light

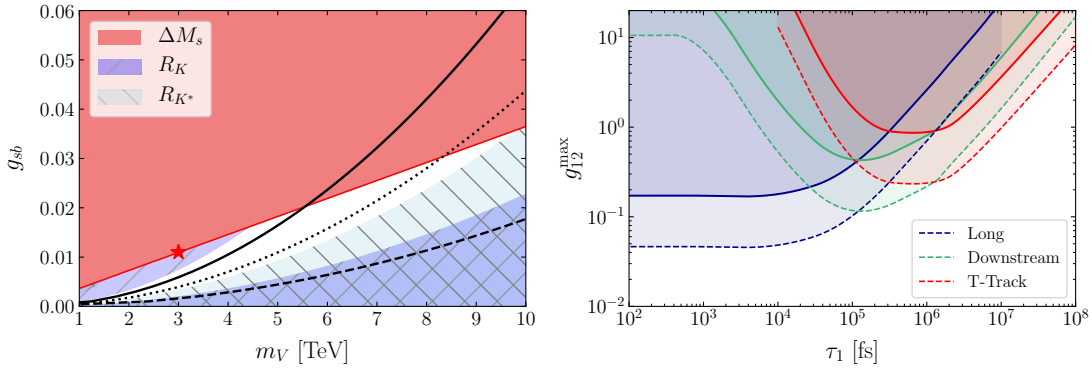


Figure 4.10: (Left) The minimum vector-quark coupling that could be tested with the search proposed in this work in the channel $B^+ \to K^+ 3\mu^+ 3\mu^-$. The light masses, couplings and lifetimes are assumed to be $(m_1, m_2) = (1.0, 2.5)$ GeV, $g_{12} = 1.5$ and $\tau_1 = 1$ ns. The solid, dotted and dashed lines show, respectively, the projected limits after Run 3, Run 4 and Run 5 of the LHCb experiment. (Right) The minimum vector-scalar coupling that could be tested with the same analysis, as a function of the lightest scalar lifetime. The same notation and benchmark masses as in the left panel are considered, as well as the mass and vector coupling marked with a star therein.

scalars are discussed, assuming the presence of flavour violation in the quark sector. Strong bounds from meson mixing constrain the plane (m_V, g_{sb}), which are represented (in red) in the left panel of Figure 4.10. Such an exclusion region was found using the recent weighted averages reported in Ref. [262] for the SM prediction and the 2σ limits on ΔM_s presented in Ref. [263]. Superimposed (in blue) are the 2σ regions where a V explanation to the $R_{K^{(*)}}$ anomalies could have been ruled out. The tree-level contribution of V to these observables was computed with EOS [264] and the updated results from LHCb [265, 266] were considered to constrain this contribution.

By performing the analysis proposed in this work, a significant region of the phase space where a combined solution to the neutral anomalies is possible could be tested already at Run 4, even if the vector decays mostly into the hidden long-lived sector. In turn, at Run 5, also the V explanation to R_K alone could be entirely probed. (Such a conclusion would hold if the four-muon search is applied to the $B_s \to a_1 a_2$ channel, although the limits are typically weaker by a factor of $\sim 3-4$ due to the lower hadronization fraction of the B_s^0 mesons.)

Assuming the maximum allowed g_{sb} coupling for a TeV vector resonance, constraints can be instead applied on its coupling to the light pNGBs, as shown in the right panel of Figure 4.10. Such coupling is a smoking gun feature of the composite scenario, being predicted to be $g_{12} \sim g_* \sim \mathcal{O}(1)$. Furthermore, the latter can be entirely determined from the CCWZ prescription [111] and is independent of the explicit breaking details of the model. It is evident that for lifetimes of the lightest scalar $\tau_1 \gtrsim 1$ ns, the composite nature cannot be probed at LHCb by searching only for long tracks. This conclusion is, in good approximation, independent of the benchmark masses. Codex-b could provide additional sensitivity to the composite coupling for $\tau_1 > 100$ ns; however, for the chosen

benchmark masses in Figure 4.10, only $g_{12} \gtrsim \mathcal{O}(10)$ could be reached.

Other experiments could, in principle, compete with LHCb in the signatures being discussed. A particularly relevant example concerns the future sensitivity projections for Belle II, which could compete in the $B^+ \to K^+ a_1 a_2$ due to its low backgrounds and improved sensitivity in displaced reconstruction with an inclusive approach [267]. Nevertheless, this search will be limited by the smaller amount of data that Belle II will acquire with respect to the Run 5 of LHCb. Important constraints may also come from the study of long-lived dimuon resonances with a dedicated dimuon trigger in the CMS experiment [268]. That analysis achieved an exclusion down to $\mathcal{B}\left(B_s^0 \to a_1 a_2\right) \sim 10^{-7}$ covering lifetimes up to 10^4 ps. The existing prospects for LHCb would surpass these quotes by several orders of magnitude until that point, losing the game from 10^4 ps onwards.

USC
UNIVERSIDADE DE SANTIAGO DE COMPOSTELA

5

Multimuon Searches at LHCb

The analysis of the experimental data according to the model 1.3.1 is performed by using the LHCb Run 2 dataset, comprising 5.6 fb^{-1} of pp collision data[1]. Limits will be placed on their BFs or, in the event of a discovery, they will be measured. The analysis is developed within a team of experts in very rare decays and LLP signatures. Specifically, the contribution of this thesis is directed towards the simulation, selection (including stripping, offline, and MVA), background analysis, fit model, systematics (background generation and parametrization model), and the final results, including bump hunting, exclusion limit calculation, and sensitivity extrapolation in the decay-time of the Long-Lived scalar.

5.1 Analysis strategy

This analysis aims to search for the following very rare decays proceeding via scalar intermediate resonances:

- $B_s^0 \to a_1 a_2 \to 2\mu^+ 2\mu^- \quad (B_s^0 \to 4\mu)$
- $B^+ \to K^+ a_1 a_2 \to K^+ 2\mu^+ 2\mu^- \quad (B^+ \to 4\mu K^+)$
- $B_s^0 \to a_1(a_2 \to a_1 a_1) \to 3\mu^+ 3\mu^- \quad (B_s^0 \to 6\mu)$
- $B^+ \to K^+ a_1(a_2 \to a_1 a_1) \to K^+ 3\mu^+ 3\mu^- \quad (B^+ \to 6\mu K^+)$

where the case of both prompt and long-lived intermediate scalars is considered. The analysis is restricted to Run 2 as the relevant stripping lines have not been run over the Run 1 sample. Limits will be placed on their Branching Ratio or, in the event of a discovery, measured.

[1] The analysis is restricted to Run 2 as the relevant stripping lines have not been included for Run 1.

In order to reduce systematic effects, the branching fraction (BF) measurement is determined relative to the decay $B_s^0 \to J/\psi(\mu^+\mu^-)\phi(\mu^+\mu^-)$, which is itself a rare decay with a BF of $(1.741 \pm 0.156) \cdot 10^{-8}$ [46], according to Equation 4.2.

Guided by the phenomenological analysis 4.1, different reconstruction techniques are introduced through dedicated stripping lines:

- **Prompt**: The intermediate scalars have a negligible lifetime compared to the decay time resolution and are indistinguishable from the situation where the final muons arise directly from the B vertex ($B \to N\mu$). These 'prompt' samples are polluted by quarkonia resonances such as ϕ, J/ψ and $\psi(2S)$.
- **Long-lived**: The intermediate scalars live long enough to produce decay vertices displaced from the B decay vertex. Since quarkonia resonances decay promptly, these samples are less polluted by these backgrounds. In this thesis, these samples are often referred to as **displaced LL** and **displaced LLL** for the 4μ and 6μ modes, respectively (L = long track).
- **Downstream**: Similar to the long-lived case, but where one or more of the intermediate scalars decay downstream of the VELO, leading to a reduced reconstruction efficiency. As there was no dedicated trigger for downstream muons in Run 2, at least one of the other dimuon candidates in a decay must be formed from long tracks. These samples can be subdivided by the number of downstream dimuon candidates (D = downstream track):
  - **Displaced LD**: 4μ modes where one dimuon forms a long track and the other from a downstream track.
  - **Displaced LLD**: 6μ modes with two dimuons from long tracks, with the third from a downstream track.
  - **Displaced LDD**: 6μ modes where one dimuon is forms a long track and the other two form downstream tracks.

The selection procedure for the signal decay modes follows a similar pattern, with more specific requirements depending on the mode and reconstruction category. A loose preselection, which removes unphysical candidates and cloned dimuon pairs, and the trigger selection shown in Section 3.4.1 is used for all modes. Decay modes with prompt and long-lived intermediate scalars are separated with a selection on the intermediate decay time. Intermediate resonance selections are applied to select both the signal and normalisation modes. For the prompt signal modes, the opposite-sign dimuon invariant masses are used to veto decays proceeding via intermediate quarkonia resonances, whereas for $B_s^0 \to J/\psi(\mu^+\mu^-)\phi(\mu^+\mu^-)$ and $B_s^0 \to J/\psi(\mu^+\mu^-)\phi(K^+K^-)$, the invariant mass of one of the dimuon pairs must fall within the J/ψ region whilst the other is in the ϕ region. For the 6μ modes, it is required that the lighter (a_1) intermediate scalars have the same mass within a certain mass resolution. Loose PID requirements are imposed on all muons to suppress the presence of misidentified physical

USC DE SANTIAGO

backgrounds, particularly hadron-muon misID. Following the aforementioned selection, minimal background contributions remain. Potential exclusive background decays are studied with dedicated simulation.

Simulated Monte Carlo (MC) samples (Table 5.3 are used to calculate efficiencies, train MVA classifiers and ascertain invariant mass shapes. The relatively high-yield $B_s^0 \to J/\psi(\mu^+\mu^-)\phi(K^+K^-)$ mode is used to determine a series of weights, which comprise generator, trigger and reconstruction level weights, to correct discrepancies between data and simulation.

Due to the high muon multiplicity of the final states, these channels suffer from relatively few physical peaking backgrounds, leaving combinatorial background as the largest source of background. In 4μ channels, multivariate (MVA) classifiers are used to suppress combinatorial background, and they aare optimized using a Punzi figure of merit (FoM) [269]. For 6μ final states, combinatorial background is low and requirements on the masses of the intermediate scalars are deemed sufficient to isolate the signal.

The analysis is developed with the signal B mass regions blinded. In the event of a significant signal observation, the decay BF will be measured with a maximum likelihood fit to the B invariant mass distribution. However, if no significant signal is observed, limits will also be set on the decay BF using the CL_s method [270]. The searches are performed with simultaneous fits between reconstruction categories, sharing the same physical BFs.

5.2 Data and MC samples

In this section, a description of the data and the MC that is used is provided. Due to the inevitable use of specific jargon, the reader is suggested to visit Section 3.4.3 and 3.4.1 for more information.

As said, this analysis makes use of LHCb Run 2 data. Table 5.1 lists the integrated luminosities collected each year and the versions of the reconstruction software and the stripping used.

Year	$\sqrt{s}$ [TeV]	Reco	Stripping [Signal/Control]	$\mathcal{L}_{\text{int}}$ [fb^{-1}]
2016	13	16	28r2p1/28r1	1.67
2017	13	17	29r2p3/29r2	1.71
2018	13	18	34r0p3/34	2.19

Table 5.1: Integrated luminosities of the data samples used in this analysis. The values are taken from the LHCb Operations Plots [271].

USC UNIVERSIDADE DE SANTIAGO DE COMPOSTELA

Dedicated signal MC samples are produced to effectively cover the regions of interest

in the parameter space. Two mass points are chosen from the mass distributions from Figure 4.3, ensuring the analysis focuses on the most representative points. The full simulation set comprises MC productions for each decay and regime:

- For Prompt samples, both full phase space (PHSP) $B \to N\mu$ and hierarchical model (Hier) $B \to aa(a)$ with $t_a = 0$ ps are produced. The first ones will be used throughout all the analysis, whereas the second ones will allow for cross-checking between models.
- For Displaced scenarios, the hierarchical structure is produced with a set of lifetimes (namely, 1, 10, 100 and 1000 ps) by requiring that the scalars are produced within the LHCb acceptance.

These samples are summarised in Table 5.3, where information about the Generation approach, the statistics per year and the generation efficiencies is included.

Decay	SimType	Gen. Events
$B_s^0 \to J/\psi(\mu^+\mu^-)K^+K^-$	Sim09k	1214942
$B_s^0 \to J/\psi(\mu^+\mu^-)\pi^+\pi^-$	Sim09h	9973072
$B^0 \to J/\psi(\mu^+\mu^-)\pi^+\pi^-$	Sim09h	12000000
$B^0 \to J/\psi(\mu^+\mu^-)K^{0*}(K^+\pi^-)$	Sim09f	8000000
$\Lambda_b \to \Lambda(p\pi^-)\mu^+\mu^-$	Sim09h	20250000
$B^+ \to J/\psi(\mu^-\mu^-)\mu^+\mu^-K^+$	Sim09m	3000000
$B^+ \to J/\psi(\mu^+\mu^-)\pi^+\pi^-K^+$	Sim09h	2000000
$B^+ \to \mu^+\mu^-\pi^+\pi^-K^+$	Sim09m	3000000
$B^+ \to J/\psi(\mu^+\mu^-)\eta(\mu^+\mu^-\gamma)K^+$	Sim09m	3000000

Table 5.2: Summary of background simulation samples used in the analysis.

Studies of the most relevant backgrounds are carried out with dedicated simulation samples, summarized in Table 5.2. It includes information about the decay, simulation type and number of generated events. All of them correspond to the 2018 simulated data.

USC UNIVERSIDADE DE SANTIAGO DE COMPOSTELA

Decay	SimType	Mode	$m(a_1)$, $m(a_2)$ [GeV]	τ_{a_1} [ps]	Year 2016/2018	ε_{Gen}
$B_s^0 \to 2\mu^+2\mu^-$	Sim09i	PHSP		0	503071 / 508599	0.15866 ± 0.00053
	Sim09m	Hier	0.25, 0.40	0	947112 / 918541	0.18692 ± 0.00043
				1	857105 / 1007941	0.18321 ± 0.00033
				10	1029349 / 1078683	0.18321 ± 0.00033
				100	1079988 / 1050852	0.18323 ± 0.00033
				1000	718623 / 777102	0.18328 ± 0.00033
	Sim09m	Hier	2.00, 2.75	0	508761 / 509950	0.15620 ± 0.00036
				1	515425 / 499471	0.13489 ± 0.00026
				10	520036 / 512603	0.13489 ± 0.00026
				100	508826 / 482990	0.13478 ± 0.00025
				1000	512284 / 507372	0.13514 ± 0.00025
$B^+ \to 2\mu^+2\mu^-K^+$	Sim09m	PHSP		0	644069 / 646504	0.15456 ± 0.00042
	Sim09m	Hier	0.25, 0.40	0	898466 / 896811	0.17148 ± 0.00047
				1	1064130 / 1126119	0.16336 ± 0.00030
				10	1038030 / 1004961	0.16351 ± 0.00029
				100	1119980 / 1144466	0.16343 ± 0.00029
				1000	748809 / 817560	0.16335 ± 0.00030
	Sim09m	Hier	2.00, 2.75	0	527708 / 509708	0.15380 ± 0.00043
				1	1015302 / 1046284	0.14317 ± 0.00027
				10	1141012 / 1031421	0.14593 ± 0.00027
				100	1035555 / 1103612	0.14558 ± 0.00027
				1000	1058738 / 994160	0.14590 ± 0.00027
$B_s^0 \to 3\mu^+3\mu^-$	Sim09m	PHSP		0	727288 / 576504	0.14149 ± 0.00034
	Sim09l	Hier	0.50, 1.50	0	660963 / 670898	0.15737 ± 0.00036
				1	1247624 / 1084988	0.16946 ± 0.00031
				10	1063856/ 1078513	0.13715 ± 0.00026
				100	1040952 / 1007816	0.13682 ± 0.00026
	Sim09m	Hier	1.25, 3.50	0	463378 / 453326	0.13797 ± 0.00033
				1	1173551 / 1016353	0.10771 ± 0.00021
				10	1027998 / 1102992	0.10785 ± 0.00021
				100	1107452 / 1092501	0.10763 ± 0.00021
$B^+ \to 3\mu^+3\mu^-K^+$	Sim09l	PHSP		0	693145 / 697255	0.14220 ± 0.00034
	Sim09l	Hier	0.50, 1.50	0	624074 / 624761	0.14718 ± 0.00035
				1	1087026/ 1161916	0.12716 ± 0.00024
				10	1053063 / 1067415	0.12735 ± 0.00024
				100	1041162 / 1074934	0.12703 ± 0.00024
	Sim09m	Hier	1.25, 3.50	0	485485 / 483742	0.13625 ± 0.00034
				1	1044308 / 1104794	0.11017 ± 0.00021
				10	1004462/ 1124554	0.11034 ± 0.00021
				100	1066506 / 1151012	0.11007 ± 0.00021
$B_s^0 \to J/\psi(\mu^+\mu^-)\phi(\mu^+\mu^-)$	Sim09i	PHSP			1019402 / 1106568	0.15714 ± 0.00052
$B_s^0 \to J/\psi(\mu^+\mu^-)\phi(K^+K^-)$	Sim09i	PHSP			2009714 / 4014714	0.17757 ± 0.00060

Table 5.3: Summary of the signal and control simulation samples used in the analysis. In order, it is specified: the decay chain, simulation type, decay model, lifetime, total statistics per year and the corresponding generator efficiency. All simulation samples are run with the associated stripping in the corresponding data. Note that, as only simulated data from two years are needed, and since data-taking conditions are similar for 2016 and 2017, only 2016 and 2018 are analysed.

USC UNIVERSIDADE DE SANTIAGO DE COMPOSTELA

5.3 Signal Selection

5.3.1 Stripping Selection

The data used in this analysis is selected using Stripping 28r2p2, Stripping 29r2p3 and Stripping 34r0p3, in 2016, 2017 and 2018, respectively. Dedicated stripping lines have been used for each signal decay mode, including lines for each of the different reconstruction categories. A summary of the stripping lines used can be found in Table 3.3. In addition, $B_s^0 \to J/\psi(\mu^+\mu^-)\phi(\mu^+\mu^-)$ and $B_s^0 \to J/\psi(\mu^+\mu^-)\phi(K^+K^-)$ modes are selected using the `B2MuMuMuMuB24MuLine` and `Bs2MuMuLinesBs2JPsiPhiLine` stripping lines, respectively. In the last case, a breakdown of the Stripping selection for control modes can be found in Table 5.4.

Variable	Applied to	$B_s^0 \to J/\psi(\mu^+\mu^-)\phi(\mu^+\mu^-)$	$B_s^0 \to J/\psi(\mu^+\mu^-)\phi(K^+K^-)$
track χ^2/ndf	μ	< 2.5	< 4
DOCA		< 0.3 mm	< 0.3 mm
χ^2_{IP}		> 9	> 25
p_T		> 250 MeV/c	> 250 MeV/c
isMuon		true	true
ghost probability			< 0.4
VDS	4μ,$\mu\mu$	> 10	> 15
m		$4000 < m(4\mu) < 6366.3$ MeV	$3087 < m(\mu\mu) < 3197$ MeV
$\chi^2_{\text{PV dist}}$	B	< 25	< 25
vertex χ^2/ndf		< 9	< 75
cos(DIRA)		> 0	
vertex χ^2/ndf	J/ψ		< 9
cos(DIRA)			> 0
χ^2_{IP}	ϕ		< 25
m	$J/\psi\phi$		$4867 < m(J/\psi\phi) < 5867$ MeV
track χ^2/ndf	K		< 4
χ^2_{IP}			< 4
p_T			> 250 MeV/c
isLong			true
ghost probability			< 0.4
m	KK		$999 < m(KK) < 1039$ MeV

Table 5.4: Stripping selection for $B_s^0 \to J/\psi(\mu^+\mu^-)\phi(\mu^+\mu^-)$ and $B_s^0 \to J/\psi(\mu^+\mu^-)\phi(K^+K^-)$.

In the stripping stage, reconstructed final-state particles that satisfy specific criteria are sequentially combined to form "mother candidates", such that the full decay chain is built. Examples of the variables commonly used in the stripping selections are the following:

- **DOCA:** Distance of closest approach between two tracks.
- **DIRA:** Cosine of the angle between the reconstructed momentum vector of a candidate and the line connecting the associated PV to its decay vertex.

USC UNIVERSIDADE DE SANTIAGO DE COMPOSTELA

- **Vertex χ^2:** Quality of the vertex fit when combining several tracks into a candidate.
- **Track χ^2:** Quality of the individual track fit.
- **IPχ^2:** Measure of the inconsistency of a particle with originating from a given vertex, defined as the increase in the vertex-fit χ^2 when including the particle.

These variables can be found at every stage of the stripping algorithm. Some representatives are:

- **BPVIPχ^2:** Impact parameter χ^2 of a reconstructed candidate with respect to the associated PV.
- **BPVVDχ^2:** Flight-distance significance between the associated PV and the decay vertex of the candidate.
- **Min IPχ^2DV:** Minimum impact parameter χ^2 of the final-state particles with respect to the PV, ensuring that all daughters are significantly displaced.

As discussed in Section 5.1, the differentiation between Prompt and Displaced regimes is introduced with the different stripping selections. This is primarily achieved through cuts in the fit quality, holding steady in the Prompt case and easing off in the Displaced case. In terms of PID, the Displaced case opts to tighten this criterion to maintain a manageable bandwidth. Below, both cases are discussed in detail.

Prompt Stripping Lines

In the **Prompt** regime, reconstructed final state muons are combined directly to form a B vertex using an n-body combiner. Loose cuts are applied over successive muon combinations to reduce the combinatorics before the B candidate fit is performed. All requirements are shown in Table 5.5. These stripping lines also select decays involving promptly-decaying resonances such as ϕ, J/ψ and $\psi(2S)$ mesons since, due to their prompt nature, they are technically indistinguishable from the B vertex. These modes, with which $B_s^0 \to J/\psi(\mu^+\mu^-)\phi(\mu^+\mu^-)$ can be constructed, are removed using vetoes on the dimuon masses, as it is reviewed in Section 5.3.6.

Displaced Dimuon Lines

Dedicated stripping lines are used to select B decays via long-lived dimuon states, with different lines depending on how many dimuon pairs are formed from long tracks and downstream tracks, as shown in Table 5.6. In the stripping lines, J/ψ, K_S^0, and Λ^0 are just labels for short-lived (J/ψ), long-lived (K_S^0) and long-lived downstream (Λ^0) dimuon candidates. As illustrated in the table, requirements imposed on muons and

Applied to	**Variable**	$B^+ \to 4\mu K^+$	$B_s^0 \to 4\mu$	$B^+ \to 6\mu K^+$	$B_s^0 \to 6\mu$
μ	Track χ^2/DOF	< 3	< 3	< 3	< 3
	Track $\text{Prob}_{\text{Ghost}}$	< 0.3	< 0.3	< 0.3	< 0.3
2μ	DOCA χ^2	< 9		< 9	
	m	< 6700 MeV	< 7700 MeV	< 6700 MeV	
	N isMuon	2	2	1	> 2
	DOCA				< 0.7 mm
	P_T				> 500 MeV
	N ProbNNmu > 0.1	2	2		
3μ	DOCA χ^2	< 9		< 9	
	P_T	> 500 MeV		> 500 MeV	
	m	< 6800 MeV		< 6800 MeV	
4μ	DOCAχ^2	< 10		< 10	
	m	< 6900 MeV		< 6900 MeV	
	N isMuon	4		2	
	Min IPχ^2DV	$> 2, < 6$		$> 2, < 6$	
5μ	DOCAχ^2			< 11	
	m			< 7000 MeV	
	N isMuon			3	
	Min IPχ^2DV			$> 3, < 6$	
6μ	DOCAχ^2			< 12	< 16
	m			< 7100 MeV	
	N isMuon			4	> 5
	Min IPχ^2DV			$> 4, < 6$	
B^+/B_s^0	Vχ^2/VDOF	< 16	< 12	< 16	< 16
	BPVIPCHI2	< 25	> 9	< 25	> 9
	BPVDIRA	> 0.999		> 0.999	> 0.995
	BPVVDχ^2	< 36		< 36	
	m	< 6100 MeV		< 7500 MeV	
	N isLong	> 3		> 4	
	N ProbNNmu > 0.1	> 3	> 3		> 4
	N ProbNNmu > 0.0			> 4	
	$P_T > 300$ MeV		> 3		
	N $P_T > 400$ MeV		> 1		> 1
	N isMuon				> 1
K^+	P_T MeV	> 250		> 250	
	Min IPχ^2DV	> 4		> 4	

Table 5.5: Stripping selection for prompt reconstruction.

dimuon pairs are relaxed for downstream candidates, although PID requirements are strengthened to maintain reasonable rates. The requirements for the rest of the decay chain, whether for 'Long-Lived' or 'Downstream' candidates, remain largely the same, as no significant impact on bandwidth or data quality has been observed. Full details of the requirements can be found in Tables 5.7 and 5.8.

Contrary to the other cases in which the fit to the B vertex is performed by combining three or four objects (dimuon intermediates and kaon track candidates), the $B_s^0 \to 4\mu$ mode cannot be reconstructed in this way since a precise decay vertex cannot be obtained by combining two long-lived intermediates. This affects the precision of the B vertex location and consequently the lifetime of the scalars, deteriorating further with longer scalar lifetimes. A solution to this problem is to require one intermediate scalar to decay promptly, and that the second scalar point back to this decay vertex.

Variable	$2\mu_{\text{Long}}$	$2\mu_{\text{Downstream}}$
Track χ^2/DOF	< 3	< 15
Track $\text{Prob}_{\text{Ghost}}$	< 0.3	< 0.35
Proxy	$K^0_S \to \mu^+\mu^-$	$\Lambda^0 \to \mu^+\mu^-$
m	> 0 MeV	> 0 MeV
DOCA	< 0.75 mm	< 6 mm
V χ^2/PDOF	< 9	< 9
MIPχ^2DV	> 0	> 0
BPVVDχ^2	> 10	> 10

Table 5.6: Dimuon builder requirements for displaced dimuon lines.

Applied to	**Variable**	$B^+ \to 4\mu K^+$	$B^+ \to 6\mu K^+$	$B^0_s \to 6\mu$
K^+	P_T	> 250 MeV	> 250 MeV	
	Min IPχ^2DV	> 4	> 4	
B^+/B^0_s	Vχ^2/VDOF	< 16	< 16	< 16
	BPVIPχ^2	< 25	< 25	< 25
	BPVDIRA	> 0.999	> 0.999	
	BPVVDχ^2	> 36	> 36	
	m	< 6100 MeV	< 6100 MeV	
	N isLong	> 3		> 5
	N isMuon	> 3		> 1
	N ProbNNmu > 0.2	> 3		
	N ProbNNmu > 0.1		> 5	
	NP_{T} > 400MeV			> 4

Table 5.7: Summary of stripping selection for $B^+ \to 4\mu K^+$, $B^+ \to 6\mu K^+$ and $B^0_s \to 6\mu$ displaced stripping lines with long tracks only.

Applied to	**Variable**	$B^+ \to 4\mu K^+$ LD	$B^+ \to 6\mu K^+$ LLD|LDD	$B^0_s \to 6\mu$ LLD|LDD
K^+	P_T	> 250 MeV	> 250 MeV	
	Min IPχ^2DV	> 4	> 4	
$K^0_S \to \mu^+\mu^-$	N isLong	> 1	2|1	2|2
	N isMuon	> 1		
$\Lambda^0 \to \mu^+\mu^-$	N isMuon	2	$2\| > 1$	$2\| > 1$
B^+/B^0_s	Vχ^2/VDOF	< 16	< 16	< 16
	BPVIPχ^2	< 25	< 25	< 25
	BPVDIRA	> 0.999	> 0.999	
	BPVVDχ^2	> 36	> 36	
	m	< 6100 MeV	< 6100 MeV	
	N isMuon	> 3		> 1
	NProbNNmu > 0.1	> 3	$> 4\| > 4$	$> 5\| > 3$

Table 5.8: Summary of stripping selection for long-lived lines composed of both long tracks and downstream tracks for $B^+4\mu \to K^+$, $B^+ \to 6\mu K^+$ and $B^0_s \to 6\mu$. In $B^+ \to 6\mu K^+$ and $B^0_s \to 6\mu$ channels, the displaced-LLD and displaced-LDD are differentiated.

A breakdown of the stripping requirements for the $B_s^0 \to 4\mu$ displaced stripping lines can be found in Table 5.9.

Applied to	**Variable**	$B_s^0 4\mu$ Long	$B_s^0 4\mu$ Down
$J/\psi(\mu^+\mu^-)$	DOCA	< 0.3 mm	< 0.3 mm
	BPDIRA	> 0	> 0
$K_S^0(\mu^+\mu^-)$	$\sum_\mu P_T$ MeV	> 1000 MeV	
	DOCA	0.5 mm	
	V χ^2/DOF	< 16	
	BPVVD χ^2	> 16	
$\Lambda^0(\mu^+\mu^-)$	$V\chi^2/DOF$		< 9
	Min IPχ2 PV		> 0
	BPVVD χ^2		> 10
$J/\psi K_S^0$	$\sum_\mu P_T$	> 1000 MeV	
	m	> 4600 MeV, < 6000 MeV	
$J/\psi\Lambda^0$	$\sum_\mu P_T$	> 1000 MeV	
	m		< 6100 MeV
B_s^0	Vχ^2/DOF	< 6	< 12
	BPVVDχ^2	> 50	
	BPVIPχ^2	< 16	
	BPVDIRA	> 0	> 0.999
	m		< 7500 MeV
	Max P_T^μ		> 550 MeV
	$NP_T^\mu > 300$ MeV		> 2
	NProbNNmu > 0.1		> 4
	BPVDLS		> 3

Table 5.9: Summary of stripping selection for $B_s^0 \to 4\mu$ long-lived lines composed of both long and downstream tracks.

5.3.2 Trigger requirements

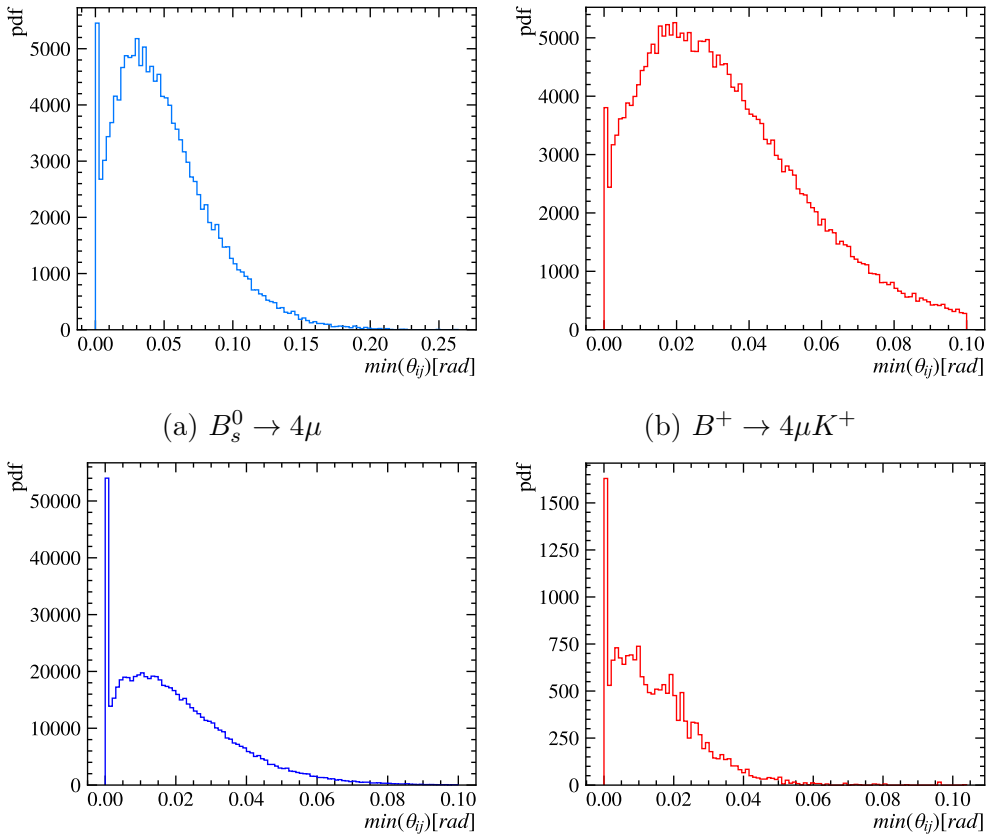
All candidates are subject to the same trigger requirements, which ensure the (partial) cancellation of systematic uncertainties associated with trigger line selections. The full trigger selection is outlined in Table 3.2. To pass the trigger selection, candidates must be identified as TOS by at least one of the trigger lines at each stage.

The L0DiMuon trigger was initially considered. However, due to low statistics, the simulation correction procedure was quite unstable and it was decided to only consider the L0Muon trigger. This is supported by the fact that almost all candidates that passed the L0 trigger requirements were identified with the L0Muon trigger, with only 1-2 % of candidates being selected with just L0DiMuon and not L0Muon.

5.3.3 Clones

The high multiplicity of the signal modes leads to the possible existence of clones after the full reconstruction, i.e. duplicated tracks arising due to overlapping hit patterns in the tracking detectors. This issue is inherited from the fact that the phase space gets restricted as the multiplicity increases, and the finite resolution of the detector

makes it unable to properly identify dimuon pairs with low opening angles. A visual proof can be found in Figure 5.1, comprising the distributions of the minimum angle between muons in different samples.



(a) $B_s^0 \to 4\mu$ (b) $B^+ \to 4\mu K^+$

(c) $B_s^0 \to 6\mu$ (d) $B^+ \to 6\mu K^+$

Figure 5.1: Minimum angle between muons in different data channels. Peaks are observed at $min(\theta_{ij}) = 0$ in each case, and are particularly prominent in the 6μ modes.

In terms of removing those events, a rectangular cut $\min(\theta_{ij}) > 0.1$ mrad has been included, demonstrating in all the cases a signal efficiency greater than 98%. As expected, the mass of rejected events tends to lie close to the kinematic $2m_\mu$ threshold (Figure 5.2), therefore defining the minimal dimuon mass to which this analysis is sensitive.

5.3.4 Prompt and Displaced regimes

A natural differentiation between Prompt and Displaced events relies on the quality of the vertexing during reconstruction, as discussed in Section 5.3.1. Nevertheless, as some Prompt events could even survive the displaced preselection, an additional selection is further needed to properly separate both physical regimes.

For prompt samples, the four- and six-muon track fits are constrained to the B-meson vertex. In the first case, the surviving combinatorials are so prominent that an MVA selection is needed to clean undesired pollution (see Section 5.5). On the second,

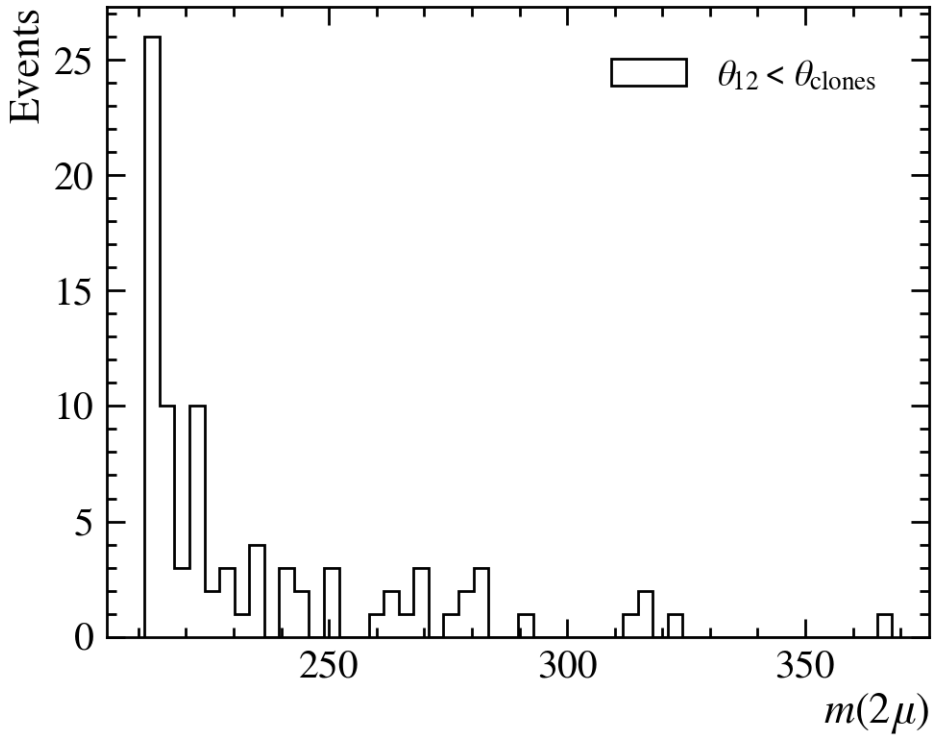


Figure 5.2: Invariant mass of opposite-sign dimuon pairs rejected by $\min(\theta_{ij})$ criterium in $B_s^0 \to 4\mu$ decays.

it is found that loose rectangular cuts are sufficient to achieve a powerful background suppression while keeping a high signal efficiency. In Figure 5.3, a set of variables for $B_s^0 \to 6\mu$ Prompt events are compared between MC and Data. On the B decay vertex, `B_ENDVERTEX_CHI2` < 30 and `B_IPCHI2_OWNPV` < 9 is set, whereas a resolution of `min_PT_mu` < 150 MeV is chosen for the muons. Such an approach keeps a final efficiency of $\sim 5\%$.

For displaced modes, a decay-time cut is investigated for removing prompt dimuon candidates. To determine this cut, the expected Run 2 $B_s^0 \to J/\psi\phi$ yield in the signal region without the ϕ and J/ψ resonance vetoes is estimated. This serves as the most dangerous proxy for prompt modes. The selection of those events is performed by running the $B_s^0 \to 4\mu$ long-lived stripping selection over MC for the control mode. Afterwards, the decay time cut is chosen such that the expected number of $B_s^0 \to J/\psi\phi$ decays in Run 2 is less than 1, concretely:

$$\mathcal{N} = \varepsilon_t \, \sigma \, \mathcal{L} \, \mathcal{B}(B_s^0 \to J\psi\phi) \tag{5.1}$$

where ε_t refers to the efficiency of the decay time cut applied on the J/ψ candidate, $\sigma = 1.44\,\mu$b, $\mathcal{L}$ is the total luminosity in Run 2 and $\mathcal{B}(B_s^0 \to J\psi\phi) = 1.736 \cdot 10^{-8}$ is taken from the PDG [46]. This approach points to a decay time cut of $t_{cut} = 0.2$ ps. This is illustrated in figure 5.4, where the total number of expected events falls to 0.78 with the chosen decay time cut.

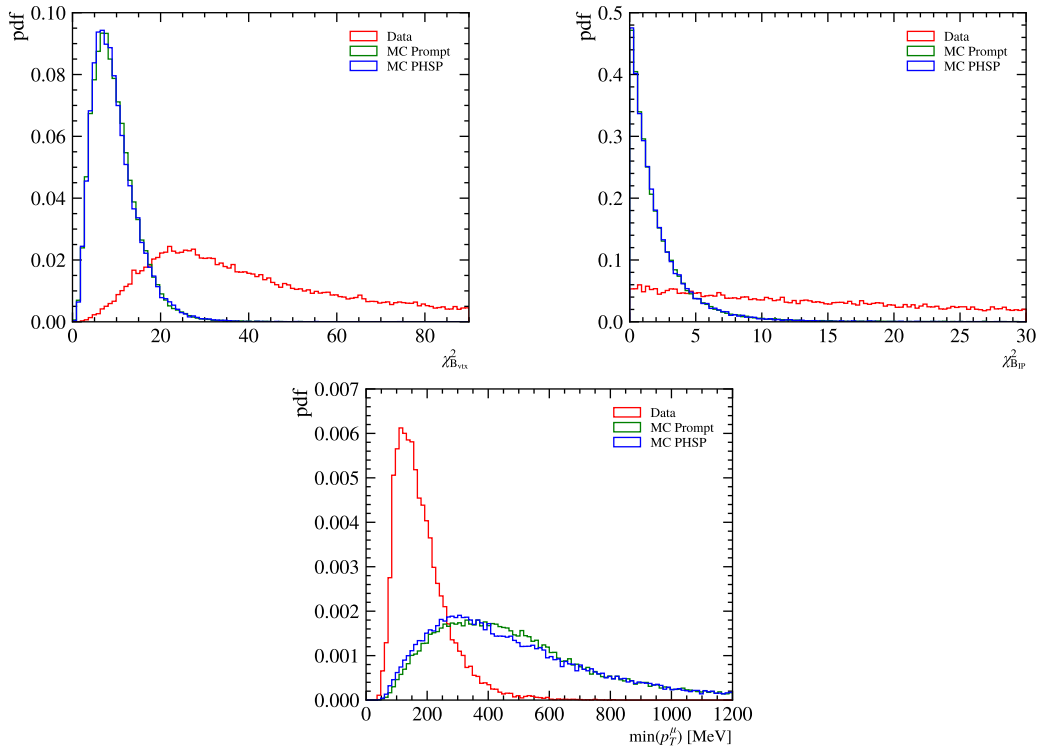


Figure 5.3: Comparison of variables belonging to Prompt $B_s^0 \to 6\mu$ events. For MC, two prospects are investigated: in blue, a pure PHSP decay to N final particles and, in green, a Prompt model-dependent decay with intermediate scalar lifetimes set to 0 ps. In every case, preselection cuts, clones, trigger and prompt resonance selections are applied.

Figure 5.5 shows how effective this selection is for $B^+ \to 4\mu K^+$ (left) and $B_s^0 \to 4\mu$ (right) sideband distributions. In both cases, the rejection factor is greater than 85%, and the presence of prompt charmonium resonances like J/ψ and $\psi(2S)$ is strongly reduced.

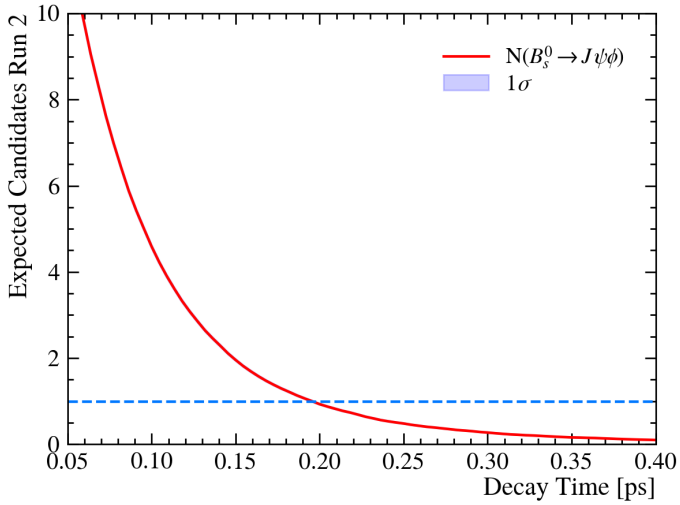


Figure 5.4: Total number of expected $B_s^0 \to J/\psi\phi$ candidates during Run 2 as a function of the cut on the decay time of the intermediate scalars.

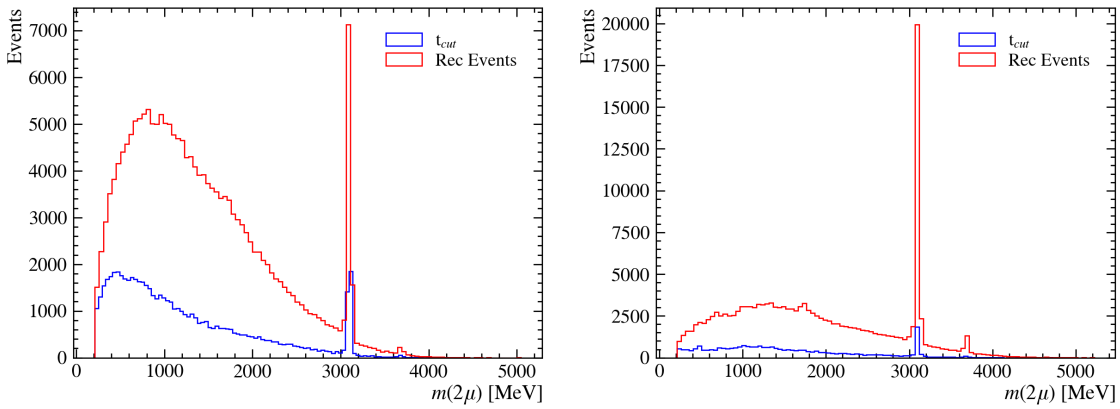


Figure 5.5: Comparison of $B^+ \to 4\mu K^+$ data (left) and $B_s^0 \to 4\mu$ data (right) dimuon mass distributions in the B mass sidebands before and after the cut in the decay time of the intermediate scalars.

5.3.5 Mass ranges

The goal of this analysis is to search for the decay modes with a fit to the B meson invariant mass. To avoid the introduction of biases, a blinded region is defined around the B meson mass, $[m_B - 75\text{ MeV}, m_B + 75\text{ MeV}]$, which corresponds to the region containing up to 95% of the simulated events (see figure 5.6).

- **Signal region**: defined over the nominal mass of the B meson which is the head of the decay chain:
  - B^+: $5195\text{ MeV} \leq m_d \leq 5345\text{ MeV}$
  - B_s^0: $5285\text{ MeV} \leq m_s \leq 5435\text{ MeV}$.

The full range is the region over which the final fit will be performed and contains the sidebands and signal window.

- **Full range**: defined as the mass range $[4850\text{ MeV}, 6000\text{ MeV}]$ selected for fitting the invariant mass.

5.3.6 Intermediate scalar selection

Mass requirements are placed on the intermediate resonances to select signal modes and the normalisation mode. According to the theoretical framework, 4-body decays dominate when $m_2 < 2m_1$ and 6-body decays when $m_2 > 2m_1$.

Prompt resonance vetoes

Specific vetoes are needed in the case in which a_1 or a_2 promptly decay in the mass window of prompt particles such as ϕ and charmonium (J/ψ and $\psi(2S)$). The following regions are taken from the previous $B_{(s)}^0 \to \mu^+\mu^-\mu^+\mu^-$ analysis [117]:

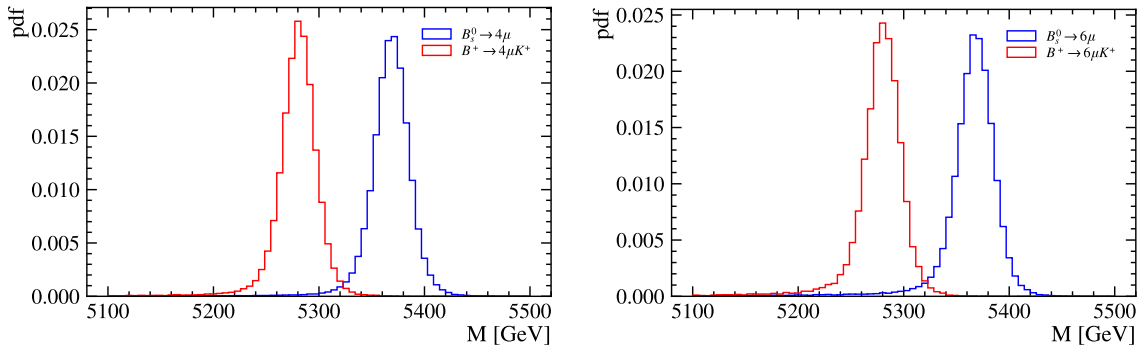


Figure 5.6: Reconstructed mass comparisons for 4μ and 6μ simulation samples.

- J/ψ region: $|m(\mu^+\mu^-) - m(J/\psi)| < 100$ MeV
- $\psi(2S)$ region: $|m(\mu^+\mu^-) - m(\psi(2S))| < 100$ MeV
- ϕ region: 950 MeV $< m(\mu^+\mu^-) <$ 1090 MeV

where $m(\mu^+\mu^-)$ is the intermediate invariant mass, $m(J/\psi) = 3096.900 \pm 0.006$ MeV/c^2, $m(\psi(2S)) = 3686.093 \pm 0.034$ MeV/c^2 and $m(\phi) = 1019.455 \pm 0.020$ MeV/c^2 [46].

All opposite-sign two-muon combinations are required to have masses outside these regions in the prompt selection, effectively vetoing these standard model backgrounds. In the case of 4-muon decays, there are four such mass variables (m_{11}, m_{22}, m_{12} and m_{21} whereas for 6-muon decays, there are nine in total (m_{ij} where $i = 1, 2, 3$ and $j = 1, 2, 3$).

In 4μ samples, it is verified that a considerable presence of those resonances is still present in the trainning stage of the MVA; therefore, it has been decided to apply prompt-resonance vetos even on the long-lived dimuon candidate, resulting in an enhancement of the BDT response. For the 6μ modes, the effect of the intermediate mass criteria (next section) is shown to be sufficient to avoid such an undesirable population.

Intermediate scalar mass requirements

In the case of 6-muon displaced decays, mass requirements are used to suppress combinatorial background by exploiting the fact that all three intermediate scalars (which decay to dimuons) should have similar masses. In those modes, a unique choice of muon pairs is possible, and a resolution cut would lie as:

$$S = \sqrt{(\Delta m_{12})^2 + (\Delta m_{13})^2} < 50 \text{ MeV}/c^2 \tag{5.2}$$

where $\Delta m_{ij} = m_i - m_j$ are the mass differences between pairs of dimuons. A circular cut is chosen by observing dimuon mass resolution in data, as it is the simplest way to reduce background levels while keeping a high signal efficiency. The effect of this requirement on simulation can be seen in Figure 5.7 and 5.8, for $B_s^0 \to 6\mu$ and $B^+ \to 6\mu K^+$ respectively.

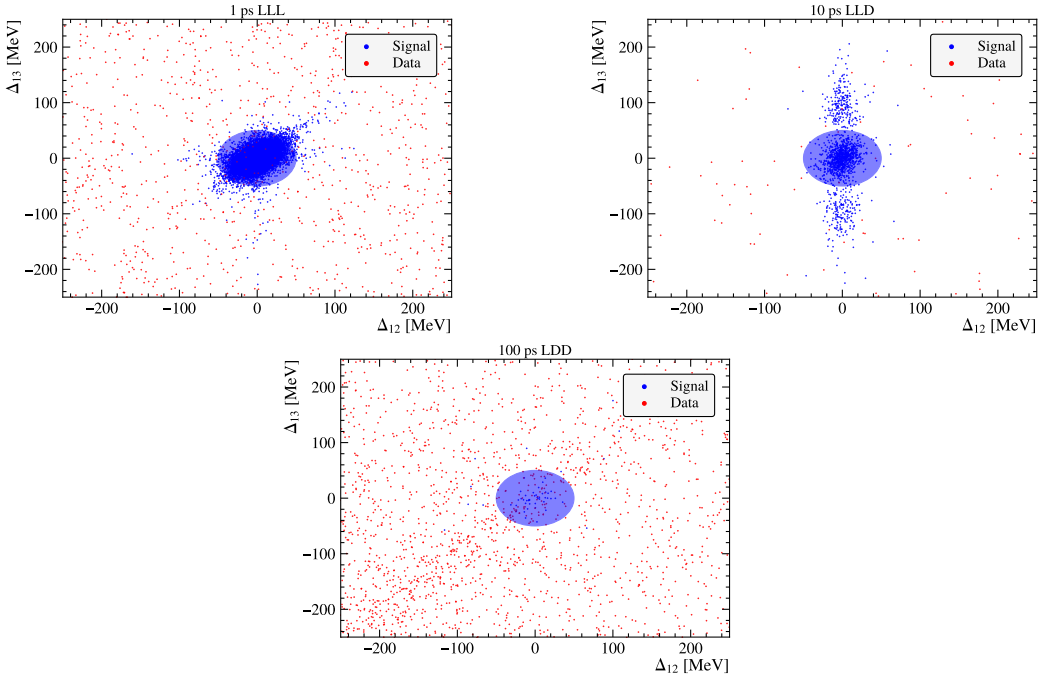


Figure 5.7: Mass resolution check for $B_s^0 \to 6\mu$ with $m_1 = 1.25$ GeV, $m_2 = 3.50$ GeV.

5.3.7 Normalisation and Control modes

Finally, control modes $B_s^0 \to J/\psi(\mu^+\mu^-)\phi(\mu^+\mu^-)$ and $B_s^0 \to J/\psi(\mu^+\mu^-)\phi(K^+K^-)$ are selected by requiring that the invariant mass of one of the dimuon pairs falls within the J/ψ region whilst the other is in the ϕ region.

5.3.8 Particle Identification Selection

Before the BDT training, and in addition to the loose preselection described in Section 5.3.1, PID requirements are included to reduce hadronic background and possible misidentifications. Initially, a 2D optimization of the BDT and PID was carried out. However, this resulted in very soft PID cuts, which is likely explained by the fact that no hadronic combinatorial background species populate the sidebands.

To reduce any potentially dangerous contamination from hadronic misID (discussed in section 5.6), all muons are required to pass $\mathrm{DLL}_\mu > 0$ and kaons $\mathrm{DLL}_K > 0$.

No offline PID requirements (in addition to stripping level PID requirements of all muons being selected with the isMuon requirement) are applied when selecting the $B_s^0 \to J/\psi(\mu^+\mu^-)\phi(K^+K^-)$ control mode, because backgrounds are less concerning, given the decay's large BF.

For the normalisation mode $B_s^0 \to J/\psi(\mu^+\mu^-)\phi(\mu^+\mu^-)$, a loose PID selection of $\mathrm{DLL}_\mu > 0.5$ on all muons is applied. It was demonstrated in the previous search for $B_s^0 \to \mu^+\mu^-\mu^+\mu^-$ decays that (with these requirements) all hadronic backgrounds considered had predicted yields less than 1 signal candidate in the region close to the B_s^0 mass compared to the $B_s^0 \to J/\psi(\mu^+\mu^-)\phi(\mu^+\mu^-)$ yield of approximately 230 [117].

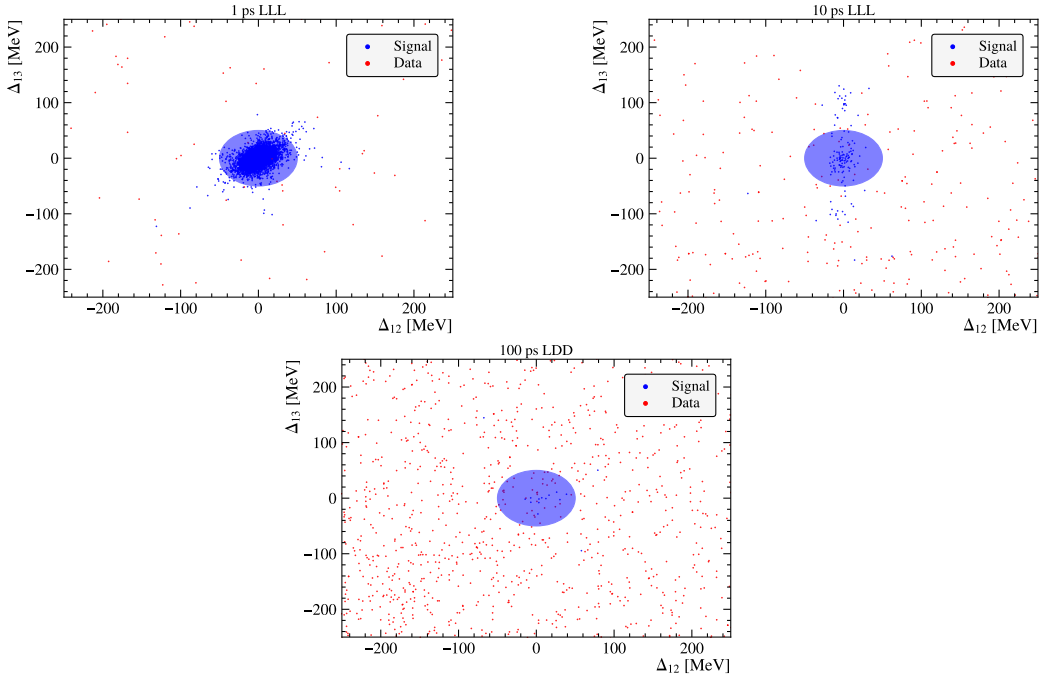


Figure 5.8: Mass resolution check for $B^+ \to 6\mu K^+$ with $m_1 = 1.25$ GeV, $m_2 = 3.50$ GeV.

5.3.9 BDT selection

For $B^+ \to 4\mu K^+$ and $B_s^0 \to 4\mu$, the combinatorial background is expected to be higher than in the high-multiplicity modes, in part due to the lack of intermediate mass scalar requirements (the two dimuons do not have the same mass). For these 4-muon modes, a BDT is therefore trained to combat combinatorial background.

Separate BDTs are trained for each final state and reconstruction category:

- **Prompt**: Candidates reconstructed by the prompt stripping line, where all tracks are combined directly at the B vertex.
- **Displaced-LL (Long-Long)**: Candidates with displaced intermediate scalar vertices, all reconstructed from long tracks, and where the scalars pass the decay time cut $t > t_{cut}$.
- **Displaced-LD (Long-Downstream)**: Candidates with displaced intermediate scalar vertices, where one dimuon is formed from long tracks, the other from downstream tracks.

The BDTs are trained using simulated signal decays, with simulation corrections applied (see Sec. 5.4) as signal proxy, and upper- and lower-mass sideband data (i.e., the full range, excluding the signal region) as a proxy for combinatorial background. For a more detailed discussion of the BDT selection, please refer to section 5.5.

5.3.10 Truth matching

Truth matching will be applied exclusively for selection purposes, namely for representing Data-MC comparisons, tuning the selection and BDT training and optimization. An overview of the true IDs to use can be found in Table 5.10. For efficiency computation, as the truth-matching is not completely reliable in the low transverse momentum regime, truth matching is set off and the strategy detailed in Section 5.7.3 is applied.

Particle	B^+/B_s^0	$a1$	$a2$	μ	K^+
MC ID	521/531	25	35	13	321

Table 5.10: MC IDs applied to particles in MC samples

5.3.11 Duplicates and Multiple Candidates

Due to the high-muon multiplicity of the decay modes being studied in this analysis, duplicates and multiple candidates can arise. The following definitions are taken: duplicates as being candidates that share the same set of tracks but are reconstructed in different ways; and multiple candidates for which one or more tracks used to reconstruct the candidates differ.

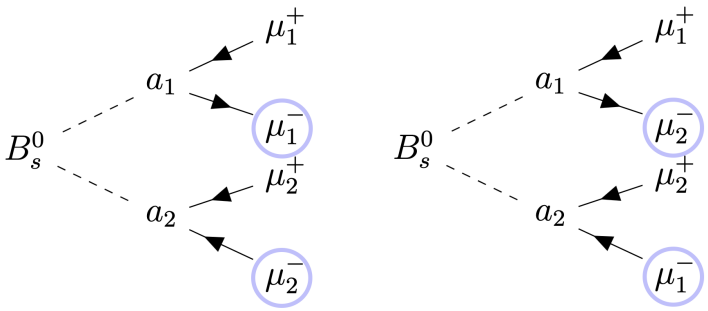


Figure 5.9: Schematic diagram showing how duplicates can arise, where the same set of muon tracks is swapped between intermediate scalars.

To veto such a source of unphysical candidates, the following approach is taken:

- **Duplicated Candidates:** Events are ranked based on their fit quality (as it must be poorer for wrong combinations) and the best is kept. For Prompt reconstruction, the vertex of the B is used, whereas for Displaced lines, the sum of the fit qualities of the dimuon pairs using the scalar vertex χ^2 (`'Sum_a_ENDVERTEX_CHI2'`).
- **Multiple Candidates:** Events are asked not to share the Run identification and, if so, not to share the event identification.

USC UNIVERSIDADE DE SANTIAGO DE COMPOSTELA

The number of duplicates is computed right after the BDT application, as each MVA should be able to reject a high amount of such a kind of candidates by relying

on their variable distributions. In general, a higher ocurrence is observed in 4μ modes with respect those of 6μ. The explanation resides in the hierarchical structure for the latter modes, which restricts the combinations able to provide feasible candidates.

5.3.12 Selection Summary

Tables 5.11 and 5.12 summarise the selection being applied to all the different cases. Optimal cuts for each BDT category have also been included, which will be discussed in more detail in Section 5.5.

Selection	**Prompt**	**Displaced-LL**	**Displaced-LD**
$min(\theta^{\mu}_{ij})$ [mrad]	> 0.1	> 0.1	> 0.1
Decay time [ns]		$t_{a_1}\|t_{a_2} > t_{cut}$	$t_{a_1}\|t_{a_2} > t_{cut}$
PID			
$\rightarrow B^0_s \rightarrow 4\mu$	$\text{DLL}_{\mu} \geq 0$	$\text{DLL}_{\mu} \geq 0$	$\text{DLL}_{\mu} \geq 0$
$\rightarrow B^+ \rightarrow 4\mu K^+$	DLL_{μ}, $\text{DLL}_K \geq 0$	DLL_{μ}, $\text{DLL}_K \geq 0$	DLL_{μ}, $\text{DLL}_K \geq 0$
BDT			
$\rightarrow B^0_s \rightarrow 4\mu$	>0.790	>0.790	>0.755
$\rightarrow B^+ \rightarrow 4\mu K^+$	>0.755	>0.545	>0.545

Table 5.11: Selection overview for 4μ searches.

Selection	**Prompt**	**Displaced-LLL**	**Displaced-LLD**	**Displaced-LDD**
$min(\theta^{\mu}_{ij})$ [mrad]	> 0.1	> 0.1	> 0.1	> 0.1
Vertexing	`B_ENDVERTEX_CHI2` < 30			
	`B_IPCHI2_OWNPV` < 9			
	`min_PT_mu` > 150 MeV			
Decay time [ns]		$t_{a_{1,1}}\|t_{a_{1,2}}\|t_{a_{1,3}} > t_{cut}$	$t_{a_{1,1}}\|t_{a_{1,2}}\|t_{a_{1,3}} > t_{cut}$	$t_{a_{1,1}}\|t_{a_{1,2}}\|t_{a_{1,3}} > t_{cut}$
Mass Cut [MeV]		$S < 50$	$S < 50$	$S < 50$
PID				
$\rightarrow B^0_s \rightarrow 6\mu$	$\text{DLL}_{\mu} \geq 0$	$\text{DLL}_{\mu} \geq 0$	$\text{DLL}_{\mu} \geq 0$	$\text{DLL}_{\mu} \geq 0$
$\rightarrow B^+ \rightarrow 6\mu K^+$	DLL_{μ}, $\text{DLL}_K \geq 0$	DLL_{μ}, $\text{DLL}_K \geq 0$	DLL_{μ}, $\text{DLL}_K \geq 0$	DLL_{μ}, $\text{DLL}_K \geq 0$

Table 5.12: Selection overview for 6μ searches.

5.4 Simulation Corrections

Simulation does not perfectly replicate real data. It is important to account for these discrepancies as accurately as possible to precisely determine the efficiencies for the normalisation and signal modes used to extract the branching ratios, ascertain invariant mass PDF shapes and effectively train MVA classifiers. In the current analysis, MC calibration is incorporated through weights, whose value is determined from the reliability with respect to the control mode $B^0_s \rightarrow J/\psi(\mu^+\mu^-)\phi(K^+K^-)$.

The use of a control channel involving prompt resonances is supported by a published analysis testing lepton universality with $B^0 \rightarrow K^0_S\ell^+\ell^-$ and $B^+ \rightarrow K^{*+}\ell^+\ell^-$

decays [272]. In that study, kinematic and reconstruction variables of the prompt $B^0 \to K^0_S J/\psi(\mu^+\mu^-)$ channel are compared to those of simulated samples, showing a considerable agreement. This fact demonstrates that the detector simulation accurately models tracking and vertexing performance in the LHCb detector for displaced Long and Downstream tracks, which provides confidence that these samples are also well modeled in simulation for the present analysis.

5.4.1 Generator-level weights

The production of B-hadrons in pp collisions is difficult to model accurately, resulting in an imperfect agreement between data and MC kinematic distributions of B-mesons and of the final-state particles, as well as the multiplicity of events, which is generally underestimated by simulation.

The introduction of generator level weights is done through a `BinsReweighter` algorithm, which allows for a simultaneous reweighting of the B p_T and η (Pseudorapidity) and the event multiplicity ($\mathrm{n_{Tracks}}$). For such a purpose, signal MC events with truth matching are included, as well as signal events for $B^0_s \to J/\psi(\mu^+\mu^-)\phi(K^+K^-)$ after the application of the *Splot* technique [273] to the background plus signal hypothesis. Separate weights are determined for each data-taking year.

5.4.2 Trigger weights

Simulation also does not perfectly reproduce the trigger response. Discrepancies are investigated using data and MC passing the preselection. This is carried out by evaluating efficiencies of the trigger requirements as a function of relevant kinematic variables using the TISTOS method [203]. For more information on the trigger criteria at the L0 level, it is advisable to return to the Section 3.4.1.

L0 Trigger

Modelling of the L0 trigger response is examined by evaluating the efficiencies for the `L0Muon` trigger. This is carried out by first requiring candidates to be tagged as TIS with the `L0Global` trigger (which selects any candidate that triggers at least one of the L0 lines) and to have passed the HLT trigger requirements. The TOS efficiency is determined by additionally requiring TOS with respect to the `L0Muon` trigger.

$$\epsilon_{\mathrm{TOS}} = \frac{N_{\mathrm{TISTOS}}}{N_{\mathrm{TIS}}} \tag{5.3}$$

USC DE SANTIAGO

where N_{TIS} is the number of TIS candidates and N_{TISTOS} is the number of candidates satisfying both TIS and TOS. The efficiency of the `L0Muon` response in data and MC is evaluated in bins of p_T. The resulting efficiency curves are fitted with the following

empirical function to smooth out statistical fluctuations:

$$\epsilon(p_T) = \frac{a}{2}\left[1 + \mathrm{erf}\left(\frac{p_T - b}{c\sqrt{2}}\right)\right] + \frac{d}{2}\left[1 + \mathrm{erf}\left(\frac{p_T - b}{e\sqrt{2}}\right)\right] \tag{5.4}$$

where the parameters a, b, c, d and e are determined from a maximum likelihood fit to the data.

A representative example of the `L0Muon` response of data and MC is shown in figure 5.10 as a function of muon p_T for 2018. The greatest deviations arise close to the threshold muon p_T, which is expected considering both the differing resolutions of data and MC, and that the trigger thresholds often change during the course of a data-taking run.

Efficiency profiles determined with equation 5.4 are used to calculate weights to correct the data-MC discrepancy. The `L0Muon` weight for a given candidate is given by

$$w_{\mathrm{L0Muon}} = \frac{1 - \left\{\prod_{i=1}^{n}\left[1 - \epsilon^{\mathrm{L0Muon}}_{\mathrm{Data}}(p_T^n)\right]\right\}}{1 - \left\{\prod_{i=1}^{n}\left[1 - \epsilon^{\mathrm{L0Muon}}_{\mathrm{MC}}(p_T^n)\right]\right\}} \tag{5.5}$$

where n is the number of muons in the signal mode and p_T^n is the transverse momentum of the n^{th} muon. The weight w_{L0Muon} is effectively the ratio of the probabilities that at least one muon triggers `L0Muon` for data (numerator) and MC (denominator). The trigger weights applied to the signal modes are close to unity in each case.

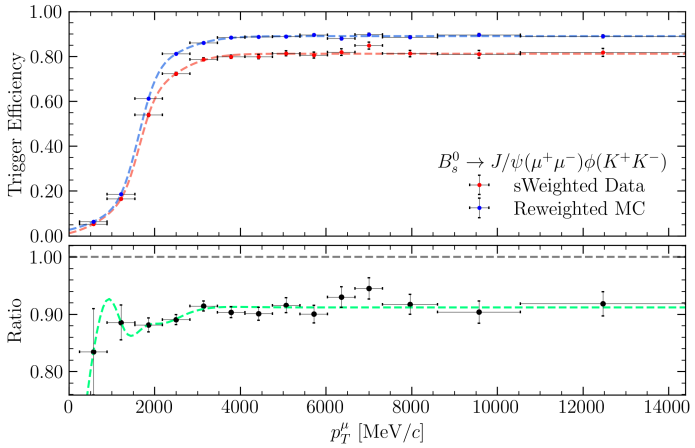


Figure 5.10: The efficiency of the L0Muon trigger line as a function of muon p_T for 2018 $B_s^0 \to J/\psi(\mu^+\mu^-)\phi(K^+K^-)$ data (red) and MC (blue). Generator-level corrections have been applied to the MC, but not TISTOS corrections. The lower subplot shows the ratio of the data and MC, with the green curve being the ratio of the fitted efficiency curves.

USC UNIVERSIDADE DE SANTIAGO DE COMPOSTELA

HLT

The HLT response is investigated with several variables used to define the HLT trigger lines. The efficiency is again evaluated using the TISTOS method for these variables, where candidates are initially required to be selected as TOS by the L0 line and also be TIS with respect to `Hlt1Phys` and `Hlt2Phys`, which are similar to `L0Global` but only make decisions using lines related to physics processes. In each case, the ratio of the data and MC efficiencies is ≈ 1 for all variables with a disagreement of $<5\%$, suggesting that corrections to the HLT response are not required.

5.4.3 PID weights

In general, PID variables are not well modelled in simulation. The calibration is generally performed using the *PIDCalib* software package [274], which determines a PID efficiency derived from calibration data for each track in bins of track p, η and $\mathrm{n_{Tracks}}$, for a given set of PID requirements. Such a procedure is of wide interest because simulation might not have a perfect coverage of the low p_T region, as reported in [117].

Studies of the discrepancy between the PID response of data and MC were carried out, showing a relatively good agreement between them across the muon p_T spectrum. This is observed for both 4μ and 6μ modes.

Although residual differences are not observed to play a big role, a systematic error is introduced to account for the calibration of the PID lying outside of the efficiency computation. More information is provided in Section 5.9.4.

5.4.4 Reconstruction weights

Even with the current corrections, residual differences might arise in reconstruction variables, thus biasing the BDT response or the efficiency determination. The calibration is performed simultaneously in a set of input variables for the BDTs using `GBReweighter` from the `hep_ml` package [275]. Such variables are:

- **B_ENDVERTEX_CHI2:** Quality of the fit of the B meson decay vertex.
- **B_FDCHI2_OWNPV:** Flight-distance significance of the B candidate with respect to its origin vertex.
- **B_IPCHI2_OWNPV:** Impact Parameter significance of the B candidate with respect to its origin vertex.
- **B_PT:** Transverse momentum of the B meson.
- **B_Pseudorapidity:** Pseudorapidity of the B meson.

USC UNIVERSIDADE DE SANTIAGO DE COMPOSTELA

It is observed that reconstruction weights lie generally close to unity, reporting an effective cancellation of discrepancies between truth-matched MC and sWeighted Data.

5.5 BDT selection

As mentioned in section 5.3.9, BDTs are trained to separate signal and combinatorial background in 4μ final states. For 6μ final states, the intermediate scalar mass requirements reduce combinatorial background to a very low level, so a further BDT selection is not required. Separate BDTs are trained on each reconstruction category (Prompt, Displaced-LL and Displaced-LD) and for the two decays ($B_s^0 \to \mu^+\mu^-\mu^+\mu^-$ and $B^+ \to \mu^+\mu^-\mu^+\mu^-K^+$) using candidates surviving the preselection, trigger, mass, decay time and PID selections. Optimisation of the BDT cut is performed using the same samples. In all cases, signal MC corresponding to the higher-mass dataset is used for the signal sample, while the background is taken from both low-mass and high-mass sidebands in data. This choice is supported by the fact that, in the high-momentum regime associated with heavier intermediate states, the signal occupies a kinematic region where a clearer separation from background features can be achieved. Several attempts to use a cocktail of masses were rejected, as they inevitably biased the BDT performance in this regime.

During the training, weights from Section 5.4 are taken into account and, for both data and MC categories, they are normalised to their sums, which ensures the imbalance between categories does not affect the final performance of the classifiers. Additionally, in order to make optimal use of the available statistics while avoiding overtraining, k-folding with $k = 5$ is performed in all the cases. The method works by splitting the combined dataset (signal and background proxies) into $k = 5$ folds, performing the training in $k-1$ folds and using the remaining fold as a test sample. As a result, $k = 5$ BDTs are trained, and when determining the BDT response for a certain candidate, the BDT fold in which that candidate is in the test sample is used. A priori, this split is made through the generation of random numbers, but a seed is introduced in terms of reproducibility.

Mode	Reconstruction	Estimators	Learning Rate
$B_s^0 \to 4\mu$	Prompt	350	0.05
	Displaced-LL	220	0.05
	Displaced-LD	250	0.05
$B^+ \to 4\mu K^+$	Prompt	400	0.1
	Displaced-LL	250	0.05
	Displaced-LD	250	0.05

Table 5.13: Hyperparameter selection for classifiers. Additionally, all of them share; *DecisionTreeClassifier* as base estimator, `MinNodeSize` equal to 2.5% and `MaxDepth` of 3.

USC UNIVERSIDADE DE SANTIAGO

For the signal training samples in each reconstruction category, simulation with the following intermediate scalar lifetimes is used in the training:

- **Prompt:** MC samples simulated with $\tau_{a_1} = 0$ ps.
- **Displaced-LL:** MC samples simulated with $\tau_{a_1} = 1$ ps.
- **Displaced-LD:** A mixture of MC samples with $\tau_{a_1} = 10$ ps, 100 ps and 1000 ps.

Several types of algorithms have been considered, such as *AdaBoost* [276], *GradientBoosting* [277] and *Extreme Gradient Boosting* [278], with *AdaBoost* showing the best performance. *Adaboost* is an ensemble method that combines several weak learners (Decision Trees) into a stronger learner. The particularity of such an algorithm is that new predictors correct the predecessors' decisions by paying special attention to the training instances under-fitted, which results in new predictors focusing on the hard cases. The hyperparameters of the classifiers are determined using a Halving Grid Search method [279] (search over specified parameter values with successive halving) based on optimising the area under the ROC curve. They can be seen in table 5.13.

Channel	Reconstruction	Training Variables
$B_s^0 \to 4\mu$	Prompt	$\chi^2_{B_{IP}}$, B_τ, $\chi^2_{B_{\rm vtx}}$, $B_{\rm P_T}$, $\max(\rm p_T^\mu)$, $\log(1-\theta_{\rm B}^{\rm dir})$, $\min(\rm IP_\mu)$, B_η
	Displaced LL	$\chi^2_{B_{IP}}$, B_τ, $\rm IP_{a_2}$, $\rm DOCA(a_1, a_2)$, $B_{\rm P_T}$, $\max(\rm p_T^\mu)$, $\log(1-\theta_{\rm B}^{\rm dir})$, $\chi^2_{\rm B_{FD}}$
	Displaced LD	$\chi^2_{B_{IP}}$, B_τ, $\rm IP_{a_2}$, $\rm DOCA(a_1, a_2)$, $B_{\rm P_T}$, $\max(\rm p_T^\mu)$, $\log(1-\theta_{\rm B}^{\rm dir})$, $\chi^2_{\rm B_{FD}}$
$B^+ \to 4\mu K^+$	Prompt	$B_{\rm P_T}$, B_τ, $\chi^2_{B_{IP}}$, $\max(\rm p_T^\mu)$, $\min(\rm IP_\mu)$, $\chi^2_{J/\psi_{\rm vtx}}$, $\chi^2_{J/\psi_{\rm IP}}$
	Displaced LL	$B_{\rm P_T}$, $\chi^2_{\rm B_{FD}}$, $\chi^2_{B_{\rm vtx}}$, B_τ, $\rm IP_{a_2}$, $\min(\chi^{2\,\rm a_2}_{\mu_{\rm IP}})$, $\rm DOCA(a_1, a_2)$
	Displaced LD	$B_{\rm P_T}$, $\chi^2_{\rm B_{FD}}$, $\chi^2_{B_{\rm vtx}}$, B_τ, $\rm IP_{a_2}$, $\min(\chi^{2\,\rm a_2}_{\mu_{\rm IP}})$, $\rm DOCA(a_1, a_2)$

Table 5.14: List of variables used to train each of the Multivariate Classifier, each one trained per channel and reconstruction mode.

The choice of input features for the BDT is empirically driven. A large basis set common for all decay modes is chosen. Other specific features are added on top of this set for each decay and reconstruction category. Then the BDT is retrained several times, successively removing the variables with the lowest feature importance until the area under the ROC drops visibly. The resulting variables for each category are collected in Table 5.14

USC UNIVERSIDADE DE SANTIAGO DE COMPOSTELA

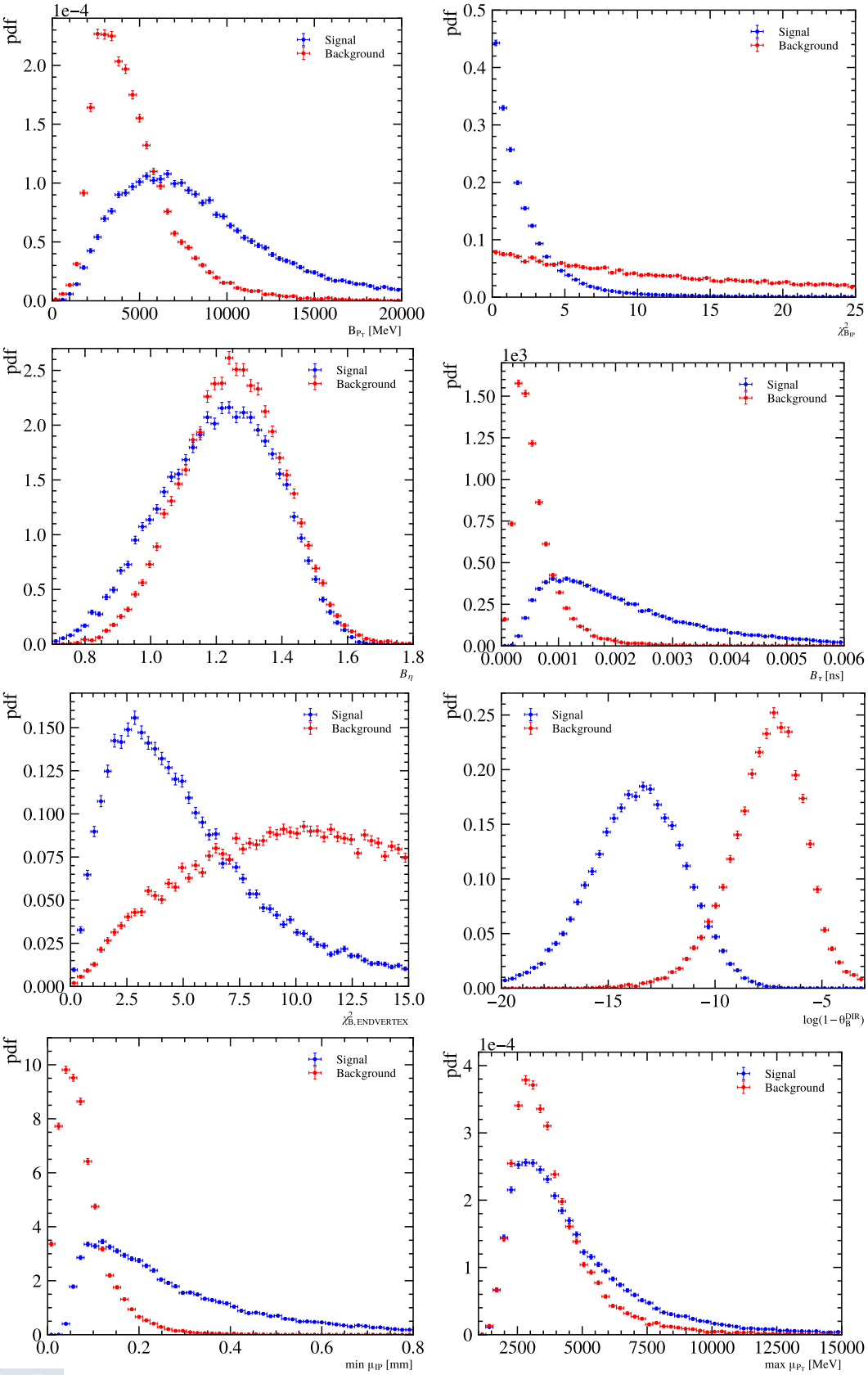


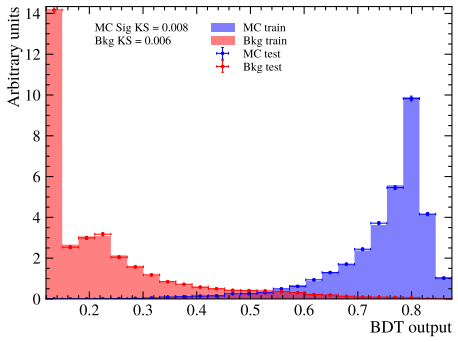
Figure 5.11: Distributions of BDT training variables in MC and Data for the $B_s^0 \to 4\mu$ Prompt reconstruction.

5.5.1 Classifiers for $B_s^0 \to 4\mu$

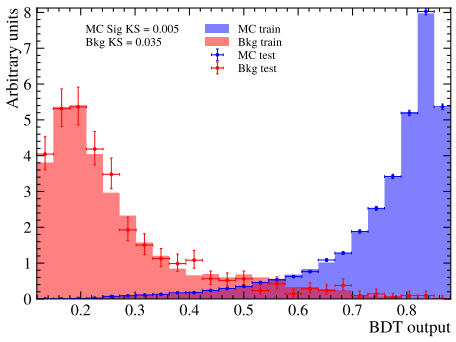
In the prompt reconstruction category of the $B_s^0 \to 4\mu$ search, a mix of input variables were chosen following the ones from [117] and new ones such as the transverse flight distance of the B candidate ($FD_\perp$) and the B pseudorapidity (η) are included, as illustrated in Figure 5.11. No isolation variables are included. This decision is motivated by two factors: first, the decay topology alone already provides good discrimination; second, the data stream for $B^+ \to 4\mu K^+$ does not retain full underlying event information, making isolation-based features non-generalisable.

In the displaced categories (LL and LD), the cocktail of lifetimes included in the training makes the BDTs somewhat model-dependent. To avoid biases on the scalar's lifetime, only features derived from the short-lived scalar (such as its IP) or from the muons coming from it ($\min(\chi^2_{\mu^{a2}_{IP}})$) are used. The DOCA between scalar candidates has also been validated to be uncorrelated with lifetime. The χ^2 of the B vertex fit is normalised by the number of degrees of freedom (i.e., divided by the number of degrees of freedom involved). Additionally, variables not directly related to the scalar mass are preferred.

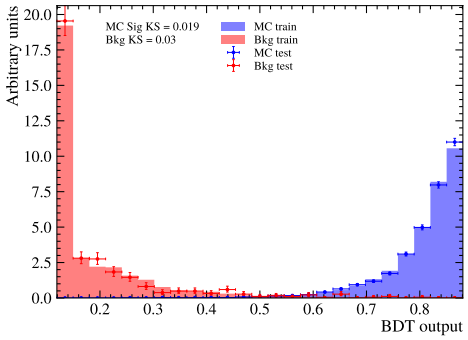
This approach yields good signal–background separation, with performance improving as the scalar lifetime increases (see Figure 5.12). The BDT performance can be found in Figure 5.14. No signs of overtraining are observed: this is verified using Kolmogorov–Smirnov (KS) tests [280] and through inspection of learning curves 5.15.



(a) Prompt



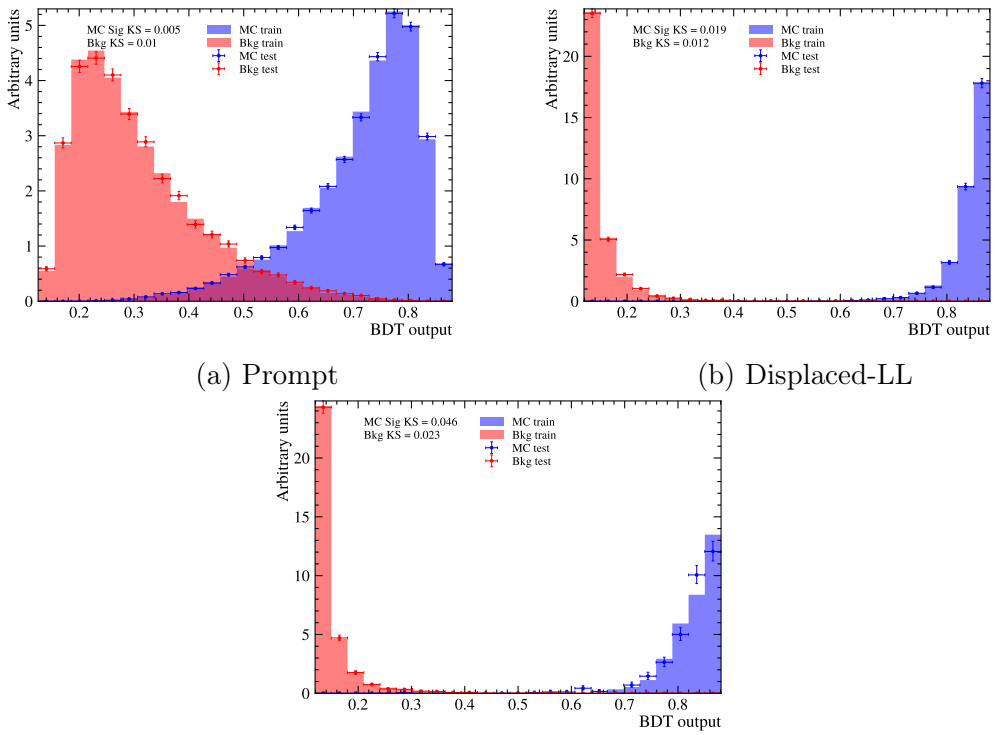
(b) Displaced-LL



(c) Displaced-LD

USC UNIVERSIDADE DE SANTIAGO DE COMPOSTELA

Figure 5.12: BDT output for $B_s^0 \to 4\mu$ searches.



(a) Prompt

(b) Displaced-LL

(c) Displaced-LD

Figure 5.13: BDT output for $B_s^0 \to 4\mu K^+$ searches.

5.5.2 Classifiers for $B^+ \to 4\mu K^+$ decays

In this search channel, the presence of an additional prompt track (the K^+) allows the reconstruction of two dimuon vertices (remember discussion in Section 5.3.1), each displaced from the B vertex. Due to the similarity in decay topology, many of the input variables used to train the $B_s^0 \to 4\mu$ BDTs can be reused here as a starting point.

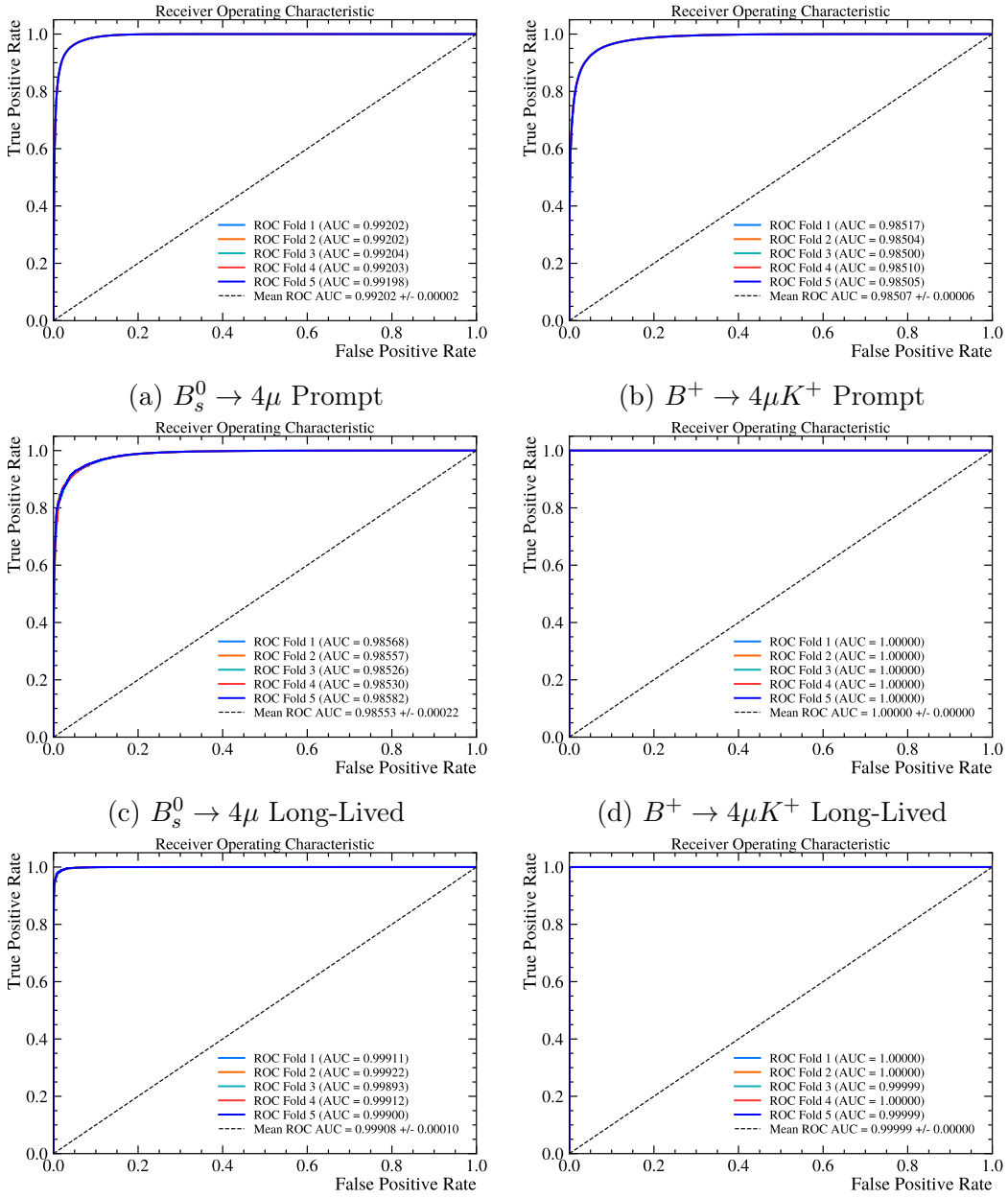
In the Prompt reconstruction category, B^+ candidates are reconstructed at stripping level as $B^+ \to (J/\psi \to 4\mu)\, K^+$. The set of variables used for BDT training includes those already employed in the $B_s^0 \to 4\mu$ prompt classifier, along with additional variables related to the reconstructed J/ψ, such as its lifetime, vertex χ^2, and impact parameter with respect to the primary vertex.

For the displaced reconstruction categories (LL and LD), the overall strategy and input variable selection closely follow that of the $B_s^0 \to 4\mu$ displaced classifiers. In this case, the discriminating power of the $B^+ \to 4\mu K^+$ classifiers benefits from the presence of two long-lived intermediate particles, leading to clearer topological features and improved variable separation between signal and background.

The BDT response of $B^+ \to 4\mu K^+$ samples can be observed in Figure 5.13. Additionally, the quantification of classifiers' performance is included in Figure 5.14 and the behaviour of the associated learning curves in Figure 5.15.

USC UNIVERSIDADE DE SANTIAGO DE COMPOSTELA

All BDTs show a clear separation between signal and background, which improves



(a) $B_s^0 \to 4\mu$ Prompt

(b) $B^+ \to 4\mu K^+$ Prompt

(c) $B_s^0 \to 4\mu$ Long-Lived

(d) $B^+ \to 4\mu K^+$ Long-Lived

(e) $B_s^0 \to 4\mu$ Down

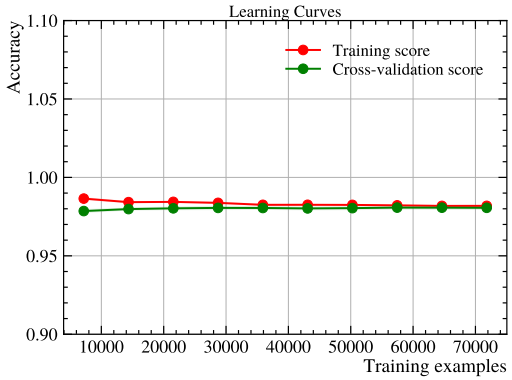
(f) $B^+ \to 4\mu K^+$ Down

Figure 5.14: ROC curves for all six BDTs.

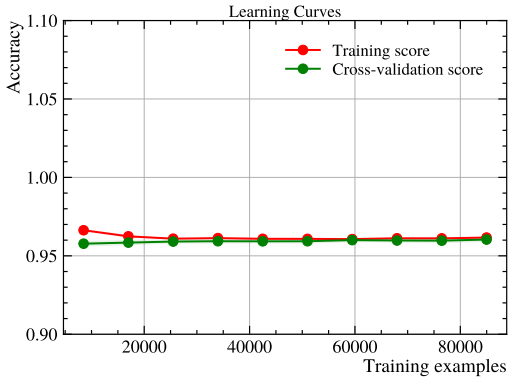
as the displaced regime is considered. This can be directly observed in the BDT output distributions (Figures 5.12 and 5.13) and in the area under the ROC curve (Figure 5.14), with most cases lying close to ideal performance. It is particularly noteworthy that, in the $B_s^0 \to 4\mu$ displaced category, the removal of a displaced vertex requirement and the demand that the muons originate directly from the B meson reduce the separation between components compared to the $B^+ \to 4\mu K^+$ case. This is also reflected in the KS test values for the background, underlining the greater challenge in parametrizing that component. Nevertheless, this effect is not expected to pose a significant problem.

Possible overtraining is carefully checked through KS tests for signal and background in all six MVA algorithms. In general, a good agreement is observed between the

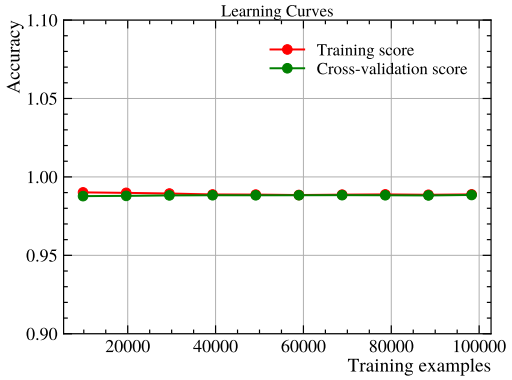
training and test samples for all categories. This is further supported by the learning curves, which show how quickly the accuracy stabilizes for both training and test instances, reaching similar values by the end of training. Such behaviour confirms that no overtraining effects are present at this stage.



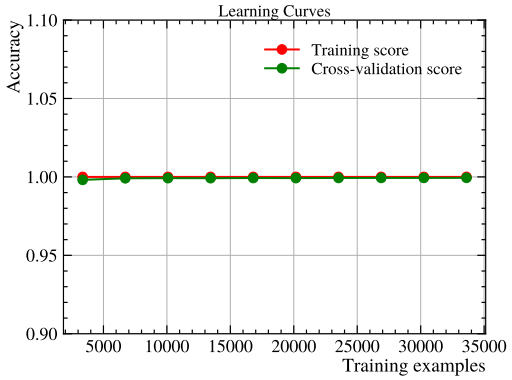
(a) $B_s^0 \to 4\mu$ Prompt



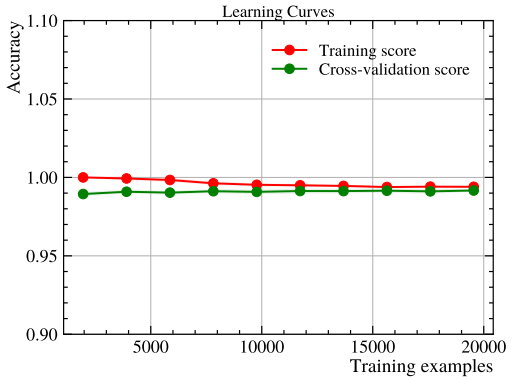
(b) $B^+ \to 4\mu K^+$ Prompt



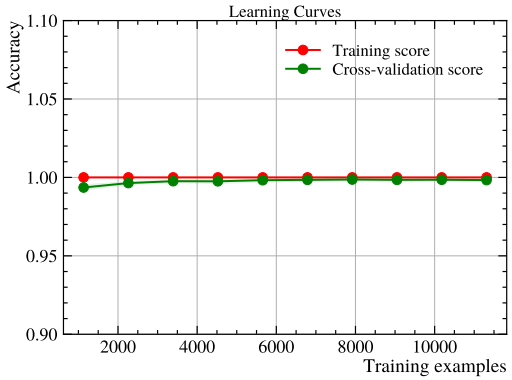
(c) $B_s^0 \to 4\mu$ Long-Lived



(d) $B^+ \to 4\mu K^+$ Long-Lived



(e) $B_s^0 \to 4\mu$ Down



(f) $B^+ \to 4\mu K^+$ Down

Figure 5.15: Learning Curves. Training score stands for the performance of the BDT evaluated on the same data it was trained on, whereas Cross Validation Score is the average performance of the BDT on multiple held-out validation subsets.

USC UNIVERSIDADE DE SANTIAGO DE COMPOSTELA

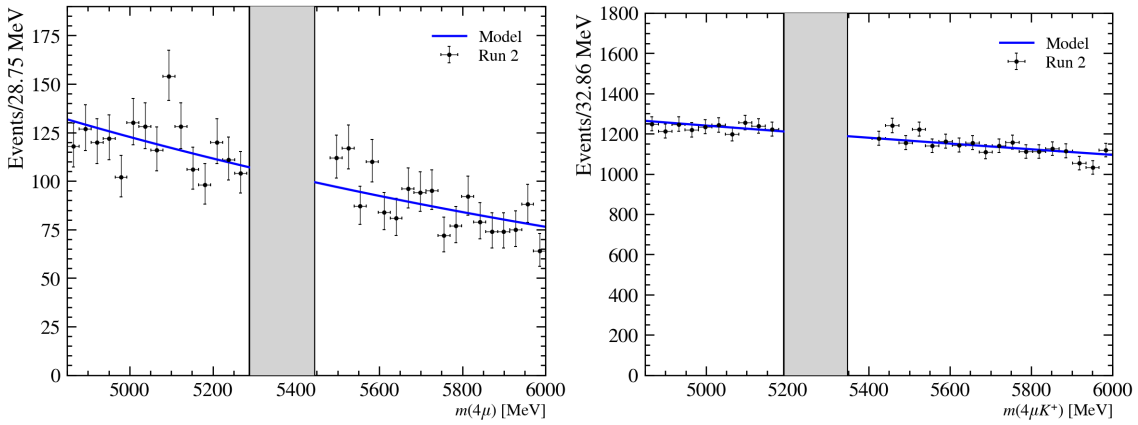
5.5.3 Optimization of the BDT response

The optimal BDT cut for each classifier is chosen by maximising the Punzi figure of merit (FoM) [269], defined as:

$$\mathrm{FoM}(\sigma) = \frac{\varepsilon}{\frac{\sigma}{2} + \sqrt{N_{\mathrm{back}}}} \tag{5.6}$$

where σ is the target significance, ε is the signal efficiency (taken from simulation), and N_{back} is the estimated number of background candidates in the signal region. The background yield is estimated by fitting an exponential function to the invariant mass distribution in the data sidebands and interpolating into the signal region. An example of such a fit is shown in Figure 5.16, and the resulting FoM curves as a function of the BDT cut are presented in Figure 5.17.

In some categories, particularly those with very low background, the optimisation procedure is affected by statistical fluctuations due to a limited number of events surviving the full selection in the sidebands. To mitigate instability in these situations, a conservative estimate of one background event in the signal region is assumed whenever fewer than two events are present in the sidebands.

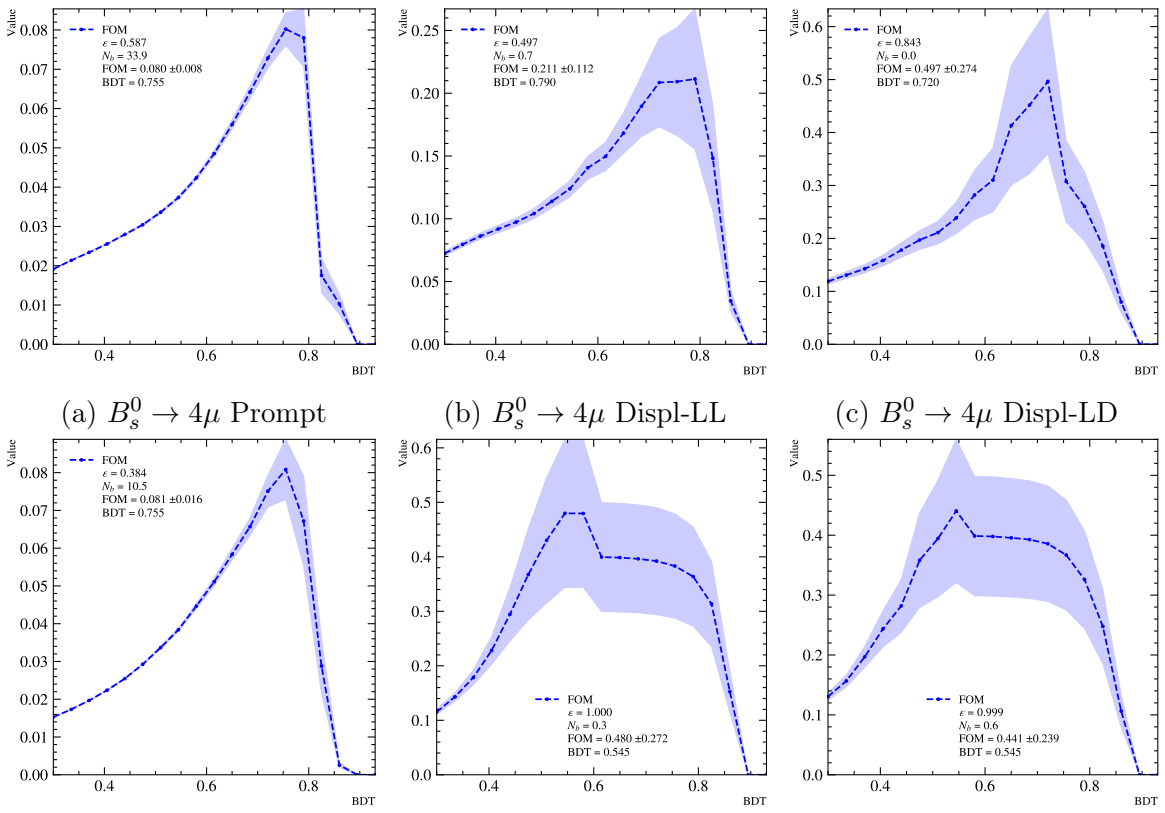


(a) $B_s^0 \to 4\mu$. (b) $B^+ \to 4\mu K^+$.

Figure 5.16: Example of fits to the data mass sidebands used to estimate the number of background events in the signal region for the BDT optimisation, with BDT > 0.1.

Of big importance is to ensure that in the FoM curves, no alternative maxima can be found within an uncertainty band. For that, error propagation is applied over Equation 5.6 and 1σ bands are also included in Figure 5.17. As seen, only an absolute maximum is present at each curve, allowing to consider it as the optimal BDT configuration.

USC UNIVERSIDADE DE SANTIAGO DE COMPOSTELA



(a) $B_s^0 \to 4\mu$ Prompt (b) $B_s^0 \to 4\mu$ Displ-LL (c) $B_s^0 \to 4\mu$ Displ-LD

(d) $B^+ \to 4\mu K^+$ Prompt (e) $B^+ \to 4\mu K^+$ Displ-LL (f) $B^+ \to 4\mu K^+$ Displ-LD

Figure 5.17: Scans of the Punzi figure of merit for each decay and stripping line sample. The scan is shown zoomed around the optimum cut point.

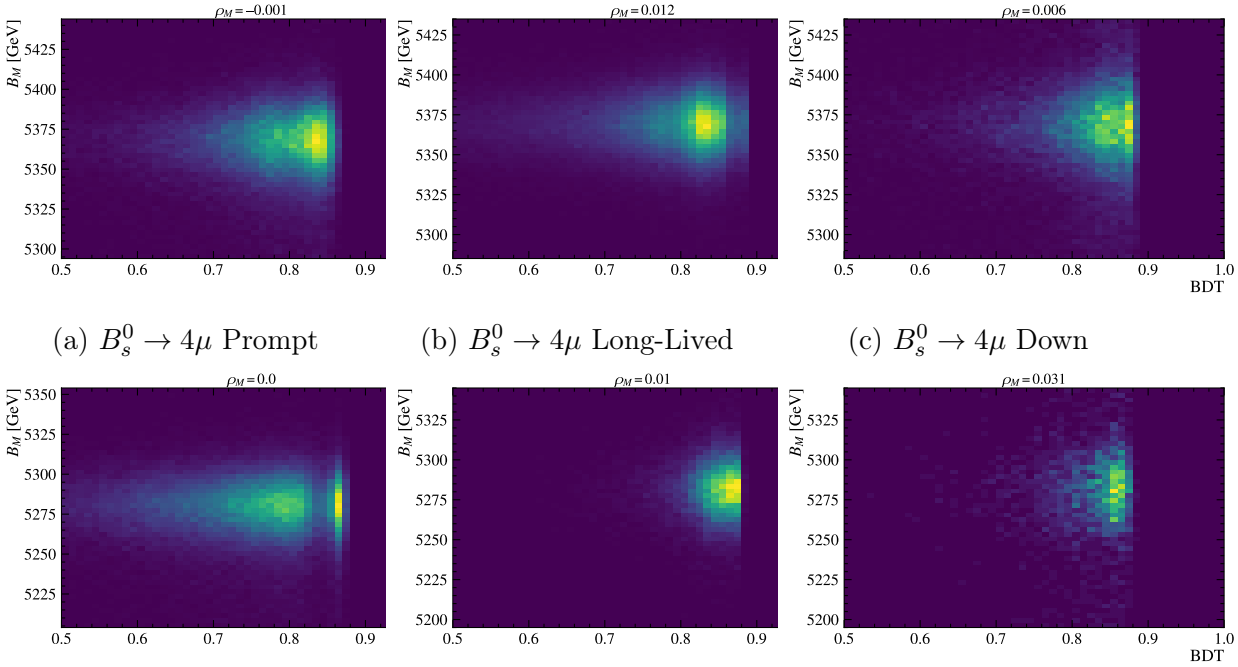
5.5.4 Potential BDT biases

After training the BDTs, a series of sanity checks is performed to verify that the classifiers do not introduce undesired biases. The goals of the analysis are to perform a bump hunt in the B mass and, for the mass points specified in Table 5.3, extrapolate sensitivities in the decay time of the long-lived scalar. Therefore, no correlations with the B mass or scalar's lifetime must be appreciated.

In the displaced categories, the input variables related to the scalar candidates are selected to avoid mass dependence. This is validated by examining the two-dimensional distribution of BDT score versus B mass (Figure 5.18) of MC candidates which pass stripping, clones, trigger and PID selections. No preferred orientation or artificial sculpture is appreciated, as well as the Pearson correlation coefficients (between the BDT score and scalar mass) are below 0.2 in all cases, confirming the absence of significant correlation.

A similar check is performed to ensure that the BDT response is not correlated with the lifetime of the long-lived scalar. For events within the signal mass window, the BDT score is compared to the true scalar lifetime, and the Pearson correlation coefficient is again computed (see Figure 5.19). As with mass, no significant correlation is observed, supporting the validity of extrapolating results from individual lifetime seed points

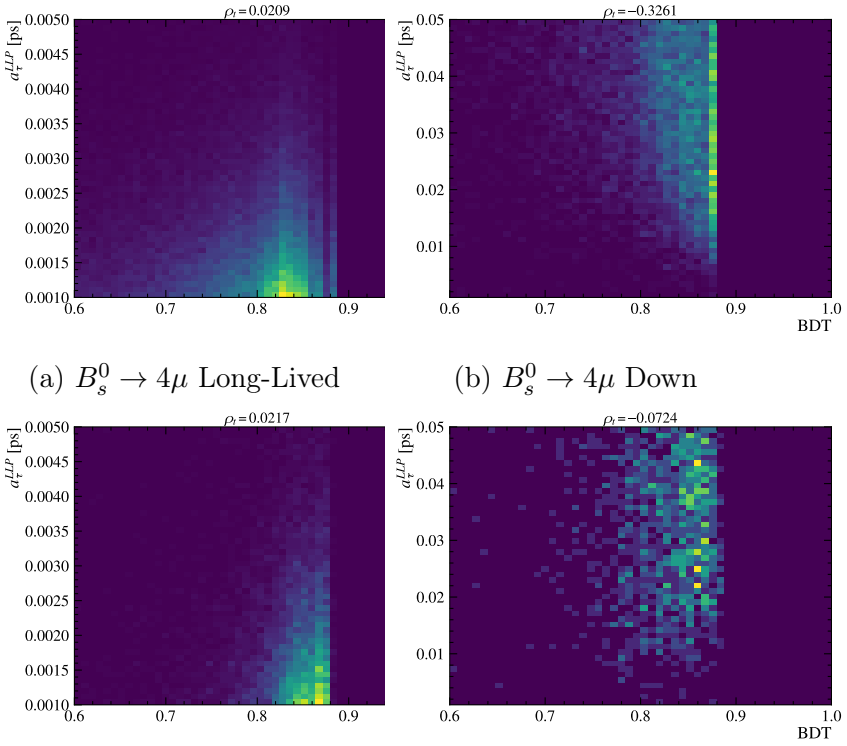
across the full model parameter space.



(a) $B_s^0 \to 4\mu$ Prompt (b) $B_s^0 \to 4\mu$ Long-Lived (c) $B_s^0 \to 4\mu$ Down

(d) $B^+ \to 4\mu K^+$ Prompt (e) $B^+ \to 4\mu K^+$ Long-Lived (f) $B^+ \to 4\mu K^+$ Down

Figure 5.18: 2D distributions between BDT output and the Mass of the B.



(a) $B_s^0 \to 4\mu$ Long-Lived (b) $B_s^0 \to 4\mu$ Down

(c) $B^+ \to 4\mu K^+$ Long-Lived (d) $B^+ \to 4\mu K^+$ Down

Figure 5.19: 2D distributions between BDT output and lifetime of the LLP.

USC UNIVERSIDADE DE SANTIAGO DE COMPOSTELA

5.6 Backgrounds

The use of different reconstruction categories implies that the backgrounds must be categorized according to the influence they may have on each physics regime. The same arguments discussed in Section 4.3 apply again.

For the Prompt reconstruction, the largest source of physical background comes from B decays via unflavoured and charmonium resonances, including $\phi \to \mu^+\mu^-$, $J/\psi \to \mu^+\mu^-$ and $\psi(2S) \to \mu^+\mu^-$, which are explicitly vetoed with the prompt selection criteria. Resonances such as ω, ρ and η can also pollute the low mass dimuon spectrum. Semi-hadronic or hadronic b-hadron decays (e.g. $B_s^0 \to \pi^+\pi^-\mu^+\mu^-$, $B^0 \to \pi^+\pi^-\pi^+\pi^-$ or $\Lambda_b \to p^+K^-\mu^+\mu^-$) with two or more hadrons misidentified as muons are another possible source of background.

In the displaced regime, several issues might appear. First, the finite vertex resolution of the detector might produce leaks from Prompt events surviving the Long-Lived selection. Additionally, pure decays of Long-Lived particles able to build a real B candidate might show up in the expected signal region (see the cases of Λ^0 or K_S^0). Likewise, but in a residual way, Λ_b candidates resembling a similar topology to the signal modes can be pushed to the region of interest because of their proximity to the B meson mass.

While for the 4μ scenarios a plethora of possible decays can mimic the signal, there are hardly any backgrounds that can fake a 6μ decay. One example is $B_s^0 \to J/\psi\phi\phi$ with an estimated branching fraction of the order 10^{-13}, far from the reachable signal sensitivities and which in any case would fail the resonance vetoes.

Given the large range of potential backgrounds, a rule-of-thumb method is developed in Section 5.6.1 to provide a rough estimation of the potential pollution from each process. This strategy aims to quickly reject those decays with negligible contributions, whereas those with a significant expected yield are afterwards studied in detail with official simulation.

5.6.1 Preliminary background estimations

Making use of Equation 4.2, the yield of each decay is normalized to the $B_s^0 \to J/\psi(\mu^+\mu^-)\phi(\mu^+\mu^-)$ control mode, such that:

$$N_{\text{back}} = \frac{N_{\text{norm}}}{\mathcal{B}_{\text{norm}}} \times \frac{\varepsilon_{\text{back}}}{\varepsilon_{\text{norm}}} \times \frac{f_{\text{back}}}{f_{\text{norm}}} \times \mathcal{B}_{\text{back}} \tag{5.7}$$

where the index "norm" refers to the normalization channel and "back" to the specific background component being investigated. The symbol f denotes the hadronization fraction of the B-hadron concerned [281].

As a conservative estimate, the background efficiency ε_{back} in Equation 5.7 is assumed to be of the same order of magnitude as that of the corresponding signal efficiency. In order to check the effects of the prompt mass vetoes and the decay time cut, the reconstruction from $B_s^0 \to 4\mu$ is run over the control channel MC, and the effect on J/ψ and ϕ is calculated. The efficiencies are:

$$\varepsilon_m^{J/\psi} = 5.1 \cdot 10^{-2}; \quad \varepsilon_m^{\phi} = 2.9 \cdot 10^{-2} \tag{5.8}$$

$$\varepsilon_t^{J/\psi} = 2.0 \cdot 10^{-2}; \quad \varepsilon_t^{\phi} = 5.5 \cdot 10^{-3} \tag{5.9}$$

Another factor to be included in Eq. 5.7 is hadron-to-muon misidentification. Thanks to the high-yield mode $B_s^0 \to J/\psi(\mu^+\mu^-)\phi(K^+K^-)$ with similar kinematics as the signal, an approximate kaon to muon misID efficiency can be estimated. The inclusion of other species misID (namely, proton and pion to muon) should be computed with adequate control channels, which goes beyond the scope of these ballpark estimates. However, the hadron to muon misID is measured in bins of pT (see Tab 2 in [282]), therefore, for these simplified studies, the p_T spectrum of the final state particles is convolved with the misID efficiencies to obtain an estimate of the overall efficiency. For the calculus with the control mode, trigger and intermediate mass requirements are applied and kaons are required to pass isMuon and $PID_\mu > 0$. Since there are three possibilities (Kaon 1 with muon hypothesis, Kaon 2 with muon hypothesis, or both), the calculus of such a quantity is obtained from:

$$\varepsilon(K \to \mu) = \varepsilon(K_1 \to \mu) + \varepsilon(K_2 \to \mu) - \varepsilon(K_1 \to \mu) \cdot \varepsilon(K_2 \to \mu) \tag{5.10}$$

where $\varepsilon(K_i \to \mu)$ is the misidentification of the Kaon i$^{\text{th}}$ as muon. Such factors, representing efficiencies, are extracted as the number of events satisfying the condition over the total yield, both extracted from invariant mass fits with a double crystal ball for the signal and an exponential for the combinatorial background component (Figure 5.20). The result of such an estimation is:

$$\epsilon(K \to \mu) = 0.82\% \tag{5.11}$$

Finally, the rule-of-thumb estimations will obey the following considerations

- All considered modes must have at least two final state muons. This is supported by the fact that modes with no muons would be highly suppressed by the stringent selection requirements.

USC UNIVERSIDADE DE SANTIAGO DE COMPOSTELA

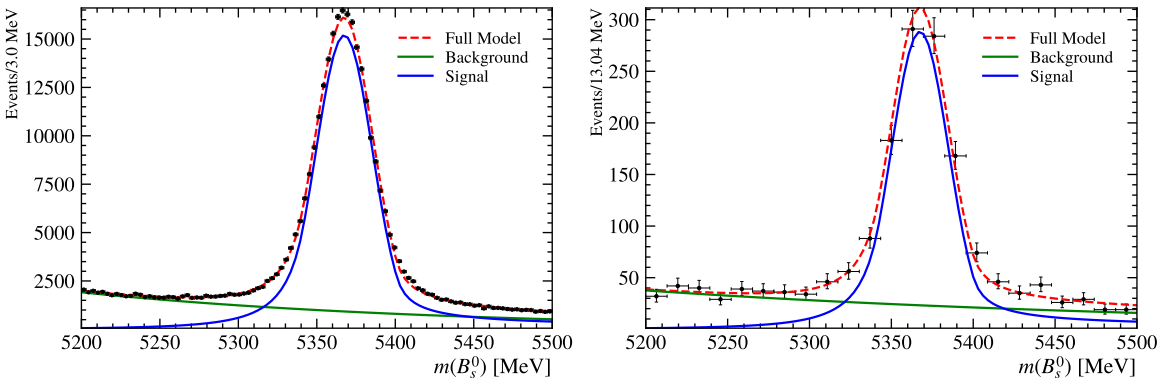


Figure 5.20: Fits to the high-yield $B_s^0 \to J/\psi(\mu^+\mu^-)\phi(K^+K^-)$ channel with the kaons without PID cut (left) and one kaon identified as muon (right) hypothesis.

- As previously stated, all background efficiencies are supposed to be of the same order as the corresponding signal one.
- Vetoes 5.8 and 5.9 multiply the expected yield if the particle over they act (in the corresponding Prompt or Displaced regime) is present in the decay.
- Final expected yields are multiplied by a factor $\text{misID}_{X\to\mu}$ when a particle X different from muons is present in the final state.

This approach is implemented on Tables 5.16, 5.17 and 5.15. In red, expected values are considered dangerous as they lie close to 1. Note that some values with 10^{-1} and 10^{-2} were marked in red for belonging to a decay able to pollute in both Prompt and Displaced regimes, but others with 10^{-1} were not, for example, $B^+ \to J/\psi\omega K^+$. The reason is that they have a branching fraction slightly lower than the expected for signal, and since the estimations were implemented in an already important conservative way, they do not pose a threat. Predictions also show that pollution affecting 6μ modes has a residual effect.

Mode	**Br**	f_s/f_u	$\mathbf{N_{sig}}$	**Prompt**	**Displaced**
$B_s^0 \to J/\psi(\mu^-\mu^+)\pi^+\pi^-\pi^+\pi^-$	$4.47 \cdot 10^{-6}$	4	$3.16 \cdot 10^4$	$1.86 \cdot 10^{-5}$	$2.68 \cdot 10^{-7}$
$B^0 \to J/\psi(\mu^-\mu^+)K^*(K^+\pi^-)\pi^+\pi^-$	$3.9336 \cdot 10^{-5}$	4	$1.1 \cdot 10^6$	$5.76 \cdot 10^{-4}$	$8.26 \cdot 10^{-6}$
$B^0 \to J/\psi(\mu^-\mu^+)\pi^+\pi^-\pi^+\pi^-$	$8.5824 \cdot 10^{-7}$	4	$2.42 \cdot 10^4$	$1.43 \cdot 10^{-5}$	$2.06 \cdot 10^{-7}$
$B^+ \to J/\psi(\mu^-\mu^+)K_s^0(\pi^+\pi^-)\pi^+\pi^-\pi^+$	$4.81 \cdot 10^{-7}$	4	$1.36 \cdot 10^4$	$8.03 \cdot 10^{-6}$	$1.15 \cdot 10^{-7}$

Table 5.15: Expected contamination for $B_s^0 \to 6\mu$ and $B^+ \to 6\mu K^+$. N_{sig} denotes the number of expected decays assuming the same efficiency as the signal channels. The Prompt and Displaced categories refine these efficiencies, applying a ballpark efficiency for PID and vetoes.

USC UNIVERSIDADE DE SANTIAGO DE COMPOSTELA

Mode	Br	f_s/f_u	N_{sig}	Prompt	Displaced
Prompt and Displaced					
$B_s^0 \to J/\psi(\mu^+\mu^-)\phi(K^+K^-)$	$2.99 \cdot 10^{-5}$	1	$1.80 \cdot 10^5$	$1.79 \cdot 10^{-2}$	$1.33 \cdot 10^{-3}$
$B_s^0 \to J/\psi(\mu^+\mu^-)\phi(\mu^+\mu^-)$	$1.76 \cdot 10^{-8}$	1	$1.06 \cdot 10^2$	$1.57 \cdot 10^{-1}$	$1.17 \cdot 10^{-2}$
$B_s^0 \to J/\psi(\mu^+\mu^-)K^+K^-$	$4.70 \cdot 10^{-5}$	1	$2.84 \cdot 10^5$	$9.69 \cdot 10^{-1}$	$3.80 \cdot 10^{-1}$
$B_s^0 \to J/\psi(\mu^+\mu^-)K_s^0(\pi^+\pi^-)$	$7.80 \cdot 10^{-7}$	1	$4.71 \cdot 10^3$	$8.93 \cdot 10^{-3}$	$3.50 \cdot 10^{-3}$
$B_s^0 \to \phi(K^+K^-)\mu^+\mu^-$	$4.00 \cdot 10^{-7}$	1	$2.41 \cdot 10^3$	$4.69 \cdot 10^{-3}$	$3.23 \cdot 10^{-3}$
$B_s^0 \to J/\psi(\mu^+\mu^-)\pi^+\pi^-$	$1.25 \cdot 10^{-5}$	1	$7.54 \cdot 10^4$	$1.43 \cdot 10^{-1}$	$5.61 \cdot 10^{-2}$
$B_s^0 \to J/\psi(\mu^+\mu^-)p\bar{p}$	$3.10 \cdot 10^{-7}$	1	$1.87 \cdot 10^3$	$2.12 \cdot 10^{-4}$	$8.31 \cdot 10^{-5}$
$B_s^0 \to \pi^+\pi^-\mu^+\mu^-$	$8.40 \cdot 10^{-8}$	1	$5.07 \cdot 10^2$	$1.89 \cdot 10^{-2}$	$1.89 \cdot 10^{-2}$
$B_s^0 \to \bar{D}^0(K^+\pi^-)\phi(\mu^+\mu^-)$	$3.33 \cdot 10^{-10}$	1	$2.01 \cdot 10^0$	$2.91 \cdot 10^{-6}$	$5.52 \cdot 10^{-7}$
$B^0 \to J/\psi(\mu^+\mu^-)p\bar{p}$	$2.68 \cdot 10^{-8}$	3.94	$6.37 \cdot 10^2$	$7.21 \cdot 10^{-5}$	$1.41 \cdot 10^{-3}$
$B^0 \to J/\psi(\mu^+\mu^-)K^+K^-$	$1.51 \cdot 10^{-7}$	3.94	$3.59 \cdot 10^3$	$1.23 \cdot 10^{-2}$	$4.81 \cdot 10^{-3}$
$B^0 \to J/\psi(\mu^+\mu^-)\pi^+\pi^-$	$1.99 \cdot 10^{-6}$	3.94	$4.73 \cdot 10^4$	$8.98 \cdot 10^{-2}$	$3.52 \cdot 10^{-2}$
$B^0 \to J/\psi(\mu^+\mu^-)K^*(K^+\pi^-)$	$2.44 \cdot 10^{-6}$	3.94	$5.80 \cdot 10^4$	$1.48 \cdot 10^{-1}$	$5.79 \cdot 10^{-2}$
$B^0 \to J/\psi(\mu^+\mu^-)\phi(K^+K^-)$	$5.60 \cdot 10^{-8}$	3.94	$1.33 \cdot 10^3$	$1.32 \cdot 10^{-4}$	$9.80 \cdot 10^{-6}$
$B^0 \to D^0(K^+K^-)\omega(\mu^+\mu^-)$	$7.77 \cdot 10^{-11}$	3.94	$1.85 \cdot 10^0$	$1.24 \cdot 10^{-4}$	$1.24 \cdot 10^{-4}$
$B^0 \to J/\psi(\mu^+\mu^-)K_s^0(\pi^+\pi^-)$	$1.79 \cdot 10^{-5}$	3.94	$4.25 \cdot 10^5$	$8.07 \cdot 10^{-1}$	$3.17 \cdot 10^{-1}$
$B^0 \to K^*(K^+\pi^-)\mu^+\mu^-$	$9.40 \cdot 10^{-7}$	3.94	$2.23 \cdot 10^4$	1.12	1.12
$B^0 \to D^{*-}(K^-\pi^+\pi^-)\mu^+\nu$	$9.35 \cdot 10^{-6}$	3.94	$2.22 \cdot 10^5$	$6.77 \cdot 10^{-2}$	$6.77 \cdot 10^{-2}$
Displaced					
$\Lambda_b \to p\pi^-\mu^+\mu^-$	$6.90 \cdot 10^{-8}$	2	$8.63 \cdot 10^2$	-	$7.84 \cdot 10^{-3}$
$\Lambda_b \to pK^-\mu^+\mu^-$	$2.60 \cdot 10^{-7}$	2	$3.25 \cdot 10^3$	-	$3.96 \cdot 10^{-2}$
$\Lambda_b \to \Lambda(p\pi^-)\phi(\mu^+\mu^-)$	$1.79 \cdot 10^{-9}$	2	$2.24 \cdot 10^1$	-	$2.24 \cdot 10^{-8}$
$\Lambda_b \to \Lambda(p\pi^-)\mu^+\mu^-$	$6.92 \cdot 10^{-7}$	2	$8.65 \cdot 10^3$	-	$7.86 \cdot 10^{-2}$
$\Lambda_b \to J/\psi(\mu^+\mu^-)p\pi^-$	$1.60 \cdot 10^{-6}$	2	$2.00 \cdot 10^4$	-	$3.64 \cdot 10^{-3}$

Table 5.16: Expected contamination for $B_s^0 \to 4\mu$. N_{sig} denotes the number of expected decays assuming the same efficiency as the signal channels. The Prompt and Diplaced categories refine these efficiencies, applying a ballpark efficiency for PID and vetoes.

USC UNIVERSIDADE DE SANTIAGO DE COMPOSTELA

Mode	Br	f_s/f_u	N_{sig}	Prompt	Displaced
Prompt and Displaced					
$B^+ \to J/\psi(\mu^+\mu^-)\phi(\mu^+\mu^-)K^+$	$8.43 \cdot 10^{-10}$	3.94	$1.60 \cdot 10^{1}$	$2.37 \cdot 10^{-2}$	$1.76 \cdot 10^{-3}$
$B^+ \to J/\psi(\mu^+\mu^-)\phi(K^+K^-)K^+$	$1.46 \cdot 10^{-6}$	3.94	$2.78 \cdot 10^{4}$	$2.75 \cdot 10^{-3}$	$2.05 \cdot 10^{-4}$
$B^+ \to J/\psi(\mu^+\mu^-)\mu^+\mu^-K^+$	$1.50 \cdot 10^{-5}$	3.94	$2.85 \cdot 10^{5}$	$1.45 \cdot 10^{4}$	$5.70 \cdot 10^{3}$
$B^+ \to \phi(K^+K^-)\mu^+\mu^-K^+$	$3.95 \cdot 10^{-8}$	3.94	$7.51 \cdot 10^{2}$	$1.46 \cdot 10^{-3}$	$2.77 \cdot 10^{-4}$
$B^+ \to J/\psi(\mu^+\mu^-)\pi^+\pi^-K^+$	$4.83 \cdot 10^{-5}$	3.94	$9.18 \cdot 10^{5}$	1.74	$6.83 \cdot 10^{-1}$
$B^+ \to J/\psi(\mu^+\mu^-)K^+K^-K^+$	$2.01 \cdot 10^{-6}$	3.94	$3.82 \cdot 10^{4}$	$1.30 \cdot 10^{-1}$	$5.11 \cdot 10^{-2}$
$B^+ \to J/\psi(\mu^+\mu^-)p\bar{p}\pi^+$	$2.98 \cdot 10^{-8}$	3.94	$5.67 \cdot 10^{2}$	$6.42 \cdot 10^{-5}$	$2.52 \cdot 10^{-5}$
$B^+ \to \mu^+\mu^-\pi^+\pi^-K^+$	$4.30 \cdot 10^{-7}$	3.94	$8.18 \cdot 10^{3}$	$3.04 \cdot 10^{-1}$	$3.04 \cdot 10^{-1}$
$B^+ \to J/\psi(\mu^+\mu^-)\omega(\mu^+\mu^-)K^+$	$2.75 \cdot 10^{-10}$	3.94	$5.23 \cdot 10^{0}$	$2.67 \cdot 10^{-1}$	$1.05 \cdot 10^{-1}$
$B^+ \to J/\psi(\mu^+\mu^-)\omega(p\bar{p})K^+$	$2.91 \cdot 10^{-7}$	3.94	$5.53 \cdot 10^{3}$	$6.27 \cdot 10^{-4}$	$2.46 \cdot 10^{-4}$
$B^+ \to J/\psi(\mu^+\mu^-)\eta(\mu^+\mu^-\gamma)K^+$	$2.20 \cdot 10^{-9}$	3.94	$4.18 \cdot 10^{1}$	2.13	$8.37 \cdot 10^{-1}$
$B^+ \to \phi(\mu K^-)\phi(\mu K^-)K^+$	$5.88 \cdot 10^{-10}$	3.94	$1.12 \cdot 10^{1}$	$6.30 \cdot 10^{-7}$	$2.26 \cdot 10^{-8}$
$B^+ \to J/\psi(\mu^+\mu^-\mu^+\mu^-)K^+$	$1.15 \cdot 10^{-9}$	3.94	$2.19 \cdot 10^{1}$	$2.19 \cdot 10^{1}$	$2.19 \cdot 10^{1}$
$B^+ \to \chi_{c1}(J/\psi(\mu^+\mu^-)\pi^+\pi^-)K^+$	$9.89 \cdot 10^{-7}$	3.94	$1.88 \cdot 10^{4}$	$3.57 \cdot 10^{-2}$	$1.40 \cdot 10^{-2}$
Displaced					
$B^+ \to J/\psi(\mu^+\mu^-)\Lambda_b(p\pi^-)p$	$5.57 \cdot 10^{-7}$	3.94	$1.06 \cdot 10^{4}$	-	$1.93 \cdot 10^{-3}$
$B^+ \to \Lambda_b(p\pi^-)\phi(\mu^+\mu^-)K^+$	$1.46 \cdot 10^{-10}$	3.94	$2.78 \cdot 10^{0}$	-	$1.53 \cdot 10^{-2}$

Table 5.17: Expected contamination for $B^+ \to 4\mu K^+$. N_{sig} denotes the number of expected decays assuming the same efficiency as the signal channels. The Prompt and Displaced categories refine these efficiencies, applying a ballpark efficiency for PID and vetoes.

5.6.2 Detailed background studies

As discussed in the previous section, those values which exceed the expected production limit are specifically discussed with the use of the standard LHCb simulation (Section 3.4.3), described in Table 5.2. A priori, not all the aforementioned configurations are dangerous in both prompt and displaced regimes. Despite this, to make the discussion as general as possible, channels with at least one value exceeding the barrier are studied in the three possible reconstruction categories: Prompt, Long-Lived and Downstream.

In order to study those specific channels, events are requested to survive reconstruction and full selection requirements, and to compute full efficiencies, the geometric acceptance is also taken into account. At this step, efficiencies are computed from simulation without any correction applied (which are partially added later). Full reconstructed events for all the categories can be observed in Figure 5.21 corresponding to $B_s^0 \to 4\mu$ Prompt channel and 5.22 for $B^+ \to 4\mu K^+$ Long-Lived.

For $B_s^0 \to 4\mu$, the distribution of the invariant mass throughout the full mass range indicates the presence of peaking structures in decays involving dipion processes, whereas in other decays like $B_s^0 \to J/\psi K^+K^-$ the change of mass hypothesis provokes the displacement of the peak within the low-mass sideband, where also partially-reconstruction decays are present. In displaced scenarios, $B_s^0 \to J/\psi\pi^+\pi^-$ continues to be the predominant source (provided the abundance of this decay) with part of these

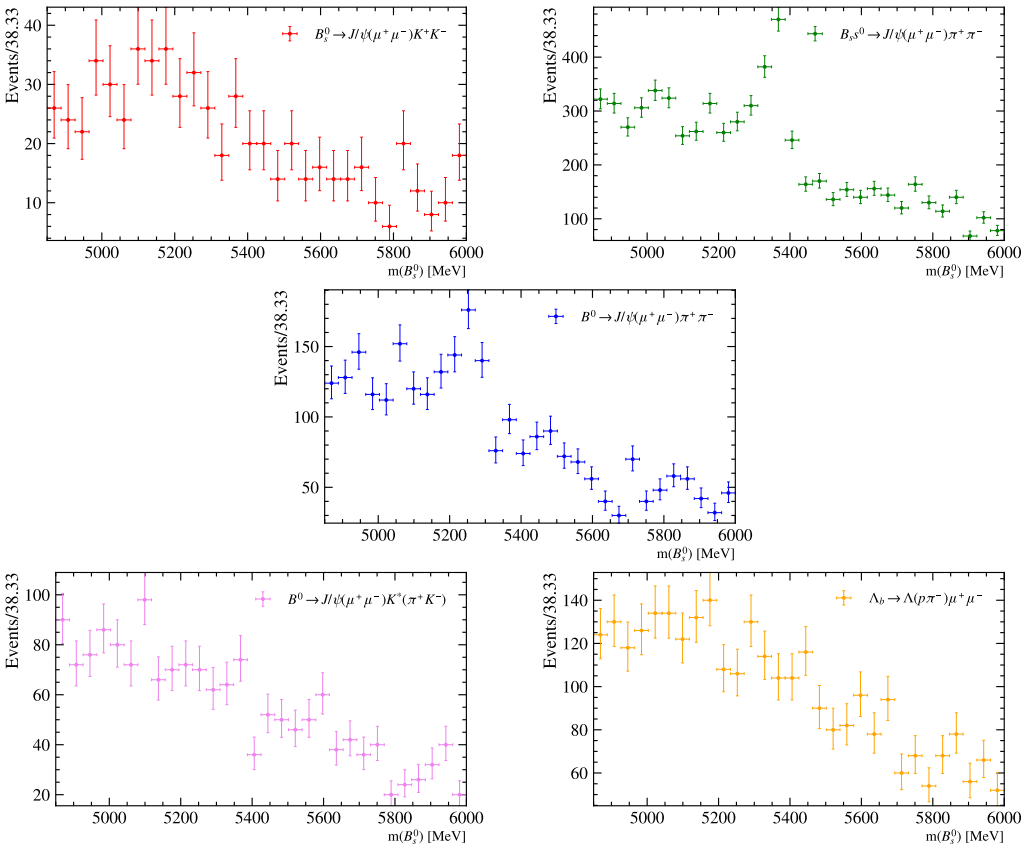


Figure 5.21: Surviving events after $B_s^0 \to 4\mu$ Prompt reconstruction

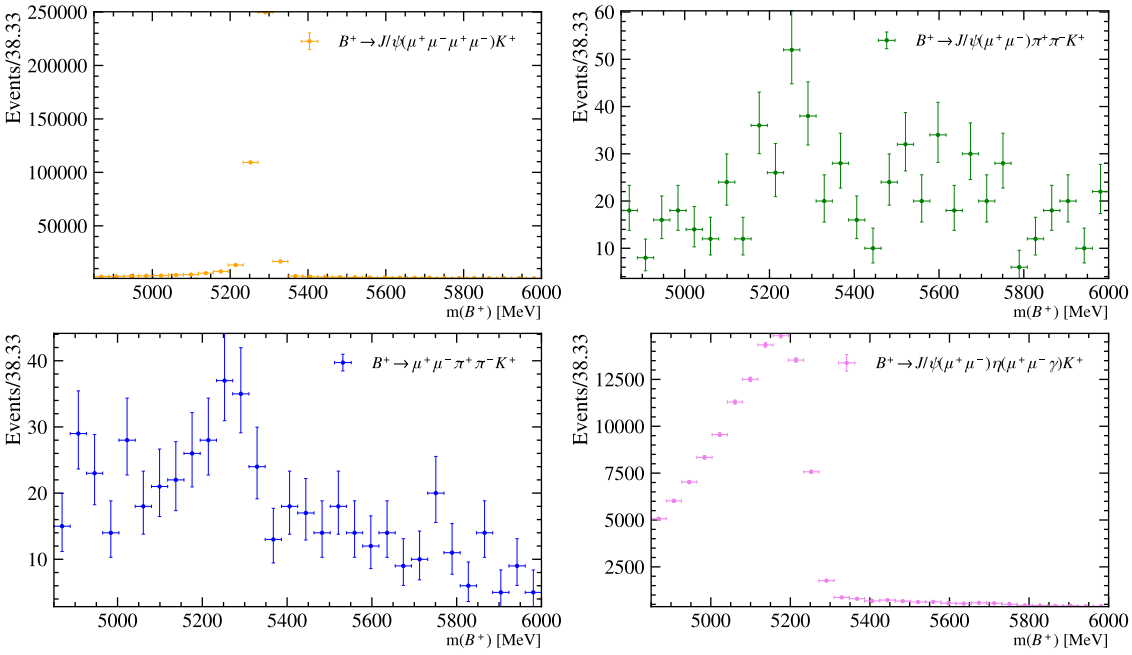


Figure 5.22: Surviving events after $B^+ \to 4\mu K^+$ displaced-LL reconstruction

events surviving the decay-time veto. Furthermore, the presence of $\Lambda_b \to \Lambda(p\pi^-)\mu^+\mu^-$ is not negligible any more. The outcome of the detailed study can be seen in Table 5.18.

Decay Mode	$\varepsilon_{\text{Prompt}}$	$N^{\text{Exp}}_{\text{Prompt}}$	$\varepsilon_{\text{Displaced-LL}}$	$N^{\text{Exp}}_{\text{Displaced-LL}}$	$\varepsilon_{\text{Displaced-LD}}$	$N^{\text{Exp}}_{\text{Displaced-LD}}$
			$B^0_s \to 4\mu$			
$B^0_s \to J/\psi(\mu^-\mu^+)K^+K^-$	$(0.0 \pm 2.06) \cdot 10^{-7}$	0.00 ± 5.8	$(0.0 \pm 2.06) \cdot 10^{-7}$	0.00 ± 5.8	$(0.0 \pm 2.1) \cdot 10^{-7}$	0.00 ± 5.8
$B^0_s \to J/\psi(\mu^-\mu^+)\pi^+\pi^-$	$(1.5 \pm 3.8) \cdot 10^{-8}$	0.11 ± 0.29	$(1.5 \pm 3.9) \cdot 10^{-8}$	0.11 ± 0.29	$(1.5 \pm 3.9) \cdot 10^{-8}$	0.11 ± 0.29
$B^0 \to J/\psi(\mu^-\mu^+)\pi^+\pi^-$	$(0.0 \pm 8.2) \cdot 10^{-8}$	0.00 ± 1.2	$(1.2 \pm 3.2) \cdot 10^{-8}$	0.18 ± 0.46	$(0.0 \pm 8.2) \cdot 10^{-8}$	0.000 ± 1.2
$B^0 \to J/\psi(\mu^-\mu^+)K^*(K^+\pi^-)$	$(0.0 \pm 1.23) \cdot 10^{-7}$	0.00 ± 0.18	$(1.9 \pm 4.8) \cdot 10^{-8}$	$(2.7 \pm 7.1) \cdot 10^{-2}$	$(1.9 \pm 4.8) \cdot 10^{-8}$	$(2.7 \pm 7.1) \cdot 10^{-2}$
$\Lambda_b \to \Lambda(p\pi^-)\mu^+\mu^-$	$(0.0 \pm 4.88) \cdot 10^{-7}$	$(0.0 \pm 7.6) \cdot 10^{-2}$	$(1.5 \pm 2.7) \cdot 10^{-7}$	$(2.3 \pm 4.3) \cdot 10^{-2}$	$(0.7 \pm 1.9) \cdot 10^{-7}$	$(1.2 \pm 3.0) \cdot 10^{-2}$
			$B^+ \to 4\mu K^+$			
$B^+ \to J/\psi(\mu^-\mu^+)\mu^+\mu^-K^+$	$(0.0 \pm 3.3) \cdot 10^{-7}$	0.00 ± 11.9	$(0.0 \pm 3.2) \cdot 10^{-7}$	0.0 ± 11.9	$(0.00 \pm 3.3) \cdot 10^{-7}$	0.0 ± 11.9
$B^+ \to J/\psi(\mu^-\mu^+)\pi^+\pi^-K^+$	$(0 \pm 4.9) \cdot 10^{-7}$	0.00 ± 57.6	$(0 \pm 4.9) \cdot 10^{-7}$	0.0 ± 57.6	$(0.0 \pm 4.9) \cdot 10^{-7}$	0.0 ± 57.6
$B^+ \to \mu^+\mu^-\pi^+\pi^-K^+$	$(1.5 \pm 2.2) \cdot 10^{-7}$	$(0.15 \pm 0.23) \cdot 10^{-2}$	$(0.0 \pm 3.3) \cdot 10^{-7}$	0.00 ± 0.34	$(0.0 \pm 3.3) \cdot 10^{-7}$	0.000 ± 0.34
$B^+ \to J/\psi(\mu^-\mu^+)\eta(\mu^+\mu^-\gamma)K^+$	$(6.8 \pm 1.5) \cdot 10^{-6}$	$(3.6 \pm 1.0) \cdot 10^{-2}$	$(4.9 \pm 1.3) \cdot 10^{-6}$	$(2.6 \pm 0.8) \cdot 10^{-2}$	$(0.0 \pm 3.3) \cdot 10^{-7}$	$(0.00 \pm 1.8) \cdot 10^{-3}$
$B^+ \to J/\psi(\mu^-\mu^+\mu^-\mu^+)K^+$	$(3.2 \pm 0.04) \cdot 10^{-3}$	9.1 ± 1.5	$(3.1 \pm 0.4) \cdot 10^{-5}$	$(8.4 \pm 1.5) \cdot 10^{-2}$	$(3.0 \pm 3.9) \cdot 10^{-7}$	$(0.8 \pm 1.1) \cdot 10^{-3}$

Table 5.18: Detailed study for background sources in the signal window, located at $(m_B - 75,\ m_B + 75)$ MeV.

Decay Mode	$\varepsilon_{\text{Prompt}}$	$N^{\text{Exp}}_{\text{Prompt}}$	$\varepsilon_{\text{Displaced-LL}}$	$N^{\text{Exp}}_{\text{Displaced-LL}}$	$\varepsilon_{\text{Displaced-LD}}$	$N^{\text{Exp}}_{\text{Displaced-LD}}$
			$B^0_s \to 4\mu$			
$B^0_s \to J/\psi(\mu^-\mu^+)K^+K^-$	$(0.0 \pm 1.1) \cdot 10^{-8}$	0.0 ± 0.3	$(0.6 \pm 1.6) \cdot 10^{-9}$	$(1.8 \pm 4.6) \cdot 10^{-2}$	$(0.0 \pm 4.1) \cdot 10^{-9}$	0.00 ± 0.11
			$B^+ \to 4\mu K^+$			
$B^+ \to J/\psi(\mu^-\mu^+)\mu^+\mu^-K^+$	$(0.0 \pm 1.6) \cdot 10^{-8}$	0.0 ± 0.08	$(0.0 \pm 6.6) \cdot 10^{-9}$	0.00 ± 0.03	$(0.0 \pm 6.6) \cdot 10^{-9}$	0.00 ± 0.03
$B^+ \to J/\psi(\mu^-\mu^+)\pi^+\pi^-K^+$	$(0.0 \pm 8.3) \cdot 10^{-10}$	$(0.0 \pm 9.7) \cdot 10^{-2}$	$(1.9 \pm 1.3) \cdot 10^{-9}$	(0.22 ± 0.15)	$(1.3 \pm 3.5) \cdot 10^{-10}$	$(1.5 \pm 4.1) \cdot 10^{-2}$

Table 5.19: Additional background estimates, applying mass and/or decay time effects after full selection. In this case, the full fit region $(4850, 6000)$ MeV is considered.

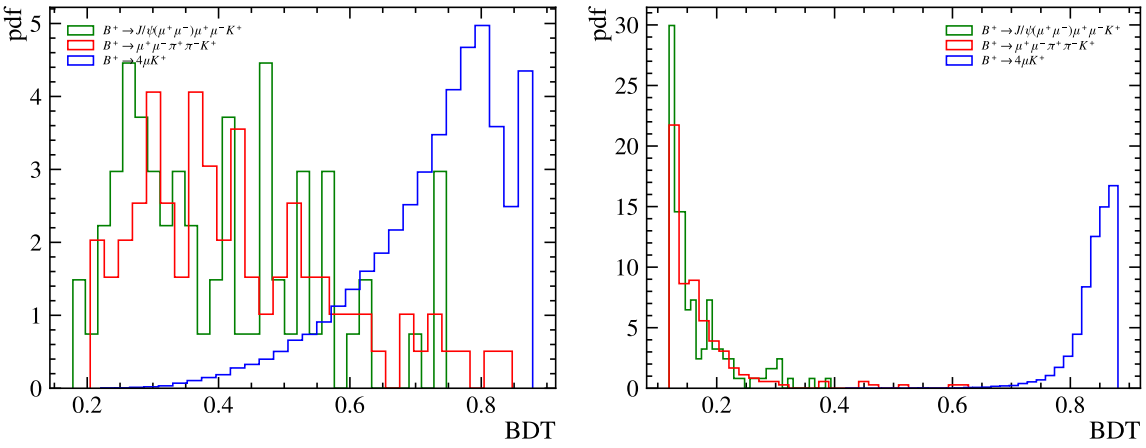


Figure 5.23: BDT response comparison for Prompt sources (left) and Displaced modes (right). It does not include a comparison for Down samples, since the efficiency of the BDT is the same as the Displaced Long reconstruction.

On the other hand, in $B^+ \to 4\mu K^+$, it may be assumed that the same arguments hold. Again, dipion processes dominate the spectrum and this time, contrary to the previous discussion, no obvious peaking structures appear in the area defined by the blinded region. Apart from that, partially-reconstructed decays also come into play, being $B^+ \to J/\psi(\mu^-\mu^+)\eta(\mu^+\mu^-\gamma)K^+$, a decay showing off especially in the Prompt and Displaced LL categories, but with a limited presence with Downstream reconstruction.

This study confirms the validity of the preliminary estimates, with a much finer adjustment as it takes into account reconstruction effects, multivariate classifier and particle identification variables. The most dangerous contamination comes from $B^+ \to J/\psi(4\mu)K^+$ decays, clearly being able to show up in the signal region. In order to veto this decay, a new cut can be introduced in the invariant mass $|m(4\mu) - 3090| < 100$ MeV with the same spirit that the prompt mass vetoes. This way, no pollution from this channel is expected.

Some additional checks are done for the channels $B_s^0 \to J/\psi(\mu^+\mu^-)K^+K^-$,$B^+ \to J/\psi(\mu^+\mu^-)\mu^+\mu^-K^+$ and $B^+ \to J/\psi(\mu^+\mu^-)\pi^+\pi^-K^+$ to demonstrate that, although the important uncertainty, the expected yield is compatible with zero:

The $B_s^0 \to J/\psi(\mu^+\mu^-)K^+K^-$ simulation is processed through the different stripping lines and the effect of intermediate mass (Prompt) and decay-time (Displaced) requirements is factorized out from the selection chain by applying the values from Equations 5.8 and 5.9. As seen in Table 5.19, this procedure is sufficient to definitely discard any contamination for B_s^0 modes.

For B^+ modes, the same approach determines that $B^+ \to J/\psi(\mu^+\mu^-)K^+K^-K^+$ is residual, whereas in $B^+ \to J/\psi(\mu^+\mu^-)\pi^+\pi^-K^+$ does not. A deeper test of the Selection chain reveals that the BDT is responsible for such high error bands, since no candidates survived. To demonstrate that the expected yield is compatible with zero, a mode with a similar topology, such as $B^+ \to \mu^+\mu^-\pi^+\pi^-K^+$, is used to demonstrate

an analogous BDT response (Figure 5.23). This value is therefore extrapolated to the aforementioned mode and also factorized out from the efficiency calculus. The result (also shown in Table 5.19) shows yields compatible with zero, finally reassuring that no peaking background sources are expected within the signal region.

5.6.3 Partially-reconstructed Backgrounds

Final comments on partially-reconstructed backgrounds are provided, with the most important effects coming from semileptonic decays and partial reconstruction in signal mode events.

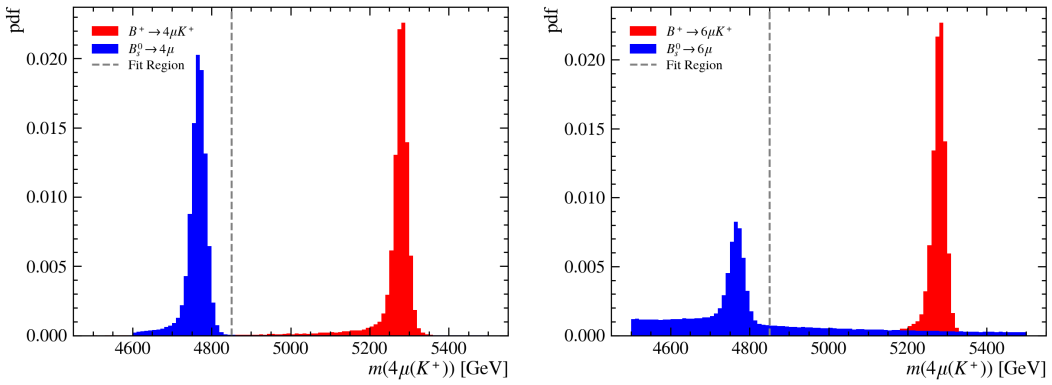


Figure 5.24: Partial reconstruction from high-multiplicity modes with 1 ps samples for $B^+ \to 4\mu K^+$ with $m_{a_1} = 2.00$ GeV and $m_{a_2} = 2.75$ GeV (right) and $B^+ \to 6\mu K^+$ with $m_{a_1} = 1.25$ GeV and $m_{a_2} = 3.50$ GeV.

First, with the ballpark estimations on hand, the extent of contamination from semileptonic processes can be determined. Decays of semileptonic origin have high branching fractions and lead to potentially high background yields. In these types of decays, losing the neutrino could lead to a 4-body vertex reconstruction[2], imitating a $B_s^0 \to 4\mu$ decay. One example would be the decay $B^0 \to D^-\mu^+\nu_\mu$, with $D^- \to K^-\pi^+\pi^-$. With such a production, despite expecting a yield of $\sim 10^5$ events, the misID affecting kaons and pions reduces it to $\sim 10^{-2}$, so they would not pose a threat. This affirmation can be translated into the rest of the family of decays. Above that, the topology of the decay would suffer from the action of the strong vertexing and trigger requirements of the selection.

Second, the partial reconstruction of high-multiplicity signal modes might lead to the appearance of 4μ modes as peaking backgrounds in 6μ samples. In order to check this effect, stripping lines of 4μ modes are run over MC samples from 6μ cases, and the B meson mass is recalculated. This effect, a priori, could only be critical in Prompt samples, since it has been confirmed that partial reconstruction of very displaced samples locates below the current signal sensitivity after applying the full selection. In

[2]Note that under this assumption, the B mass distribution would be smeared out from the signal region, affecting the low-mass sideband.

Figure 5.24, B mass distributions over the full (red) and partial (blue) reconstruction are shown. As appreciated, the lack of one charged track is enough to displace the core of the distribution out of the full fit region, leaving a pure combinatorial component falling exponentially but never overlapping with the full reconstructed signal.

5.7 Normalization and Sensitivities

The signal branching fractions are normalised to the resonant decay $B_s^0 \to J/\psi(\mu^+\mu^-)\phi(\mu^+\mu^-)$ through the relation:

$$\mathcal{B}(\text{sig}) = \underbrace{\frac{\mathcal{B}_{\text{norm}}}{N_{\text{norm}}} \times \frac{\epsilon_{\text{norm}}}{\epsilon_{\text{sig}}} \times \frac{f_{\text{norm}}}{f_{\text{sig}}}}_{\alpha_{\text{sig}}} \times N_{\text{sig}} \tag{5.12}$$

where the subscripts "sig" and "norm" refer to the signal and normalisation modes, N is the yield, ϵ is the efficiency and f is the fragmentation fraction.

The normalisation factor α_{sig} effectively sets the scale at which $\mathcal{B}(\text{sig})$ can be measured if signal candidates are observed. N_{norm} is determined from a fit to the invariant mass distribution of the normalisation mode, ϵ_{norm} and ϵ_{sig} are determined from simulation and $\mathcal{B}_{\text{norm}}$ is determined from existing BFs of intermediate resonances. The BFs of the aforementioned resonances are:

$$\mathcal{B}(B_s^0 \to J/\psi\phi) = (1.081 \pm 0.032 \pm 0.037) \times 10^{-3} \tag{5.13a}$$

$$\mathcal{B}(J/\psi \to \mu^+\mu^-) = (5.961 \pm 0.033) \times 10^{-2} \tag{5.13b}$$

$$\mathcal{B}(\phi \to \mu^+\mu^-) = (2.860 \pm 0.190) \times 10^{-4} \tag{5.13c}$$

where $\mathcal{B}(B_s^0 \to J/\psi\phi)$ has been taken from an LHCb measurement [281] and $\mathcal{B}(J/\psi \to \mu^+\mu^-)$ and $\mathcal{B}(\phi \to \mu^+\mu^-)$ BFs are PDG values [46]. $\mathcal{B}_{\text{norm}}$ is therefore given by

$$\begin{aligned} \mathcal{B}_{\text{norm}} &= \mathcal{B}(B_s^0 \to J/\psi\phi) \times \mathcal{B}(J/\psi \to \mu^+\mu^-) \times \mathcal{B}(\phi \to \mu^+\mu^-) \\ &= (1.736 \pm 0.143) \times 10^{-8}. \end{aligned} \tag{5.14}$$

The yield N_{norm} and efficiency ϵ_{norm} must also be determined. N_{norm} is obtained by performing a fit to the invariant mass distribution using data, where the full normalisation mode selection is applied, and ϵ_{norm} is determined using MC. Subsequent sections outline the procedures for obtaining these values.

5.7.1 Normalisation mode yield

USC UNIVERSIDADE DE SANTIAGO

The yield of the normalisation mode is determined from a fit to the invariant mass distribution, where the full normalisation mode selection is applied. Before fitting to the data, an unbinned maximum-likelihood fit is performed on the MC to determine

the expected form of the signal peak. The MC is reweighted using the corrections discussed in section 5.4, and the proportion of each year's MC in the combined sample is also weighted considering $\mathcal{L}_{\text{int}}$ and $\sigma_{b\bar{b}}$ for each year:

$$w_y = \frac{1}{N^y_{gen}} \frac{\left(\mathcal{L}^y_{int}\right)}{\sum_{y=2016}^{2018} \left[\left(\mathcal{L}^y_{int}\right)\right]} \sum_{y=2016}^{2018} N^y_{gen}. \tag{5.15}$$

The fit to data is composed of the sum of a Double Crystal Ball PDF for the signal and an exponential PDF to model the combinatorial background. Results of the fit to MC are taken into account through Gaussian constraints for both tail parameters (α and n), whereas μ and σ are allowed to float. Figure 5.25 shows the fit to 2016-2018 data and the values of the optimised model parameters. The fitted yield of normalisation candidates is $N_{\text{norm}} = 145 \pm 13$.

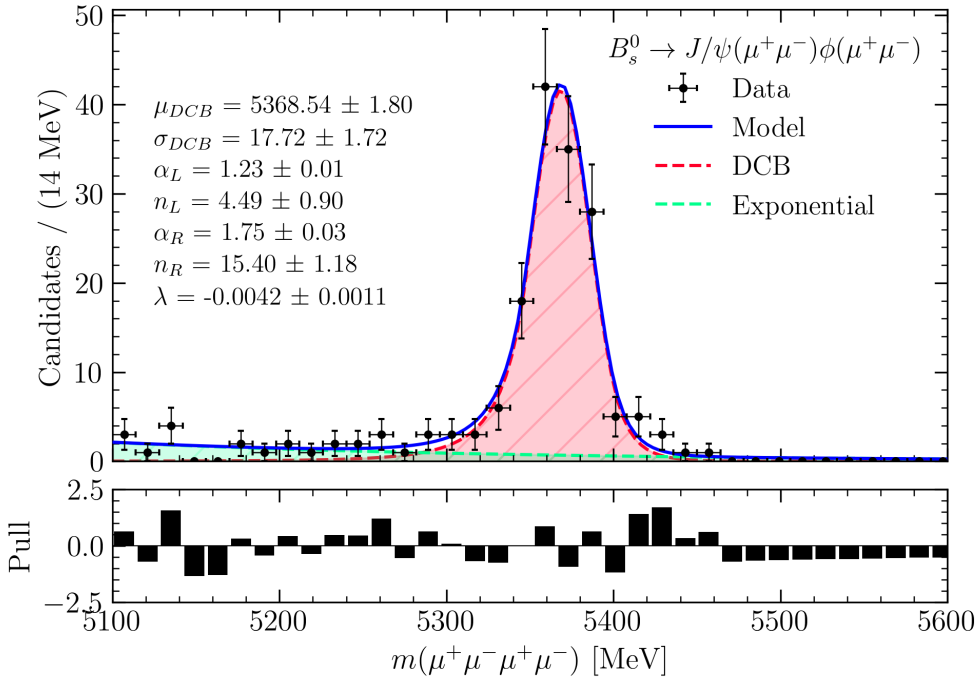


Figure 5.25: Fit to invariant mass distribution of a combined sample of 2016-2018 $B^0_s \to J/\psi(\mu^+\mu^-)\phi(\mu^+\mu^-)$ data that passes the full selection.

5.7.2 Efficiency calculation

Efficiencies are computed according to a binomial distribution with weighted events, being the efficiency [283]:

$$\varepsilon = \frac{W_1}{W_1 + W_2} \tag{5.16}$$

where $W_1 = \sum_{i=1}^{\text{passed}} w_i$ and $W_2 = \sum_{i=1}^{\text{total}} w_i - W_1$. At the same time, it can be factorised, accounting for different selection stages:

$$\varepsilon = \varepsilon_{\text{geo}} \times \varepsilon_{\text{presel|geo}} \times \varepsilon_{\text{trig|presel}} \times \varepsilon_{\text{sel|trig}} \tag{5.17}$$

where ε_{geo} is the detector geometrical acceptance efficiency, $\varepsilon_{\text{presel|geo}}$ is the preselection efficiency for events within the detector acceptance, $\varepsilon_{\text{trig|presel}}$ is the efficiency of preselection (Stripping) events passing the trigger selection and $\varepsilon_{\text{sel|trig}}$ is the efficiency of events passing the full selection given the trigger selection. Therefore, the efficiency can be expressed as

$$\varepsilon = \varepsilon_{\text{geo}} \times \frac{\sum_{\text{presel}} w_{\text{gen}}}{\sum_{\text{gen}} w_{\text{gen}}} \times \frac{\sum_{\text{trig}} w_{\text{gen}} w_{\text{L0}}}{\sum_{\text{presel}} w_{\text{gen}}} \times \frac{\sum_{\text{sel}} w_{\text{gen}} w_{\text{L0}} w_{\text{rec}}}{\sum_{\text{trig}} w_{\text{gen}} w_{\text{L0}} w_{\text{rec}}} \tag{5.18}$$

where w_{gen}, $w_{\text{L0}} = w_{\text{L0Muon}}$ and w_{rec} refer to generator-, trigger- and reconstruction-level weights, the sum suffix "gen" refers to generator-level simulation before reconstruction and the other subscripts are as previously defined.

Uncertainties for efficiencies are calculated directly from error propagation in 5.16:

$$\sigma_\varepsilon = \sqrt{\frac{W_1^2 \sigma_{W_2}^2 + W_2^2 \sigma_{W_1}^2}{(W_1 + W_2)^4}} \tag{5.19}$$

where

$$\sigma_{W_1}^2 = \sum_{i=1}^{\text{passed}} w^2 \qquad \sigma_{W_2}^2 = \sum_{i=1}^{\text{total}} w_i^2 - \sigma_{W_1}^2. \tag{5.20}$$

Efficiencies are calculated for each year separately, then a weighted average is used to calculate the average efficiency $\bar{\varepsilon}$ such that

$$\bar{\epsilon}_{(2016-2018)} = \frac{\sum_{y=2016}^{2018} \mathcal{L}_{\text{int}}^y \epsilon_y}{\sum_{y=2016}^{2018} \mathcal{L}_{\text{int}}^y} \tag{5.21}$$

where $\mathcal{L}_{\text{int}}$ in each year is used to weight the efficiencies (Table 5.1). No appreciable difference is observed in the efficiencies between different years.

All efficiencies are calculated using simulation samples with simulation corrections applied (see Section 5.4). For the normalisation mode, the average efficiency over 2016-2018 is $\epsilon_{\text{norm}} = 1.223 \pm 0.004$ %. The efficiencies for each signal decay mode sample can be found in Tables 5.20-5.24.

USC UNIVERSIDADE DE SANTIAGO DE COMPOSTELA

Prompt PHSP

Decay Mode	Total Efficiency (%)
$B_s^0 \to 4\mu$	$(4.477 \pm 0.027) \times 10^{-1}$
$B^+ \to 4\mu K^+$	$(2.376 \pm 0.013) \times 10^{-1}$
$B_s^0 \to 6\mu$	$(9.535 \pm 0.033) \times 10^{-2}$
$B^+ \to 6\mu K^+$	$(2.957 \pm 0.016) \times 10^{-2}$

Table 5.20: Total efficiencies for prompt PHSP samples, including the full selection requirements. Efficiencies are averaged across all data-taking years.

Hierarchical $B_s^0 \to 4\mu$

$m(a_1)$, $m(a_2)$ [GeV]	τ_{a_1} [ps]	Prompt (%)	LL (%)	LD (%)
0.25, 0.40	0	$(3.205 \pm 0.015) \times 10^{-1}$		
0.25, 0.40	1		$(5.082 \pm 0.059) \times 10^{-2}$	
0.25, 0.40	10		$(1.945 \pm 0.034) \times 10^{-2}$	$(1.167 \pm 0.008) \times 10^{-1}$
0.25, 0.40	100		$(2.519 \pm 0.121) \times 10^{-3}$	$(6.489 \pm 0.059) \times 10^{-2}$
0.25, 0.40	1000		$(4.613 \pm 0.602) \times 10^{-4}$	$(1.277 \pm 0.030) \times 10^{-2}$
2.00, 2.75	0	$(8.271 \pm 0.033) \times 10^{-1}$		
2.00, 2.75	1		$(3.524 \pm 0.016) \times 10^{-1}$	
2.00, 2.75	10		$(3.871 \pm 0.016) \times 10^{-1}$	$(1.789 \pm 0.031) \times 10^{-2}$
2.00, 2.75	100		$(9.448 \pm 0.078) \times 10^{-2}$	$(7.981 \pm 0.070) \times 10^{-2}$
2.00, 2.75	1000		$(1.097 \pm 0.025) \times 10^{-2}$	$(1.420 \pm 0.028) \times 10^{-2}$

Table 5.21: Total efficiencies for $B_s^0 \to 4\mu$, including the stripping, reconstruction, trigger, offline and BDT selection requirements. Efficiencies are averaged across all data-taking years.

Hierarchical $B^+ \to 4\mu K^+$

$m(a_1)$, $m(a_2)$ [GeV]	τ_{a_1} [ps]	Prompt (%)	LL (%)	LD (%)
0.25, 0.40	0	$(1.845 \pm 0.010) \times 10^{-1}$		
0.25, 0.40	1		$(6.526 \pm 0.188) \times 10^{-3}$	
0.25, 0.40	10		$(3.114 \pm 0.133) \times 10^{-3}$	$(1.610 \pm 0.071) \times 10^{-3}$
0.25, 0.40	100		$(4.579 \pm 0.433) \times 10^{-4}$	$(1.152 \pm 0.055) \times 10^{-3}$
0.25, 0.40	1000		$(5.185 \pm 1.578) \times 10^{-5}$	$(2.371 \pm 0.271) \times 10^{-4}$
2.00, 2.75	0	$(2.448 \pm 0.013) \times 10^{-1}$		
2.00, 2.75	1		$(7.844 \pm 0.069) \times 10^{-2}$	
2.00, 2.75	10		$(9.238 \pm 0.163) \times 10^{-2}$	$(1.015 \pm 0.053) \times 10^{-3}$
2.00, 2.75	100		$(2.377 \pm 0.038) \times 10^{-2}$	$(5.403 \pm 0.141) \times 10^{-3}$
2.00, 2.75	1000		$(2.457 \pm 0.105) \times 10^{-3}$	$(9.827 \pm 0.533) \times 10^{-4}$

Table 5.22: Total efficiencies for $B^+ \to 4\mu K^+$, including the stripping, reconstruction, trigger, offline and BDT selection requirements. Efficiencies are averaged across all data-taking years.

USC UNIVERSIDADE DE SANTIAGO DE COMPOSTELA

Hierarchical $B_s^0 \to 6\mu$

$m(a_1)$, $m(a_2)$ [GeV]	τ_{a_1} [ps]	Prompt (%)	LLL (%)	LLD (%)	LDD (%)
0.50, 1.50	0	$(6.688 \pm 0.026) \times 10^{-1}$			
0.50, 1.50	1		$(1.783 \pm 0.010) \times 10^{-1}$		
0.50, 1.50	10		$(5.852 \pm 0.058) \times 10^{-2}$	$(3.858 \pm 0.046) \times 10^{-2}$	$(6.341 \pm 0.157) \times 10^{-3}$
0.50, 1.50	100		$(2.677 \pm 0.361) \times 10^{-4}$	$(2.059 \pm 0.104) \times 10^{-3}$	$(2.728 \pm 0.110) \times 10^{-3}$
1.25, 3.50	0	$(1.339 \pm 0.005) \times 10^{0}$			
1.25, 3.50	1		$(2.362 \pm 0.012) \times 10^{-1}$		
1.25, 3.50	10		$(1.025 \pm 0.008) \times 10^{-1}$	$(1.021 \pm 0.024) \times 10^{-2}$	$(3.680 \pm 0.356) \times 10^{-4}$
1.25, 3.50	100		$(1.030 \pm 0.073) \times 10^{-3}$	$(1.032 \pm 0.072) \times 10^{-3}$	$(3.318 \pm 0.342) \times 10^{-4}$

Table 5.23: Total efficiencies for $B_s^0 \to 6\mu$, including the stripping, reconstruction, trigger and offline selection requirements. Efficiencies are averaged across all data-taking years.

Hierarchical $B^+ \to 6\mu K^+$

$m(a_1)$, $m(a_2)$ [GeV]	τ_{a_1} [ps]	Prompt (%)	LLL (%)	LLD (%)	LDD (%)
0.50, 1.50	0	$(2.303 \pm 0.014) \times 10^{-1}$			
0.50, 1.50	1		$(7.642 \pm 0.064) \times 10^{-2}$		
0.50, 1.50	10		$(2.977 \pm 0.042) \times 10^{-2}$	$(7.249 \pm 0.175) \times 10^{-3}$	$(1.569 \pm 0.076) \times 10^{-3}$
0.50, 1.50	100		$(2.766 \pm 0.396) \times 10^{-4}$	$(5.308 \pm 0.456) \times 10^{-4}$	$(1.334 \pm 0.068) \times 10^{-3}$
1.25, 3.50	0	$(2.450 \pm 0.016) \times 10^{-1}$			
1.25, 3.50	1		$(5.070 \pm 0.052) \times 10^{-2}$		
1.25, 3.50	10		$(2.148 \pm 0.035) \times 10^{-2}$	$(7.484 \pm 0.517) \times 10^{-4}$	$(6.419 \pm 1.543) \times 10^{-5}$
1.25, 3.50	100		$(2.228 \pm 0.337) \times 10^{-4}$	$(8.816 \pm 1.632) \times 10^{-5}$	$(8.005 \pm 1.451) \times 10^{-5}$

Table 5.24: Total efficiencies for $B^+ \to 6\mu K^+$, including the stripping, reconstruction, trigger and offline selection requirements. Efficiencies are averaged across all data-taking years.

The behaviour of the tabulated values can be understood by considering several factors. First, when comparing similar mass points across different channels, it is observed that the higher the final-state multiplicity, the less momentum is available for each muon. This results in a stronger suppression from the L0 muon trigger, which imposes a transverse momentum threshold. Within the same decay mode, the same effect explains the differences between low- and high-mass scalar configurations, with the suppression becoming more pronounced as the scalar masses decrease.

Additional effects further enhance the differences between mass points. In the 4μ modes, the BDT selection has less discriminating power for low-mass configurations, leading to reduced efficiencies. In the 6μ modes, the resolution cut plays a dominant role: lower scalar masses correspond to smaller available phase space, which increases the rejection of events at this stage.

Finally, the evolution of the different reconstruction categories with the scalar lifetime must also be noted. This behaviour is discussed in detail in Section 5.7.4, where visual efficiency maps are provided.

5.7.3 Normalisation Factors

As mentioned at the beginning of this section, the normalisation factor α_{sig} gives the single event sensitivity and sets the scale at which $\mathcal{B}(\text{sig})$ can be measured if events are observed. Such sensitivities can be found in Tables 5.25-5.29.

Prompt PHSP

Decay Mode	Normalisation Factor
$B_s^0 \to 4\mu$	$(3.287 \pm 0.548) \times 10^{-10}$
$B^+ \to 4\mu K^+$	$(1.573 \pm 0.267) \times 10^{-10}$
$B_s^0 \to 6\mu$	$(1.544 \pm 0.257) \times 10^{-10}$
$B^+ \to 6\mu K^+$	$(1.264 \pm 0.214) \times 10^{-10}$

Table 5.25: Normalisation factors (i.e., sensitivity reach) for prompt PHSP modes, including the full selection requirements.

USC UNIVERSIDADE DE SANTIAGO DE COMPOSTELA

Hierarchical $B_s^0 \to 4\mu$

$m(a_1)$, $m(a_2)$ [GeV]	τ_{a_1} [ps]	Prompt	LL	LD
0.25, 0.40	0	$(4.592 \pm 0.766) \times 10^{-10}$		
0.25, 0.40	1		$(2.896 \pm 0.484) \times 10^{-9}$	
0.25, 0.40	10		$(7.566 \pm 1.268) \times 10^{-9}$	$(1.261 \pm 0.210) \times 10^{-9}$
0.25, 0.40	100		$(5.844 \pm 1.014) \times 10^{-8}$	$(2.268 \pm 0.379) \times 10^{-9}$
0.25, 0.40	1000		$(3.191 \pm 0.675) \times 10^{-7}$	$(1.153 \pm 0.194) \times 10^{-8}$
2.00, 2.75	0	$(1.780 \pm 0.297) \times 10^{-10}$		
2.00, 2.75	1		$(4.177 \pm 0.696) \times 10^{-10}$	
2.00, 2.75	10		$(3.803 \pm 0.634) \times 10^{-10}$	$(8.230 \pm 1.379) \times 10^{-9}$
2.00, 2.75	100		$(1.558 \pm 0.260) \times 10^{-9}$	$(1.844 \pm 0.308) \times 10^{-9}$
2.00, 2.75	1000		$(1.341 \pm 0.226) \times 10^{-8}$	$(1.037 \pm 0.174) \times 10^{-8}$

Table 5.26: Normalisation Factors α_{sig} for hierarchical $B_s^0 \to 4\mu$ samples.

Hierarchical $B^+ \to 4\mu K^+$

$m(a_1)$, $m(a_2)$ [GeV]	τ_{a_1} [ps]	Prompt	LL	LD
0.25, 0.40	0	$(2.025 \pm 0.343) \times 10^{-10}$		
0.25, 0.40	1		$(5.727 \pm 0.985) \times 10^{-9}$	
0.25, 0.40	10		$(1.200 \pm 0.210) \times 10^{-8}$	$(2.321 \pm 0.407) \times 10^{-8}$
0.25, 0.40	100		$(8.161 \pm 1.584) \times 10^{-8}$	$(3.244 \pm 0.571) \times 10^{-8}$
0.25, 0.40	1000		$(7.207 \pm 2.510) \times 10^{-7}$	$(1.576 \pm 0.322) \times 10^{-7}$
2.00, 2.75	0	$(1.527 \pm 0.259) \times 10^{-10}$		
2.00, 2.75	1		$(4.764 \pm 0.809) \times 10^{-10}$	
2.00, 2.75	10		$(4.045 \pm 0.689) \times 10^{-10}$	$(3.681 \pm 0.652) \times 10^{-8}$
2.00, 2.75	100		$(1.572 \pm 0.268) \times 10^{-9}$	$(6.917 \pm 1.186) \times 10^{-9}$
2.00, 2.75	1000		$(1.521 \pm 0.266) \times 10^{-8}$	$(3.803 \pm 0.677) \times 10^{-8}$

Table 5.27: Normalisation Factors α_{sig} for hierarchical $B^+ \to 4\mu K^+$ samples.

USC UNIVERSIDADE DE SANTIAGO DE COMPOSTELA

Hierarchical $B_s^0 \to 6\mu$

$m(a_1)$, $m(a_2)$ [GeV]	τ_{a_1} [ps]	Prompt	LLL	LLD	LDD
0.50, 1.50	0	$(2.201 \pm 0.367) \times 10^{-10}$			
0.50, 1.50	1		$(8.255 \pm 1.376) \times 10^{-10}$		
0.50, 1.50	10		$(2.515 \pm 0.420) \times 10^{-9}$	$(3.815 \pm 0.637) \times 10^{-9}$	$(2.321 \pm 0.391) \times 10^{-8}$
0.50, 1.50	100		$(5.498 \pm 1.179) \times 10^{-7}$	$(7.150 \pm 1.245) \times 10^{-8}$	$(5.395 \pm 0.925) \times 10^{-8}$
1.25, 3.50	0	$(1.099 \pm 0.183) \times 10^{-10}$			
1.25, 3.50	1		$(6.233 \pm 1.039) \times 10^{-10}$		
1.25, 3.50	10		$(1.435 \pm 0.239) \times 10^{-9}$	$(1.441 \pm 0.242) \times 10^{-8}$	$(3.999 \pm 0.771) \times 10^{-7}$
1.25, 3.50	100		$(1.428 \pm 0.258) \times 10^{-7}$	$(1.427 \pm 0.258) \times 10^{-7}$	$(4.436 \pm 0.869) \times 10^{-7}$

Table 5.28: Normalisation Factors α_{sig} for hierarchical $B_s^0 \to 6\mu$ samples.

Hierarchical $B^+ \to 6\mu K^+$

$m(a_1)$, $m(a_2)$ [GeV]	τ_{a_1} [ps]	Prompt	LLL	LLD	LDD
0.50, 1.50	0	$(1.623 \pm 0.275) \times 10^{-10}$			
0.50, 1.50	1		$(4.890 \pm 0.830) \times 10^{-10}$		
0.50, 1.50	10		$(1.255 \pm 0.214) \times 10^{-9}$	$(5.155 \pm 0.883) \times 10^{-9}$	$(2.382 \pm 0.420) \times 10^{-8}$
0.50, 1.50	100		$(1.351 \pm 0.300) \times 10^{-7}$	$(7.041 \pm 1.338) \times 10^{-8}$	$(2.802 \pm 0.496) \times 10^{-8}$
1.25, 3.50	0	$(1.526 \pm 0.259) \times 10^{-10}$			
1.25, 3.50	1		$(7.372 \pm 1.252) \times 10^{-10}$		
1.25, 3.50	10		$(1.740 \pm 0.296) \times 10^{-9}$	$(4.993 \pm 0.914) \times 10^{-8}$	$(5.822 \pm 1.713) \times 10^{-7}$
1.25, 3.50	100		$(1.677 \pm 0.381) \times 10^{-7}$	$(4.239 \pm 1.064) \times 10^{-7}$	$(4.668 \pm 1.159) \times 10^{-7}$

Table 5.29: Normalisation Factors α_{sig} for hierarchical $B^+ \to 6\mu K^+$ samples.

5.7.4 Efficiency extrapolation in time

Efficiency values already presented correspond to the full selection requirements applied over events generated with a fixed lifetime: the so-called seeds. For extrapolating that sensitivity across the decay time of the scalars, a reweighting algorithm is introduced on top of the existing weights to determine the shape of the efficiency curves.

To model this dependence, the true decay time of the long-lived particle (both at generation and reconstruction level) is used to add per-event weights of the form:

$$\omega_i = \frac{\tau_{\text{Gen}}}{\tau_{\text{Tar}}} \times \frac{e^{-t_i/\tau_{\text{Tar}}}}{e^{-t_i/\tau_{\text{Gen}}}} \tag{5.22}$$

where t_i is the true decay time of the scalar, τ_{Gen} is the lifetime with which the simulation sample was generated, and τ_{Tar} is the target lifetime. The prefactor $\frac{\tau_{\text{Gen}}}{\tau_{\text{Tar}}}$ ensures that the total sum of weights is normalised to unity.

For each sample, the reweighting comprises a scan across the lowest seed point (1 ps) until the highest (1000 ps for 4μ modes and 100 ps for the 6μ ones), computing the full selection efficiency with the weights $\omega_t \times \omega_{\text{tot}}$, where ω_t are the new weights computed from Equation 5.22 and ω_{tot} the weights computed in Section 5.4.

Once efficiency curves are obtained for each sample, a weighted average is performed to avoid acceptance saturation. The latter stands for the fact that, at certain $t_{scan} > t_{gen}$, because of the corresponding exponential law for lifetimes, the number of events with lifetime compressed by the generation drops to zero, and therefore the efficiency turns constant.

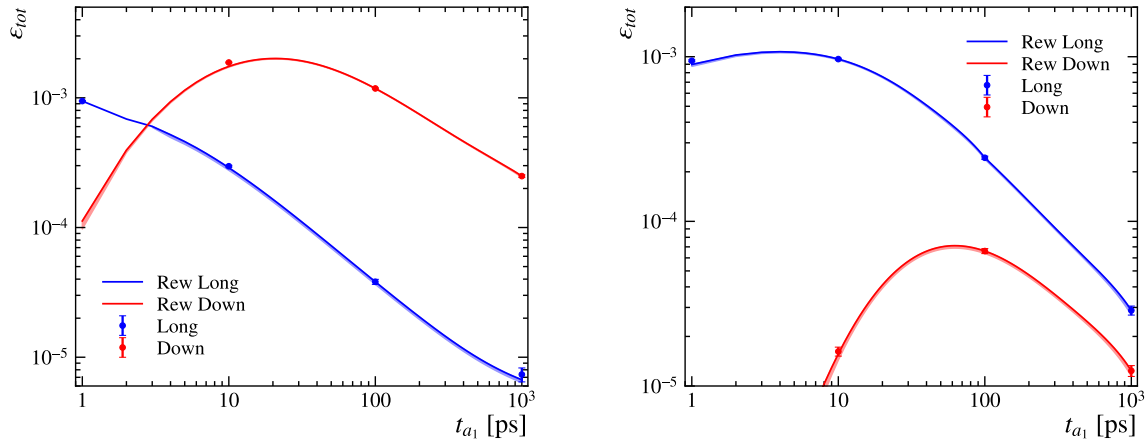
For the weighted average, the finite elements method [284] is performed. In that sense, in between two generation seeds, i.e. $g_1 < t_{scan} < g_2$, the corresponding efficiency would lie as $\varepsilon_t = w_1\varepsilon_t^{g_1} + w_2\varepsilon_t^{g_2}$, where the corresponding weights are:

$$\begin{aligned} w_1 &= 1 - f \\ w_2 &= f = \frac{t - g_1}{g_2 - g1} \end{aligned} \tag{5.23}$$

An additional remark has to be taken into account, though. Both mass points (for each case) define different kinematic regimes: for the lowest, the lower the transverse momentum, the higher the longitudinal boost across the propagation axis, which makes the lifetimes measured in the laboratory frame artificially high. This translates into the fact that, for $(m1, m2) = (0.25, 0.40)$ GeV and for $(m1, m2) = (0.50, 1.50)$ GeV modes, the average has to be done counting all available lifetimes whereas for the rest, the 100 ps sample is enough to effectively contain a representative amount of events for every scan point below its value.

USC UNIVERSIDADE DE SANTIAGO DE COMPOSTELA

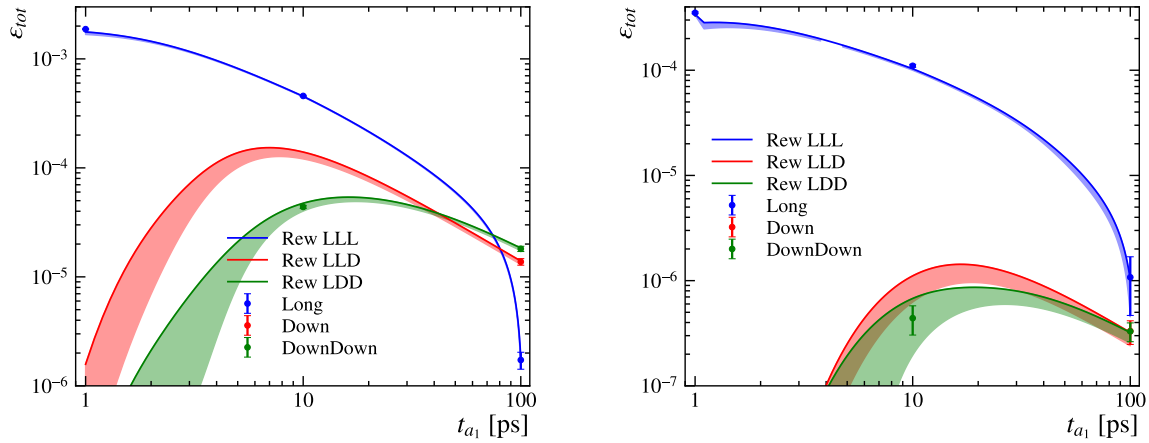
Representative examples can be found in Figure 5.26 and 5.27, for 4μ and 6μ modes, respectively. Results for the different reconstruction categories are included, namely



(a) $B_s^0 \to 4\mu$ (b) $B^+ \to 4\mu K^+$

Figure 5.26: Extrapolation of sensitivity results for 4μ modes. Left: low-mass configuration $(m_{a_1}, m_{a_2}) = (0.25, 0.40)$ GeV. Right: high-mass configuration $(m_{a_1}, m_{a_2}) = (2.00, 2.75)$ GeV.

LL/LLL (blue), LD/LLD (red) and LDD (green). Across the lifetime scan, dedicated displaced lines (LD, LLD and LDD) verify the results achieved in Section 4.1, demonstrating their competitiveness at the high end of the spectrum, due to the inevitable loss of resolution with Long tracks due to the finite size of the VELO. At low lifetimes, the increase in the size of the error bands is explained by the low (or zero) probability of reconstructing traces without hits in the VELO.



(a) $B_s^0 \to 6\mu$ (b) $B^+ \to 6\mu K^+$

Figure 5.27: Extrapolation of sensitivity results for 6μ modes. Left: low-mass configuration $(m_{a_1}, m_{a_2}) = (0.50, 1.50)$ GeV. Right: high-mass configuration $(m_{a_1}, m_{a_2}) = (1.25, 3.50)$ GeV.

USC UNIVERSIDADE DE SANTIAGO DE COMPOSTELA

5.8 Fit Model

Maximum likelihood fits to the invariant mass of the B meson candidates are used to search for hints of the signal modes and to extract their branching fractions. In the case that no significant signal is observed, 95% confidence level (CL) upper limits on the branching fractions are set using the CLs method.

As discussed, the signal modes are subdivided into several reconstruction categories, depending on the topology of the decay. All these categories, despite reconstruction effects, share the same branching fraction. Therefore, simultaneous fits are developed to find the branching fraction of each decay or to impose limits. Each measurement or limit calculation is done independently for each decay mode, so there is no attempt to do a simultaneous search across all the signal channels.

The signal component is modelled using a Double Crystal Ball (DSCB) function, which has been shown to provide a good description for B decays [117]. The shape parameters of the DSCB function are obtained by fitting to truth-matched simulation candidates with the full selection applied. Complementarily, checks are made with a generalized Asymmetrical DSCB [285], not showing an evident improvement in the pull distributions.

Regarding the fit to the invariant mass distributions in data, several comments must be provided. On the signal core, the shape parameters remain fixed during the mass fit, and the single event sensitivities for each category are Gaussian constrained. Complementarily, the signal yields are related to the branching fraction via:

$$N_{s,i} = \frac{\mathcal{B}_{\text{sig}}}{\alpha_i} \tag{5.24}$$

where α_i is the single event sensitivity for category i. This allows the full likelihood across categories to be written as:

$$\mathcal{L} = \prod_j \left[\mathcal{B}_{\text{sig}} \left(\sum_i \frac{f_i}{\alpha_i} \times \text{pdf}_i(x_j) \right) + \sum_i N_{b,i} e^{-\lambda_i x_j} \right] \prod_k \mathcal{G}(c_k) \tag{5.25}$$

where f_i stands for the weight that the algorithm assigns to every reconstruction component pdf_i, and a subindex j refers to the j-th measurement x_j entering the fit. The $\mathcal{G}$ refers to the various Gaussian constraints applied.

The following sections present studies of the fit components, along with validation checks to ensure the fit behaves as expected in the presence of a signal.

5.8.1 Sideband fits

As discussed in section 5.6, the background in this analysis is dominated by combinatorial contributions, with no significant peaking structures observed in the signal

region. Exponential fits to the B candidate invariant mass are performed in the low- and high-mass sidebands, as shown in Figures 5.28, 5.29, 5.30, and 5.31.

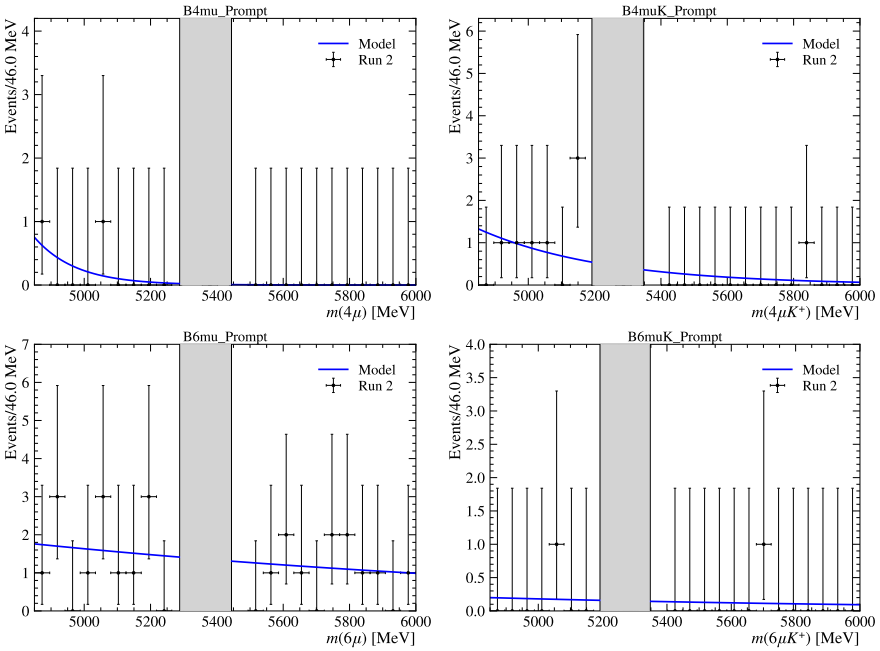


Figure 5.28: Blinded B mass distribution reconstructed with the Prompt selection. The full Run 2 dataset has been used.

In all cases, the exponential PDF provides a good description of the invariant mass distribution across the full fit range. While statistical uncertainties are large due to the low event yields, the fits suggest that the background shape can be reliably interpolated into the blinded signal region.

The background estimates obtained from these sideband fits are also used to construct validation studies of the fit model in the presence of signal. For this purpose, an expected number of background events in the signal window is computed via interpolation. Toy datasets are then generated under the signal-plus-background hypothesis, with the total number of events drawn as:

$$N = \frac{\mathcal{B}}{\alpha} + N_{\text{bkg}},$$

where $\mathcal{B}$ is the signal branching fraction hypothesis and α is the single event sensitivity. A pull study is then performed on the extracted signal strength to assess the performance of the fit model. The results are presented in Section 5.8.4.

USC UNIVERSIDADE DE SANTIAGO DE COMPOSTELA

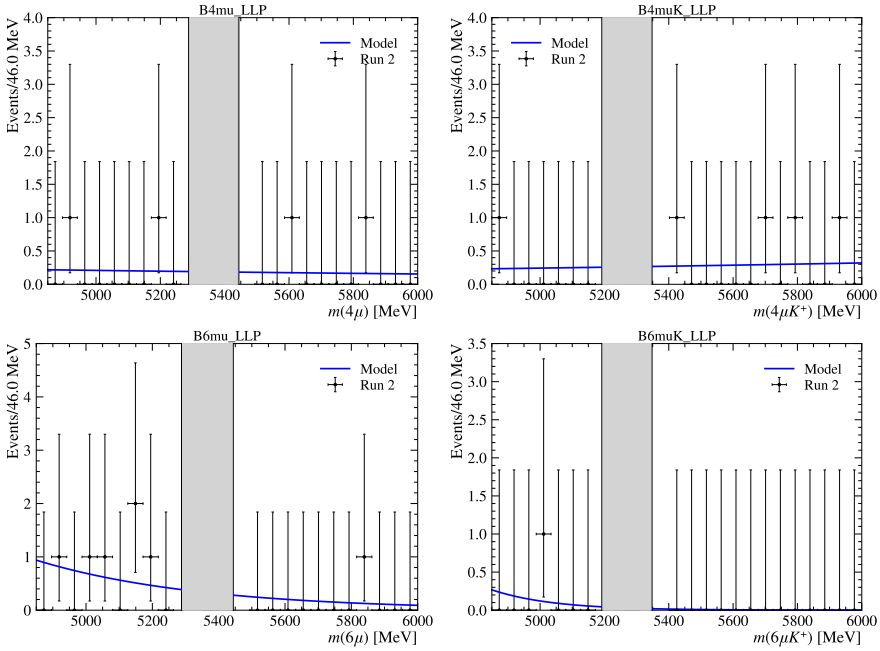


Figure 5.29: Blinded B mass distribution reconstructed with the displaced selection, only LL (4μ modes) and LLL (6μ modes). The full Run 2 dataset has been used.

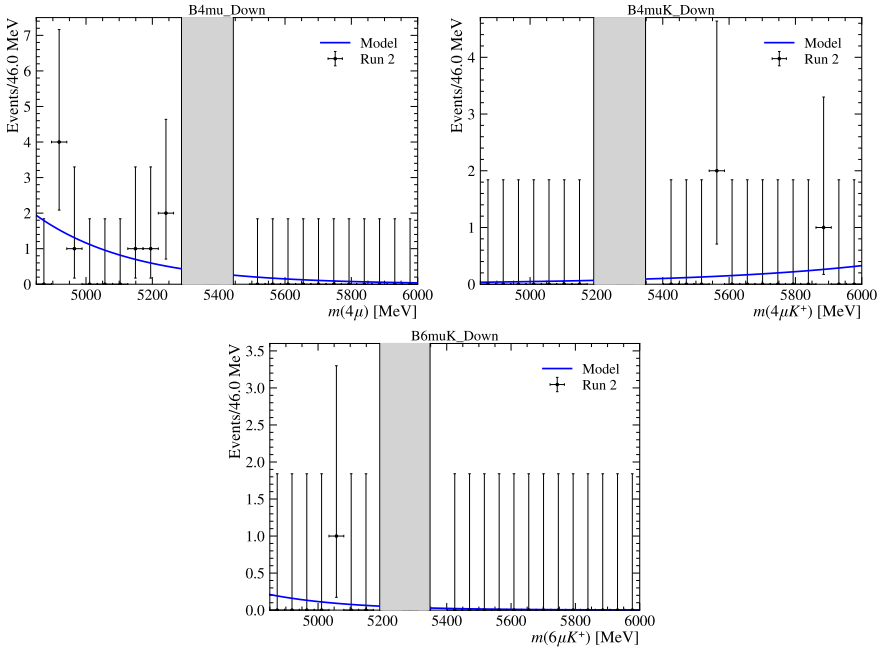


Figure 5.30: Blinded B mass distribution reconstructed by requiring one dimuon to be reconstructed with Downstream tracks, therefore LD (4μ modes) and LLD (6μ modes). No events surviving the selection for $B_s^0 \to 6\mu$. The full Run 2 dataset has been used.

USC UNIVERSIDADE DE SANTIAGO DE COMPOSTELA

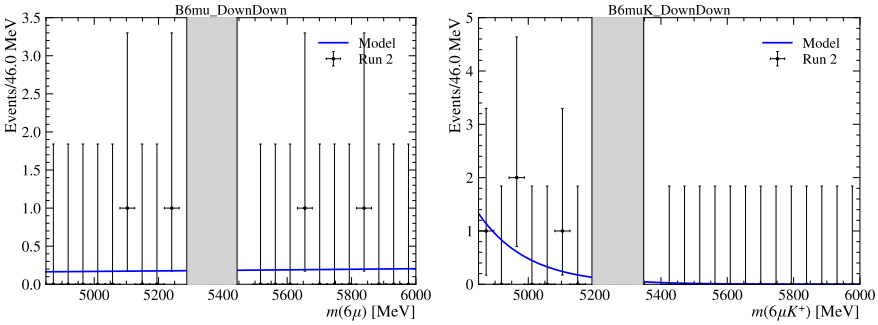


Figure 5.31: Blinded B mass distribution reconstructed by requiring two dimuons to be reconstructed with Downstream tracks, therefore displaced LDD. The full Run 2 dataset has been used.

5.8.2 Signal Fit

A double-sided Crystal Ball (DSCB) PDF [285] is used to fit to the signal peak. The DSCB PDF is a combination of two CB functions with a common mean μ and width σ:

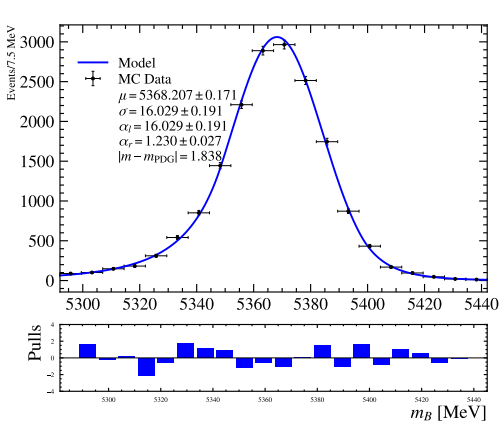
$$f(x;\mu,\sigma,\alpha_L,n_L,\alpha_R,n_R) = \begin{cases} A_L \cdot (B_L - \frac{x-\mu}{\sigma})^{-n_L}, & \text{if } \frac{x-\mu}{\sigma} < -\alpha_L, \\ exp\big(-\frac{(x-\mu)^2}{2\sigma^2}\big), & \text{if } -\alpha_L \leqslant \frac{x-\mu}{\sigma} \leqslant \alpha_R \\ A_R \cdot (B_R - \frac{x-\mu}{\sigma})^{-n_R}, & \text{if } \frac{x-\mu}{\sigma} > \alpha_R \end{cases} \tag{5.26}$$

with

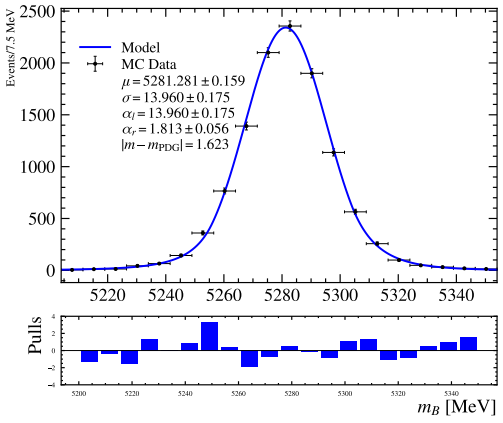
$$A_{L/R} = \left(\frac{n_{L/R}}{|\alpha_{L/R}|}\right)^{n_{L/R}} exp\left(-\frac{|\alpha_{L/R}|^2}{2}\right)$$
$$B_{L/R} = \frac{n_{L/R}}{|\alpha_{L/R}|} - |\alpha_{L/R}|$$

Here, x is the observable (in this case, the invariant mass), α_L and α_R define the points at which to switch the power-tails on the left and the right, respectively, and n_L and n_R are the exponents of the power-tails on the left and the right, respectively.

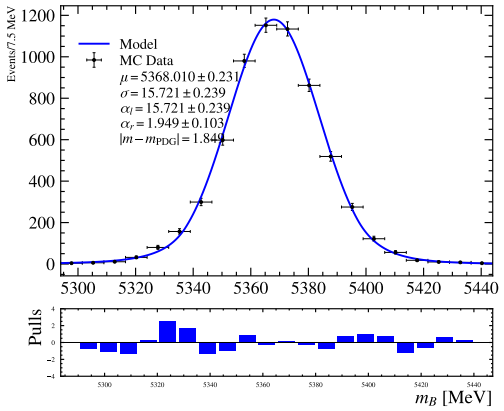
Fitting the Double-Sided Crystal Ball (DSCB) function to simulation can present challenges beyond basic convergence issues, particularly related to the determination of the tail parameters. In particular, large pulls exceeding 2σ are often observed, impacting the stability of other fit parameters. Due to the strong correlation between the α_i and n_i parameters, the power-law exponents $n_{L,R}$ are fixed during the fit, while the transition points $\alpha_{L,R}$ are allowed to float. This procedure has been shown to improve fit stability, although relatively big pulls are still present, for example, in Figure 5.32, which contains a cocktail of fits as an example.



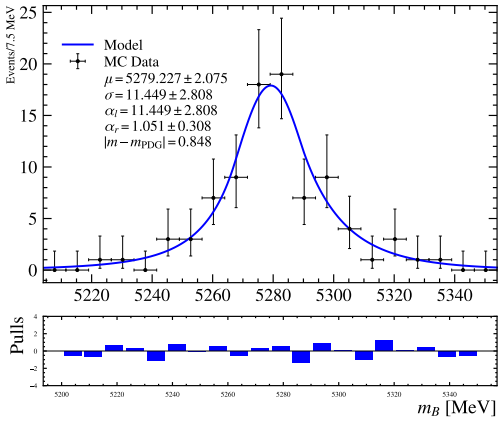
(a) $B_s^0 \to 4\mu$ PHSP.



(b) $B^+ \to 4\mu K^+$ LD with $m_{a_1} = 2.00$ GeV, $m_{a_2} = 2.75$ GeV and $t_{a_1} = 10$ ps



(c) $B_s^0 \to 6\mu$ LLL with $m_{a_1} = 0.50$ GeV, $m_{a_2} = 1.50$ GeV and $t_{a_1} = 10$ ps.



(d) $B^+ \to 6\mu K^+$ LLD with $m_{a_1} = 1.25$ GeV, $m_{a_2} = 3.50$ GeV and $t_{a_1} = 10$ ps.

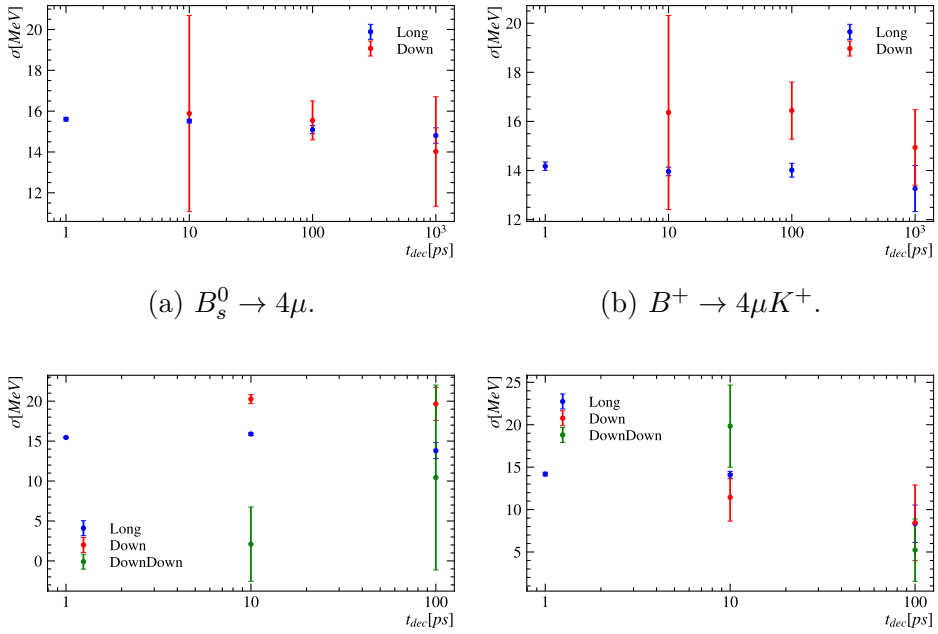
Figure 5.32: Miscellanea of Signal fits to a DSCB using MC.

5.8.3 Resolution Studies

The core resolution of the DSCB PDF is studied for different reconstruction categories to validate the assumption that the signal mass resolution is similar across different scalar lifetimes. The results, as an example, are shown in Figure 5.33 for the high-mass configuration modes. For most categories, the fitted resolutions are found to be compatible within uncertainties for different lifetimes. However, for samples corresponding to the high-lifetime regime, the limited statistics lead to larger discrepancies, but still bring a good convergence during the fits.

5.8.4 Fit model validation

If a significant signal is observed, it is important to validate that the fit model behaves as expected, particularly with respect to convergence. To assess the fit performance



(a) $B_s^0 \to 4\mu$. (b) $B^+ \to 4\mu K^+$.

(c) $B_s^0 \to 6\mu$. (d) $B^+ \to 6\mu K^+$.

Figure 5.33: Resolution Studies for high-mass configurations.

and sensitivity, pseudo-experiments are generated under the signal-plus-background hypothesis, and pulls for $\mathcal{B}(B \to N\mu(K^+))$ are calculated. The pseudo-experiments are implemented as follows:

First, as described in previous sections, mass PDFs are constructed for each reconstruction category. For the background component, an exponential PDF is obtained by fitting the low-mass and high-mass sidebands, and interpolation is used to estimate the expected background yield within the signal region. For the signal component, events are sampled from the signal PDF obtained from truth-matched simulation.

In each toy experiment, the expected numbers of background (N_{bkg}) and signal (N_{sig}) events are determined as follows:

- The number of background events N_{bkg} is drawn from a Poisson distribution around the expected background yield.
- The number of signal events is computed as $N_{\text{sig}} = \mathcal{B}/\alpha$, where $\mathcal{B}$ is the reference branching fraction and α is the single event sensitivity.

The total number of events in the pseudo-experiment is thus $N = N_{\text{bkg}} + N_{\text{sig}}$, and the invariant mass values are sampled according to the combined background and signal PDFs.

These pseudo-experiments are then fitted, and the pull distribution of the extracted branching fraction is analysed to validate the fit model.

Once the samples have been generated from the signal and background PDFs, fits

Channel	$\mathcal{B}$	μ	σ
$B_s^0 \to 4\mu$	$1 \cdot 10^{-9}$	-0.175 ± 0.031	0.958 ± 0.022
$B^+ \to 4\mu K^+$	$3.0 \cdot 10^{-9}$	-0.132 ± 0.028	0.88 ± 0.02
$B_s^0 \to 6\mu$	$8.0 \cdot 10^{-9}$	0.01 ± 0.04	1.25 ± 0.028
$B^+ \to 6\mu K^+$	$1.0 \cdot 10^{-9}$	-0.201 ± 0.033	1.052 ± 0.024

Table 5.30: Pull studies results for PHSP samples. For each case, 1000 pseudo-experiments are run. Amount of failed toys remains stable and below 1%.

are performed either individually or simultaneously across reconstruction categories:

- For Prompt reconstruction categories, or in low-lifetime scenarios where Downstream reconstruction is not available, individual fits are performed.
- For the 4μ final states, simultaneous fits are performed across the displaced-LL and -LD categories to account for differences in sensitivity.
- For the 6μ final states, simultaneous fits are performed across the displaced-LLL, -LLD, and -LDD categories.

In all cases involving simultaneous fits, due to the limited statistics, all DSCB parameters are fixed during the fit, with only the yields floated.

Following each fit, the branching fractions $\mathcal{B}\left(B \to N\mu(K^+)\right)$ are extracted and compared to the injected value. Pulls are constructed according to:

$$\text{Pull} = \frac{\mathcal{B}_r^{\text{fit}} - \mathcal{B}_r^{\text{gen}}}{\sigma\left(\mathcal{B}_r^{\text{fit}}\right)}$$

where $\mathcal{B}_r^{\text{gen}}$ is the injected reference branching fraction, and $\sigma\left(\mathcal{B}_r^{\text{fit}}\right)$ is the fitted uncertainty.

In the ideal case of an unbiased fit, the pull distribution should follow a standard normal distribution with mean $\mu = 0$ and width $\sigma = 1$, indicating both correct central values and properly estimated uncertainties. However, due to the low statistics regime in some categories, it is expected that certain deviations as well as a fraction of fits failing to converge. These two features are studied in detail under the analysis conditions.

USC UNIVERSIDADE DE SANTIAGO DE COMPOSTELA

Channel	Mass [GeV]	τ [ps]	$\mathcal{B}$	μ	σ
$B_s^0 \to 4\mu$	[0.25, 0.50]	0	$3.5 \cdot 10^{-9}$	-0.063 ± 0.032	0.998 ± 0.023
		1	$2.5 \cdot 10^{-9}$	-0.176 ± 0.037	1.059 ± 0.026
		10	$3.5 \cdot 10^{-9}$	-0.058 ± 0.031	0.984 ± 0.022
		100	$3.5 \cdot 10^{-9}$	-0.135 ± 0.031	0.932 ± 0.022
		1000	$1.5 \cdot 10^{-8}$	-0.236 ± 0.023	0.985 ± 0.022
$B^+ \to 4\mu K^+$	[0.25, 0.50]	0	$4.0 \cdot 10^{-10}$	-0.184 ± 0.034	1.055 ± 0.024
		1	$2.0 \cdot 10^{-9}$	-0.066 ± 0.037	1.030 ± 0.026
		10	$3.5 \cdot 10^{-9}$	-0.163 ± 0.029	0.916 ± 0.021
		100	$2.0 \cdot 10^{-8}$	-0.106 ± 0.031	0.975 ± 0.022
		1000	$8.0 \cdot 10^{-8}$	0.001 ± 0.032	0.915 ± 0.023
$B_s^0 \to 6\mu$	[0.50, 1.50]	0	$4.0 \cdot 10^{-10}$	-0.075 ± 0.031	0.912 ± 0.022
		1	$2.0 \cdot 10^{-10}$	0.092 ± 0.029	0.867 ± 0.021
		10	$8.0 \cdot 10^{-9}$	-0.161 ± 0.029	0.913 ± 0.030
		100	$6.5 \cdot 10^{-8}$	-0.131 ± 0.036	0.964 ± 0.025
$B^+ \to 6\mu K^+$	[0.50, 1.50]	0	$2.5 \cdot 10^{-10}$	-0.020 ± 0.027	0.786 ± 0.019
		1	$2.5 \cdot 10^{-10}$	-0.184 ± 0.034	1.055 ± 0.024
		10	$5.0 \cdot 10^{-9}$	-0.160 ± 0.036	1.036 ± 0.026
		100	$6.5 \cdot 10^{-8}$	-0.152 ± 0.033	0.916 ± 0.023

Table 5.31: Pull studies results. A mass configuration has been chosen per channel and the fit model analysis is performed across the generated lifetimes set. For each case, 1000 pseudo-experiments are run. In all the cases, the number of fits failing is stabilized below 1% of the run toys.

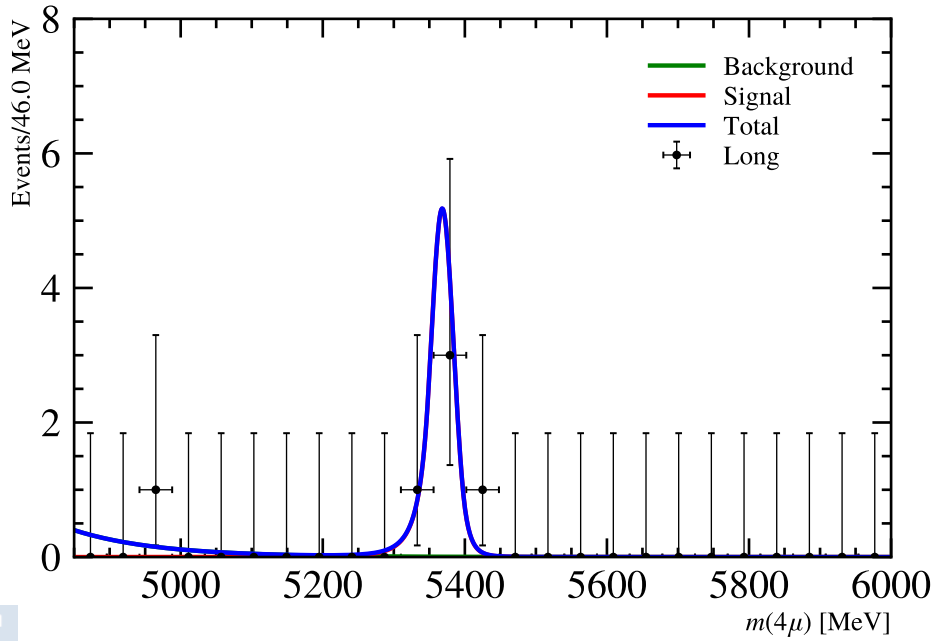


Figure 5.34: Toy study relative to a single fit for $B_s^0 \to 4\mu$ case.

The results of the aforementioned toy studies are summarised in Table 5.30 and 5.31, for PHSP prompt and hierarchical samples, respectively. To test the fit model's robustness, signal strengths are chosen such that a modest number of signal events are injected into the signal region, ensuring that the model is evaluated under meaningful conditions. Examples of the toy generation can be found in Figure 5.34, 5.35 and 5.36.

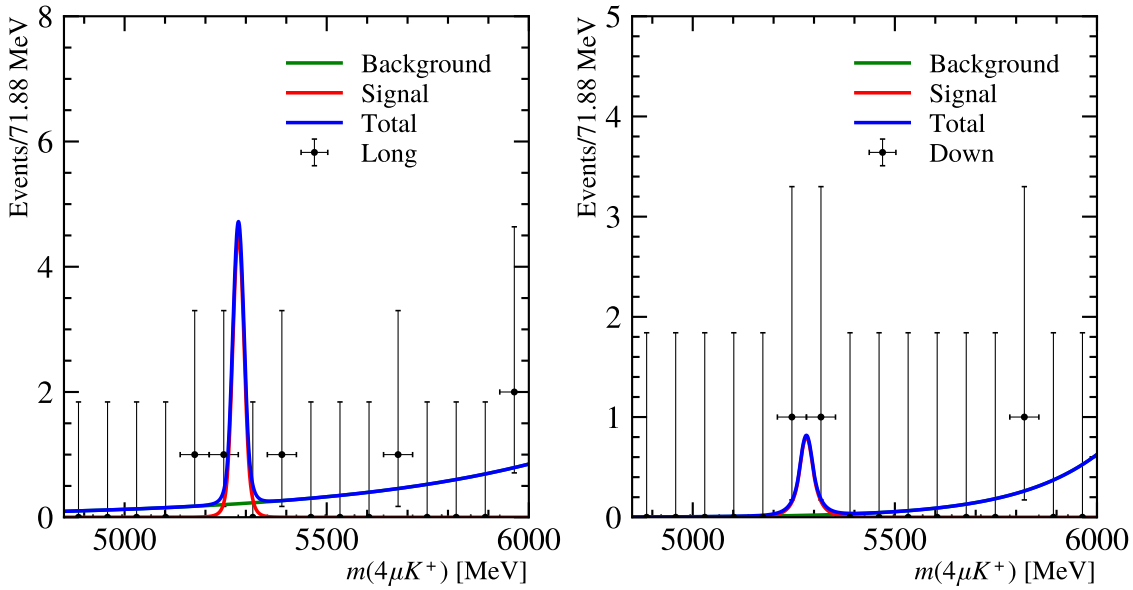


Figure 5.35: Toy study relative to a simultaneous fit to displaced LL and LD reconstruction categories for $B^+ \to 4\mu K^+$, 100 ps case.

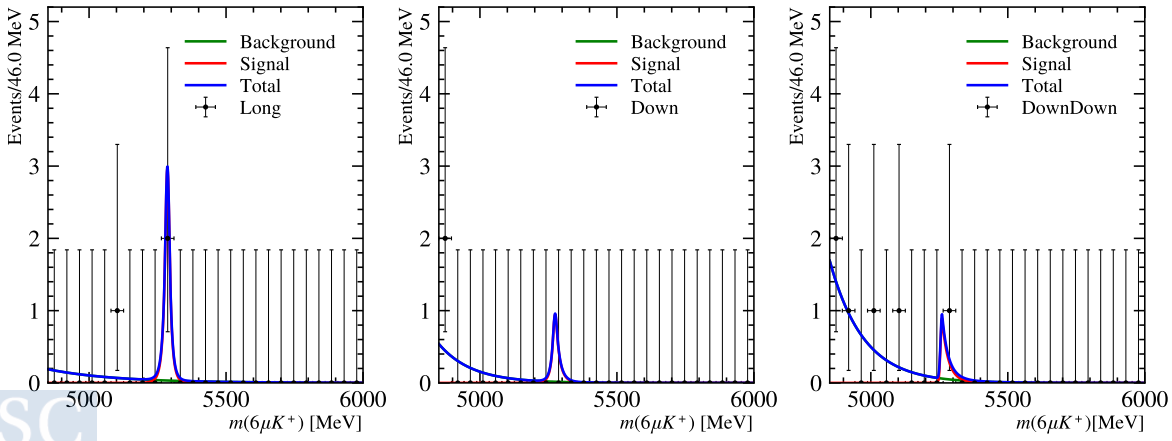


Figure 5.36: Toy study relative to a simultaneous fit to displaced LLL, LLD and LDD reconstruction categories for $B_s^) \to 6\mu$, 100 ps case.

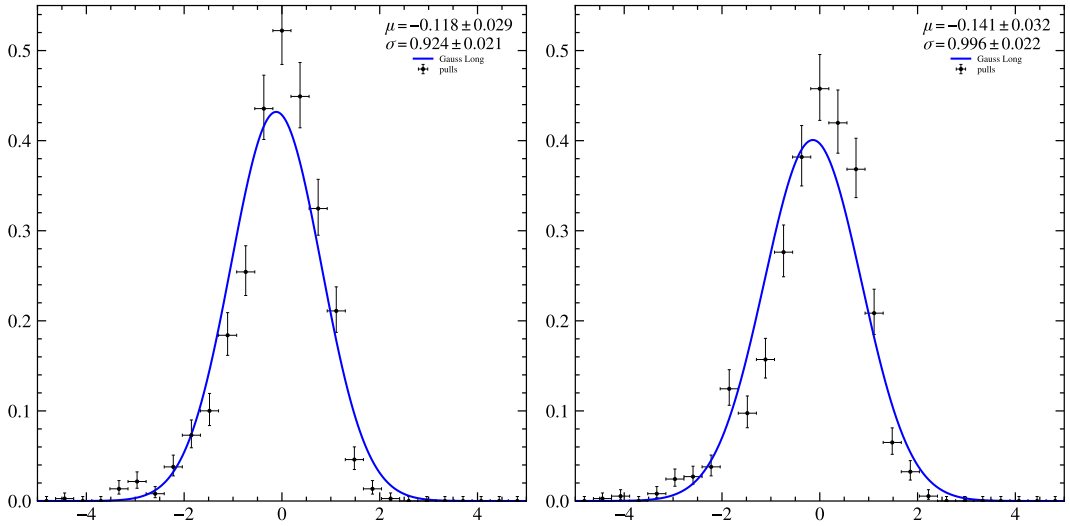


Figure 5.37: Fit to the pulls distribution for: $B_s^0 \to 4\mu$ PHSP (left) and $B^+ \to 4\mu K^+$ with $m_{a_1} = 2.00$ GeV, $m_{a_2} = 2.75$ GeV and $t_{a_1} = 100$ ps (right).

All in all, at first glance, the developed toy studies bring satisfactory results. On the one hand, despite of values of μ and σ non-compatible with 0 and 1, respectively, the fact that they lie close to these boundaries is regarded as satisfactory. As it was reported, in such a low-statistics regime, fits are expected to fail in some extreme cases and the uncertainty estimation is expected not to effectively cover deviations from the aforementioned boundaries. Two examples can be found in Figure 5.37, in which the deviation from some of the pull points with respect to the expected Normal distribution indicates a slight uncertainty under-estimation.

5.9 Systematic Uncertainties

This section describes the determination of systematic uncertainties for this analysis. Most of these uncertainties are determined as either shifts in the signal efficiencies, or the ratio of the signal- and normalisation-mode efficiencies $\frac{\epsilon_{\text{norm}}}{\epsilon_{\text{sig}}}$.

5.9.1 Simulation PHSP Model

Due to the underlying decay topology, decays such as $B^+ \to K^+ a_1 a_2$ may exhibit a non-trivial q^2 dependency. However, this is not represented in the simulation samples used in this analysis that are generated under a phase-space (PHSP) model assumption, which does not accurately reflect the real q^2 spectrum of signal decays. In particular, [116] shows that for $B^+ \to K^+ a_1 a_2$ decays, the differential width $d\Gamma/dq^2$ follows a non-flat, physically motivated distribution. The corresponding analytic form is:

$$\begin{aligned}\frac{d\Gamma}{dq^2} =& \frac{1}{768 m_B^2 \pi^3 (q^2)^2} \sqrt{-4m_2^2 + \frac{\left(-m_1^2 + m_2^2 + q^2\right)^2}{q^2}} \sqrt{-4m_B^2 + \frac{\left(m_B^2 - m_K^2 + q^2\right)^2}{q^2}} \\ &\times \left(\frac{0.3267(-m_1^2 + m_2^2)^2 (m_B^2 - m_K^2)^2}{\left(1 - 0.034 q^2\right)^2} + \left(\frac{0.173}{\left(1 - 0.034 q^2\right)^2} + \frac{0.162}{1 - 0.034 q^2} \right)^2 \right) \\ &\times \left((-m_1^2 + m_2^2)^2 + 2(-m_1^2 - m_2^2) q^2 + (q^2)^2 \right) \\ &\times \left((-m_B^2 - m_K^2)^2 + 2(-m_B^2 - m_K^2) q^2 + (q^2)^2 \right)\end{aligned} \tag{5.27}$$

where $q^2 = (p_1 + p_2)^2$ is the invariant mass squared of the scalar pair (i.e. the squared four-momentum transferred to the $a_1 a_2$ system), p_1 and p_2 denote the four-momenta of the intermediate scalar particles a_1 and a_2, respectively, m_1 and m_2 are the masses of the scalars a_1 and a_2, respectively, m_B is the mass of the decaying B-meson and m_K is the mass of the kaon.

To assess the impact of this mismatch on selection efficiency, we compute weights to reweight the PHSP signal MC to follow the above q^2 distribution. This is performed with a 1D binned reweighting using generator-level variables. These weights are then applied to both generator-level and reconstructed-level candidates using the same truth-matched variables. This allows us to recompute the overall reconstruction and stripping efficiency as

$$\epsilon = \frac{\sum_i \omega_i^{\text{reco}}}{\sum_i \omega_i^{\text{gen}}}.$$

The systematic uncertainty is then assigned as half the absolute shift between the nominal (unweighted) and reweighted efficiency values:

$$\sigma_{\text{PHSP}} = \frac{1}{2} |\epsilon_{\text{PHSP}} - \epsilon_{\text{weighted}}|$$

This procedure has shown a relatively good behaviour, even though several decay configurations suffer from the outliers coming from the tail of the distributions, where a small number of events can be found.

In figure 5.38, an example of how the reweighting procedure works for each of the modes is shown. Following this approach, full efficiencies are calculated for both nominal and q^2 reweighted samples and differences not falling within the $\pm 2\sigma$ significance (defined as the nominal value over its corresponding uncertainty) are assigned as a systematic uncertainty.

USC UNIVERSIDADE DE SANTIAGO DE COMPOSTELA

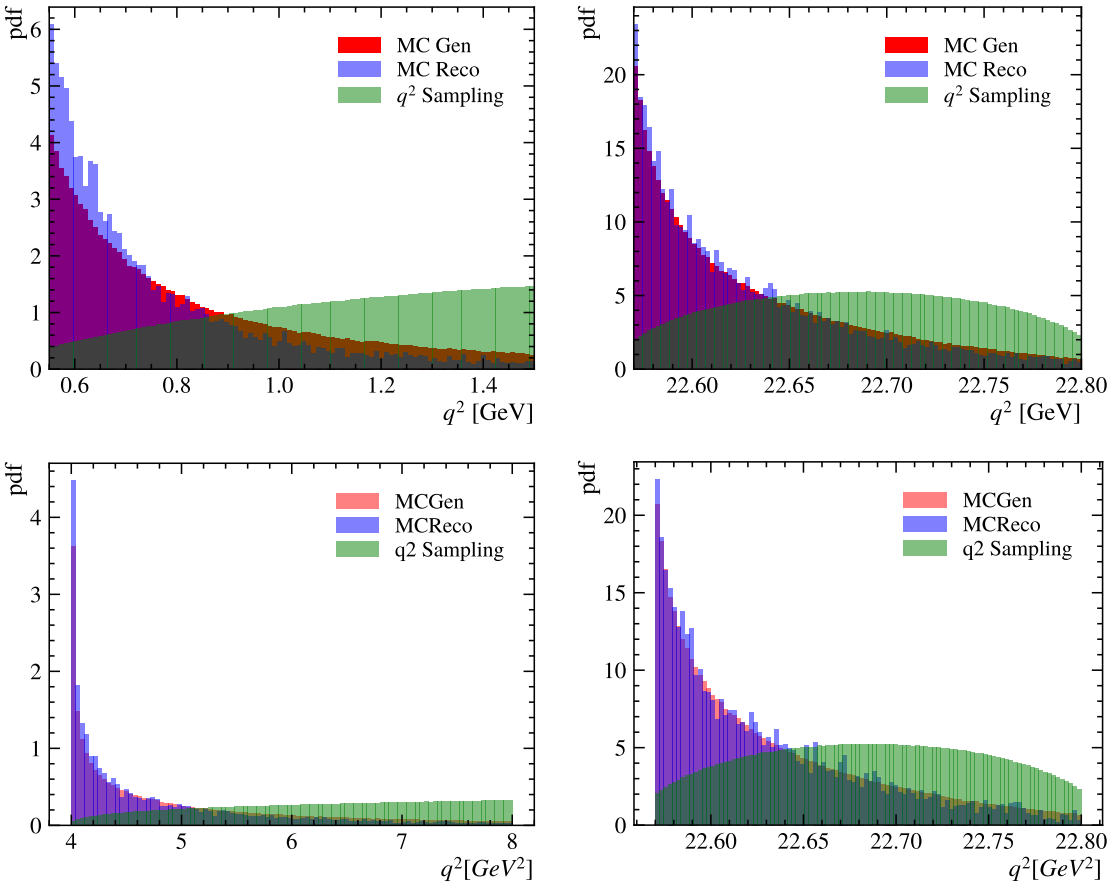


Figure 5.38: Reweighting procedure for $B^+ \to 4\mu K^+$ with $m_{a_1} = 0.25\,\text{GeV}$, $m_{a_2} = 0.40\,\text{GeV}$ (top left) and $m_{a_1} = 2.00\,\text{GeV}$, $m_{a_2} = 2.75\,\text{GeV}$ (top right), and for $B^+ \to 6\mu K^+$ with $m_{a_1} = 0.50\,\text{GeV}$, $m_{a_2} = 1.50\,\text{GeV}$ (bottom left) and $m_{a_1} = 1.25\,\text{GeV}$, $m_{a_2} = 3.50\,\text{GeV}$ (bottom right).

USC UNIVERSIDADE DE SANTIAGO DE COMPOSTELA

$m(a_1)$, $m(a_2)$ [GeV]	τ_{a_1} [ps]	Prompt (%)	LL (%)	LD (%)
0.25, 0.40	0	9.64 ± 1.19		
0.25, 0.40	1		7.80 ± 4.54	
0.25, 0.40	10		17.01 ± 7.77	14.77 ± 4.62
0.25, 0.40	100		6.19 ± 11.72	10.82 ± 6.70
0.25, 0.40	1000		1.75 ± 32.06	22.96 ± 9.25
2.00, 2.75	0	5.03 ± 0.97		
2.00, 2.75	1		3.36 ± 1.18	
2.00, 2.75	10		3.68 ± 1.22	0.16 ± 6.30
2.00, 2.75	100		3.75 ± 2.17	5.27 ± 3.37
2.00, 2.75	1000		2.31 ± 6.26	4.12 ± 3.36

Table 5.32: PHSP systematics overview for $B^+ \to 4\mu K^+$ samples. Values that are not compatible with the $\pm 2\sigma$ error bands are marked in red.

In tables 5.32 and 5.33, an overview of the systematics associated with the PHSP reweighting can be found. These are stated as relative uncertainties on the signal efficiencies. Note that systematic uncertainties below 20 % have hardly any impact on an upper limit at all. Remarkable though is the influence of outliers in the displace-low-mass configurations, since in the limits of the phase space, there are bins with a pair of events as maximum, being able to introduce bias when defining the reweighting bins. Additional checks have been made restricting the q^2 range within the procedure takes place, observing variations of $1, 2$ % as maximum. At the end, in terms of being as conservative as possible, the full range is still kept.

$m(a_1)$, $m(a_2)$ [GeV]	τ_{a_1} [ps]	LLL (%)	LLD (%)	LDD (%)
0.50, 1.50	0	23.53 ± 0.99		
0.50, 1.50	1	1.56 ± 1.70		
0.50, 1.50	10	4.61 ± 7.43	2.45 ± 3.48	20.31 ± 4.30
0.50, 1.50	100	6.51 ± 21.72	0.07 ± 11.68	6.72 ± 5.87
1.25, 3.50	0	13.95 ± 1.5		
1.25, 3.50	1	1.25 ± 1.87		
1.25, 3.50	10	0.58 ± 3.18	8.45 ± 8.37	7.97 ± 29.36
1.25, 3.50	100	15.74 ± 14.55	1.29 ± 23.63	15.25 ± 27.11

Table 5.33: PHSP systematics overview for $B^+ \to 6\mu K^+$ samples. Values that are not compatible with the $\pm 2\sigma$ error bands are marked in red.

5.9.2 Effective Lifetime of B_s^0 decay modes

USC

The effective lifetime of any B_s^0 signal mode is unknown a priori and can vary between the lifetimes of the light and heavy eigenstates, denoted as τ_L and τ_H, respectively. These lifetimes are measured to be;

- $\tau_L = 1.429 \pm 0.006$ ps,
- $\tau_H = 1.622 \pm 0.008$ ps

as given in the PDG [46]. Simulation samples used in this analysis for B_s^0 signal modes are generated with an effective lifetime of $\tau_{\text{gen}} = 1.512$ ps. Since the selection efficiencies depend on the B_s^0 flight distance, the effective lifetime introduces a source of systematic uncertainty on the efficiencies. To quantify this, the simulated candidates are reweighted such that their true decay times correspond to an effective lifetime of either τ_L or τ_H. The reweighting is applied to both the generator-level and offline reconstructed simulation samples to ensure consistency. The weights applied to each candidate are calculated using the formula:

$$w(t) = \frac{\tau_{\text{gen}}}{\tau_{L/H}} e^{-t\left(\frac{1}{\tau_{L/H}} - \frac{1}{\tau_{\text{gen}}}\right)}$$

where t is the decay time, τ_{gen} is the effective lifetime used to generate the MC samples, and $\tau_{L/H}$ represents either τ_L or τ_H.

Table 5.34 shows the associated systematics for the $B_s^0 \to 4\mu$ channel, included as a relative uncertainty on the efficiency ratio $\frac{\epsilon_{\text{norm}}}{\epsilon_{\text{sig}}}$. Such a systematic source represents the biggest contribution to B_s^0 modes.

$m(a_1)$, $m(a_2)$ [GeV]	τ_{a_1} [ps]	Prompt (%)	LL (%)	LD (%)
PHSP	0	4.031		
0.25, 0.40	0	6.3661		
0.25, 0.40	1		7.119	
0.25, 0.40	10		5.5549	0.3999
0.25, 0.40	100		5.3371	1.1057
0.25, 0.40	1000		5.3208	1.217
2.00, 2.75	0	7.1433		
2.00, 2.75	1		1.7233	
2.00, 2.75	10		1.2609	0.0469
2.00, 2.75	100		1.2215	0.7529
2.00, 2.75	1000		1.7707	1.2962

Table 5.34: Systematic uncertainties for $B_s^0 \to 4\mu$ associated with the effective B_s^0 lifetime.

5.9.3 Simulation Corrections

USC UNIVERSIDADE DE SANTIAGO

Systematic uncertainties associated with simulation corrections are evaluated using bootstrapping to assess the reliability of the reweighting procedure. Here, bootstrapping involves generating multiple samples from a given sample by randomly selecting

candidates with replacement. Some candidates may be selected multiple times, whilst others may not be selected at all.

Once the bootstrapped samples are generated, new sets of weights are determined and applied to the simulation samples. This process is repeated 20 times, generating an ensemble of selection efficiencies. These efficiencies are then used to calculate the ratio of signal- and normalisation-mode efficiencies and the systematic uncertainties are taken as the standard deviation of the distributions of these ratios. These systematic uncertainties are represented as a relative uncertainty on the efficiency ratio $\frac{\epsilon_{\text{norm}}}{\epsilon_{\text{sig}}}$, as for the effective B_s^0 lifetime systematic uncertainty. These uncertainties are generally larger for more statistically limited samples. In all the cases, the reweighting systematics stabilize below 5%, with some values close to 10% due to loss of statistics in the datasets with higher lifetime.

5.9.4 PID Efficiency

As discussed in section 5.4.3, no PID corrections are applied to the simulation samples due to poor coverage of *PIDCalib* samples at low p_T^μ. To quantify the potential bias this introduces, per-muon PID weights are calculated as a function of p_T^μ with $B_s^0 \to J/\psi(\mu^+\mu^-)\phi(K^+K^-)$. Weights are then applied to each muon in the simulation samples based on p_T^μ and a per-event weight is calculated as follows:

$$w_{\text{PID}} = \prod_i^n (w^n_{p_T^\mu}).$$

Efficiency ratios are re-evaluated with these weights included in the efficiency calculation and the shift is taken as a systematic uncertainty on the ratio of efficiencies, in a similar way to the systematic uncertainties assigned for the B_s^0 lifetime and simulation corrections.

USC UNIVERSIDADE DE SANTIAGO DE COMPOSTELA

$m(a_1)$, $m(a_2)$ [GeV]	τ_{a_1} [ps]	Prompt (%)	LL (%)	LD (%)
PHSP	0	4.3405		
0.25, 0.40	0	7.1455		
0.25, 0.40	1		6.7456	
0.25, 0.40	10		5.9868	1.1284
0.25, 0.40	100		6.4212	1.2638
0.25, 0.40	1000		6.099	0.7697
2.00, 2.75	0	7.5834		
2.00, 2.75	1		2.3216	
2.00, 2.75	10		2.194	1.3239
2.00, 2.75	100		2.3205	1.2575
2.00, 2.75	1000		2.5279	1.9059

Table 5.35: Systematic uncertainties for $B_s^0 \to 4\mu$ associated with the PID efficiency, given as a relative uncertainty on the efficiency ratio $\frac{\epsilon_{\text{norm}}}{\epsilon_{\text{sig}}}$.

In Table 5.35, the associated systematics for $B_s^0 \to 4\mu$ modes can be found. There, it can be clearly observed how the lower coverage of low p_T events causes the ratio to increase.

5.9.5 Fit Model

The fit model comprises a signal (parametrized with a Double Crystal-Ball) plus a combinatorial background component. Both parametrizations are critical for imposing upper limits on the branching fraction of the decays. Specifically, in such a low statistics regime, it is important to assess the effect of different sidebands' shapes on the final sensitivity of the CLs method. In this manner, a change in the sidebands' description is taken, choosing a linear function as a background input to the limit setting. Consequently, limits are re-evaluated, and half of the difference between the values is considered systematic.

In Table 5.36, the model associated systematics are stored. Note that only the differences are reported here, whereas the 95% CL Upper Limits on the branching fraction for both parametrizations are stored in Table 5.39.

USC UNIVERSIDADE DE SANTIAGO DE COMPOSTELA

$m(a_1)$, $m(a_2)$	τ_{a_1}	$B_s^0 \to 4\mu$	$B^+ \to 4\mu K^+$
PHSP	0	$3.31 \cdot 10^{-14}$	$1.06 \cdot 10^{-17}$
0.25, 0.40	1	$6.56 \cdot 10^{-10}$	$3.90 \cdot 10^{-10}$
	10	0.0	$5.70 \cdot 10^{-11}$
	100	$1.3 \cdot 10^{-15}$	$1.12 \cdot 10^{-9}$
	1000	$6.79 \cdot 10^{-10}$	$4.2 \cdot 10^{-10}$
2.00, 2.75	1	$2.66 \cdot 10^{-11}$	$6.9 \cdot 10^{-13}$
	10	0.0	0.0
	100	0.0	0.0
	1000	$5.12 \cdot 10^{-11}$	$4.78 \cdot 10^{-10}$
$m(a_1)$, $m(a_2)$	τ_{a_1}	$B_s^0 \to 6\mu$	$B^+ \to 6\mu K^+$
PHSP	0	$5.25 \cdot 10^{-10}$	$3.11 \cdot 10^{-10}$
0.50, 1.50	1	$2.75 \cdot 10^{-11}$	$2.09 \cdot 10^{-11}$
	10	0.0	0.0
	100	$1.92 \cdot 10^{-9}$	$1.84 \cdot 10^{-10}$
1.25, 3.50	1	$8.22 \cdot 10^{-13}$	$1.35 \cdot 10^{-11}$
	10	0.0	0.0
	100	$1.67 \cdot 10^{-8}$	$1.85 \cdot 10^{-8}$

Table 5.36: Systematic uncertainties resulting in the difference between Expected Upper Limits at 95% CL on the branching fraction parameter.

5.9.6 Summary of Systematic Uncertainties

Tables 5.37 and 5.38 combine all the systematic sources of this analysis. Note that the systematic uncertainty related to the background model is separated from the rest of the "combined" systematics. The combined systematic is given as a relative uncertainty, whereas the background model systematic uncertainty is reported as an absolute uncertainty on the branching fraction upper limit estimate. In the case of the B_s^0 modes, the dominant systematic uncertainty is the uncertainty associated with the effective lifetime of the B_s^0. In the case of the B^+ modes, the dominant systematic uncertainty is attributed to the decay model (for samples where this is applicable). Also, for the 4μ modes, the PID efficiency systematic uncertainty is relatively large, in particular for the samples simulated with the lower scalar mass configuration.

The leading systematic uncertainties could be reduced through several improvements, most of them linked to the detector performance during Run 3. For the B_s^0 modes, enhanced tracking and dedicated displaced-vertex triggers would improve the decay-time acceptance, critical for long-lived topologies. In the B^+ channels, the dominant uncertainty from the decay-model simulation could be mitigated by developing more realistic signal models. Concerning PID uncertainties, a refined calibration could reduce the associated systematic in low-p_T multi-muon samples. Finally, larger datasets

$m(a_1)$, $m(a_2)$ [GeV]	τ_{a_1} [ps]	Comb. Syst. [%]	Bkg Model
	$B_s^0 \to 4\mu$		
PHSP	0	5.95	$3.31 \cdot 10^{-14}$
0.25, 0.40	1	9.83	$6.56 \cdot 10^{-10}$
0.25, 0.40	10	2.95	0.0
0.25, 0.40	100	3.22	$1.3 \cdot 10^{-15}$
0.25, 0.40	1000	3.30	$6.79 \cdot 10^{-10}$
2.00, 2.75	1	2.95	$2.66 \cdot 10^{-11}$
2.00, 2.75	10	2.66	0.0
2.00, 2.75	100	3.24	0.0
2.00, 2.75	1000	4.34	$5.12 \cdot 10^{-11}$
	$B_s^0 \to 6\mu$		
PHSP	0	2.00	$5.25 \cdot 10^{-10}$
0.50, 1.50	1	2.03	$2.75 \cdot 10^{-12}$
0.50, 1.50	10	3.13	0.0
0.50, 1.50	100	3.07	$1.92 \cdot 10^{-9}$
1.25, 3.50	1	1.75	$8.22 \cdot 10^{-13}$
1.25, 3.50	10	1.66	0.0
1.25, 3.50	100	6.04	$1.67 \cdot 10^{-8}$

Table 5.37: Systematic uncertainties on $\mathcal{B}(B_s^0 \to 4\mu)$ and $\mathcal{B}(B_s^0 \to 6\mu)$.

(remember the increase in the pile-up during Run 3) with the aforementioned prospects would further constrain background-related systematics.

USC UNIVERSIDADE DE SANTIAGO DE COMPOSTELA

$m(a_1)$, $m(a_2)$ [GeV]	τ_{a_1} [ps]	Comb. Syst. [%]	Bkg Model
$B^+ \to 4\mu K^+$			
PHSP	0	8.67	$1.06 \cdot 10^{-17}$
0.25, 0.40	1	12.84	$3.9 \cdot 10^{-10}$
0.25, 0.40	10	17.24	$5.7 \cdot 10^{-11}$
0.25, 0.40	100	14.18	$1.12 \cdot 10^{-9}$
0.25, 0.40	1000	16.52	$4.2 \cdot 10^{-10}$
2.00, 2.75	1	2.78	$6.9 \cdot 10^{-13}$
2.00, 2.75	10	2.73	0.0
2.00, 2.75	100	2.01	0.0
2.00, 2.75	1000	4.39	$4.78 \cdot 10^{-10}$
$B^+ \to 6\mu K^+$			
PHSP	0	1.71	$3.11 \cdot 10^{-10}$
0.50, 1.50	1	1.31	$2.09 \cdot 10^{-11}$
0.50, 1.50	10	2.11	0.0
0.50, 1.50	100	3.86	$1.84 \cdot 10^{-10}$
1.25, 3.50	1	1.38	$1.35 \cdot 10^{-11}$
1.25, 3.50	10	1.03	0.0
1.25, 3.50	100	6.34	$1.85 \cdot 10^{-8}$

Table 5.38: Systematic uncertainties on $\mathcal{B}(B^+ \to 4\mu K^+)$ and $\mathcal{B}(B^+ \to 6\mu K^+)$ from different sources.

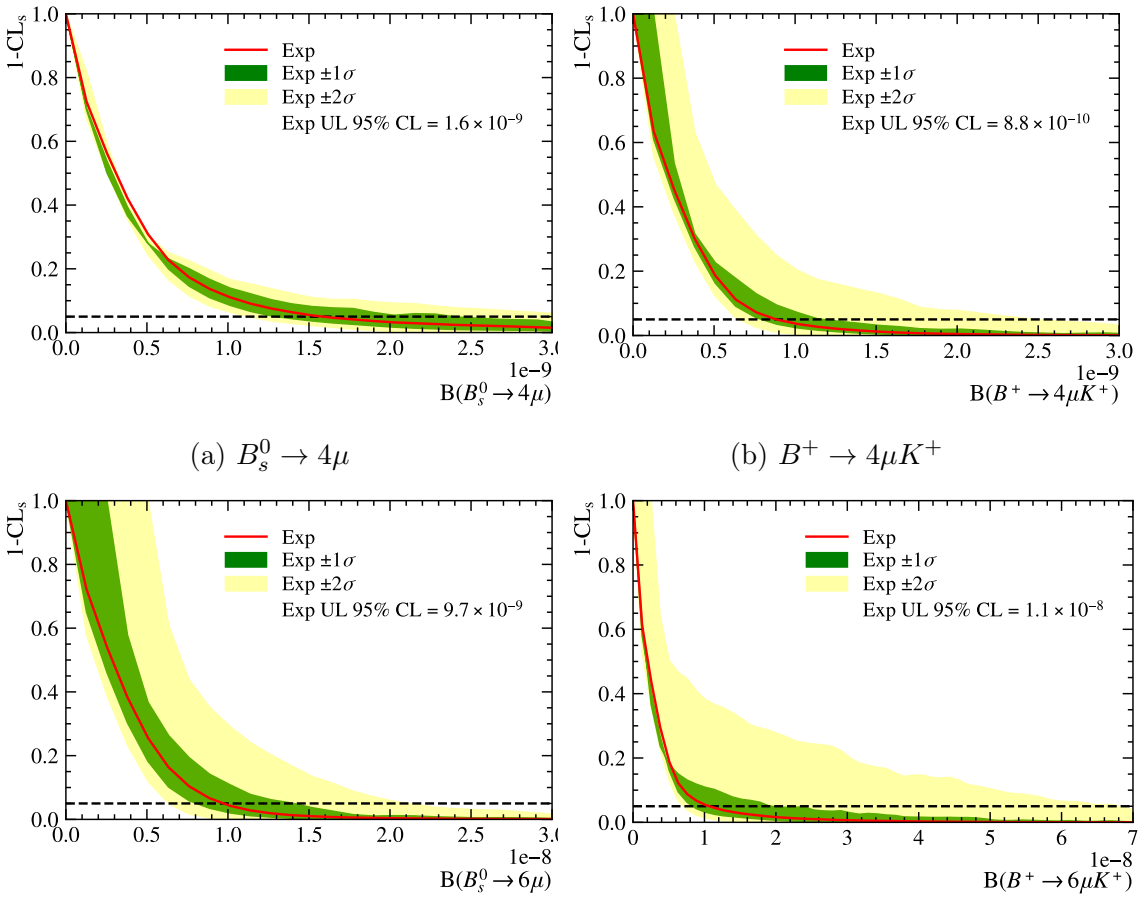
5.10 Results

The CLs method [286] is a hypothesis test which compares the null hypothesis, that the data is described by a only-background hypothesis, to the alternative one, in which the data is better explained by a signal plus background hypothesis. This statistical method allows the calculus of exclusion limits at a certain confidence level, which apply to a concrete parameter or set of them. In this analysis, a limit on the Branching ratio $\mathcal{B}$ is determined.

In searches for rare decays, it is highly expected that the measured branching fraction for a decay is compatible with 0. In those cases, the lower limit of the confidence interval is chosen as 0, whereas the test-statistic is built in a way that only values of the parameter of interest μ bigger than $\hat{\mu}$ can contribute to the limit. The so-called one-sided test statistics takes the form:

$$\tilde{q}_\mu = \begin{cases} -2\ln\frac{\mathcal{L}(\mu,\hat{\hat{\theta}}(\mu))}{\mathcal{L}(0,\hat{\hat{\theta}}(0))} & \hat{\mu} < 0, \\ -2\ln\frac{\mathcal{L}(\mu,\hat{\hat{\theta}}(\mu))}{\mathcal{L}(\hat{\mu},\hat{\hat{\theta}})} & 0 \leq \hat{\mu} < \mu \\ 0 & \hat{\mu} > \mu \end{cases} \tag{5.28}$$

where μ denotes the signal strength, θ the nuisance parameters and $\mathcal{L}(\mu,\theta)$ the likelihood in function of μ and θ. In the last equation, parameters with a hat denote the maximum-likelihood estimator for that parameter and parameters with two denote the conditional maximum-likelihood estimator for such a parameter, provided a particular signal strength.



(a) $B_s^0 \to 4\mu$ (b) $B^+ \to 4\mu K^+$

(c) $B_s^0 \to 6\mu$ (d) $B^+ \to 6\mu K^+$

Figure 5.39: Expected limits at 95% CL and associated error bands for PHSP samples.

The hypothesis contrast is performed through the distributions of the test statistic $\tilde{q}_\mu$ under the signal plus background **(s+b)** and only-background **(b)** hypothesis. Under certain hypotheses, i.e., a sufficient number of events or no background fluctuations, p-values can be extracted from a χ^2 distribution, which is denominated the

asymptotic approach [286]. Nevertheless, in the low statistics regime, such an assumption is no longer valid, which means that the p-values are computed from the use of pseudo-experiments. Then, if p_i (p-value) represents the probability of finding a value of $\tilde{q}$ with equal or less compatibility than $\tilde{q}_{obs}$ under a certain hypothesis, namely,

$$p_{s+b} = \int_{\tilde{q}_{obs}}^{\infty} f(\tilde{q}|s+b)d\tilde{q} = CL_{s+b} \tag{5.29}$$

$$p_b = \int_{\tilde{q}_{obs}}^{\infty} f(\tilde{q}|b)d\tilde{q} = 1 - CL_b \tag{5.30}$$

the confidence level for the signal hypothesis CL_s can be built from the ratio:

$$CL_s = 1 - \alpha = \frac{CL_{s+b}}{CL_b} \tag{5.31}$$

which effectively covers the range $[0, \mathcal{B}]$ in which the observed limit will be located independently of its value.

The application of the CL_s method is performed through the `Gammacombo` package [287], a tool built on top of ROOT and oriented towards measurements combination, datasets fitting and confidence intervals. Whereas the analysis datasets remain blinded, expected limits at 95% CL are computed.

For such a purpose, first, a sampling from the null hypothesis (see section 5.8.1) is performed throughout the full mass range as the case may be. Afterwards, the full model PDF is built by adding the corresponding signal PDFs, which are extended with a factor $\mathcal{B}/\alpha$[3]. Both generation and fitting steps are performed with systematic uncertainties in the α and $\mathcal{B}$ being included through Gaussian constraints. In terms of constraining the $\mathcal{B}$ parameter, only systematics $\delta\mathcal{B} > 10^{-12}$ are introduced as Gaussian constraints, since lower values result in fit breaks due to the extreme rigidity of the fit model. For channels whose associated systematic is below that threshold, the branching ratio is allowed to float during the limit setting.

In Table 5.39, the different expected limits at 95% CL can be consulted and in Figure 5.39 and 5.40, expected limits for PHSP samples and a miscellanea of Long-Lived samples with simultaneous fits across reconstruction categories can be seen, respectively. For the elaboration of the plots, 80 scan points are introduced and 1500 pseudo-experiments are run per scan point. The application of the CL_s method returns a number of failed toys that remains stable below the 1%. At such a low statistics regime, the description of the background template might suffer from fluctuations that

USC UNIVERSIDADE DE SANTIAGO DE COMPOSTELA

[3]Note that, for displaced samples, the $\mathcal{B}$ parameters are shared across different reconstruction categories.

$m(a_1)$, $m(a_2)$ [GeV]	τ_{a_1} [ps]	Upper Limit Exp 95% CL	
		$B_s^0 \to 4\mu$	$B^+ \to 4\mu K^+$
PHSP	0	$1.6 \cdot 10^{-9}$	$8.8 \cdot 10^{-10}$
0.25, 0.40	1	$1.9 \cdot 10^{-8}$	$2.7 \cdot 10^{-8}$
	10	$3.9 \cdot 10^{-9}$	$2.9 \cdot 10^{-8}$
	100	$8.9 \cdot 10^{-9}$	$8.0 \cdot 10^{-8}$
	1000	$3.9 \cdot 10^{-8}$	$4.6 \cdot 10^{-7}$
2.00, 2.75	1	$2.9 \cdot 10^{-9}$	$2.4 \cdot 10^{-9}$
	10	$1.4 \cdot 10^{-9}$	$1.5 \cdot 10^{-9}$
	100	$3.3 \cdot 10^{-9}$	$4.6 \cdot 10^{-9}$
	1000	$2.2 \cdot 10^{-8}$	$3.9 \cdot 10^{-8}$
		$B_s^0 \to 6\mu$	$B^+ \to 6\mu K^+$
PHSP	0	$9.7 \cdot 10^{-9}$	$2.6 \cdot 10^{-9}$
0.50, 1.50	1	$3.7 \cdot 10^{-9}$	$2.6 \cdot 10^{-9}$
	10	$8.0 \cdot 10^{-9}$	$5.5 \cdot 10^{-9}$
	100	$1.7 \cdot 10^{-7}$	$6.4 \cdot 10^{-8}$
1.25, 3.50	1	$2.7 \cdot 10^{-9}$	$3.6 \cdot 10^{-9}$
	10	$5.2 \cdot 10^{-9}$	$4.8 \cdot 10^{-9}$
	100	$4.1 \cdot 10^{-7}$	$2.5 \cdot 10^{-7}$

Table 5.39: Expected 95% CL upper limits on the $\mathcal{B}(B_s^0 \to 4\mu)$, $\mathcal{B}(B^+ \to 4\mu K^+)$, $\mathcal{B}(B_s^0 \to 6\mu)$ and $\mathcal{B}(B^+ \to 6\mu K^+)$ for the sideband shape method.

may take the fit out of convergence.

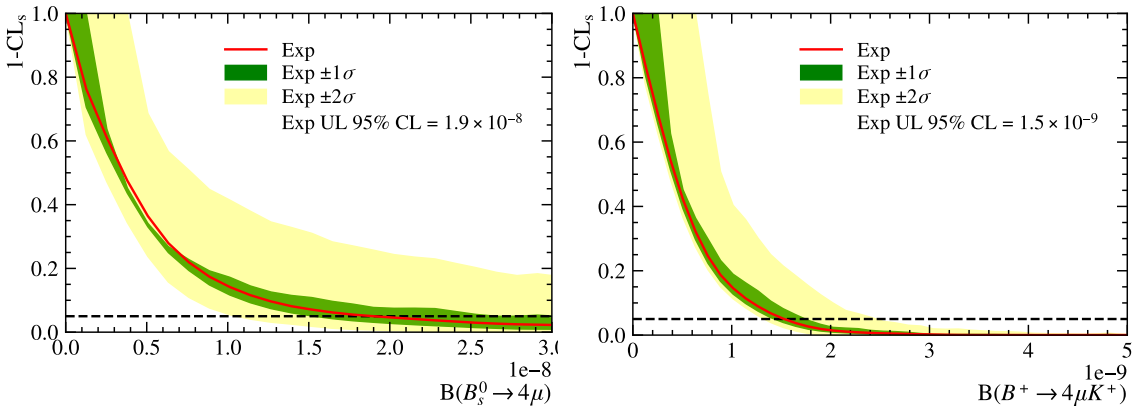
With the results in hand, lifetime-dependent limits can be obtained. Before official approval to unblind results, a 1-D B-spline curve [288] is used to interpolate mass integrated limits in the range $(1, 1000)$ ps and $(1, 100)$ ps for 4μ and 6μ modes, respectively. Results can be observed in Figure 5.41.

The limits obtained largely confirm the expectations generated by the phenomenological analysis. Note that, here, effects from both the efficiency behaviours discussed in Section 5.7.2 and background suppression apply:

- First, the larger phase-space in 4μ modes allows larger transverse-momentum variations, which results in a more pronounced bump around the maximum sensitivity point. At higher lifetimes, the $B_s^0 \to 4\mu$ brings more sensitivity because of the higher background suppression with respect to $B^+ \to 4\mu K^+$. Within each channel, the behaviour between the lower and higher mass points can be explained by the sensitivity profile, as discussed in Section 5.7.4.

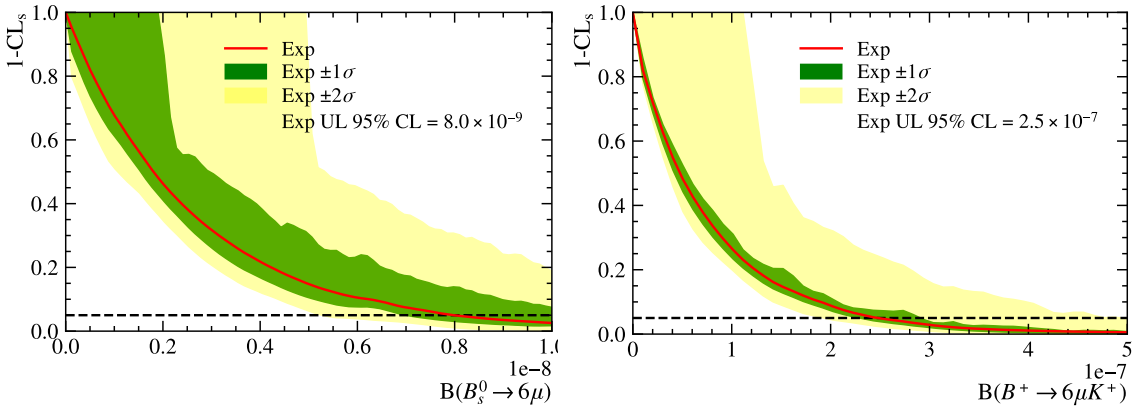
USC UNIVERSIDADE DE SANTIAGO DE COMPOSTELA

- Second, the lower sensitivity reach in 6μ channels can be explained, again, by the more-restricted phase-space regarding transverse momentum. Here, the lower



(a) $B_s^0 \to 4\mu$, $(m_{a_1}, m_{a_2}, t_{a_1}) = (0.25$ GeV, 0.40 GeV, 1 ps).

(b) $B^+ \to 4\mu K^+$, $(m_{a_1}, m_{a_2}, t_{a_1}) = (2.00$ GeV, 2.75 GeV, 10 ps).



(c) $B_s^0 \to 6\mu$, $(m_{a_1}, m_{a_2}, t_{a_1}) = (0.50$ GeV, 1.50 GeV, 10 ps).

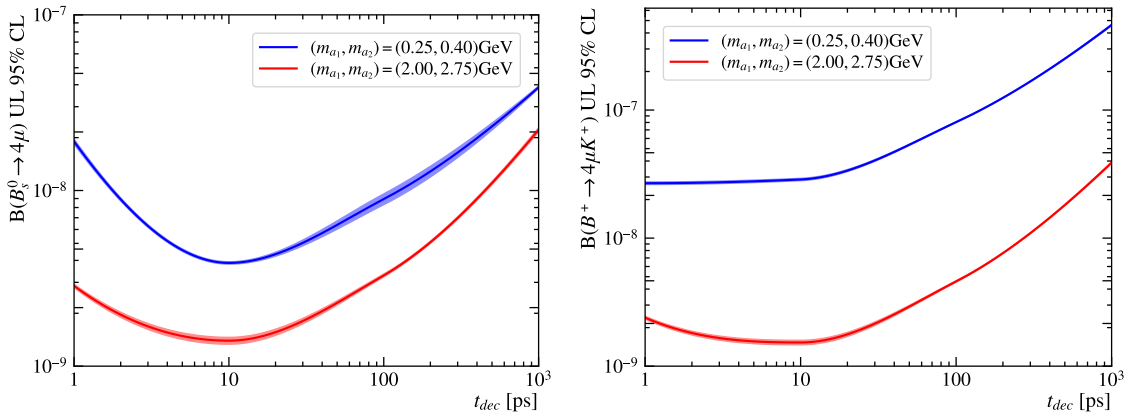
(d) $B^+ \to 6\mu K^+$, $(m_{a_1}, m_{a_2}, t_{a_1}) = (1.25$ GeV, 3.5 GeV, 100 ps).

Figure 5.40: Miscelanea of Expected limits at 95% CL and associated error bands for different modes with masses and lifetimes.

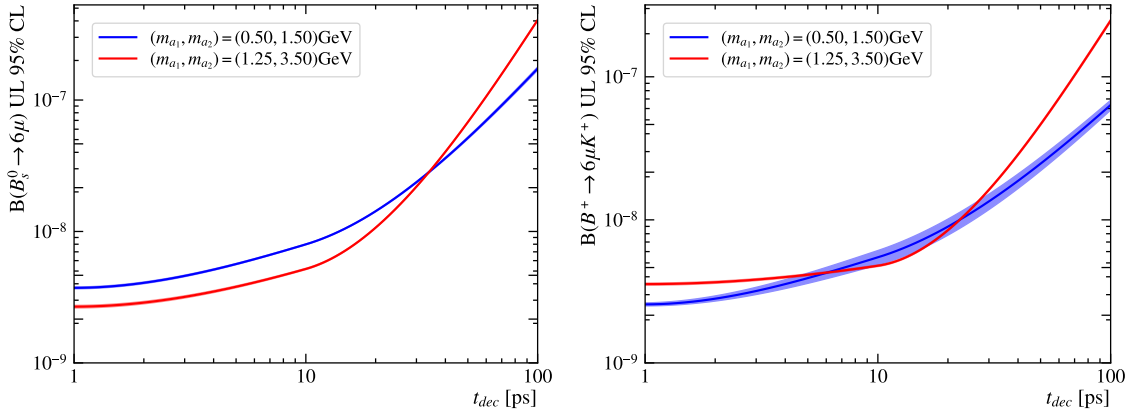
levels of background allow the effect of high-boost muons coming from a lighter resonance dominate at high lifetimes. At lower lifetimes, a clear difference can be observed between the masses corresponding to the $B_s^0 \to 6\mu$ and $B^+ \to 6\mu K^+$ channels. Such a difference can be explained by the fact that, the higher the number of final particles, momentum balance causes the higher-mass mode to suffer to achieve trigger requirements.

As seen in Section 5.6, an important contribution from $B^+ \to J/\psi(\mu^+\mu^-\mu^+\mu^-)K^+$ is expected to be present in the signal region. A pre-unblinding check is done by selecting, within the unblinded signal region, $m(4\mu)$ compatible with the hypothesis of J/ψ and the full selection is applied. The result is displayed in Figure 5.42, where a fit to the invariant mass with a background plus signal hypothesis is shown. The result of the fit is $N_{sig} = 5.1 \pm 2.3$

With the results of the fit, the Branching Fraction measurement for the corresponding channel can be performed and can be compared with the SM value $\mathcal{B}^{\rm SM}(B^+ \to$



(a) $B_s^0 \to 4\mu$. (b) $B^+ \to 4\mu K^+$.



(c) $B_s^0 \to 6\mu$. (d) $B^+ \to 6\mu K^+$.

Figure 5.41: Lifetime-dependent mass-integrated expected limits for Multimuon modes.

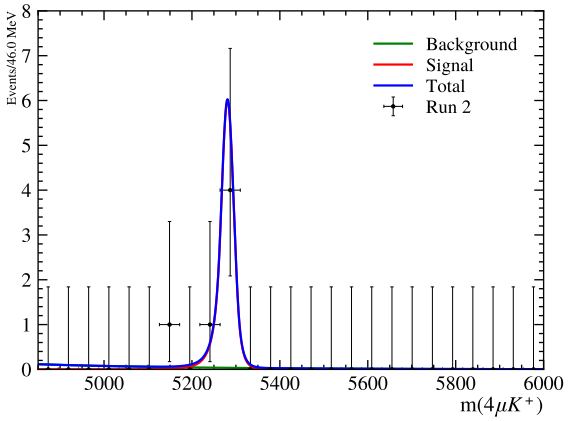


Figure 5.42: Mass fit to the invariant mass $m(4\mu K^+)$, corresponding to the $B^+ \to J/\psi(\mu^+\mu^-\mu^+\mu^-)K^+$ channel. The full statistics for Run 2 data are used.

$J/\psi(\mu^+\mu^-\mu^+\mu^-)K^+) = (1.13 \pm 0.14) \cdot 10^{-9}$. The result of the check is:

$$\mathcal{B}(B^+ \to J/\psi(\mu^+\mu^-\mu^+\mu^-)K^+) = (7.72 \pm 3.6) \cdot 10^{-10} \tag{5.32}$$

which is compatible within 1σ with the SM value and therefore validating the sensitivity of the analysis for the full unblinding stage.

USC UNIVERSIDADE DE SANTIAGO DE COMPOSTELA

6

Installation of a demonstrator detector: CODEX-β

The exploitation of the full High-Luminosity LHC (HL-LHC) dataset for new physics searches with CODEX-b depends critically on the development of a reliable, shielded, and displaced prototype that demonstrates the future feasibility of the experiment. CODEX-β, currently an LHCb R&D project, is integrated as a sub-detector for Run 3. This configuration is designed to enhance the physics reach of both LHCb and CODEX-β, providing a crucial stepping stone toward future large-scale detectors targeting LLP signatures.

The work presented in this thesis contributes to this effort through several key aspects related to the construction of RPC detectors and the installation of CODEX-β. The initial tasks comprise the construction and testing of the first RPCs, including the gluing process, the application of resistors to the readout strips, and the installation of the front-end boards. These steps are followed by the assembly of the Faraday cage and subsequent cosmic ray testing. Once the preparations are completed, the assembly phase proceeds with the preparation of voltage and gas services, the construction of the support structure, and the installation of the RPC detectors. All these activities are carried out within a large collaborative team, with major contributions from IGFAE, the University of Cincinnati, and CERN.

6.1 RPC Assembly and Commissioning

The baseline design of the CODEX-β prototype consists of a 2 m cubic structure with all six faces instrumented with Resistive Plate Chamber (RPC) tracking technology. Each face hosts two $2 \times 1\,\mathrm{m}^2$-pitch RPC modules, resulting in a total of 14 RPC triplets. Every triplet is mounted within a dedicated aluminium frame (Figure 6.1, left), adapted from the ATLAS BIS-78 design and optimized for transportation, as

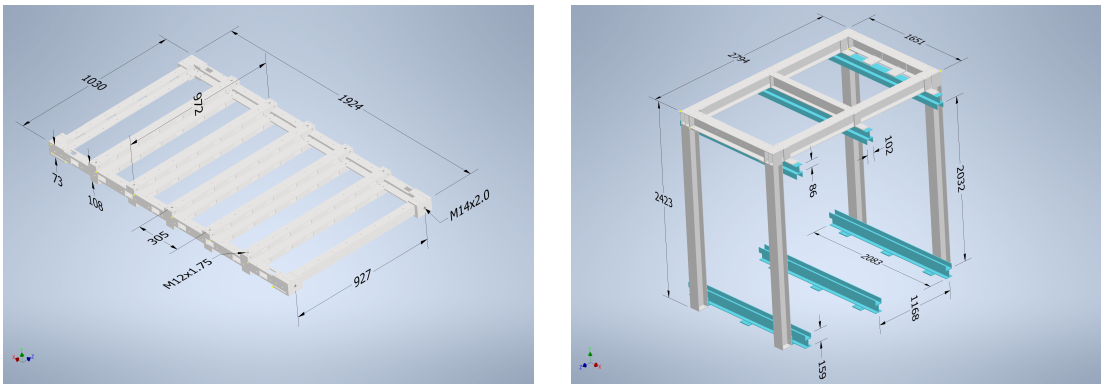


Figure 6.1: Left: Aluminium frame for RPC triplets. Right: Mechanical support structure for the CODEX-β detector. Obtained from [241] under CC BY 4.0.

well as streamlined delivery of gas and power services.

Two opposing faces (the η and ϕ readout sides) are designed with apertures to allow installation of orthogonal strip panels, while the other two faces are blind sides, electrically grounded to improve shielding. The full cubic assembly is supported by a mechanical structure equipped with six aluminium rails, enabling the installation of 10 out of 14 tracking modules. The remaining modules are positioned on mobile transport carts attached to opposite sides of the cube (Figure 6.1, right).

The first stage of RPC construction consists of gluing the copper-clad insulating sheets and readout strip panels onto lightweight PVC foam boards (FOREX), chosen for their rigidity and low weight. A rolling press and metal alignment guides ensure precise positioning and uniform adhesive spread. During this stage, careful inspection is required to detect trapped air bubbles between the foam and strip panels, as these may degrade capacitive coupling—resulting in signal attenuation or amplification—and compromise long-term mechanical stability. Each RPC module (Figure 3.19) is assembled using two FOREX–copper panels that sandwich a single gas gap, with orthogonal strip panels (η and ϕ) mounted on opposite sides.

After gluing, resistors are mounted on the strip panels to connect the readout elements and guard lines to their reference potentials. The readout structure consists of copper strips traversing the length (η coordinate) or width (ϕ coordinate) of the panel. Additional fine copper traces act as guard lines to collect induced currents and are routed to ground through a perimeter ring (Figure 6.2, right). Resistors of 20 Ω are used for strip readout connections, while 1 kΩ resistors are used for guard-line grounding. Each resistor is tested individually to ensure proper conductivity. To complete electromagnetic shielding, a 2 mm copper wire is soldered around the perimeter of each panel, forming a continuous Faraday cage.

The readout of the RPC strip panels is performed by custom front-end Printed Circuit Boards (PCBs). Each board hosts eight channels of a newly designed preamplifier, two four-channel custom ASIC discriminators, and integrated Low-Voltage Differential Signaling (LVDS) transmitters [241]. A schematic of the PCB layout is shown in Fig-

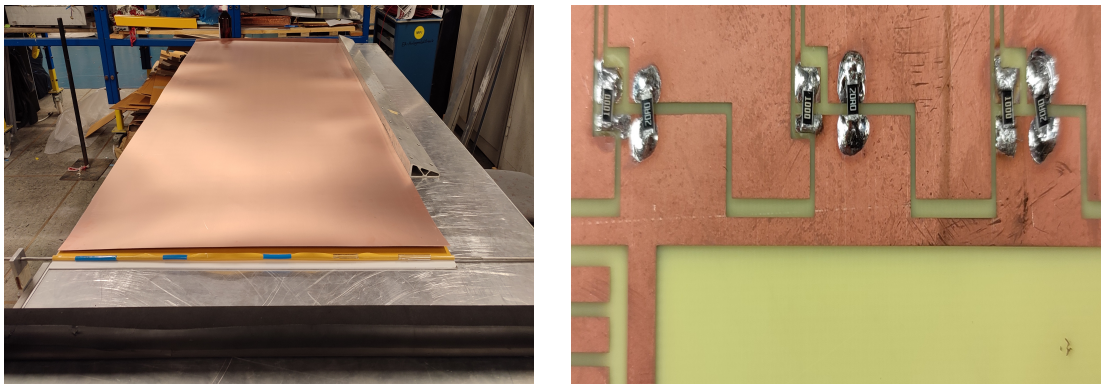


Figure 6.2: Left: Panel gluing and rolling setup. Right: Resistor installation on a readout strip panel.

ure 6.3.

The PCBs are connected to the readout strips as follows:

- **Bottom side:** Six soldering pads connect to the wiring harness. The first pad is ground, while the remaining five provide low-voltage power to the board[1].
- **Top side:** Sixteen soldering pads alternate between strip and ground connections (strip–ground–strip–ground) across the full board length.

This configuration supports simultaneous readout of eight channels per PCB. Boards are grouped into sets of four for a full η panel or eight for a ϕ panel.

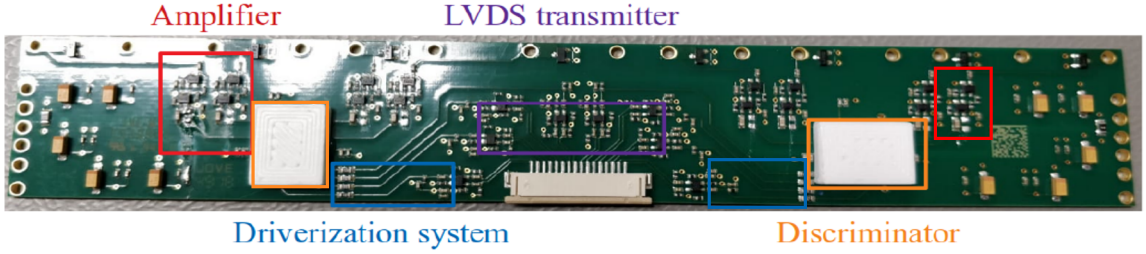


Figure 6.3: Front-end PCB designed for single-gap RPC modules of the CODEX-β detector.

Rigorous testing accompanies each stage of assembly and integration to ensure long-term detector stability and reliable data acquisition.

- **Electrical continuity tests:** After resistor installation, all connections between soldered points, ground, and strips are verified using a precision ohmmeter.
- **Power verification:** With the board connected to a controlled power supply, measured voltages at the input pads are compared to nominal values to ensure correct operation.

[1]From bottom to top: 1—Threshold voltage, 2—Preamplifier supply, 3—Pull-up bias, 4—Discriminator supply, and 5—LVDS transmitter supply.

- **"Touching finger" response test:** This test checks the integrity of the readout chain by inducing a capacitive signal via a human touch. The response confirms proper connectivity of strips, preamplifiers, and discriminators, serving as a rapid diagnostic of channel functionality.

An RPC gas gap consists of a 1mm-wide gap whose uniformity relies on polycarbonate spacers of 10 mm diameter, elements embedded in between two sheets of phenolic High Pressure Laminate (HPL), with resistivity between 10^{10} and $10^{11}\Omega cm$. The external surface of the electrodes is paint with graphite with a superficial resistivity ρ of $\sim 500k\Omega/\square$ [241], allowing a uniform distribution of the high voltage and at the same time allowing the inductive pick-up of the charge created within the gas. The inner surfaces of the electrodes are coated with a few μm thick layer of polymerized linseed oil to avoid the spike effect, which creates an electrical field inhomogeneity and increases the detector noise [241]. A picture of an operational gas-gap element is shown in Figure 6.4 left.

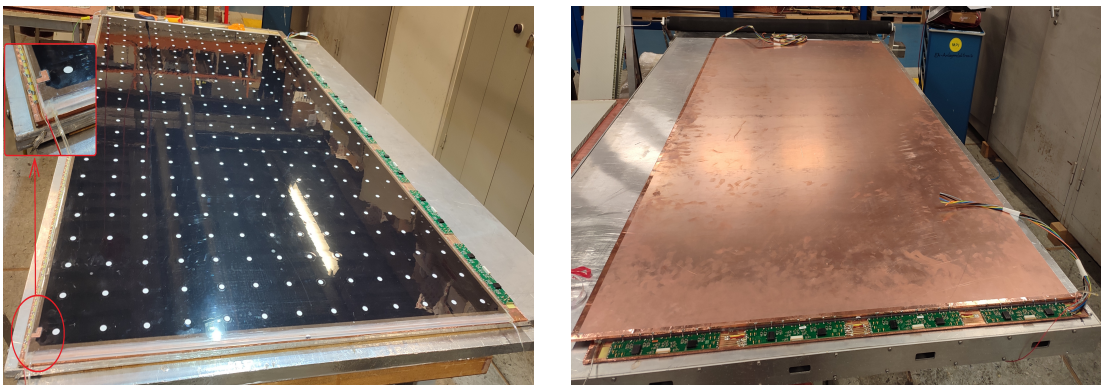


Figure 6.4: Left: Gas Gap placement and orientation. Right: Full Singlet assembly.

In terms of fully assembling the RPC module (Figure 6.4 right), the gas gap is placed between the orthogonal strip panels, with a ϕ card lying down and electronics facing up and with a η card on top and electronics facing down. Once it is ensured a perfect alignment among the different layers, the sides are covered with Aluminium tape and thin FOREX wires are included to enhance uniformity. At the end, all the top grounds of the board (8 per board) must be soldered with a copper wire bridge to the ground reference of the panel.

At this point, several tests have to be performed in order to check the quality of the chamber:

- **Faraday Cage test:** Electromagnetic shielding of the cage is checked by turning up the low-voltage supply on the PCBs, observing no radio frequencies or other spurious signals on the oscilloscope. The base level must correspond to the voltage of the LVDS transmitter. By increasing the threshold voltage from the discriminator, the noise is not able to jump across that limit, and the Faraday

USC UNIVERSIDADE DE SANTIAGO DE COMPOSTELA

cage is activated, returning clear avalanche signals. The test is repeated with the High Voltage on. An illustration can be observed in Figure 6.5.

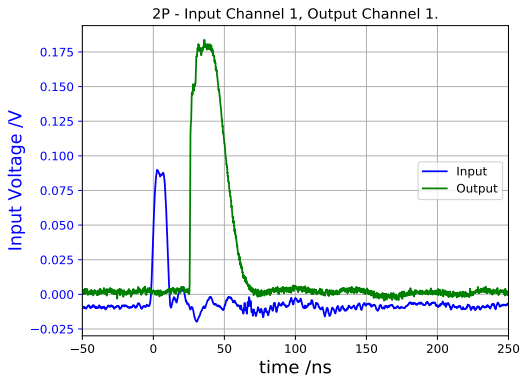
- **Current-Voltage curve test:** Evaluates the current flow in the active detector (gas gap) with the high voltage that is applied. An example can be consulted in Figure 6.5 b), where the different charge regimes are observed:

  – Low Voltage ($\sim 1 - 3\,\text{kV}$): Ohmic leakage through resistive electrodes, electron avalanche is not sustained.

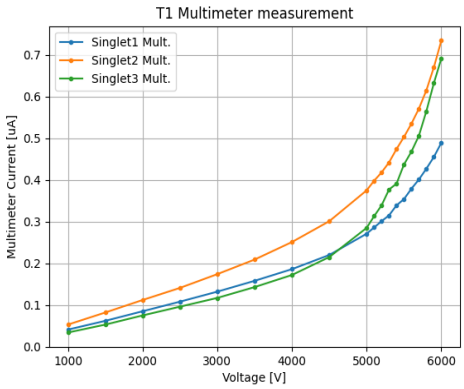
  – Transition region ($\sim 4 - 5\,\text{kV}$): Intensity growth due to the starting point of electron avalanches, though not dominant.

  – Avalanche region ($> 5\,\text{kV}$): Controlled avalanche processes occur, with current being limited by the resistivity.

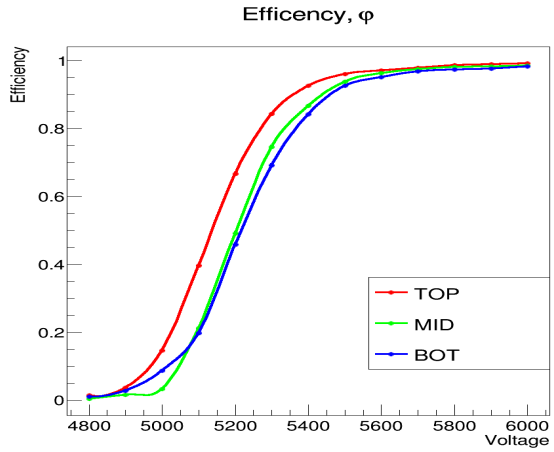
  At higher voltages, discharge processes will begin to occur, with greater or lesser occurrence depending on the gas mixture or the material chosen. Therefore, the nominal operation point is located below 6 kV.



(a) Faraday cage test.



(b) I-V curve test.



(c) Efficiency computation on ϕ card.

Figure 6.5: Results of different tests over RPC modules.

The final test to ensure RPC operability includes the assessment of the DAQ response of each triplet working in coincidence mode. The procedure makes use of cosmic ray muons and comprises the following steps:

- **Operation test:** Each singlet is set to the nominal working point (~ 5.8 kV) and the trigger is set on. No dead channels must be observed, with a homogeneous occupancy in the strips.

- **Chamber noise:** Each singlet is set to the working point and the trigger off, so that every single hit on the RPCs is stored. It must be verified that the background noise rate remains uniform between channels and over the acquisition time, which rules out discharges in the material as well as structural imperfections.

- **Fake muon test:** The first two RPCs are set to the working point and the third one to 0 V. The trigger is therefore fired by the first layers in coincidence. The synchronous monitoring of the third layer must not reveal any hits, which would be indicative of unwanted couplings or correlated noise.

- **Efficiency test:** Finally, the efficiency of the layers in coincidence mode is evaluated with the tag-and-probe method. The procedure relies on setting 2 out of 3 RPCs to the working point, whereas in the remaining one a scan between 4 and 6 kV is performed. On each point, the efficiency is computed as the ratio:

$$\varepsilon = \frac{N_{3,\text{hits}}}{N_{2,\text{hits}}} \tag{6.1}$$

  where $N_{3,\text{hits}}$ stands for the number of hits recorded in coincidence mode on the three layers and $N_{2,\text{hits}}$ for the number of hits which fired the trigger. An example can be found in Figure 6.5 c), which shows the breakdown of efficiencies per singlet in a ϕ card. In every check, the efficiency exceeds the 98% threshold.

In total, 42 RPC singlets are assembled and commissioned, with satisfactory results. In a few cases, some channels exhibit an unusual noise rate or even show dead. For such specific cases, resistoring of the different components is reconsidered, the soldering of active elements revisited and the Faraday cage structure re-built. Again, the latter ones are subjected to the same test procedure, alleviating the causes of these errors and explaining the deviations previously observed.

6.2 Mechanical integration and Service Routing

USC UNIVERSIDADE DE SANTIAGO

Triplets are assembled within an Aluminium mechanical frame, optimized for alignment preservation (keeping a uniform pressure over the singlets' surfaces), services supply

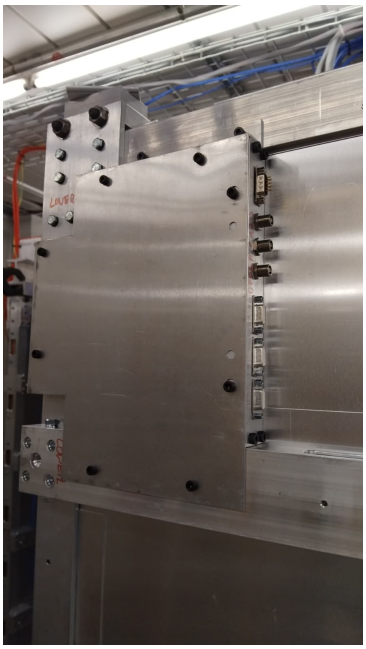


Figure 6.6: Usual frame configuration for a set of triplets (left) and assignment of connections (right).

(high and low voltage and gas) and transportation. The modular structure allows for the assembly and dismantling of any component at any time [241].

The structure of CODEX-β consists of 7 instrumentalized faces, enclosing two RPC triplet modules. Each one is equipped with four service boxes, which provide each RPC with the needed services. An example of a service box with current readout, high voltage and low voltage suppliers is displayed in Figure 6.6. Under such a configuration, low voltage connectors power η card PCBs, whereas the ϕ side is supplied by an exclusive low voltage service box. Regarding gas circulation, two exclusive service boxes serve as input and output for each triplet.

A critical aspect in the preparation of services is the connection between the RPC modules and the power and gas suppliers. The first is supplied through a CAEN mainframe SY4527 [289] with a total power of 1200 W, which provides both low voltage and high voltage components. The second consists of a recirculation system [290] connected with a return line to the surface (Figure 6.7 left), to control the gas distribution and minimize emissions. In order to correctly prepare the connection between the RPCs and such services, the following actions were taken:

- **High Voltage:** 42 RG58 coaxial high-voltage cables with corresponding female panel-mount coaxial connectors [241] were manufactured to connect the power alimentation to each RPC. As only 12 HV ports were available, each output wires are split into 4 through heavily insulated splitters.

- **Low Voltage:** Connection between the power supply and the RPCs is carried through a patch panel, which distributes low voltage throughout all the panels. In terms of keeping modularity, each 2 RPC ensembles contains a Low-Voltage

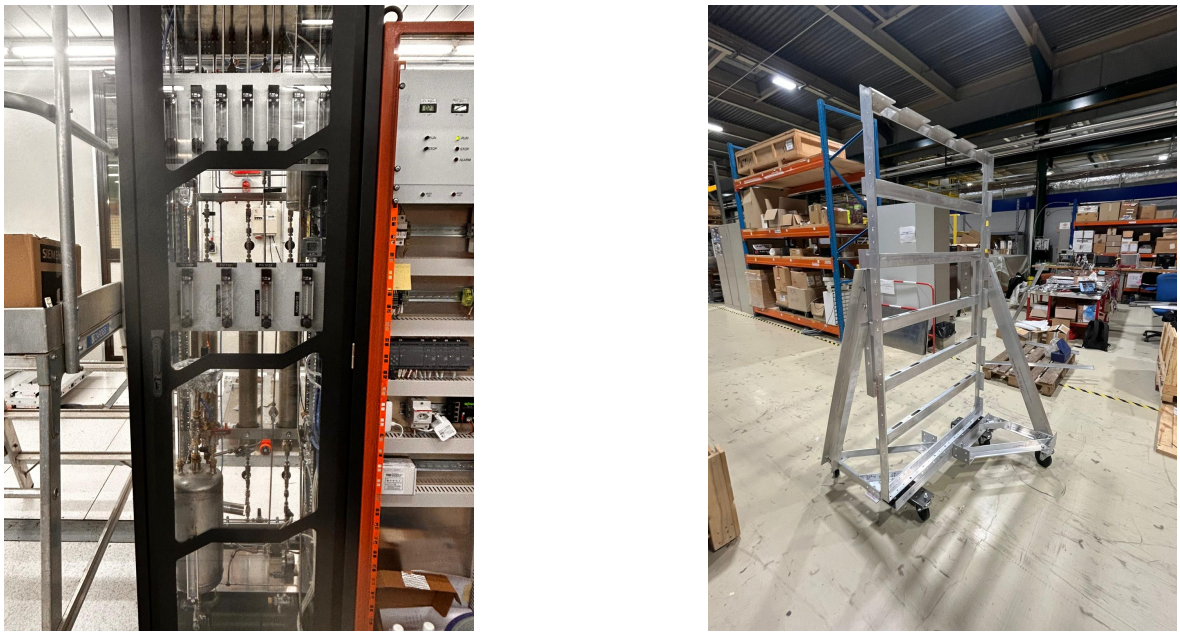


Figure 6.7: Transportation cart for a full assembled RPC triplet frame (left) and Gas Recirculating system in D1 barracks (right).

Distribution Board (LVDB) which is in charge of routing all connections to the corresponding service boxes. Additionally, all data acquisition modules (DCTs) are independently powered through dedicated LV cables. In total, 12 LV cables to connect the power supply and the patch panel, 7 to connect the corresponding LVDBs, and $\sim$ 98 for distribution to the service boxes.

- **Data:** All DCTs comprise 2 types of acquisition connections, 3 with 68 channels and 3 with 80 channels, making up to 112 data acquisition cables to manufacture.

- **Gas:** Each module is connected with 1 input and 1 output line, which is consecutively divided into 2 (to reach each frame) and 3 lines (to feed each RPC). Two dedicated gas service boxes are located on top and bottom of each frame, the last being the gas input due to its lighter weight compared to air. Each gas line is equipped with an impedance to control the gas flow over the entire circuit.

In terms of minimizing the vibration that each triplet suffers during transport while simplifying the technical aspect as much as possible, dedicated modular carts have been designed for this purpose. Such a design consists of an aluminium base channel bar that rests on mobile axes and distributes the 150 kilos of weight of a full-assembled frame through triangular rails that support the clamping bars. All the carts can adopt two forms: transportation mode, featured by the removal of two diagonal triangular rails (Figure 6.7 right), and installation mode, with all the triangular rails properly installed. This last mode is selected when the lateral frames complete the full detector envelope (remember Figure 6.1 right).

USC

6.3 Installation of CODEX-β

The location to install CODEX-β, apart from coinciding with the one for the future CODEX-b (Figure 3.18), responds to the optimization of the physics reach, while keeping as much accessibility as possible to all the detector elements. During its timeline, the installation procedure overcomes a set of drawbacks that the future idea of CODEX can profit from.

The first action is the preparation of the D1 barracks, for which the server racks are dismantled and the service racks settle down. The dimensions and weight of the demonstrator force that the assembly must be done entirely on-site; therefore, a sufficiently large space must be enabled to accommodate the demonstrator, the service racks and access to each element of the detector. This fact, together with the need to maximize the physics case, leads CODEX-β to be installed in the bottom-right corner of the D1 barracks, in front of the principal access and with 0.5 m from the wall.

Once the experimental area is prepared, the triplets are assembled in their respective frames, while the internal connections (electricity and gas) between the RPCs and the service boxes are enabled. The triplets begin to be transported to the experimental cavern, where they remain stored until the support structure is completely assembled. For such a purpose, up to five transporting carts are enabled.

The transportation procedure relies on the flexibility of the cart structure and the dimensions of the frame-cart set. Under such a possibility, the path connecting the personnel elevator located at the PZ85 shaft with the D1 barracks is used. The reliability of the cart-frame set is highlighted by the fact that, with no operability of the personnel elevator, several triplets are diverted through the LHCb's main shaft via the main crane. Evaluation in situ regarding the status of frames and trolleys reflects the lack of adverse effects caused by the transport.

After the initial preparation is complete, some additional prerequisites must be fulfilled on-site to start the cube assembly. The weight of the superstructure, evaluated in several tons, must be distributed uniformly to prevent the collapse of the D1 barracks floor, made from 150 mm-wide beams with tiles lying over them. The solution, supported by the CERN safety teams, is to directly anchor the entire cube structure on top of the top flanges, which effectively allows it be anchored on the floor. Structural bolting on the beams is the preferred method since the lack of crossing beams on the bottom face design prevents columns from suffering lateral stress.

As introduced in Figure 6.1 right, the cubic support structure contains a set of rails which, after the rolling of the frames, allow for positioning them with the corresponding orientations across the envelope. Three different types of modules are differentiated:

USC UNIVERSIDADE DE SANTIAGO DE COMPOSTELA

- **Upright-rail modules:** They are kept in an upright position once they are rolled in the corresponding rails. Each of them contains wheels attached to the bottom edge of the frame. A total of 8 frames adopt such a position.

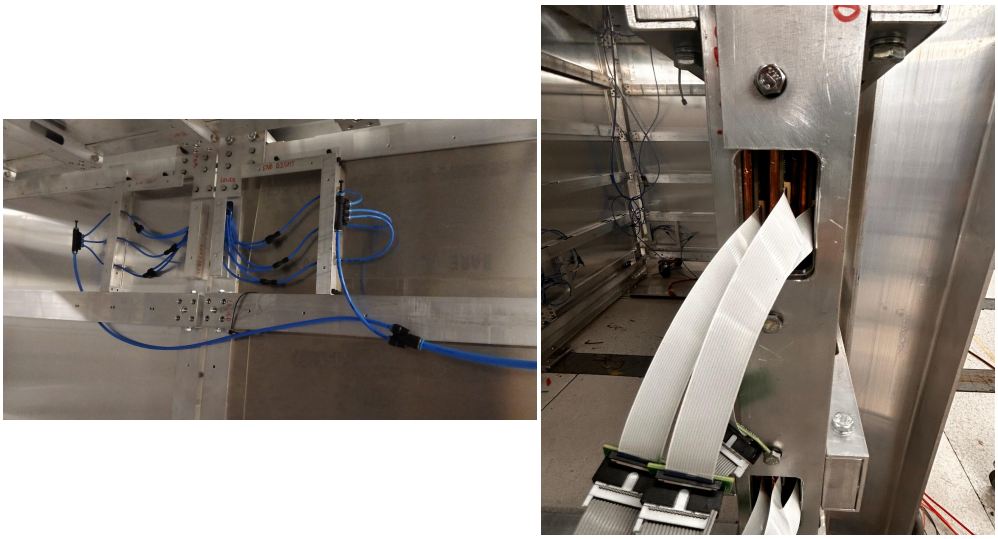


Figure 6.8: Provision of services during the installation phase: gas input and output lines installation in the service box (left) and assembled triplet of RPCs with the data acquisition cables installed.

- **Upright-lateral modules:** They are kept at all times attached to their transporting carts, which adopt the installation position. A total of 4 frames are kept in such a position.

- **Flat modules:** They are configured in a flat position, on the floor and bottom parts of the superstructure. Those modules are characterized by wheels wthat are attached to the faces of the frames. There are a total of 4 frames installed in such a position.

The final assembly and inclusion of the RPC frames lead to the alignment of every element on the cube. As the spatial resolution of an RPC can reach ~ 1 mm, a mechanical alignment precision of less than 10 mm is desirable [241]. For such a purpose, several external bolt locations on each frame can be used to secure them to both the support structure and adjacent frames via precision brackets. In this manner, the physical position of the active element for each RPC triplet is already defined before installation, and as long as all the brackets are in place, the modules should be aligned to within 5 mm for adjacent modules.

After the completion of the previous stages, the provision of services is carried out directly on the final assembly. In Figure 6.8 it is displayed the completion of the gas circuit in a module (left) and the inclusion of the PCB connector cables in a fully-assembled triplet are displayed. In this same configuration, it must be verified that the power and gas services can be safely connected from their distributors to each of the modules, as well as verifying that they cover the needs of each active element of the detector. Likewise, the tests described above for each RPC must be repeated to ensure that no action during the transport and assembly process could have caused structural damage to any of the modules. At the time of writing this thesis, these tests are still



Figure 6.9: The detector CODEX-β, successfully installed in the LHCb experimental cavern.

USC UNIVERSIDADE DE SANTIAGO DE COMPOSTELA

in progress.

In Figure 6.9, a picture of the full CODEX-β demonstrator can be found, representing a consolidation milestone for the CODEX-b collaboration. Before the detector can begin its journey in Run 3, however, the reaffirmation tests as well as the installation of all DCT modules must be completed. A major challenge to be faced before the start of the Run 3 journey is related to the DAQ system. As already mentioned, each DCT reads two modules simultaneously and interacts with a backend module bidirectionally through the lpGBT protocol [291], sending data and receiving commands and control instructions. However, the LHCb DAQ finds these two split into two boards: the TELL40, responsible for sending the data to the LHCb acquisition system and the SOLL40, responsible for command transmission. The reconciliation between those architectures requires the installation of an additional intermediate layer to allow bidirectional communication between them. This way, the acquired data from CODEX might be treated the same way as the data required from LHCb HLT1 and HLT2.

USC UNIVERSIDADE DE SANTIAGO DE COMPOSTELA

7

Fast Simulation Framework for CODEX-b

A core challenge in the design and optimization of any LLP detector is the choice of benchmark scenarios with which to evaluate the response under variations of the detector geometry and layouts [292]. For CODEX, its relatively big size and the space limitations in the LHCb cavern make it unavoidable to consider a relaxation of the experimental criteria of the nominal design (Section 3.6), as well as possible location reassignment in case of technical drawbacks. For such a purpose, a fast-simulation framework is designed to analyze the different designs under the broad signal morphologies CODEX would show sensitivity to. Such a framework is also the seed for a future complete simulation project.

The baseline design of CODEX-b seeks to ensure a high track acceptance and reconstruction of the LLP decay vertex, as well as a powerful background suppression. For these purposes, a hermetic design is combined with a substantial amount of internal (and external) tracking stations to ensure hits as close as feasible to the decay vertex, and therefore maximizing the reconstruction efficiency. The intrinsic nature of the experiment[1], however, would allow reaching those levels of precision, whereas commuting to a non-hermetic configuration approach by reducing the number of tracking elements.

It is important to highlight that the simulation framework currently used in CODEX-b originates from the work carried out at Lawrence Berkeley National Laboratory (LBNL), which was initially oriented toward the optimization of geometries in LLP detectors [292]. Initially, the work in this line focused on performing estimates using the already established software; however, it eventually contributed to the development of several components — including geometry definitions, tracking, result analysis, and execution pipelines — in order to improve the physics case and streamline the framework

USC UNIVERSIDADE DE SANTIAGO DE COMPOSTELA

[1] Full instrumentalization of internal and external faces, as well as tracking layers organized in RPC triplets.

for an effective transfer to the rest of the collaboration.

7.1 Simulation Framework

The foundation of the fast simulation package rests on two independent modules to facilitate simulation generation and analysis:

- **Event Generator:** Pythia 8 [247] is used to simulate the corresponding generation mechanism, as well as the decay chains of interest.
- **Geometry kernel:** Each detector configuration is implemented as a set of geometric elements whose union denotes a volumic element in the 3-dimensional space. At a fundamental level, volumes are implemented as unions, intersections or complements of convex polytopes, compact convex shapes in any dimension, defined as the convex hull of a finite set of points [293].
- **Processors class:** A set of actions that are applied over lists of events whose output is used for analysis purposes. It allows the preparation of the desired files, checking conditions over a defined geometry or efficiency computation.

The modes which are preliminary included within the generation module are the dark photon portal $H^0 \to A'(e^+e^-)A'(e^+e^-)$ and the Higgs scalar portal $B \to X\varphi(e^+e^-)$ or $B \to X\varphi(\pi^+\pi^-)$, for which several masses and p_T distributions of the LLPs are created. In this manner, by encompassing a high and moderate boost production respectively, a wide range of multiplicities, kinematics and angular distributions of the expected final products in the CODEX fiducial volume are effectively covered.

From a statistical point of view, the generation of displaced vertexes finds a set of drawbacks that restrict statistics for physics purposes: subtended solid angle by the CODEX geometry extremely small (1%, normalized to 4π), number of decays attenuated by a factor $\sim e^{-\beta\gamma c\tau}$ and main generation of events in the pseudorapidity range of $3 < \eta < 5$, so that only relatively-high masses can reach the CODEX angular production. The analysis pipeline, in terms of optimizing the available statistics in the acceptance of the detector, comprises the following drivers:

- **Unit Setter:** Allows the configuration of units to use throughout the analysis chain.
- **Beam Splitter:** Performs partition of events with multiple LLP-producing decays into separate events with a LLP decay each. Applies especially for events containing $b\bar{b}$ pairs.
- **Reflection Processor:** Enhances the available statistics by a factor of 2 by performing a mirror transformation in the longitudinal momentum of the LLP $p_L \to -p_L$. The generation efficiency transforms as $\varepsilon_{Gen} \to \varepsilon/2$.

USC UNIVERSIDADE DE SANTIAGO DE COMPOSTELA

- **Rotation Processor:** Determines the flight direction of the LLP and calculates the maximum subtended angle between the production point and the CODEX geometry. Afterwards, the LLP is rotated N times[2] until it falls within the CODEX acceptance. Consequently, the generation efficiency transforms as $\varepsilon \rightarrow \varepsilon/N$.

- **Reweighting Algorithm:** Introduces generation weights according to an exponential distribution of the form $e^{-\beta\gamma c\tau}$. In this manner, the sensitivity reach can be analyzed in bins of the lifetime of the LLP. Additionally, it also resamples the LLP decay vertices and the daughters associated with them.

- **Volume Filter:** It evaluates the LLPs whose decay vertex is located within the CODEX acceptance.

- **Tracking Algorithm:** Each charged track associated with an LLP is propagated inside a geometry. Tracks are propagated in straight lines of the form $\vec{r} = \vec{r_0} + \lambda\vec{v}$. For each of the planes comprised by the geometry, the factor λ is computed, indicating: 1) $\lambda < 0$ crossing in the backward propagation direction, 2) $\lambda = 0$ no crossing and 3) $\lambda > 0$ a crossing point in the direction of propagation. Only if each track crosses a minimum of N_{min} planes, the event is triggered. Additionally, each track is requested to have a minimum momentum of 600 MeV for ensuring reconstructability and preventing multi-scattering [240]. Likewise, it is also requested that different tracks do not share hits across the tracking layers.

In terms of efficiency computation, weighted distributions are used to account for decay time weights and possibly dedicated generation weights (remember Equation 5.16), giving:

$$\varepsilon = \frac{1}{N_{Gen}} \sum_{i=1}^{N_{Gen}} w_i \sum_{j=1}^{n_i} r_j \tag{7.1}$$

where N_{Gen} is the total number of generated events, w_i the generation weight and r_j the decay-time weight. Note, additionally, the following indices: i runs over each event which is generated, whereas j runs over the possible LLPs allocated within each event. Given that the analysis framework works by creating multiple subsamples depending on the kind of process to be applied, the total amount of events which become discarded is tracked over the full procedure to properly normalize the LLP event weights. The Equation 7.1 is also updated according to the transformations discussed in the Reflection and Rotation steps, if applicable.

The nominal CODEX design ensures, with the active and passive vetoes, that any reconstructed event inside the detector can be assumed to be signal-like. Under such an assumption, if N_{CODEX} is the number of LLP events inside the detector, $\mathcal{L}$ the

[2]The unitary circumference is divided into N partitions with the relation $N = \frac{2\pi}{\Delta\Omega}$.

Luminosity and σ the cross-section of the decay of interest, the excluded Branching Ratio is given by:

$$\mathcal{B} = \frac{N_{\text{CODEX}}}{\varepsilon \sigma \mathcal{L}} \tag{7.2}$$

where the efficiency ε is estimated through the pipeline already discussed.

7.2 Results: ESPPU update

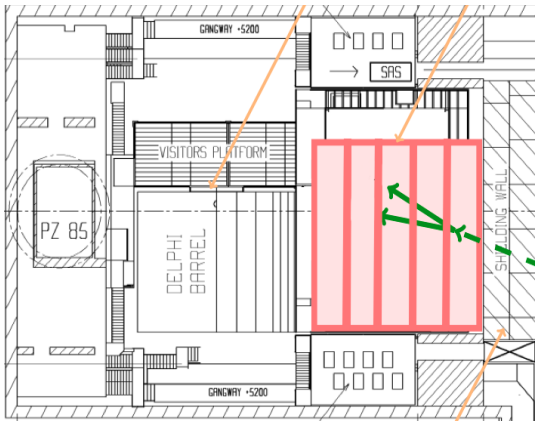
As an input for the European Strategy for Particle Physics Update (ESPPU), the fast-simulation framework is used to re-evaluate the nominal CODEX-b layout in light of technical constraints at the LHCb cavern. In this manner, a set of alternative layouts, highlighting the possibility of non-hermetic designs, is tested against several physics cases.

The lack of viability of the nominal design, based on the optimization of vertexing capabilities and the suppression of backgrounds, resides in the impossibility of dismantling the D1 barracks. Maintaining the original design despite this adversity would require the inclusion of different materials (servers, service racks, etc.) between detection planes, which would add difficulty to the simulation system and the provision of the necessary services for the RPCs. For such a reason, the following designs are studied (a schematic map can be found in Figure 7.1):

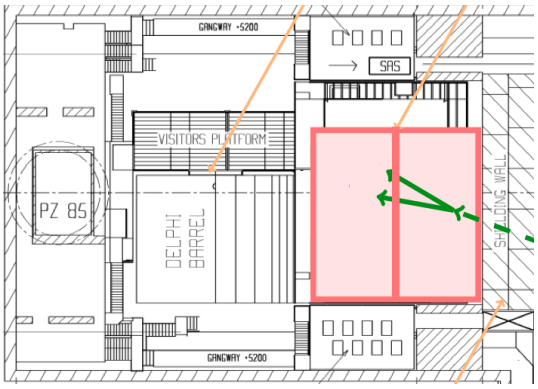
- **Nominal:** Discussed in Section 3.6, comprises 800 RPC singlets and located in the D1 barracks (Figure 7.2 a).
- **D1 barracks with 1 tracking layer:** The original design, with the envelope and 4 inner faces, is modified so that the envelope is formed by 3 RPC triplets separated by 0.5 m and an additional triplet is included in the middle, separated by 5 m from each of the external faces (Figure 7.2 b). With such a configuration, a high tracking efficiency should be kept while maximizing the internal space in terms of storing material.
- **D1 barracks plus DELPHI visitors platform:** 3-RPC triplet envelope without inner tracking station; an adjacent module is installed in the DELPHI visitor platform, which could enhance sensitivity reach at higher lifetimes with respect to the latter ones (Figure 7.2 c).

For the purpose of sensitivity analysis, 50.000 events are generated with Pythia 8 in two different mass points for both the Dark Photon and the Higgs-Scalar portals. In the latter case, in order to properly reproduce the broad p_T spectrum of produced B-candidates, the total amount of events is divided into different p_T bins. Once completed, the datasets are passed through the different steps already discussed.

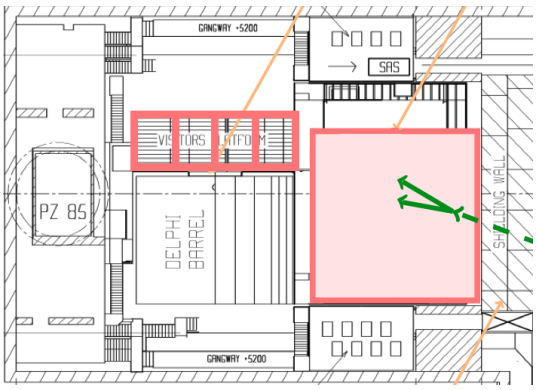
USC



(a) CODEX-b baseline proposal.



(b) CODEX-b alternative with only one internal plane.



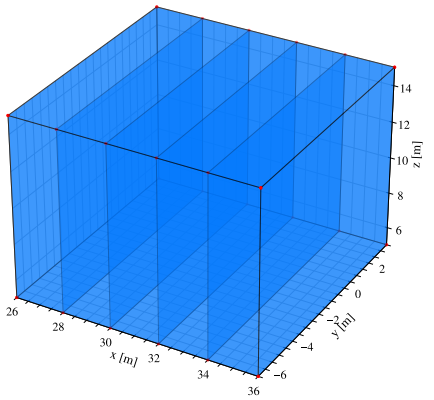
(c) CODEX-b with additional tracking cube in DELPHI visitors platform.

Figure 7.1: Location and configuration of nominal and alternative CODEX geometries.

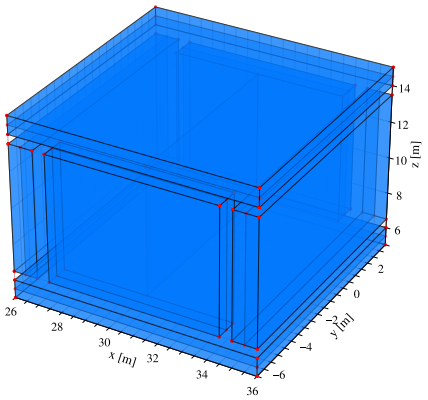
With respect to the calculation of the exclusion limits, the consideration of a background-free experiment allows to the use of Equation 7.2, being the different inputs $\sigma(H \to A^0A^0) = 50\,\text{pb}$ [294] and $\sigma(B \to KX) = 500\,\mu\text{b}$ [120] for the corresponding production modes and $\mathcal{L} = 300\,\text{fb}^{-1}$ for the expected target luminosity during Run 4. In terms of sampling the displacement characteristic $c\tau$, monotonic steps of $log(c\tau)$ of 0.5 are simulated in between 1.0 and 12.0, being the resulting curves interpolated with a PCHIP shape-preserving interpolator [295] and correspondingly interpolated to extremely-high lifetimes. The sensitivity reach to each benchmark can be observed in Figure 7.3 and 7.4.

One of the most remarkable facts is observed in the difference in sensitivity between the curves of the different benchmarks, which is explained by the different kinematic regimes: whereas in $H \to A^0A^0$, the LLPs are produced with a high-momentum distribution, the $B \to KX$ channel is limited by the mass of the B-meson, thus affected to a greater extent by the multi-scattering cut. Likewise, this difference in regime also affects the final topology, which explains the observed behaviour.

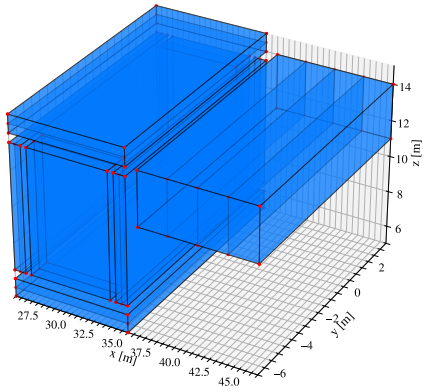
On the one hand (Figure 7.3), the nominal CODEX-b design remains the most



(a) Geometrical description of CODEX-b nominal design.



(b) Geometrical description for alternative CODEX-b, with one internal layer.



(c) Geometrical description for alternative CODEX-b, comprising nominal D1 barracks with an envelope of 3 RPC triplets plus a section in DELPHI visitors platform.

Figure 7.2: Alternative layouts for the CODEX-b experiment.

sensitive geometry to the dark photon portal across a great part of the spectrum, only surpassed by the D1 barracks and Delphi splitted volume at very high lifetimes. The main reason[3] lies in the fact that the higher the boost, the more collinear the charged daughters are with respect to the mother particle; therefore being the number of tracking planes to cross is the main cause of differences between curves.

On the other hand (Figure 7.4), a more restricted boost causes the opening angles with respect to the mother to be larger, making the number of stations in the transverse direction to the flight have a greater weight in determining the tracking efficiency. Under such circumstances, the nominal design only dominates in the region of small

[3]Note that the geometric efficiency (up to some extent) is constant between detector configurations

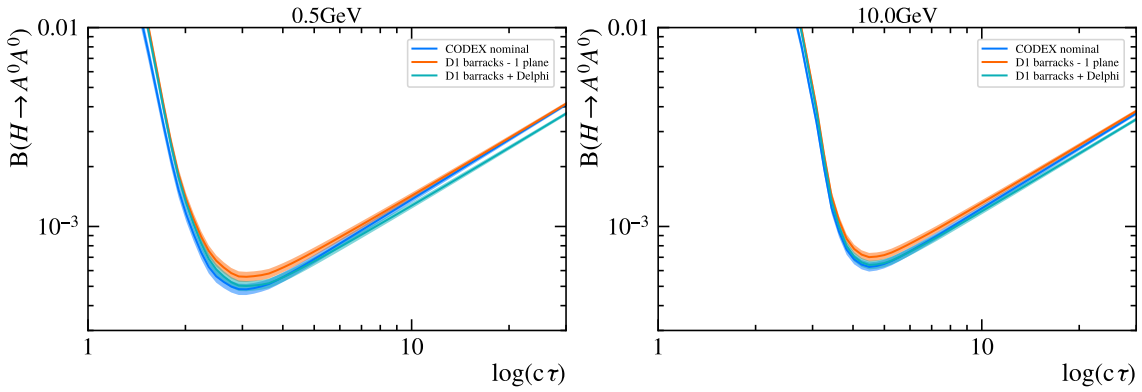


Figure 7.3: Comparison between CODEX-b proposals to the benchmark $H \to A^0 A^0$, considering two mass points for the Dark Photon particle. An integrated luminosity of 300 fb^{-1} is assumed.

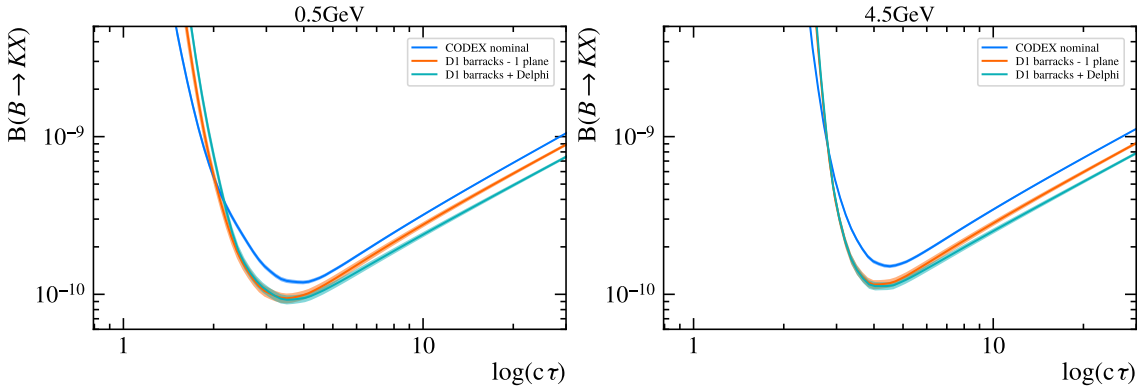


Figure 7.4: Comparison between CODEX-b proposals to the benchmark $B \to KX$, considering two mass points for the Dark Photon particle. An integrated luminosity of 300 fb^{-1} is assumed.

lifetimes, suggesting an enhanced detector performance with the reinforced envelope. Again, the configuration mixing D1 barracks and Delphi is the most optimal one at high lifetimes.

Another important conclusion of this study is that small variations in the number of tracking stations are not as important (in terms of efficiency) as their spatial arrangement. Dedicated studies have been developed with an optimization framework, which shows that even with half of the RPC modules, a considerably high efficiency can be maintained. In the future, more detailed analyses must be performed, including material propagation, detector inefficiencies (with a dedicated tracking algorithm and detector misalignments) or the effect of potential backgrounds as multi-scattering signatures or cosmic ray fluxes. For the moment, such a project represents the first attempt to move towards simulation software in Codex, and should become a fundamental pillar of the future operation of Codex in the (hopefully near) future.

USC UNIVERSIDADE DE SANTIAGO DE COMPOSTELA

8

Results and Discussion

This chapter consolidates the key findings of this thesis and provides their interpretation, significance, and context. The comprehensive details for each analysis are available in the dedicated chapters referenced throughout.

8.1 Phenomenological analysis

Model-dependent signatures of Long-Lived scalars decaying into muons are analysed. It is considered the Prompt and the Displaced cases, analyzing in such a case the sensitivity gain of alternative reconstructions.

On the one hand, results concerning exclusion limits depending on the scalar's lifetime can be found in Figure 4.1 and 4.2. It is observed, by using 6μ decays, that branching ratios can be excluded down to $\sim 10^{-10}$ in Run 3 and $\sim 10^{-11}$ with Run 5 conditions under the hypothesis of zero background. Additionally, a clear gain is obtained with the inclusive search approach, for which the reach of the future CODEX-b detector is also included.

On the other hand, mass-dependent limits are displayed in Figure 4.3, 4.4 and 4.5. In such a case, it is appreciated the effect of different kinematic regimes on the exclusion limits. The maximun exclusion regions are determined by:

- First, at low m_1 values, muons tend to be produced collinearly and the transverse momentum is defined by the B ancestor.
- Second, the higher the mass of the scalar, the wider all muon p_T distributions and thus more easily achievable the trigger requirements.

USC
UNIVERSIDADE DE SANTIAGO DE COMPOSTELA

Finally, the use of B_s and B^+ modes with 4μ and 6μ multiplicities allows for the determination of the full phase-space associated with those decays.

8.2 Multimuon searches at LHCb

Principally, the analysis of Run 2 experimental data validates the results of the Phenomenological study, which refers to backgrounds and sensitivity reach.

On the background's side, the signal selection is demonstrated to be sufficient to veto peaking components for 4μ modes. Specifically, the most dangerous component belongs to the channel $B^+ \to J/\psi(4\mu)K^+$, mode which is used to validate the final analysis strategy.

Concerning the sensitivities, the CLs method is used to compute the expected upper limits for all the modes defined in such an analysis; they can be found in Table 5.39 and Figure 5.41. Simultaneous fits across different reconstruction categories in the displaced samples allow for the recovery, to a large extent, of the sensitivities predicted by the phenomenological study. It should be noted, however, that combinatorial background effects—an irreducible component that cannot be fully vetoed—introduce variations in the obtained limits, so comparisons should be made at the level of order of magnitude. On one hand, the most stringent exclusions are achieved for the prompt samples, reaching branching fraction limits around 10^{-9}, with the $B^+ \to 4\mu K^+$ channel falling below the 10^{-10} threshold. On the other hand, acceptance effects dominate the shape of the characteristic exclusion curves in the $(\mathcal{B}, t)$ plane for displaced modes, which in several cases reach sensitivities of order 10^{-9}.

Finally, the full Selection approach is validated with the measurement of $\mathcal{B}(B^+ \to J/\psi(\mu^+\mu^-\mu^+\mu^-)K^+) = (7.72 \pm 3.6) \cdot 10^{-10}$, compatible within 1σ with the SM prediction.

8.3 Installation of a demonstrator detector: CODEX-β

The successful assembly and installation of the CODEX-β demonstrator (Figure 6.9), comprising 14 RPC triplets, marks a critical hardware milestone. This achievement is a vital proof-of-concept, validating the use of RPC technology in the LHCb cavern environment and de-risking the mechanical integration for the full CODEX-b detector. The pending final steps of connecting services and installing acquisition cards represent the path toward the ultimate goal of commissioning during the final part of Run 3, which will provide invaluable in-situ background measurements to validate the future CODEX-b operation.

USC UNIVERSIDADE DE SANTIAGO DE COMPOSTELA

8.4 Fast Simulation Framework for CODEX-b

The sensitivity curves corresponding to the different geometries (Figure 7.1) are displayed in Figures 7.3 and 7.4 for the $H^0 \to A'A'$ and $B \to KX$ benchmarks, respectively. The key finding is that low-p_T LLP modes are more sensitive to geometrical changes than high-p_T modes, providing a clear guideline for future optimization efforts. Additionally, it is verified that a non-hermetic configuration could solve the problems of spatial organization in the experimental cavern without directly influencing the final sensitivity, although more detailed simulations (presumably involving interactions with the material) need to be performed.

USC UNIVERSIDADE DE SANTIAGO DE COMPOSTELA

9

Conclusions

This thesis constitutes an original contribution to the study of LLPs conducted in the context of the LHCb and CODEX-b experiments. Within the scope of this work, several key conclusions can be highlighted.

The phenomenology analysis demonstrates the feasibility of studying the hierarchical sector through low-energy multimuon decays at LHCb and CODEX-b. It is shown that, in addition to favorable sensitivity conditions, background contamination can be efficiently suppressed. To extend the sensitivity range for long lifetimes, alternative reconstruction strategies (Downstream and T-Tracks) were investigated. These outperform the standard Long-track reconstruction due to the finite size of the VELO. Moreover, an inclusive approach significantly improves the limits, although careful consideration of zero-background assumptions is required before its application to real detector data.

The analysis of multimuon tracks using real detector data confirms the phenomenological predictions, particularly regarding the use of Long and Downstream tracks. Expected limits are reported for the decay modes $B_s^0 \to 4\mu$, $B^+ \to 4\mu K^+$, $B_s^0 \to 6\mu$, and $B^+ \to 6\mu K^+$, for both the Prompt and Long-Lived cases. Except for the $B_s^0 \to 4\mu$ Prompt case, these represent the first-ever experimental results for these channels. The study highlights the potential of using specific reconstruction modes within LHCb and demonstrates the reliability and competitiveness of the Downstream reconstruction, although Run 2 trigger limitations require at least one candidate dimuon reconstructed with Long tracks for all events. While awaiting official permission to unblind the signal region, the branching ratio of $B^+ \to (J/\psi \to 4\mu)K^+$ was measured, yielding a value compatible with the Standard Model prediction and validating the sensitivity results.

Regarding the CODEX-β detector, the installation is progressing successfully. Completion of the 14 RPC triplets that form the detector structure allows for its transport, insertion into the support framework, and final testing to ensure proper functionality. Service connections are being finalized, with acquisition cards pending installation.

USC DE COMPOSTELA

Although the project is already largely successful, some steps remain before commissioning can begin during the final part of Run 3.

Finally, the fast simulation software provides crucial information to quantify the effects of different locations and geometries on the benchmark scenarios underlying the physics case of the future CODEX-b detector. The results indicate that LLP modes with lower transverse momentum (p_T) are more sensitive to changes in geometry and location, whereas high-p_T modes exhibit relatively stable behavior. In the medium term, this simulation framework is expected to be fully integrated into the collaboration's workflow, providing valuable guidance for optimizing the design and understanding the experimental landscape that CODEX-b will face.

USC
UNIVERSIDADE
DE SANTIAGO
DE COMPOSTELA

10

Resumo en Galego

10.1 Introducción

O Modelo Estándar da física de partículas (SM) nace como produto da curiosidade humana por entender os constituíntes básicos do Universo, ou sexa, os bloques elementais de materia e as interaccións que rexen entre eles.

O SM acomoda, satisfactoriamente, tres das catro forzas fundamentais que gobernan a natureza baixo o grupo de simetría $U(1) \times SU(2) \times SU(3)$ (concretamente as interacións nucleares forte e feble e a electromagnética) e o mecanismo de xeración de masa para as partículas [21, 18], confirmado no ano 2012 polo descubrimento do bosón de Higgs polas colaboracións ATLAS e [39]. O SM, a pesar de constituirse como a teoría da natureza máis exitosa e precisa na curta historia da humanidade [42], atopa certas tensións que se convertiron en candelas que guían os intentos de descubrir nova física [46].

As inconsistencias máis importantes no modelo son a incapacidade de incluir a interación gravitatoria, cuxo marco teórico é a Relatividade Xeral de Einstein [48], explicar a natureza da materia escura [62, 61] ou do bosón de Higgs [73], da hipotética masa dos neutrinos [82, 83, 84] ou da inxente dominancia da materia sobre antimateria [87, 88]. A non observación de nova física ate o momento motivou o desenvolvemento de novas teorías que buscan acomodar ditas tensións. Moitas delas predín a existencia de Partículas de Longa Vida (LLPs), definidas como partículas que voan unha distancia macroscópica antes de decaer [98, 95, 122]. Pese que aos detectores do Gran Colisor de Hadróns (LHC) poderían ter sensitividade a estes novos estados, á proposición de novos experimentos ou novas técnicas de reconstrucción e análise levaron consigo un cambio de paradoxo tal que se convirtiron nun piar fundamental da estratexia do LHC a curto-medio prazo [95, 122].

USC UNIVERSIDADE DE SANTIAGO

Dende un punto de vista morfolóxico, os mecanismos de xeración de LLPs son independentes da natureza da física que exista detrás. Os mecanismos de supresión e,

polo tanto da xeración dunha vida media longa, son fundamentalmente: i) decaemento mediado por unha partícula off-shell de alta masa, ii) forte supresión do espazo de fases asociado ó proceso e iii) ancho de desintegración dominado por un pequeno parámetro adimensional asociado a unha simetría aproximada [98]. Unha ampla gama de teorías predín a existencia de ditas partículas, o que concorre nun certo prexuizo experimental. Nesta tese, explórase a sensitividade a certos modelos que recollen LLPs no seu espectro, específicamente o modelo de Higgs Composto (CH) e portais minimais.

O modelo CH vén motivado polos problemas da xerarquía e naturalidade [74, 112, 115, 76]. Éste considera ó Higgs é un estado ligado de constituintes máis elementais a certa escala enerxética maior ca do SM [76]. Se o modelo é non minimal, a elección dos xeradores que excitan o baleiro certifica o número de (pseudo) partículas de Nambu-Goldstone que acompañan ao Higgs despois da ruptura espontánea da simetría global [112, 115, 76]. A baixas enerxías, a aparición de dous escalares lixeiros a_1 e a_2 acoplados a un bosón vectorial V off-shell ($\sim$ TeV) podería xerar LLPs no espectro da teoría. Se a física detrás ten un carácter xerárquico e V acóplase dominantemente aos quarks da terceira xeración, desintegracións multimuónicas (estados de 4 e 6 muóns) con vértices potencialmente desprazados poderían ocurrir en decaementos extraños de mesóns B [116]. A tales efectos, LHCb aportaría unha competitividade difícil de igualar.

Complemetariamente, o detector proposto CODEX-b [120, 95, 122, 240] aportaría novas posibilidades ao que procuras de LLPs se refire. Especialmente, no que aos modelos minimais se refire, os cales definen os tipos de portais polos que nova física podería acoplarse ao SM. Ditos portáis clasifícanse polo espín e números cuánticos da partícula que actúa de nexo, específicamente: sector oculto abeliano, sector Higgs-Escalar, Leptóns neutrais de alta masa e pseudo-partículas Axiónicas [120]. Con respecto ós anteriores, CODEX-b podería ter unha sensitividade que abra portas a posibilidades nunca antes imaxinadas. Constitúense, pois, como motivación do seu caso de física, tanto con respecto á súa validación como funcionamento.

10.2 Condicións Experimentais

O detector LHCb [159, 160], localizado no punto de interaccón 8 do LHC, é o detector no cal se engloba a búsqueda experimental desta tese. Empréganse datos correspondentes á Run 2, período que engloba os anos 2016-2018, con colisións protón-protón a unha enerxía do dentro de masas de 13.6 GeV.

Particularmente, LHCb é un experimento orixinalmente orientado á física de sabor de alta precisión [159], pero a súa estructura fai que sexa especialmente adecuado para as procuras de LLPs. Dito detector ten unha estructura modular que consiste en varios subdetectores con actuacións específicas. Os subdetectores de tracking son o VELO (localizador de vértices) [171], o Tracker Turicensis (estación posterior ao VELO e anterior ao imán) e as estacións T (que engloban ao tracker interior e exterior, con diferente granularidade) [179, 180, 182]. A éstes, inclúense detectores cuxo obxectivo é a

identificación de partículas, como os dous detectores RICH [296], que identifican o tipo específico de partícula cargada pola apertura do ángula Cherenkov, e os calorímetros hadrónico e electromagnético [186, 189], cuxo obxectivo é a identificación de hadróns, e electróns e fotóns, respectivamente. Así mesmo, no extremo lonxitudinal inclúense estacións de muóns [190] intercaladas con capas de chumbo para a identificación de partículas de natureza muónica.

Os subdetectores salientados traballan de forma síncrona, mesturando a diferente información en diferentes etapas. Primeiro, un trigger tipo hardware garda ou rexeita partículas cuxas enerxías ou momentos transversos superan certo umbral, de seguido por un trigger tipo software que se encarga da reconstrucción e seguimento do detector de forma offline [202]. Resulta crítico un funcionamento case perfecto, de modo que o máximo número de colisións (acontecendo cada 25 ns) sexa rexistrado.

Como se comentou, aínda que os detectores actuais do LHC poderían amosar sensitividade a certas procuras de LLPs, o plantexamento experimental recolle a actualización dos detectores de obxectivo xeral e a proposición de detectores específicos para abarcar o amplo espacio de parámetros definido pola inxente cantidade de posibilidades teóricas [95, 122]. Entre outros, os tipos de experimentos específicos para as procuras de LLPs divídense en: i) beam-dump, nos que os feixes de protóns diríxense cara un obxectivo fixo e denso, ii) transversos, que se colocan na dirección transversal á propagación dos protóns en aceleradores de partículas, e iii) detectores cara adiante, que analizan os productos que saen cara adiante nunha colisión de protóns.

O detector CODEX-b [120] pertence á categoría de detectores transversais, e está orientado a reconstruir firmas exóticas que proveñan do detector LHCb. A súa base de funcionamento recae en detectores tipo gaseoso por avalancha electrónica (RPC) con gran resolución espacial e de temporización [242]. A proposta busca acadar un ambiente case libre de fondos de contaminación (o detector atópase detrás dun muro de formigón de 3 metros de ancho) mediante o emprego de vetos activos e pasivos [120, 139]. Búscase, ademáis, que dito detector integre o sistema de lectura de LHCb, incrementando potencialmente as posibilidades de física de ambos detectores.

10.3 Estudo fenomenolóxico de pistas Multimuónicas en LHCb

Os decaementos multimuónicos a partir de mesóns B que o modelo CH podería predecir a baixas enerxías (Figuras 1.9 e 1.10) non teñen sido estudados con anterioridade en LHCb. O obxectivo é efectuar un análise fenomenolóxico que, avaliando as diferentes posibilidades topolóxicas, se constitúa como condutor de futuras procuras con datos reais do detector. A tales efectos, as conclusións da análise [117] tómanse como punto de referencia para validar o procedemento da análise por simulación.

En primeiro lugar, o software Pythia [247] é empregado para simular colisións

protón-protón a unha enerxía do centro de masas de 13.6 GeV e extraer mesóns B_s^0 e B^+ que actúen como nais das cadeas de decaemento. A posteriori, a ferramenta `TGenPhaseSpace` [255] de ROOT é empregada para efectuar as desintegracións envolvendo aos escalares e subsecuentemente ás partículas do estado final. Unha serie de masas son xeradas para os escalares de forma que se poida abarcar o espazo de fases dispoñible para ditas desintegracións. Así mesmo, diferentes tempos de decaemento son xerados para o escalar máis lixeiro mediante a xeración de números aleatorios dende unha exponencial co método da inversa da distribución acumulativa. En todos os casos, o escalar máis masivo é considerado con tempo de vida de 0 fs.

Baixo a xustificación de procuras libres de fondos de contaminación, cortes puramente xeométricos etiquetan ós diferentes tipos de reconstruccións que son estudadas. Concretamente, os cortes especificados na Táboa 4.1 definen as categorías Long (trazas con hits en todos os subdetectores), Down (hits en todos os subdetectores menos o VELO), T (hits asociados nas estacións T) e CODEX-b (trazas que caen na aceptancia de dito detector). Baseado en diferentes estudos previamente efectuados na colaboración LHCb, na Táboa 4.1 tamén poden atoparse factores de penalización por categoría na procura de facer as estimacións o máis realistas posibles.

Con respecto aos eventos asociados con LHCb, pídese que as trazas asociadas teñan $10 < \theta < 400\,\text{mrad}$ e un $p_T > 250\,\text{MeV}$ en termos de reconstrucción e que as trazas muónicas teñan $p > 2.5\,\text{GeV}$ para asociar unha correcta identificación. Así mesmo, no tanto de incluir efectos do trigger tipo hardware, pídese que polo menos un muón por evento verifique un $p_T > 1.76\,\text{GeV}$ ou que unha parella posúa $p_{T,1} \times p_{T,2} > (1,6)^2\,(\text{GeV})^2$. Avalíase, neste punto, a diferencia de sensitividade que se pode obter cun enfoque puramente Exclusivo ou Inclusivo.

Con respecto ó cálculo de sensitividades, as eficiencias dos modos de sinal e de control (dacordo coa análise actual) son incluidas na Ecuación 4.2 e os correspondentes límites de exclusión son reportados en diferentes puntos de masa e tempo de decaemento. Nas Figuras 4.1 e 4.2 os límites con respecto ó tempo de desintegración son reportados para os modos de 6 muóns, coas estratexias Exclusiva e Inclusiva, para un punto de masa. Nas Figuras 4.3, 4.4 e 4.5 repórtanse mapas de sensitividade en función do espazo de masa dos escalares, obtidos para diferentes tempos de desintegración e modos de reconstrucción.

Con respecto á análise dos fondos, Pythia é empregado de novo para simular eventos provintes de colisións protón-protón envolvendo procesos $b\bar{b}$ e QCD non difractiva. Demóstrase que, pedindo ás partículas escalares distancias de voo considerables e requerimentos na distancia de mínima aproximación, a maioría de fondos físicos son satisfactoriamente vetados.

As conclusións da análise identifican certas rexións do espazo de parámetros onde a sensitividade resulta respresentativa da dinámica que se define no modelo, e son posteriormente estudados con datos experimentais. Así mesmo, resalta a viabilidade de aplicar técnicas alternativas de reconstrucción para o estudo experimental de ditos

USC UNIVERSIDADE DE SANTIAGO DE COMPOSTELA

procesos.

10.4 Análise experimental de Multimuóns en LHCb

A análise experimental de decaementos extraños de mesóns B a pistas Multimuónicas emprega datos tomados polo detector LHCb no periodo 2016-2018. O obxectivo fundamental reside en aportar límites de exclusión a través do tempo de desintegración do escalar de longa vida para dous puntos de masa, os cales corresponden ao mínimo e máximo poder de exclusión dos mapas de masa para cada canle de desintegración. Ditas curvas son calculadas mediante interpolación de valores individuais de sensitividade que se corresponden con mostras simuladas cunha vida media característica. De acordo cos resultados do estudo fenomenolóxico, diferentes tipos de reconstrucción son empregados: i) Prompt, para escalares cuxo tempo de decaemento é efectivamente 0 ps, ii) Long, pistas desprazadas que son reconstruidas con información de todos os subdetectores e iii) Dowstream, para pistas desprazadas con información de todos os subdetectores, menos o VELO. Dado que non existe en Run 2 unha liña de trigger adicada a pistas Downstream, a selección implementada pide, en todo caso, polo menos unha parella de dimuons reconstruídos con pistas Long.

A selección dos candidatos de sinal consiste na reconstrucción dunha partícula nai compatible cun mesón B a partir de eventos con multiplicidade de 4 e 6 muóns, según corresponda. No caso Prompt, a todos os muóns aplícanse uns estritos requerimentos de vertexing, de forma que os muóns do estado final sexan compatibles coa súa producción nun mismo vértice primario. No caso de longa vida, os requerimentos de vertexing son afrouxados e as partículas finais son agrupadas en candidatos dimuóns que posteriormente son combinados para formar mesóns B. En todo caso, eventos cunha masa invariante comprendida no rango $4850 < m_B < 6000$ MeV son aceptados para a posterior análise experimental. A análise realízase de forma cegada na ventá de sinal $(m_B - 75, m_B + 75)$ MeV para evitar sesgos que afecten á cuantificación dos niveis de sinal.

Unha vez os eventos de interese son reconstruidos, inclúese unha selección adicional xeral con vistas a optimizar a significancia da sinal, ou sexa, reducir os niveis de fondo ao mesmo tempo que se persigue unha alta eficiencia de sinal. Primeiramente, un corte no ángulo mínimo entre muóns é aplicado para evitar clonación de eventos por defectos de resolución a baixa masa. Por riba, unha selección de trigger é aplicada sobre os muóns do estado final, tanto nas súas enerxías transversas a nivel de hardware como topolóxica segundo o número de muóns a nivel de software. Aos eventos que superan satisfactoriamente devandita selección aplícaselles un corte de $\mathrm{PID}_\mu > 0$ para a supresión de fondos de natureza hadrónica.

A partir deste punto, seleccións específicas son aplicadas segundo o réxime de estudo das diferentes desintegracións. Para o caso Prompt, vetos na masa invariante de candidatos dimuón son introducidos para evitar contaminación de resonancias como ϕ,

J/ψ e $\psi(2S)$; mentres que no caso de longa vida, un corte no tempo de desintegración $t > 0.2$ ps é implementado para minimizar o número de fondos de contaminación reais construídos sobre resonancias cunha vida media efectiva de 0 ps. Adicionalmente, dependendo da multiplicidade do estado final aplícase:

- Un algoritmo de machine learning (BDT) para a supresión de fondo combinatorio en canles con 4 muóns. Adéstrase por canle e modo de reconstrucción un BDT que é posteriormente optimizado segundo a figura de mérito de Punzi.
- Un corte de resolución entre os tres escalares de longa vida que se reconstrúen nas canles de 6 muóns.

Finalmente, duplicados e candidatos múltiples provintes da reconstrucción son vetados en base á calidade do fit ao vértice primario e ós identificadores de cada evento, respectivamente.

A simulación empregada é calibrada en varios niveis segundo a canle de control $B_s^0 \to J/\psi(\mu^+\mu^-)\phi(K^+K^-)$, en canto a unha comparativa directa das variables xeradas na simulación, da resposta do trigger e de diferencias residuais de variables empregadas no adestramento dos BDTs.

Unha vez calibrada a simulación, a eficiencia de sinal é calculada. De forma similar ao estudo fenomenolóxico, os límites de exclusión son impostos con respecto á canle de normalización $B_s^0 \to J/\psi(\mu^+\mu^-)\phi(\mu^+\mu^-)$ co emprego da Ecuación 4.2.

No estudo dos posibles fondos de contaminación reais, diferentes estimacións de corte conservativo son realizadas respecto de potenciais cadeas de desintegración que polucionen ao sinal. Aqueles modos demostrados problemáticos son estudados con simulación oficial á que son aplicadas as correspondentes liñas de reconstrucción da sinal que polucionan. Ademáis, os mesmos criterios de selección son aplicados, o que permite o cálculo do número esperado de eventos coñecida a fracción de ramificación propia da canle de fondo. A análise das posibles polucións de sinal confirma o anteriormente reseñado pola análise por simulación: todos os fondos son vetables, sen contaminación algunha nas canles de sinal.

Previo ao cálculo dos límites esperados, as parametrizacións das compoñentes de sinal e fondo deben ser preparadas. No tocante a sinal, o MC é empregado para coñecer a forma da distribución de masa invariante na rexión de interese posterior á selección. Con respecto ao fondo sobrevivinte, de natureza combinatoria, as bandas de masa son axustadas a funcións exponenciais. Así mesmo, estudios con pseudoexperimentos son empregados para validar a estratexia xeral de axuste.

A parte do erro estadístico, varias compoñentes sistemáticas son analizadas, como a do modelo de xeración do MC en canles con $B^+ \to K^+ a_1 a_2$, a do diferente tempo de vida para os autoestados do mesón B_s^0, a calibración do MC, a calibración das variables de PID e a parametrización do modelo de fondo. Ditas incertezas son implementadas, por medio de restriccións gausianas, no modelo de axuste.

USC DE SANTIAGO

Finalmente, o método CLs [286] é aplicado ás diferentes canles de interese. Os resultados individuais poden observarse na Táboa 5.39 e as curvas de sensitividade a través do tempo de vida na Figura 5.41. Os resultados acadados, a excepción do caso $B_s^0 \to 4\mu$ Prompt (que se explica por diferentes condicións de luminosidade total con respecto á análise de referencia) serían os primeiros límites impostos nas desintegracións salientadas. Así mesmo, a estratexia xeral da análise demóstrase positiva tras a medición da fracción de ramificación do proceso $B^+ \to (J/\psi \to 4\mu)K^+$, compatible coas prediccións do SM.

10.5 Instalación do demostrador CODEX-β

A validación da proposta do futuro detector CODEX-b precisa da viabilidade dun demostrador a máis pequena escala ($2\times2\times2$ m^3) que verifique o correcto funcionamento da tecnoloxía RPC, a integración no sistema de lectura de LHCb, o control sobre diferentes fondos de contaminación do SM e a súa estrutura modular [241].

O proceso de ensamblaxe dos módulos RPC engloba varias etapas. En primeiro lugar, as tiras de lectura son pegadas aos paneis de fórex, ós cales se aplican as diferentes resistencias que posibilitan a identificación das sinais de avalancha na fenda de gas. Posteriormente, os circuitos de adquisición son instalados nas tiras para a lectura das sinais correspondentes. O proceso de construcción dos módulos remata co intercalado da fenda de gas entre os paneis que conteñen as tiras e o seu conxunto illamento, o que constitúe a denominada caixa de Faraday.

Unha vez rematados, diferentes tests son desenvolvidos para asegurar o correcto funcionamento dos módulos individuais e éstes son, a posteriori, agrupados en tripletes para a súa validación final con raios cósmicos. Ditos tripletes son, unha vez debendo ser transportados, insertados nos correspondentes marcos cos cales se inclúen na estructura final. Na Figura 10.1 é posible observar o estado final da instalación dos tripletes na estrutura cúbica que forma CODEX-β.

Ao mesmo tempo, traballos para a provisión de servicios de voltaxe e gas ás RPCs e aos módulos de adquisición e envío de datos son levados a cabo. Por unha banda, as diferentes conexións e guías de gas son preparadas e axustadas aos requerimentos técnicos, no que compete á súa distribución pola xeometría cúbica e á súa conexión aos proveedores correspondentes.

Finalmente, prodúcese a instalación da estrutura de soporte de CODEX-β e a inclusión dos diferentes tripletes dentro da estrutura. Aínda que xa dentro doutra etapa, denominada comisionado, tests con raios cósmicos deben ser desenvolvidos de novo a curto prazo para verificar o correcto estado das RPCs tras o transporte e da provisión de servizos na caverna experimental. Punto clave a solucionar é a final instalación das tarxetas de adquisición de datos, indispensables para a andaina de CODEX-β na parte final da Run 3 do LHC [139].

USC DE SANTIAGO

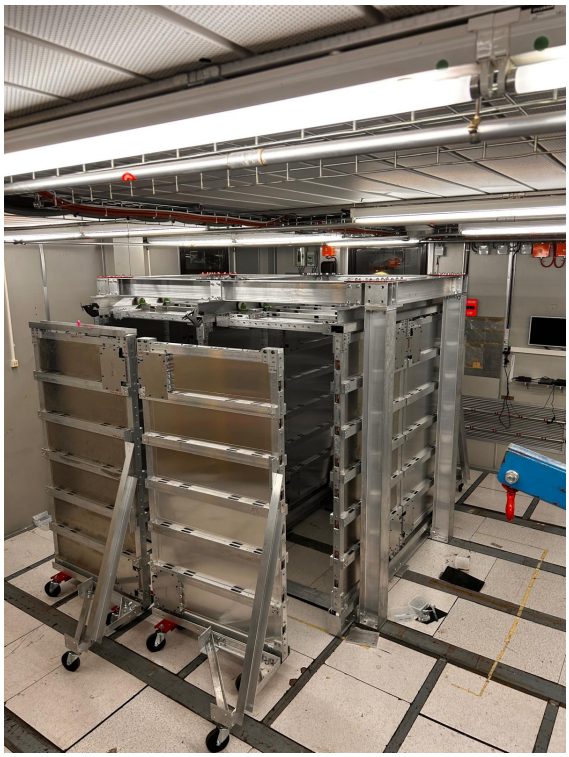


Figure 10.1: Estado final da instalación dos tripletes RPC na estrutura de CODEX-β.

10.6 Sistema de simulación rápida para CODEX-b

Basado en investigacións do personal do Lawrence Berkeley National Laboratory (LBNL) para a optimización de detectores orientados a LLPs [292], un sistema de simulación rápida está sendo desenvolvido no seo da colaboración CODEX-b. Éste consta de 3 núcleos principais: i) xerador de eventos con Pythia, ii) módulo para a definición da xeometría e localización do detector e iii) a clase procesador para a análise dos eventos xerados.

En CODEX-b, dende un punto de vista estatístico, a xeración de vértices desprazados atopa certos desafíos que limitan a estatística dispoñible para obxectivos de física: cobertura angular relativamente pequena, número de eventos fortemente atenuado por un factor $e^{-\beta\gamma c\tau}$ ou un rango de pseudorapidez $3 < \eta < 5$ que so permite a partículas o suficientemente masivas rachar o ángulo de producción necesario para decaer no volume fiduciario [240]. Dúas actuacións complementarias teñen cabida neste sistema:

- Incremento da estatística por parte de procesadores como o separador de eventos nun mesmo feixe, duplicado de eventos por reflexión en momento, aliñación da LLP co volume do detector ou a re-avaliación de vértices da LLP segundo a vida media e inclusión de pesos estatísticos.

- Procesadores para a implementación de cortes cos que calcular eficiencias e límites de exclusión, como o filtro de aceptancia e reconstrucción de trazas.

USC UNIVERSIDADE DE SANTIAGO DE COMPOSTELA

A primeira análise preliminar co devandito sistema consiste na cuantificación dos efectos na sensitividade que cambios na localización ou xeometría poidan ter sobre certos modelos de LLPs. A tales efectos, simulacións de procesos $H^0 \to (A' \to e^+e^-)(A' \to e^+e^-)$ e $B \to KX$ en diferentes puntos de masa da LLP son empregados. As localizacións e xeometrías poden ser consultadas na Figura 7.2, representando a idea nominal e posibles deseños alternativos non herméticos. Os resultados poden observarse nas Figuras 7.3 e 7.4, identificando maiores variacións nos límites de exclusión nos procesos $B \to KX$, con mínimas variacións no espazo de tempos de decaemento para $H \to A'A'$, cunha distribución de máis alto momento.

USC UNIVERSIDADE DE SANTIAGO DE COMPOSTELA

List of Figures

1.1 Representation of the different blocks that form the Standard Model of Particle Physics. Fermions, the fundamental blocks of matter, are composed of two other families: quarks, particles that experience the strong force, and leptons, the electroweak. Bosons, on the contrary, are the carriers of the fundamental interactions. Obtained from [20] under Creative Commons CC BY 3.0. 4

1.2 Charged (Up) and neutral (Down) current interaction vertices allowed by the electroweak lagrangian. For simplicity, only the first generation of quarks and leptons has been considered. Note, however, that this process is analogous for the rest of them. 7

1.3 Global fit of the parameters of the CKM matrix in the $(\overline{\rho},\overline{\eta})$ plane. Obtained from [27]. 8

1.4 Strong Coupling Constant α_s comparison. Obtained from [36] under CC BY 4.0. 10

1.5 Higss to diphoton searches at pp center-of-mass energy of 8TeV. Obtained from [39] under CC-BY-3.0. 12

1.6 Estimates of the WMAP nine-year power spectrum along with best-fit model spectra; black – the C-1-weighted spectrum and corresponding model; red – the same for the MASTER spectrum and model. Obtained from [65]. 14

1.7 Decay length versus mass scale of the particles building the SM. Obtained from [95] under CC BY 3.0. 20

1.8 Diagramatic sketch of the decays taking place within the hierarchical framework. Obtained from [116] under CC BY 4.0. 23

1.9 Low muon multiplicity decays, where $m_2 < 2m_1$. 24

1.10 High muon multiplicity decays, where $m_2 > 2m_1$. 24

1.11 Possible portals to the Standard Model triggering Long-Lived Particles: Abelian Hidden Sector (left) and Dark Higgs (right). 25

3.1 CERN accelerator complex, comprising pre-accelerator stages and experimental facilities. Obtained from [146]. 32

USC UNIVERSIDADE DE SANTIAGO DE COMPOSTELA

3.2 Simulation of individual polar distribution for a pair $b\bar{b}$ at $\sqrt{s} = 14$ TeV. Obtained from [164]. 34

3.3 View of the LHCb detector. The propagation axis is chosen across the z-axis, whereas the height is oriented towards the y coordinate. Subdetectors are displayed in colours. Obtained from [170] under CC BY-SA 3.0. 35

3.4 Front view of a schematic representation of the distribution of silicon pixels in the VELO (left) and material interaction reconstruction with secondary hadronic interactions. Obtained from [172] and [174] under CC BY 3.0 and CC BY 4.0, respectively. 36

3.5 RICH1 and RICH2 detector schematics. Obtained from [176] and [177] under CC BY 4.0 and CC-BY-3.0, respectively. 37

3.6 Reconstructed Cherenkov angle as a function of track momentum in the C4F10 radiator. Obtained from [176] under CC BY 3.0. 38

3.7 Inner and Outer tracker schematics. Obtained from [180] and [181] under CC-BY-3.0 and CC-BY-4.0, respectively. 39

3.8 Front view of the LHCb dipole magnet. Obtained from [184] under CC-BY-4.0. 39

3.9 Rear view of the hadron calorimeter (left) and schematic of the internal cell structure (right). Obtained from [28] and [187] under CC-BY-3.0 and CC BY 4.0, respectively. 40

3.10 Side and front schematics of the LHCb muon stations. Obtained from [191] under CC BY 4.0. 42

3.11 Left: Breakdown of Integrated Luminosities for Run 1 and 2. Right: Comparison between Instantaneous Luminosity for ATLAS, CMS and LHCb in a proton fill during Run 2, across operation time. Obtained from [194] under CC-BY-NC-ND-4.0 and [196], respectively. 43

3.12 LHCb trigger system breakdown. Obtained from [200] under CC BY 4.0. 45

3.13 Different track reconstruction in LHCb: Long tracks, Upstream tracks, Downstream tracks and T-Tracks are displayed. Obtained from [204] under CC BY 3.0. 47

3.14 Comparison between the generation efficiencies for a set of a_1 lifetimes in $B_s^0 \to (a_1 \to \mu^+\mu^-)a_2(\mu^+\mu^-)$ decays. 50

3.15 Detector schematics for forward experiments: FASER (left) and milliQan (right). Obtained from [228] and [229] both under CC BY 4.0. 54

3.16 Design idea and experimental setup for MATHUSLA proposal. Obtained from [232] under CC BY 4.0. 55

3.17 Experimental setup of SHiP (left) and NA64 (right) experiments. Obtained from [235] and [236] under CC BY 4.0. 56

USC UNIVERSIDADE DE SANTIAGO DE COMPOSTELA

3.18 Baseline CODEX-b detector proposal at the LHCb experimental cavern. The cubic volume is located at $x = [26, 36]$ m, $y = [-7, 3]$ m and $z = [5, 15]$ m. Obtained from [241] under CC BY 4.0. 58

3.19 Sketch of a ATLAS BIS78 RPC module. Obtained from [241] under CC BY 4.0. 60

3.20 CODEX-b reach to Dark Photon signatures through a Kinetic mixing portal. Obtained from [139] under CC BY 4.0. 62

3.21 CODEX-b reach to exotic B decays. Obtained from [240] under CC BY 4.0. 63

3.22 CODEX-β demonstrator after the installation of the support structure and all the fourteen modules assembled to it. 65

4.1 The expected upper limits on the $B_s^0 \to 3\mu^+3\mu^-$ and $B^+ \to K^+3\mu^+3\mu^-$ branching fractions that can be derived from the exclusive searches proposed in this work, for different lifetimes of the a_1 particle. In the upper (bottom) panels, the detector configuration after Run 3 (Run 5) is assumed. The benchmark masses were fixed to $(m_1, m_2) = (1.0, 2.5)$ GeV. 70

4.2 Same as in Figure 4.1, but requiring only four muons in the final state. Also included are the projected bounds for the CODEX-b experiment, requiring the presence of only one muon pair inside the acceptance. . . 71

4.3 Mass-dependent expected limits at Run 5 on the branching fractions of (top left)$B_s^0 \to 2\mu^+2\mu^-$, (top right) $B^+ \to K^+2\mu^+2\mu^-$, (bottom left) $B_s^0 \to 3\mu^+3\mu^-$ and (bottom right) $B^+ \to K^+3\mu^+3\mu^-$ for a lifetime of the long-lived scalar of 1 ps. 72

4.4 Mass-dependent expected limits at Run 5 on the branching fractions of (top left)$B_s^0 \to 2\mu^+2\mu^-$, (top right) $B^+ \to K^+2\mu^+2\mu^-$, (bottom left) $B_s^0 \to 3\mu^+3\mu^-$ and (bottom right) $B^+ \to K^+3\mu^+3\mu^-$ for a lifetime of the long-lived scalar of 100 ps. All decays are reconstructed inclusively with Downstream tracks. 73

4.5 Mass-dependent expected limits at Run 5 on the branching fractions of (top left)$B_s^0 \to 2\mu^+2\mu^-$, (top right) $B^+ \to K^+2\mu^+2\mu^-$, (bottom left) $B_s^0 \to 3\mu^+3\mu^-$ and (bottom right) $B^+ \to K^+3\mu^+3\mu^-$ for a lifetime of the long-lived scalar of 1 ns. All decays are reconstructed inclusively with T-Tracks. 73

4.6 Signal efficiencies across lifetimes for each of the decay chains. All decays are reconstructed by being compatible with the Long tracks hypothesis. 74

USC UNIVERSIDADE DE SANTIAGO DE COMPOSTELA

4.7 Dimuon mass distributions in simulated $pp \to b\bar{b}X$ events reconstructed as $B_s^0 \to a_1 a_2 \to 2\mu^+ 2\mu^-$. In the left panel, only the requirements discussed in Section 4.1 are applied. In the central panel, strong vertex requirements are applied. In the right panel, it is required instead that one of the dimuon systems has a significant flight distance. 75

4.8 Sensitivity projections of LHCb to the hierarchical phase space with the use of Downstream Tracks. Projections for Run3 and Run5 are displayed. The following values are considered: $g_{sb} = 0.01$, $g_{12} = 1.5$, $m_V = 3$ TeV and $t_{a_1} = 100$ ps. 76

4.9 Sensitivity projections of LHCb to the hierarchical phase space with the use of Downstream Tracks. Projections for Run3 and Run5 are displayed. The following values are considered: $g_{sb} = 0.01$, $g_{12} = 1.5$, $m_V = 3$ TeV and $t_{a_1} = 100$ ps. 77

4.10 (Left) The minimum vector-quark coupling that could be tested with the search proposed in this work in the channel $B^+ \to K^+ 3\mu^+ 3\mu^-$. The light masses, couplings and lifetimes are assumed to be $(m_1, m_2) = (1.0, 2.5)$ GeV, $g_{12} = 1.5$ and $\tau_1 = 1$ ns. The solid, dotted and dashed lines show, respectively, the projected limits after Run 3, Run 4 and Run 5 of the LHCb experiment. (Right) The minimum vector-scalar coupling that could be tested with the same analysis, as a function of the lightest scalar lifetime. The same notation and benchmark masses as in the left panel are considered, as well as the mass and vector coupling marked with a star therein. 78

5.1 Minimum angle between muons in different data channels. Peaks are observed at $min(\theta_{ij}) = 0$ in each case, and are particularly prominent in the 6μ modes. 90

5.2 Invariant mass of opposite-sign dimuon pairs rejected by $\min(\theta_{ij})$ criterium in $B_s^0 \to 4\mu$ decays. 91

5.3 Comparison of variables belonging to Prompt $B_s^0 \to 6\mu$ events. For MC, two prospects are investigated: in blue, a pure PHSP decay to N final particles and, in green, a Prompt model-dependent decay with intermediate scalar lifetimes set to 0 ps. In every case, preselection cuts, clones, trigger and prompt resonance selections are applied. 92

5.4 Total number of expected $B_s^0 \to J/\psi\phi$ candidates during Run 2 as a function of the cut on the decay time of the intermediate scalars. 92

5.5 Comparison of $B^+ \to 4\mu K^+$ data (left) and $B_s^0 \to 4\mu$ data (right) dimuon mass distributions in the B mass sidebands before and after the cut in the decay time of the intermediate scalars. 93

5.6 Reconstructed mass comparisons for 4μ and 6μ simulation samples. . . 94

5.7 Mass resolution check for $B_s^0 \to 6\mu$ with $m_1 = 1.25$ GeV, $m_2 = 3.50$ GeV. 95

USC UNIVERSIDADE DE SANTIAGO DE COMPOSTELA

5.8 Mass resolution check for $B^+ \to 6\mu K^+$ with $m_1 = 1.25$ GeV, $m_2 = 3.50$ GeV. 96

5.9 Schematic diagram showing how duplicates can arise, where the same set of muon tracks is swapped between intermediate scalars. 97

5.10 The efficiency of the L0Muon trigger line as a function of muon p_T for 2018 $B_s^0 \to J/\psi(\mu^+\mu^-)\phi(K^+K^-)$ data (red) and MC (blue). Generator-level corrections have been applied to the MC, but not TISTOS corrections. The lower subplot shows the ratio of the data and MC, with the green curve being the ratio of the fitted efficiency curves. 100

5.11 Distributions of BDT training variables in MC and Data for the $B_s^0 \to 4\mu$ Prompt reconstruction. 104

5.12 BDT output for $B_s^0 \to 4\mu$ searches. 105

5.13 BDT output for $B_s^0 \to 4\mu K^+$ searches. 106

5.14 ROC curves for all six BDTs. 107

5.15 Learning Curves. Training score stands for the performance of the BDT evaluated on the same data it was trained on, whereas Cross Validation Score is the average performance of the BDT on multiple held-out validation subsets. 108

5.16 Example of fits to the data mass sidebands used to estimate the number of background events in the signal region for the BDT optimisation, with BDT > 0.1. 109

5.17 Scans of the Punzi figure of merit for each decay and stripping line sample. The scan is shown zoomed around the optimum cut point. . . 110

5.18 2D distributions between BDT output and the Mass of the B. 111

5.19 2D distributions between BDT output and lifetime of the LLP. 111

5.20 Fits to the high-yield $B_s^0 \to J/\psi(\mu^+\mu^-)\phi(K^+K^-)$ channel with the kaons without PID cut (left) and one kaon identified as muon (right) hypothesis. 114

5.21 Surviving events after $B_s^0 \to 4\mu$ Prompt reconstruction 117

5.22 Surviving events after $B^+ \to 4\mu K^+$ displaced-LL reconstruction 117

5.23 BDT response comparison for Prompt sources (left) and Displaced modes (right). It does not include a comparison for Down samples, since the efficiency of the BDT is the same as the Displaced Long reconstruction. 119

5.24 Partial reconstruction from high-multiplicity modes with 1 ps samples for $B^+ \to 4\mu K^+$ with $m_{a_1} = 2.00$ GeV and $m_{a_2} = 2.75$ GeV (right) and $B^+ \to 6\mu K^+$ with $m_{a_1} = 1.25$ GeV and $m_{a_2} = 3.50$ GeV. 120

5.25 Fit to invariant mass distribution of a combined sample of 2016-2018 $B_s^0 \to J/\psi(\mu^+\mu^-)\phi(\mu^+\mu^-)$ data that passes the full selection. 122

USC UNIVERSIDADE DE SANTIAGO DE COMPOSTELA

5.26 Extrapolation of sensitivity results for 4μ modes. Left: low-mass configuration $(m_{a_1}, m_{a_2}) = (0.25, 0.40)$ GeV. Right: high-mass configuration $(m_{a_1}, m_{a_2}) = (2.00, 2.75)$ GeV. 130

5.27 Extrapolation of sensitivity results for 6μ modes. Left: low-mass configuration $(m_{a_1}, m_{a_2}) = (0.50, 1.50)$ GeV. Right: high-mass configuration $(m_{a_1}, m_{a_2}) = (1.25, 3.50)$ GeV. 130

5.28 Blinded B mass distribution reconstructed with the Prompt selection. The full Run 2 dataset has been used. 132

5.29 Blinded B mass distribution reconstructed with the displaced selection, only LL (4μ modes) and LLL (6μ modes). The full Run 2 dataset has been used. 133

5.30 Blinded B mass distribution reconstructed by requiring one dimuon to be reconstructed with Downstream tracks, therefore LD (4μ modes) and LLD (6μ modes). No events surviving the selection for $B_s^0 \to 6\mu$. The full Run 2 dataset has been used. 133

5.31 Blinded B mass distribution reconstructed by requiring two dimuons to be reconstructed with Downstream tracks, therefore displaced LDD. The full Run 2 dataset has been used. 134

5.32 Miscellanea of Signal fits to a DSCB using MC. 135

5.33 Resolution Studies for high-mass configurations. 136

5.34 Toy study relative to a single fit for $B_s^0 \to 4\mu$ case. 138

5.35 Toy study relative to a simultaneous fit to displaced LL and LD reconstruction categories for $B^+ \to 4\mu K^+$, 100 ps case. 139

5.36 Toy study relative to a simultaneous fit to displaced LLL, LLD and LDD reconstruction categories for $B_s^{)} \to 6\mu$, 100 ps case. 139

5.37 Fit to the pulls distribution for: $B_s^0 \to 4\mu$ PHSP (left) and $B^+ \to 4\mu K^+$ with $m_{a_1} = 2.00$ GeV, $m_{a_2} = 2.75$ GeV and $t_{a_1} = 100$ ps (right). 140

5.38 Reweighting procedure for $B^+ \to 4\mu K^+$ with $m_{a_1} = 0.25$ GeV, $m_{a_2} = 0.40$ GeV (top left) and $m_{a_1} = 2.00$ GeV, $m_{a_2} = 2.75$ GeV (top right), and for $B^+ \to 6\mu K^+$ with $m_{a_1} = 0.50$ GeV, $m_{a_2} = 1.50$ GeV (bottom left) and $m_{a_1} = 1.25$ GeV, $m_{a_2} = 3.50$ GeV (bottom right). 142

5.39 Expected limits at 95% CL and associated error bands for PHSP samples. 150

5.40 Miscelanea of Expected limits at 95% CL and associated error bands for different modes with masses and lifetimes. 153

5.41 Lifetime-dependent mass-integrated expected limits for Multimuon modes. 154

5.42 Mass fit to the invariant mass $m(4\mu K^+)$, corresponding to the $B^+ \to J/\psi(\mu^+\mu^-\mu^+\mu^-)K^+$ channel. The full statistics for Run 2 data are used. 154

USC UNIVERSIDADE DE SANTIAGO DE COMPOSTELA

6.1 Left: Aluminium frame for RPC triplets. Right: Mechanical support structure for the CODEX-β detector. Obtained from [241] under CC BY 4.0. 157
6.2 Left: Panel gluing and rolling setup. Right: Resistor installation on a readout strip panel. 158
6.3 Front-end PCB designed for single-gap RPC modules of the CODEX-β detector. 158
6.4 Left: Gas Gap placement and orientation. Right: Full Singlet assembly. 159
6.5 Results of different tests over RPC modules. 160
6.6 Usual frame configuration for a set of triplets (left) and assignment of connections (right). 162
6.7 Transportation cart for a full assembled RPC triplet frame (left) and Gas Recirculating system in D1 barracks (right). 163
6.8 Provision of services during the installation phase: gas input and output lines installation in the service box (left) and assembled triplet of RPCs with the data acquisition cables installed. 165
6.9 The detector CODEX-β, successfully installed in the LHCb experimental cavern. 166

7.1 Location and configuration of nominal and alternative CODEX geometries. 172
7.2 Alternative layouts for the CODEX-b experiment. 173
7.3 Comparison between CODEX-b proposals to the benchmark $H \to A^0 A^0$, considering two mass points for the Dark Photon particle. An integrated luminosity of 300 fb^{-1} is assumed. 174
7.4 Comparison between CODEX-b proposals to the benchmark $B \to KX$, considering two mass points for the Dark Photon particle. An integrated luminosity of 300 fb^{-1} is assumed. 174

10.1 Estado final da instalación dos tripletes RPC na estrutura de CODEX-β. 187

USC UNIVERSIDADE DE SANTIAGO DE COMPOSTELA

List of Tables

3.1 Breakdown of Operation LHC parameters throughout the full Run 2 period. 43

3.2 Summary of trigger selection. All candidates must be identified as TOS by at least one trigger line at each stage. 46

3.3 Summary of dedicated stripping lines used to select signal modes. In reconstruction categories, Long encloses LL and LLL samples and Downstream LD, LLD and LDD. 47

3.4 IsMuon identification requirements at HLT1. 48

4.1 Different track types at the LHCb and CODEX-b experiments that are studied in this work: corresponding geometrical requirements and track reconstruction efficiencies. For CODEX-b, no penalty for the track reconstruction can be estimated yet. 69

5.1 Integrated luminosities of the data samples used in this analysis. The values are taken from the LHCb Operations Plots [271]. 82

5.2 Summary of background simulation samples used in the analysis. . . . 83

5.3 Summary of the signal and control simulation samples used in the analysis. In order, it is specified: the decay chain, simulation type, decay model, lifetime, total statistics per year and the corresponding generator efficiency. All simulation samples are run with the associated stripping in the corresponding data. Note that, as only simulated data from two years are needed, and since data-taking conditions are similar for 2016 and 2017, only 2016 and 2018 are analysed. 84

5.4 Stripping selection for $B_s^0 \to J/\psi(\mu^+\mu^-)\phi(\mu^+\mu^-)$ and $B_s^0 \to J/\psi(\mu^+\mu^-)\phi(K^+K^-)$. 85

5.5 Stripping selection for prompt reconstruction. 87

5.6 Dimuon builder requirements for displaced dimuon lines. 88

5.7 Summary of stripping selection for $B^+ \to 4\mu K^+$, $B^+ \to 6\mu K^+$ and $B_s^0 \to 6\mu$ displaced stripping lines with long tracks only. 88

USC UNIVERSIDADE DE SANTIAGO DE COMPOSTELA

5.8 Summary of stripping selection for long-lived lines composed of both long tracks and downstream tracks for $B^+4\mu \to K^+$, $B^+ \to 6\mu K^+$ and $B_s^0 \to 6\mu$. In $B^+ \to 6\mu K^+$ and $B_s^0 \to 6\mu$ channels, the displaced-LLD and displaced-LDD are differentiated. 88

5.9 Summary of stripping selection for $B_s^0 \to 4\mu$ long-lived lines composed of both long and downstream tracks. 89

5.10 MC IDs applied to particles in MC samples 97

5.11 Selection overview for 4μ searches. 98

5.12 Selection overview for 6μ searches. 98

5.13 Hyperparameter selection for classifiers. Additionally, all of them share; *DecisionTreeClassifier* as base estimator, `MinNodeSize` equal to 2.5% and `MaxDepth` of 3. 102

5.14 List of variables used to train each of the Multivariate Classifier, each one trained per channel and reconstruction mode. 103

5.15 Expected contamination for $B_s^0 \to 6\mu$ and $B^+ \to 6\mu K^+$. N_{sig} denotes the number of expected decays assuming the same efficiency as the signal channels. The Prompt and Displaced categories refine these efficiencies, applying a ballpark efficiency for PID and vetoes. 114

5.16 Expected contamination for $B_s^0 \to 4\mu$. N_{sig} denotes the number of expected decays assuming the same efficiency as the signal channels. The Prompt and Diplaced categories refine these efficiencies, applying a ballpark efficiency for PID and vetoes. 115

5.17 Expected contamination for $B^+ \to 4\mu K^+$. N_{sig} denotes the number of expected decays assuming the same efficiency as the signal channels. The Prompt and Displaced categories refine these efficiencies, applying a ballpark efficiency for PID and vetoes. 116

5.18 Detailed study for background sources in the signal window, located at $(m_B - 75, m_B + 75)$ MeV. 118

5.19 Additional background estimates, applying mass and/or decay time effects after full selection. In this case, the full fit region $(4850, 6000)$ MeV is considered. 118

5.20 Total efficiencies for prompt PHSP samples, including the full selection requirements. Efficiencies are averaged across all data-taking years. . . 124

5.21 Total efficiencies for $B_s^0 \to 4\mu$, including the stripping, reconstruction, trigger, offline and BDT selection requirements. Efficiencies are averaged across all data-taking years. 124

5.22 Total efficiencies for $B^+ \to 4\mu K^+$, including the stripping, reconstruction, trigger, offline and BDT selection requirements. Efficiencies are averaged across all data-taking years. 124

USC UNIVERSIDADE DE SANTIAGO DE COMPOSTELA

5.23 Total efficiencies for $B_s^0 \to 6\mu$, including the stripping, reconstruction, trigger and offline selection requirements. Efficiencies are averaged across all data-taking years. 125
5.24 Total efficiencies for $B^+ \to 6\mu K^+$, including the stripping, reconstruction, trigger and offline selection requirements. Efficiencies are averaged across all data-taking years. 125
5.25 Normalisation factors (i.e., sensitivity reach) for prompt PHSP modes, including the full selection requirements. 126
5.26 Normalisation Factors α_{sig} for hierarchical $B_s^0 \to 4\mu$ samples. 127
5.27 Normalisation Factors α_{sig} for hierarchical $B^+ \to 4\mu K^+$ samples. 127
5.28 Normalisation Factors α_{sig} for hierarchical $B_s^0 \to 6\mu$ samples. 128
5.29 Normalisation Factors α_{sig} for hierarchical $B^+ \to 6\mu K^+$ samples. 128
5.30 Pull studies results for PHSP samples. For each case, 1000 pseudo-experiments are run. Amount of failed toys remains stable and below 1%. 137
5.31 Pull studies results. A mass configuration has been chosen per channel and the fit model analysis is performed across the generated lifetimes set. For each case, 1000 pseudo-experiments are run. In all the cases, the number of fits failing is stabilized below 1% of the run toys. 138
5.32 PHSP systematics overview for $B^+ \to 4\mu K^+$ samples. Values that are not compatible with the $\pm 2\sigma$ error bands are marked in red. 143
5.33 PHSP systematics overview for $B^+ \to 6\mu K^+$ samples. Values that are not compatible with the $\pm 2\sigma$ error bands are marked in red. 143
5.34 Systematic uncertainties for $B_s^0 \to 4\mu$ associated with the effective B_s^0 lifetime. 144
5.35 Systematic uncertainties for $B_s^0 \to 4\mu$ associated with the PID efficiency, given as a relative uncertainty on the efficiency ratio $\frac{\epsilon_{\text{norm}}}{\epsilon_{\text{sig}}}$. 146
5.36 Systematic uncertainties resulting in the difference between Expected Upper Limits at 95% CL on the branching fraction parameter. 147
5.37 Systematic uncertainties on $\mathcal{B}(B_s^0 \to 4\mu)$ and $\mathcal{B}(B_s^0 \to 6\mu)$. 148
5.38 Systematic uncertainties on $\mathcal{B}(B^+ \to 4\mu K^+)$ and $\mathcal{B}(B^+ \to 6\mu K^+)$ from different sources. 149
5.39 Expected 95% CL upper limits on the $\mathcal{B}(B_s^0 \to 4\mu)$, $\mathcal{B}(B^+ \to 4\mu K^+)$, $\mathcal{B}(B_s^0 \to 6\mu)$ and $\mathcal{B}(B^+ \to 6\mu K^+)$ for the sideband shape method. . . . 152

USC UNIVERSIDADE DE SANTIAGO DE COMPOSTELA

Bibliography

[1] G.S. Kirk, J.E. Raven, and M. Schofield. *The Presocratic Philosophers*. Cambridge University Press, 1983.

[2] John Dalton. *A New System of Chemical Philosophy*. Manchester, 1808.

[3] J.J. Thomson. "Cathode Rays". In: *Philosophical Magazine* 44.269 (1897), pp. 293–316.

[4] Ernest Rutherford. "The Scattering of α and β Particles by Matter and the Structure of the Atom". In: *Philosophical Magazine* 21 (1911), pp. 669–688.

[5] Max Planck. "On the Law of Distribution of Energy in the Normal Spectrum". In: *Annalen der Physik* 4 (1901), pp. 553–563.

[6] Albert Einstein. "On a Heuristic Point of View Concerning the Production and Transformation of Light". In: *Annalen der Physik* 17 (1905), pp. 132–148.

[7] Niels Bohr. "On the Constitution of Atoms and Molecules". In: *Philosophical Magazine* 26 (1913), pp. 1–25.

[8] Louis de Broglie. "Recherches sur la théorie des quanta". PhD thesis. Université de Paris, 1924.

[9] Werner Heisenberg. "Über den anschaulichen Inhalt der quantentheoretischen Kinematik und Mechanik". In: *Zeitschrift für Physik* 43 (1927), pp. 172–198.

[10] Erwin Schrödinger. "Quantisierung als Eigenwertproblem". In: *Annalen der Physik* 79 (1926), pp. 361–376.

[11] Paul A.M. Dirac. "The Quantum Theory of the Electron". In: *Proceedings of the Royal Society A* 117 (1928), pp. 610–624.

[12] Carl D. Anderson. "The Positive Electron". In: *Physical Review* 43 (1933), pp. 491–494.

[13] Freeman J. Dyson. "The Radiation Theories of Tomonaga, Schwinger, and Feynman". In: *Physical Review* 75 (1949), pp. 486–502.

[14] Richard P. Feynman. "The Theory of Positrons". In: *Physical Review* 76 (1949), pp. 749–759.

[15] Steven Weinberg. "A Model of Leptons". In: *Physical Review Letters* 19 (1967), pp. 1264–1266.

USC UNIVERSIDADE DE SANTIAGO DE COMPOSTELA

[16] Sheldon L. Glashow. "Partial-symmetries of weak interactions". In: *Nuclear Physics* 22 (1961), pp. 579–588.

[17] Harald Fritzsch, Murray Gell-Mann, and Heinrich Leutwyler. "Advantages of the Color Octet Gluon Picture". In: *Physics Letters B* 47 (1973), pp. 365–368.

[18] David J. Griffiths. *Introduction to Elementary Particles*. 2nd. Weinheim: Wiley-VCH, 2008. ISBN: 978-3-527-40601-2.

[19] John F. Donoghue, Eugene Golowich, and Barry R. Holstein. *Dynamics of the Standard Model*. 2nd ed. Cambridge Monographs on Particle Physics, Nuclear Physics and Cosmology. Cambridge University Press, 2023.

[20] Cush. *Standard Model of Elementary Particles: the 12 Fundamental Fermions and 5 Fundamental Bosons*. Wikimedia Commons. 2019. URL: https://commons.wikimedia.org/wiki/File:Standard_Model_of_Elementary_Particles.svg.

[21] Mark Thomson. *Modern Particle Physics*. Cambridge: Cambridge University Press, 2013.

[22] Richard P. Feynman. "Quantum theory of gravitation". In: *Acta Physica Polonica* 24 (1963), pp. 697–722.

[23] Antonio Pich. *The Standard Model of Electroweak Interactions*. 2008. DOI: 10.5170/CERN-2006-003.1. URL: https://cds.cern.ch/record/819632.

[24] Masataka Fukugita and Tsutomu Yanagida. *Physics of Neutrinos: and Application to Astrophysics*. Theoretical and Mathematical Physics. Springer Berlin Heidelberg, 2003, pp. xii + 593. ISBN: 978-3-540-43800-7. DOI: 10.1007/978-3-662-05119-1.

[25] Mark Srednicki. *Quantum Field Theory*. Cambridge: Cambridge University Press, 2007. ISBN: 978-0-521-86449-7. DOI: 10.1017/CBO9780511813917.

[26] Sébastien Descotes-Genon, Yasmine Amhis, and Carla Marin Benito. "Experimental determination of the CKM matrix". In: *Scholarpedia* 17.1 (2022). Peer-reviewed encyclopedia article, p. 54385. DOI: 10.4249/scholarpedia.54385.

[27] J. Charles et al. "CP violation and the CKM matrix: Assessing the impact of the asymmetric B factories". In: *Eur. Phys. J. C* 41 (2005). Updated results and plots available at http://ckmfitter.in2p3.fr, pp. 1–131. arXiv: hep-ph/0406184 [hep-ph].

[28] LHCb Collaboration. "The LHCb Detector at the LHC". In: *Journal of Instrumentation* 3.08 (2008), S08005. DOI: 10.1088/1748-0221/3/08/S08005.

[29] R. et al Aaij. "Observation of a narrow pentaquark state, $P_c(4312)^+$, and of two-peak structure of the $P_c(4450)^+$". In: *Physical Review Letters* 122 (2019), p. 222001.

USC UNIVERSIDADE DE SANTIAGO DE COMPOSTELA

[30] E. Oset L. Roca. "On the hidden charm pentaquarks in $\Lambda_b \to J/\psi K^- p$ decay". In: *European Physical Journal C* 76 (2016).

[31] Hong-Tao An et al. "Spectroscopic behavior of fully heavy tetraquarks". In: *European Physical Journal C* 83 (2023).

[32] Elena Santopinto Ilia Belov Alessandro Giachino. "Fully charmed tetraquark production at the LHC experiments". In: *Journal of High Energy Physics* (2025).

[33] F. Feng et al. "Inclusive production of fully-charmed tetraquarks at LHC". In: *arXiv preprint* (2023). eprint: 2304.11142.

[34] R. et al Aaij. "Observation and study of the doubly charmed T_{cc}^+ tetraquark". In: *Nature Physics / Nature Communications* (2022).

[35] Georges Aad et al. "A precise determination of the strong-coupling constant from the recoil of Z bosons with the ATLAS experiment at $\sqrt{s} = 8$ TeV". In: (Sept. 2023). arXiv: 2309.12986 [hep-ex].

[36] Georges Aad et al. "Determination of the strong coupling constant from transverse energy−energy correlations in multijet events at $\sqrt{s} = 13$ TeV with the ATLAS detector". In: *JHEP* 07 (2023), p. 085. DOI: 10.1007/JHEP07(2023)085. arXiv: 2301.09351 [hep-ex].

[37] Peter W. Higgs. "Broken Symmetries and the Masses of Gauge Bosons". In: *Phys. Rev. Lett.* 13 (16 1964), pp. 508–509. DOI: 10.1103/PhysRevLett.13.508. URL: https://link.aps.org/doi/10.1103/PhysRevLett.13.508.

[38] F. Englert and R. Brout. "Broken Symmetry and the Mass of Gauge Vector Mesons". In: *Phys. Rev. Lett.* 13 (9 1964), pp. 321–323. DOI: 10.1103/PhysRevLett.13.321. URL: https://link.aps.org/doi/10.1103/PhysRevLett.13.321.

[39] CMS collaboration. "Observation of a New Boson at a Mass of 125 GeV with the CMS Experiment at the LHC". In: *Phys. Lett. B* 716 (2012), pp. 30–61. DOI: 10.1016/j.physletb.2012.08.021. arXiv: 1207.7235 [hep-ex].

[40] G. Abbiendi et al. "Search for the Standard Model Higgs Boson at LEP". In: *arXiv:hep-ex/0306033* (2003). URL: https://arxiv.org/abs/hep-ex/0306033.

[41] Georges Aad et al. "Observation of a new particle in the search for the Standard Model Higgs boson with the ATLAS detector at the LHC". In: *Phys. Lett. B* 716 (2012), pp. 1–29. DOI: 10.1016/j.physletb.2012.08.020. arXiv: 1207.7214 [hep-ex].

[42] Guido ALTARELLI. *The Standard Model of Particle Physics*. 2005. arXiv: hep-ph/0510281 [hep-ph]. URL: https://arxiv.org/abs/hep-ph/0510281.

USC UNIVERSIDADE DE SANTIAGO DE COMPOSTELA

[43] Richard H. Parker et al. “Measurement of the fine-structure constant as a test of the Standard Model”. In: *Science* 360.6385 (Apr. 2018), pp. 191–195. ISSN: 1095-9203. DOI: 10.1126/science.aap7706. URL: http://dx.doi.org/10.1126/science.aap7706.

[44] Gerard ’t Hooft. “Naturalness, chiral symmetry, and spontaneous chiral symmetry breaking”. In: *NATO Sci. Ser. B* 59 (1980). Ed. by Gerard ’t Hooft et al., pp. 135–157. DOI: 10.1007/978-1-4684-7571-5_9.

[45] Leonard Susskind. “Dynamics of Spontaneous Symmetry Breaking in the Weinberg-Salam Theory”. In: *Phys. Rev. D* 20 (1979), pp. 2619–2625. DOI: 10.1103/PhysRevD.20.2619.

[46] R.L. Workman et al. (Particle Data Group). “Review of Particle Physics”. In: *Progress of Theoretical and Experimental Physics* 2024.8 (2024). Sección 39.4.2: "Binomial Distribution", p. 083C01. URL: https://pdg.lbl.gov/.

[47] Isaac Newton. *Philosophiae Naturalis Principia Mathematica*. London: Royal Society, 1687.

[48] Albert Einstein. “Die Feldgleichungen der Gravitation”. In: *Sitzungsberichte der Königlich Preußischen Akademie der Wissenschaften* (1915), pp. 844–847.

[49] Steven Weinberg. *The Quantum Theory of Fields, Vol. I*. Cambridge University Press, 1995.

[50] John F. Donoghue. “General relativity as an effective field theory: The leading quantum corrections”. In: *Phys. Rev. D* 50 (1994), p. 3874.

[51] Clifford P. Burgess. “Quantum gravity in everyday life: General relativity as an effective field theory”. In: *Living Rev. Relativ.* 7 (2004), p. 5.

[52] Suraj N. Gupta. “Quantization of Einstein’s Gravitational Field: Linear Approximation”. In: *Proc. Phys. Soc. A* 65 (1952), p. 608.

[53] Richard P. Feynman. *Feynman Lectures on Gravitation*. Addison-Wesley, 1995.

[54] Steven Weinberg. “Photons and gravitons in perturbation theory: Derivation of Maxwell’s and Einstein’s equations”. In: *Phys. Rev.* 138 (1965), B988.

[55] Particle Data Group. “Review of Particle Physics”. In: *Prog. Theor. Exp. Phys.* 2022 (2022), p. 083C01.

[56] Max Planck. *Vorlesungen über die Theorie der Wärmestrahlung*. 2nd. Leipzig: J.A. Barth, 1914.

[57] Gerard ’t Hooft and Martinus J. G. Veltman. “One-loop divergencies in the theory of gravitation”. In: *Ann. Inst. Henri Poincaré A* 20 (1974), p. 69.

[58] Theodor Kaluza. “Zum Unitätsproblem der Physik”. In: *Sitzungsber. Preuss. Akad. Wiss. Berlin (Math. Phys.)* (1921), pp. 966–972.

[59] Oskar Klein. “Quantum Theory and Five-Dimensional Theory of Relativity”. In: *Z. Phys.* 37 (1926), pp. 895–906.

USC UNIVERSIDADE DE SANTIAGO DE COMPOSTELA

[60] A. Zee. *Quantum field theory in a nutshell*. Princeton University Press, 2010.

[61] F. Zwicky. "Die Rotverschiebung von extragalaktischen Nebeln". In: *Helv. Phys. Acta* 6 (1933), pp. 110–127. DOI: 10.1007/s10714-008-0707-4.

[62] V C Rubin and W K Ford Jr. "ROTATION OF THE ANDROMEDA NEBULA FROM A SPECTROSCOPIC SURVEY OF EMISSION REGIONS." In: *Astrophys. J. 159: 379-403(Feb 1970).* (Dec. 1969). DOI: 10.1086/150317. URL: https://www.osti.gov/biblio/4148861.

[63] Douglas Clowe et al. "A Direct Empirical Proof of the Existence of Dark Matter". In: *The Astrophysical Journal* 648.2 (Aug. 2006), pp. L109–L113. ISSN: 1538-4357. DOI: 10.1086/508162. URL: http://dx.doi.org/10.1086/508162.

[64] Matteo Viel et al. "How Cold Is Cold Dark Matter? Small-Scales Constraints from the Flux Power Spectrum of the High-Redshift Lyman-Forest". In: *Physical Review Letters* 100.4 (Jan. 2008). ISSN: 1079-7114. DOI: 10.1103/physrevlett.100.041304. URL: http://dx.doi.org/10.1103/PhysRevLett.100.041304.

[65] WMAP Science Team. *WMAP Nine-Year Cosmology Results: Figures*. NASA Goddard Space Flight Center, LAMBDA Archive. Image credit: NASA / WMAP Science Team. Figures provided for use in talks and publications with proper acknowledgement. 2012. URL: https://lambda.gsfc.nasa.gov/product/wmap/pub_papers/nineyear/cosmology/wmap_9yr_cosmology_images.html.

[66] Christopher J. Miller, Robert C. Nichol, and David J. Batuski. "Acoustic Oscillations in the Early Universe and Today". In: *Science* 292.5525 (June 2001), pp. 2302–2303. ISSN: 1095-9203. DOI: 10.1126/science.1060440. URL: http://dx.doi.org/10.1126/science.1060440.

[67] G. et al Hinshaw. "NINE-YEAR WILKINSON MICROWAVE ANISOTROPY PROBE (WMAP) OBSERVATIONS: COSMOLOGICAL PARAMETER RESULTS". In: *The Astrophysical Journal Supplement Series* 208.2 (Sept. 2013), p. 19. ISSN: 1538-4365. DOI: 10.1088/0067-0049/208/2/19. URL: http://dx.doi.org/10.1088/0067-0049/208/2/19.

[68] P. J. E. Peebles. "Tests of Cosmological Models Constrained by Inflation". In: *Astrophys. J.* 284 (1984), pp. 439–444. DOI: 10.1086/162425.

[69] P. J. E. Peebles and Bharat Ratra. "The Cosmological Constant and Dark Energy". In: *Rev. Mod. Phys.* 75 (2003). Ed. by Jong-Ping Hsu and D. Fine, pp. 559–606. DOI: 10.1103/RevModPhys.75.559. arXiv: astro-ph/0207347.

[70] Planck collaboration. "Planck2018 results: VI. Cosmological parameters". In: *Astronomy and Astrophysics* 641 (Sept. 2020), A6. ISSN: 1432-0746. DOI: 10.1051/0004-6361/201833910. URL: http://dx.doi.org/10.1051/0004-6361/201833910.

USC UNIVERSIDADE DE SANTIAGO DE COMPOSTELA

[71] Gianfranco Bertone, Dan Hooper, and Joseph Silk. "Particle dark matter: evidence, candidates and constraints". In: *Physics Reports* 405.5–6 (Jan. 2005), pp. 279–390. ISSN: 0370-1573. DOI: 10.1016/j.physrep.2004.08.031. URL: http://dx.doi.org/10.1016/j.physrep.2004.08.031.

[72] Branco et al. "Theory and phenomenology of two-Higgs-doublet models". In: *Physics Reports* 516.1–2 (July 2012), pp. 1–102. ISSN: 0370-1573. DOI: 10.1016/j.physrep.2012.02.002. URL: http://dx.doi.org/10.1016/j.physrep.2012.02.002.

[73] Savas Dimopoulos and Howard Georgi. "Softly Broken Supersymmetry and SU(5)". In: *Nucl. Phys. B* 193 (1981), pp. 150–162. DOI: 10.1016/0550-3213(81)90522-8.

[74] Michael E. Peskin. *What is the Hierarchy Problem?* 2025. arXiv: 2505.00694 [hep-ph]. URL: https://arxiv.org/abs/2505.00694.

[75] Howard E. Haber and Gordon L. Kane. "The Search for Supersymmetry: Probing Physics Beyond the Standard Model". In: *Phys. Rept.* 117 (1985), pp. 75–263. DOI: 10.1016/0370-1573(85)90051-1.

[76] Juan Pablo Hoyos Daza. "Composite Higgs models". PhD thesis. Sao Paulo U., 2019. arXiv: 1908.10204 [hep-ph].

[77] Paolo et al Azzurri. "A special Higgs challenge: measuring the mass and production cross section with ultimate precision at FCC-ee". In: *The European Physical Journal Plus* 137.1 (Dec. 2021). ISSN: 2190-5444. DOI: 10.1140/epjp/s13360-021-02202-4. URL: http://dx.doi.org/10.1140/epjp/s13360-021-02202-4.

[78] Philip et al Burrows. *The International Linear Collider Design Report*. Tech. rep. Comments: See also http://www.linearcollider.org/ILC/TDR. Geneva: CERN, 2013. URL: https://cds.cern.ch/record/1601971.

[79] O. Brunner et al. *The CLIC project*. 2022. arXiv: 2203.09186 [physics.acc-ph]. URL: https://arxiv.org/abs/2203.09186.

[80] Michael et al Benedikt. *Future Circular Collider Feasibility Study Report Volume 2: Accelerators, technical infrastructure and safety*. 2025. DOI: 10.17181/CERN.EBAY.7W4X. URL: http://cds.cern.ch/record/2928793.

[81] The CEPC Study Group. *CEPC Technical Design Report – Accelerator (v2)*. 2024. arXiv: 2312.14363 [physics.acc-ph]. URL: https://arxiv.org/abs/2312.14363.

[82] Y. et al Fukuda. "Measurements of the Solar Neutrino Flux from Super-Kamiokande's First 300 Days". In: *Physical Review Letters* 81.6 (Aug. 1998), pp. 1158–1162. ISSN: 1079-7114. DOI: 10.1103/physrevlett.81.1158. URL: http://dx.doi.org/10.1103/PhysRevLett.81.1158.

USC UNIVERSIDADE DE SANTIAGO DE COMPOSTELA

[83] SNO collaboration. "Direct Evidence for Neutrino Flavor Transformation from Neutral-Current Interactions in the Sudbury Neutrino Observatory". In: *Physical Review Letters* 89.1 (June 2002). ISSN: 1079-7114. DOI: 10.1103/physrevlett.89.011301. URL: http://dx.doi.org/10.1103/PhysRevLett.89.011301.

[84] S. Bilenky. *Neutrinos: Majorana or Dirac?* 2020. arXiv: 2008.02110 [hep-ph]. URL: https://arxiv.org/abs/2008.02110.

[85] M. et al Agostini. "Improved Limit on Neutrinoless Double-β Decay of ^{76}Ge from GERDA Phase II". In: *Phys. Rev. Lett.* 120.13 (2018), p. 132503. DOI: 10.1103/PhysRevLett.120.132503. arXiv: 1803.11100 [nucl-ex].

[86] S. et al Abe. "Search for Majorana Neutrinos with the Complete KamLAND-Zen Dataset". In: (June 2024). arXiv: 2406.11438 [hep-ex].

[87] Keith A. Olive. "Big bang baryogenesis". In: *Matter Under Extreme Conditions*. Springer Berlin Heidelberg, 1994, pp. 1–37. ISBN: 9783540490425. DOI: 10.1007/3-540-58689-x_40. URL: http://dx.doi.org/10.1007/3-540-58689-X_40.

[88] A. D. Sakharov. "Violation of CP Invariance, C asymmetry, and baryon asymmetry of the universe". In: *Pisma Zh. Eksp. Teor. Fiz.* 5 (1967), pp. 32–35. DOI: 10.1070/PU1991v034n05ABEH002497.

[89] Murilo Rangel. "Search for CP violation in $B^0 \to J/\psi K^0_S$ decays with first LHCb data". In: *EPJ Web Conf.* 28 (2012). Ed. by Gregorio Bernardi, Sandro De Cecco, and Yuji Enari, p. 12032. DOI: 10.1051/epjconf/20122812032. arXiv: 1202.1214 [hep-ex].

[90] Kazuo Abe et al. "Observation of large CP violation in the neutral B meson system". In: *Phys. Rev. Lett.* 87 (2001), p. 091802. DOI: 10.1103/PhysRevLett.87.091802. arXiv: hep-ex/0107061.

[91] Roel Aaij et al. "Measurement of the time-dependent CP asymmetries in $B^0_s \to J/\psi K^0_S$". In: *JHEP* 06 (2015), p. 131. DOI: 10.1007/JHEP06(2015)131. arXiv: 1503.07055 [hep-ex].

[92] Roel Aaij et al. "Observation of CP Violation in Charm Decays". In: *Phys. Rev. Lett.* 122.21 (2019), p. 211803. DOI: 10.1103/PhysRevLett.122.211803. arXiv: 1903.08726 [hep-ex].

[93] LHCb Collaboration. "New horizon in particle physics: First observation of CP violation in baryon decays". In: *arXiv preprint* (2025). arXiv: 2504.15008 [hep-ph].

[94] C. Hagedorn et al. "CP Violation in the Lepton Sector and Implications for Leptogenesis". In: *Int. J. Mod. Phys. A* 33.05n06 (2018), p. 1842006. DOI: 10.1142/S0217751X1842006X. arXiv: 1711.02866 [hep-ph].

[95] Juliette et al Alimena. "Searching for long-lived particles beyond the Standard Model at the Large Hadron Collider". In: *J. Phys. G* 47.9 (2020), p. 090501. DOI: 10.1088/1361-6471/ab4574. arXiv: 1903.04497 [hep-ex].

USC UNIVERSIDADE DE SANTIAGO DE COMPOSTELA

[96] S. H. Neddermeyer and C. D. Anderson. "Note on the Nature of Cosmic Ray Particles". In: *Phys. Rev.* 51 (1937), pp. 884–886. DOI: 10.1103/PhysRev.51.884.

[97] V. D. Hopper and S. Biswas. "Evidence Concerning the Existence of the New Unstable Elementary Neutral Particle". In: *Phys. Rev.* 80 (6 1950), pp. 1099–1100. DOI: 10.1103/PhysRev.80.1099. URL: https://link.aps.org/doi/10.1103/PhysRev.80.1099.

[98] Simon Knapen and Steven Lowette. "A Guide to Hunting Long-Lived Particles at the LHC". In: *Ann. Rev. Nucl. Part. Sci.* 73 (2023). 31 pages, 5 figures. Invited review for Annual Reviews Nuclear Particle Science 2023, pp. 421–449. DOI: 10.1146/annurev-nucl-101920-013011. arXiv: 2212.03883. URL: https://cds.cern.ch/record/2894526.

[99] P. et al Abreu. "Measurement of inclusive production of neutral mesons in hadronic Z decays". In: *Phys. Lett. B* 444 (1998), p. 491. DOI: 10.1016/S0370-2693(98)01427-6.

[100] A. et al Heister. "Measurement of the strong coupling constant from hadronic event shapes and the four-jet rate". In: *Eur. Phys. J. C* 25 (2002), p. 339. DOI: 10.1007/s10052-002-0984-z.

[101] T. et al Aaltonen. "Measurement of the top quark mass with in situ jet energy scale calibration in the all-hadronic channel at CDF". In: *Phys. Rev. D* 78 (2008), p. 032015. DOI: 10.1103/PhysRevD.78.032015.

[102] V. M. et al Abazov. "Search for neutral Higgs bosons decaying to tau pairs in p-bar p collisions at sqrt(s) = 1.96 TeV". In: *Phys. Rev. Lett.* 97 (2006), p. 161802. DOI: 10.1103/PhysRevLett.97.161802.

[103] F. J. Hasert et al. "Observation of Neutrino Like Interactions without Muon or Electron in the Gargamelle Neutrino Experiment". In: *Nucl. Phys. B* 73 (1974), pp. 1–22. DOI: 10.1016/0550-3213(74)90038-8.

[104] Andrea Coccaro et al. "Data-driven Model-independent Searches for Long-lived Particles at the LHC". In: *Phys. Rev. D* 94 (2016), p. 113003. DOI: 10.1103/PhysRevD.94.113003. arXiv: 1605.02742 [hep-ph].

[105] Georges et al Aad. "Search for heavy charged long-lived particles with the ATLAS detector in pp collisions at $\sqrt{s}$ = 13 TeV". In: *Phys. Rev. D* 99 (2019), p. 092007. DOI: 10.1103/PhysRevD.99.092007. arXiv: 1902.01636 [hep-ex].

[106] Armen Tumasyan et al. "Search for long-lived particles decaying to leptons with large impact parameter in proton–proton collisions at $\sqrt{s} = 13\,\text{TeV}$". In: *Eur. Phys. J. C* 82.2 (2022), p. 153. DOI: 10.1140/epjc/s10052-022-10027-3. arXiv: 2110.04809 [hep-ex].

USC UNIVERSIDADE DE SANTIAGO DE COMPOSTELA

[107] Roel et al Aaij. "Search for long-lived particles decaying to jet pairs". In: *Phys. Rev. Lett.* 117 (2016), p. 151801. DOI: 10.1103/PhysRevLett.117.151801. arXiv: 1606.07898 [hep-ex].

[108] Jia Liu, Zhen Liu, and Lian-Tao Wang. "Enhancing Long-Lived Particles Searches at the LHC with Precision Timing Information". In: *Phys. Rev. Lett.* 122.13 (2019), p. 131801. DOI: 10.1103/PhysRevLett.122.131801. arXiv: 1805.05957 [hep-ph].

[109] David et al Curtin. "Long-Lived Particles at the Energy Frontier: The MATHUSLA Physics Case". In: *Rept. Prog. Phys.* 82.11 (2019), p. 116201. DOI: 10.1088/1361-6633/ab28d6. arXiv: 1806.07396 [hep-ph].

[110] Jeffrey Goldstone, Abdus Salam, and Steven Weinberg. "Broken Symmetries". In: *Phys. Rev.* 127 (3 1962), pp. 965–970. DOI: 10.1103/PhysRev.127.965. URL: https://link.aps.org/doi/10.1103/PhysRev.127.965.

[111] Giuliano Panico and Andrea Wulzer. *The Composite Nambu-Goldstone Higgs*. Springer International Publishing, 2016. ISBN: 9783319226170. DOI: 10.1007/978-3-319-22617-0. URL: http://dx.doi.org/10.1007/978-3-319-22617-0.

[112] Mikael Chala, Germano Nardini, and Ivan Sobolev. "Unified explanation for dark matter and electroweak baryogenesis with direct detection and gravitational wave signatures". In: *Phys. Rev. D* 94.5 (2016), p. 055006. DOI: 10.1103/PhysRevD.94.055006. arXiv: 1605.08663 [hep-ph].

[113] Sidney R. Coleman, J. Wess, and Bruno Zumino. "Structure of phenomenological Lagrangians. 1." In: *Phys. Rev.* 177 (1969), pp. 2239–2247. DOI: 10.1103/PhysRev.177.2239.

[114] David B. Kaplan. "Flavor at SSC energies: A New mechanism for dynamically generated fermion masses". In: *Nucl. Phys. B* 365 (1991), pp. 259–278. DOI: 10.1016/S0550-3213(05)80021-5.

[115] Mikael Chala, Ulrik Egede, and Michael Spannowsky. "Searching new physics in rare B-meson decays into multiple muons". In: *The European Physical Journal C* 79.5 (May 2019). ISSN: 1434-6052. DOI: 10.1140/epjc/s10052-019-6946-6. URL: http://dx.doi.org/10.1140/epjc/s10052-019-6946-6.

[116] Andrew Blance et al. "Novel B-decay signatures of light scalars at high energy facilities". In: *Physical Review D* 100.11 (Dec. 2019). ISSN: 2470-0029. DOI: 10.1103/physrevd.100.115015. URL: http://dx.doi.org/10.1103/PhysRevD.100.115015.

[117] R. Aaij et al. "Searches for rare B_s^0 and B^0 decays into four muons". In: *JHEP* 03 (2022), p. 109. DOI: 10.1007/JHEP03(2022)109. arXiv: 2111.11339 [hep-ex].

[118] Roel Aaij et al. "Searches for low-mass dimuon resonances". In: *JHEP* 10 (2020), p. 156. DOI: 10.1007/JHEP10(2020)156. arXiv: 2007.03923 [hep-ex].

[119] R Aaij et al. "Test of Lepton Universality in $b \to sl^+l^-$ Decays". In: *Physical Review Letters* 131.5 (Aug. 2023). ISSN: 1079-7114. DOI: 10.1103/physrevlett.131.051803. URL: http://dx.doi.org/10.1103/PhysRevLett.131.051803.

[120] Aielli et al. "Expression of interest for the CODEX-b detector". In: *The European Physical Journal C* 80.12 (Dec. 2020). ISSN: 1434-6052. DOI: 10.1140/epjc/s10052-020-08711-3. URL: http://dx.doi.org/10.1140/epjc/s10052-020-08711-3.

[121] J. Beacham et al. "Physics Beyond Colliders at CERN: Beyond the Standard Model Working Group Report". In: *J. Phys. G* 47.1 (2020), p. 010501. DOI: 10.1088/1361-6471/ab4cd2. arXiv: 1901.09966 [hep-ex].

[122] J Beacham, C Burrage, and et al Curtin. "Physics beyond colliders at CERN: beyond the Standard Model working group report". In: *Journal of Physics G: Nuclear and Particle Physics* 47.1 (Dec. 2019), p. 010501. ISSN: 1361-6471. DOI: 10.1088/1361-6471/ab4cd2. URL: http://dx.doi.org/10.1088/1361-6471/ab4cd2.

[123] David E. Morrissey, David Poland, and Kathryn M. Zurek. "Abelian Hidden Sectors at a GeV". In: *JHEP* 07 (2009), p. 050. DOI: 10.1088/1126-6708/2009/07/050. arXiv: 0904.2567 [hep-ph].

[124] Robert M. Schabinger and James D. Wells. "A Minimal spontaneously broken hidden sector and its impact on Higgs boson physics at the large hadron collider". In: *Phys. Rev. D* 72 (2005), p. 093007. DOI: 10.1103/PhysRevD.72.093007. arXiv: hep-ph/0509209.

[125] Shrihari Gopalakrishna, Sunghoon Jung, and James D. Wells. "Higgs boson decays to four fermions through an abelian hidden sector". In: *Phys. Rev. D* 78 (2008), p. 055002. DOI: 10.1103/PhysRevD.78.055002. arXiv: 0801.3456 [hep-ph].

[126] B. Abi and others (Muon g-2 Collaboration). "Measurement of the Positive Muon Anomalous Magnetic Moment to 0.14 ppm". In: *Phys. Rev. Lett.* 125 (2025), p. 121801. DOI: 10.1103/PhysRevLett.125.121801.

[127] S. Borsanyi et al. "Leading-order hadronic vacuum polarization contribution to the muon magnetic moment from lattice QCD". In: *Nature* 593 (2021), pp. 51–55. DOI: 10.1038/s41586-021-03418-1.

[128] B. Patt and F. Wilczek. "Higgs-field portal into hidden sectors". In: *hep-ph/0605188* (2006). eprint: hep-ph/0605188.

[129] LHCb Collaboration. "Search for hidden-sector bosons in $B^0 \to K^*\chi$ decays". In: *Phys. Rev. Lett.* 115 (2015), p. 161802. DOI: 10.1103/PhysRevLett.115.161802. arXiv: 1508.04094 [hep-ex].

USC UNIVERSIDADE DE SANTIAGO DE COMPOSTELA

[130] David McKeen, John N. Ng, and Douglas Tuckler. "Higgs portal interpretation of the Belle II B+→K+$\nu\nu$ measurement". In: *Phys. Rev. D* 109.7 (2024), p. 075006. DOI: 10.1103/PhysRevD.109.075006. arXiv: 2312.00982 [hep-ph].

[131] Enrique Fernández-Martínez et al. "Effective portals to heavy neutral leptons". In: *JHEP* 09 (2023), p. 001. DOI: 10.1007/JHEP09(2023)001. arXiv: 2304.06772 [hep-ph].

[132] Yi Cai et al. "Lepton Number Violation: Seesaw Models and Their Collider Tests". In: *Front. in Phys.* 6 (2018), p. 40. DOI: 10.3389/fphy.2018.00040. arXiv: 1711.02180 [hep-ph].

[133] NA62 Collaboration. "Search for heavy neutral lepton production in K^+ decays". In: *Phys. Lett. B* 807 (2020), p. 135599. DOI: 10.1016/j.physletb.2020.135599. arXiv: 2005.09575 [hep-ex].

[134] Belle Collaboration. "Search for heavy neutral leptons in τ decays at Belle". In: *Phys. Rev. D* 100.11 (2019), p. 111101. DOI: 10.1103/PhysRevD.100.111101. arXiv: 1905.08783 [hep-ex].

[135] Belle II Collaboration. "Search for heavy neutral leptons in B decays with Belle II". In: *Phys. Rev. D* 106.7 (2022), p. 072005. DOI: 10.1103/PhysRevD.106.072005. arXiv: 2212.10095 [hep-ex].

[136] LHCb Collaboration. "Search for heavy neutral leptons in B decays". In: *Eur. Phys. J. C* 81 (2021), p. 248. DOI: 10.1140/epjc/s10052-021-08971-8. arXiv: 2011.05263 [hep-ex].

[137] ATLAS Collaboration. "Search for heavy neutral leptons in W boson decays at $\sqrt{s} = 13$ TeV with the ATLAS detector". In: *JHEP* 07 (2023), p. 207. DOI: 10.1007/JHEP07(2023)207. arXiv: 2303.05440 [hep-ex].

[138] CMS Collaboration. "Nonresonant Searches for Axion-Like Particles in Vector Boson Scattering Processes at the LHC". In: *JHEP* 02 (2022), p. 036. DOI: 10.1007/JHEP02(2022)036. arXiv: 2202.03450 [hep-ex].

[139] Giulio Aielli et al. "CODEX-b: Opening New Windows to the Long-Lived Particle Frontier at the LHC: ESPP Update Comprehensive summary". In: (May 2025). arXiv: 2505.05952 [hep-ex].

[140] LHCb Collaboration. "Search for Axion-Like Particles decaying into photon pairs in pp collisions at $\sqrt{s} = 13$ TeV". In: *Phys. Rev. Lett.* 125 (2025), p. 081801. DOI: 10.1103/PhysRevLett.125.081801. arXiv: 2503.01234 [hep-ex].

[141] NA64 Collaboration. "Search for Axion-Like Particles with a high-energy electron beam". In: *Phys. Lett. B* 819 (2025), p. 136403. DOI: 10.1016/j.physletb.2025.136403. arXiv: 2504.05678 [hep-ex].

[142] FASER Collaboration. "Search for long-lived Axion-Like Particles decaying to photons and leptons at the LHC". In: *JHEP* 06 (2025), p. 045. DOI: 10.1007/JHEP06(2025)045. arXiv: 2502.08912 [hep-ex].

USC UNIVERSIDADE DE SANTIAGO DE COMPOSTELA

[143] ATLAS Collaboration. "Search for an axion-like particle with forward proton scattering in association with photon pairs at ATLAS". In: *JHEP* 07 (2023), p. 234. DOI: 10.1007/JHEP07(2023)234. arXiv: 2304.10953 [hep-ex].

[144] ALEPH Collaboration et al. "Search for the Standard Model Higgs Boson at LEP". In: *Physics Letters B* 565 (2003), pp. 61–75. DOI: 10.1016/S0370-2693(03)00614-2. arXiv: hep-ex/0306033.

[145] S. Abachi et al. "Observation of the top quark". In: *Phys. Rev. Lett.* 74 (1995), pp. 2632–2637. DOI: 10.1103/PhysRevLett.74.2632. arXiv: hep-ex/9503003.

[146] Ewa Lopienska. "The CERN accelerator complex, layout in 2022". In: (2022). General Photo. URL: https://cds.cern.ch/record/2800984.

[147] Lyndon Evans and Philip Bryant. "LHC Machine". In: *Journal of Instrumentation* 3.08 (2008), S08001. DOI: 10.1088/1748-0221/3/08/S08001.

[148] Oliver Brüning et al. "The High-Luminosity Large Hadron Collider (HL-LHC): Past, Present and Future". In: *European Physical Journal Plus* 138.3 (2023), p. 229. DOI: 10.1140/epjp/s13360-023-03803-w.

[149] ATLAS Collaboration. "Observation of a New Particle in the Search for the Standard Model Higgs Boson with the ATLAS Detector at the LHC". In: *Physics Letters B* 716.1 (2012), pp. 1–29. DOI: 10.1016/j.physletb.2012.08.020.

[150] CMS Collaboration. "Observation of a New Boson at a Mass of 125 GeV with the CMS Experiment at the LHC". In: *Physics Letters B* 716.1 (2012), pp. 30–61. DOI: 10.1016/j.physletb.2012.08.021.

[151] Author(s) CERN Courier. *The tale of a billion-trillion protons*. CERN Courier. Artículo técnico divulgativo con datos de diseño de Linac2. 2010.

[152] C. E. Hill et al. "Tests of the CERN Proton Linac Performance for LHC-Type Beams". In: *arXiv:physics/0008102* (2000).

[153] K. Hanke et al. "LHC Injector Complex Status". In: *CERN Yellow Reports (Proceedings of the Chamonix 2014 Workshop on LHC Performance)* 2 (2016), pp. 71–88. DOI: 10.5170/CERN-2015-002.71.

[154] Hannes Bartosik, Giovanni Rumolo, et al. "Performance of the LHC injector chain after the upgrade and potential development". In: *arXiv:2203.09202* (2022).

[155] B. Goddard, T. Argyropoulos, H. Bartosik, et al. "Progress with the Upgrade of the SPS for the HL-LHC Era". In: *arXiv:1409.5821* (2014).

[156] Lucio Rossi. "State-of-the-art accelerator magnets". In: *IEEE Transactions on Applied Superconductivity* 12.1 (2002), pp. 219–227. DOI: 10.1109/TASC.2002.1018387.

[157] Lyndon R. Evans and Philip Bryant. "LHC Machine". In: *Journal of Instrumentation* 3 (2008), S08001. DOI: 10.1088/1748-0221/3/08/S08001.

[158] ALICE Collaboration. "The ALICE Experiment at the CERN LHC". In: *Journal of Instrumentation* 3.08 (2008), S08002. DOI: 10.1088/1748-0221/3/08/S08002.

[159] A. Augusto Alves Jr. et al. "The LHCb Detector at the LHC". In: *JINST* 3 (2008), S08005. DOI: 10.1088/1748-0221/3/08/S08005.

[160] LHCb Collaboration. "The LHCb detector: status and recent results". In: *International Journal of Modern Physics A* 27.07 (2012), p. 1230004. eprint: arXiv:1302.1891.

[161] LHCb Collaboration. *LHCb Standard Set of Performance Numbers*. Online note, LHCb spokespersons' bureau, internal document. https://lhcb.web.cern.ch/speakersbureau/html/PerformanceNumbers.html. 2022.

[162] LHCb Collaboration. "Probing proton PDFs at high x with LHCb". In: *SciPost Physics Proceedings* (2021). eprint: arXiv:2107.00091.

[163] DELPHI collaboration. *DELPHI: A Detector with Lepton, Photon and Hadron Identification: Letter of Intent for an Experimental Program at LEP*. Tech. rep. CERN, 1982. URL: https://cds.cern.ch/record/2625461.

[164] Christian Elsasser. *$b\bar{b}$ Production Angle Plots*. LHCb Collaboration, Speakers Bureau Online Resource. https://lhcb.web.cern.ch/lhcb/speakersbureau/html/bb_ProductionAngles.html. 2025. (Visited on 09/16/2025).

[165] M. Pepe Altarelli, F. Teubert, and the LHCb Collaboration. "B Physics at LHCb". In: *Journal of Instrumentation (JINST)* 3 (2008), S08005. eprint: arXiv:0802.1901.

[166] Sander Klous. "Vertex Detector and Read-out Chip Development for the LHCb Experiment". Produced by F&N Boekservice, Amsterdam. PhD thesis. University of Amsterdam, 2005. ISBN: 90-738-3843-6.

[167] LHCb Collaboration. "LHCb detector and trigger performance in Run I". In: *Journal of Instrumentation (JINST)* 9 (2014), P09007.

[168] LHCb Collaboration. "LHCb detector and trigger performance in Run II". In: *JINST* 13 (2018), P04013.

[169] LHCb Collaboration. "The LHCb Upgrade I". In: *Journal of Instrumentation (JINST)* 19.5 (2024), P05065. DOI: 10.1088/1748-0221/19/05/P05065.

[170] CERN. *LHCb detector view among the bending plane*. Image: Wikimedia Commons. 2008. URL: https://commons.wikimedia.org/wiki/File:Lhcbview.jpg.

[171] Barbosa-Marinho et al. *LHCb VELO (VErtex LOcator)*. Technical design report. LHCb. Geneva: CERN, 2001. URL: https://cds.cern.ch/record/504321.

USC UNIVERSIDADE DE SANTIAGO DE COMPOSTELA

[172] R. Aaij et al. "Performance of the LHCb Vertex Locator". In: *JINST* 9 (2014), P09007. DOI: 10.1088/1748-0221/9/09/P09007. arXiv: 1405.7808 [physics.ins-det].

[173] S. Amato et al. "The history of LHCb". In: *Eur. Phys. J. H* 46.1 (2021), pp. 1–69. DOI: 10.1140/epjh/s13129-021-00002-z. arXiv: 2105.09052 [physics.hist-ph].

[174] M. Alexander et al. "Mapping the material in the LHCb vertex locator using secondary hadronic interactions". In: *JINST* 13.06 (2018), P06008. DOI: 10.1088/1748-0221/13/06/P06008. arXiv: 1803.07466 [physics.ins-det].

[175] LHCb VELO group. "LHCb VELO Upgrade Technical Design Report". In: *CERN Yellow Reports: Monographs* (2013). DOI: 10.17181/CERN.9YBX.D4GQ. URL: https://cds.cern.ch/record/1624070.

[176] R. Calabrese et al. "Performance of the LHCb RICH detectors during LHC Run 2". In: *JINST* 17.07 (2022), P07013. DOI: 10.1088/1748-0221/17/07/P07013. arXiv: 2205.13400 [physics.ins-det].

[177] LHCb collaboration. "LHCb PID Upgrade Technical Design Report". In: (Nov. 2013).

[178] LHCb collaboration. *LHCb RICH*. Technical design report. LHCb. Geneva: CERN, 2000. URL: https://cds.cern.ch/record/494263.

[179] LHCb collaboration. *LHCb reoptimized detector design and performance*. Technical design report. LHCb. Geneva: CERN, 2003. URL: https://cds.cern.ch/record/630827.

[180] LHCb collaboration. *LHCb inner tracker*. Technical design report. LHCb. revised version number 1 submitted on 2002-11-13 14:14:34. Geneva: CERN, 2002. URL: https://cds.cern.ch/record/582793.

[181] Bart Hommels. "The LHCb outer tracker detector design and production". In: 2005.

[182] LHCb Collaboration. *LHCb outer tracker*. Technical design report. LHCb. Geneva: CERN, 2001. URL: https://cds.cern.ch/record/519146.

[183] LHCb collaboration. "Performance of the LHCb Outer Tracker". In: *JINST* 9.01 (2014), P01002. DOI: 10.1088/1748-0221/9/01/P01002. arXiv: 1311.3893 [physics.ins-det].

[184] Maximilien Brice. "The LHCb magnet". 2004. URL: https://cds.cern.ch/record/808276.

[185] LHCb Collaboration. *LHCb magnet*. Technical design report. LHCb. Geneva: CERN, 2000. DOI: 10.17181/CERN.MCVC.Q12G. URL: https://cds.cern.ch/record/424338.

[186] LHCb collaboration. *LHCb calorimeters*. Technical design report. LHCb. Geneva: CERN, 2000. URL: https://cds.cern.ch/record/494264.

USC UNIVERSIDADE DE SANTIAGO DE COMPOSTELA

[187] Carlos Abellán Beteta et al. *Calibration and performance of the LHCb calorimeters in Run 1 and 2 at the LHC*. Aug. 2020. arXiv: 2008.11556 [physics.ins-det].

[188] Eduardo Picatoste Olloqui. "LHCb preshower(PS) and scintillating pad detector (SPD): Commissioning, calibration, and monitoring". In: *J. Phys. Conf. Ser.* 160 (2009). Ed. by M. Fraternali, Gabriella Gaudio, and Michele Livan, p. 012046. DOI: 10.1088/1742-6596/160/1/012046.

[189] S. Barsuk et al. *Design and construction of electromagnetic calorimeter for LHCb experiment*. Oct. 2000.

[190] LHCb collaboration. *LHCb muon system*. Technical design report. LHCb. Geneva: CERN, 2001. URL: https://cds.cern.ch/record/504326.

[191] F. P. Albicocco et al. "Long-term operation of the multi-wire-proportional-chambers of the LHCb muon system". In: *JINST* 14 (2019), P11031. DOI: 10.1088/1748-0221/14/11/P11031. arXiv: 1908.02178 [physics.ins-det].

[192] Emanuele Santovetti. "The LHCb muon detector". In: *Nuclear Instruments and Methods in Physics Research Section A: Accelerators, Spectrometers, Detectors and Associated Equipment* 462.1-2 (2001), pp. 297–300. ISSN: 0168-9002. DOI: 10.1016/S0168-9002(01)00127-9. URL: https://www.sciencedirect.com/science/article/pii/S0168900201001279.

[193] R. Aaij et al. "Performance of the LHCb Muon System". In: *JINST* 8 (2013), P10020. DOI: 10.1088/1748-0221/8/10/P10020. arXiv: 1306.0249 [physics.ins-det]. URL: https://cds.cern.ch/record/1561136.

[194] Jorg Wenninger. "LHC status and performance". In: *PoS* CHARGED2018 (2019), p. 001. DOI: 10.22323/1.339.0001.

[195] M Lamont. "Chapter 4: Operational Experience from LHC Run 1 and 2, and Consolidation in View of Run 3 and the HL-LHC". In: *Adv. Ser. Direct. High Energy Phys.* 31 (2024), pp. 101–120. DOI: 10.1142/9789811278952_0004. URL: https://cds.cern.ch/record/2906147.

[196] CERN LHC Performance and Statistics (LPC). *Luminosity plots and fill statistics (Run 2)*. https://lpc.web.cern.ch. Accessed: October 2025.

[197] Roel Aaij et al. "Measurement of differential $b\bar{b}$- and $c\bar{c}$-dijet cross-sections in the forward region of pp collisions at $\sqrt{s} = 13$ TeV". In: *JHEP* 02 (2021), p. 023. DOI: 10.1007/JHEP02(2021)023. arXiv: 2010.09437 [hep-ex].

[198] Roel Aaij et al. "Measurement of the b-quark production cross-section in 7 and 13 TeV pp collisions". In: *Phys. Rev. Lett.* 118.5 (2017). [Erratum: Phys.Rev.Lett. 119, 169901 (2017)], p. 052002. DOI: 10.1103/PhysRevLett.118.052002. arXiv: 1612.05140 [hep-ex].

[199] Roel Aaij et al. "Measurement of the $\eta_c(1S)$ production cross-section in pp collisions at $\sqrt{s} = 13$ TeV". In: *Eur. Phys. J. C* 80.3 (2020), p. 191. DOI: 10.1140/epjc/s10052-020-7733-0. arXiv: 1911.03326 [hep-ex].

USC UNIVERSIDADE DE SANTIAGO DE COMPOSTELA

[200] Roel et al Aaij. "Design and performance of the LHCb trigger and full real-time reconstruction in Run 2 of the LHC". In: *JINST* 14.04 (2019), P04013. DOI: 10.1088/1748-0221/14/04/P04013. arXiv: 1812.10790. URL: https://cds.cern.ch/record/2652801.

[201] R. Aaij et al. "LHCb detector performance". In: *International Journal of Modern Physics A* 30.07 (Mar. 2015), p. 1530022. ISSN: 1793-656X. DOI: 10.1142/s0217751x15300227. URL: http://dx.doi.org/10.1142/S0217751X15300227.

[202] Dordei Francesca. "LHCb detector and trigger performance in Run II". In: vol. 164. 01016. 2017, p. 10. DOI: 10.1051/epjconf/201716401016.

[203] S Tolk et al. *Data driven trigger efficiency determination at LHCb*. Tech. rep. Geneva: CERN, 2014. URL: https://cds.cern.ch/record/1701134.

[204] The LHCb collaboration. "Measurement of the track reconstruction efficiency at LHCb". In: *Journal of Instrumentation* 10.02 (Feb. 2015), P02007–P02007. ISSN: 1748-0221. DOI: 10.1088/1748-0221/10/02/p02007. URL: http://dx.doi.org/10.1088/1748-0221/10/02/P02007.

[205] Nathan Grieser et al. "The LHCb Stripping Project: Sustainable Legacy Data Processing for High-Energy Physics". In: (Sept. 2025). arXiv: 2509.05294 [hep-ex].

[206] Pierre Billoir et al. "A parametrized Kalman filter for fast track fitting at LHCb". In: *Comput. Phys. Commun.* 265 (2021), p. 108026. DOI: 10.1016/j.cpc.2021.108026. arXiv: 2101.12040. URL: https://cds.cern.ch/record/2759269.

[207] Luis Miguel Garcia et al. "Tracking performance for long-lived particles at LHCb". In: *Journal of Physics: Conference Series* 1525.1 (Apr. 2020), p. 012095. ISSN: 1742-6596. DOI: 10.1088/1742-6596/1525/1/012095. URL: http://dx.doi.org/10.1088/1742-6596/1525/1/012095.

[208] Peilian Li, Eduardo Rodrigues, and Sascha Stahl. *Tracking Definitions and Conventions for Run 3 and Beyond*. Tech. rep. Geneva: CERN, 2021. URL: https://cds.cern.ch/record/2752971.

[209] Alessio Piucci. "The LHCb Upgrade". In: *J. Phys.: Conf. Ser.* (2017).

[210] Michel De Cian et al. *Fast neural-net based fake track rejection in the LHCb reconstruction*. Tech. rep. Geneva: CERN, 2017. URL: https://cds.cern.ch/record/2255039.

[211] S Miglioranzi et al. *The LHCb Simulation Application, Gauss: Design, Evolution and Experience*. Tech. rep. Geneva: CERN, 2011. URL: https://cds.cern.ch/record/1322402.

[212] Gloria Corti et al. "New software technologies in the LHCb Simulation". In: *J. Phys.: Conf. Ser.* (2023).

[213] Oliver Brüning and Markus Zerlauth. "LHC operation and the High-Luminosity LHC upgrade project". In: *CERN Accelerator School course: Advanced Accelerator Physics*. May 2025. arXiv: 2505.03535 [physics.acc-ph].

USC UNIVERSIDADE DE SANTIAGO DE COMPOSTELA

[214] LHCb LHCb collaboration. *LHCb Upgrade II Scoping Document*. Tech. rep. Geneva: CERN, 2024. DOI: 10.17181/CERN.2RXP.HDK0. URL: https://cds.cern.ch/record/2903094.

[215] Roel Aaij et al. "The LHCb Upgrade I". In: *JINST* 19.05 (2024), P05065. DOI: 10.1088/1748-0221/19/05/P05065. arXiv: 2305.10515 [hep-ex].

[216] Lawrence Lee et al. "Collider searches for long-lived particles beyond the Standard Model". In: *Progress in Particle and Nuclear Physics* 106 (2019).

[217] ATLAS Collaboration. "Search for long-lived particles produced in p p collisions at $\sqrt{s} = 13$ TeV that decay into displaced hadronic jets in the ATLAS muon spectrometer". In: *Phys. Rev. D* (2019).

[218] ATLAS Collaboration. "Search for neutral long-lived particles that decay into displaced jets in the ATLAS calorimeter in association with leptons or jets using pp collisions at $\sqrt{s} = 13$ TeV". In: *JHEP* 11 (2024), p. 036. DOI: 10.1007/JHEP11(2024)036. arXiv: 2407.12345. URL: https://doi.org/10.1007/JHEP11(2024)036.

[219] A. M. Sirunyan et al. "Search for long-lived particles decaying to jets with displaced vertices in proton-proton collisions at $\sqrt{s} = 13$ TeV". In: *Phys. Rev. D* 104.5 (2021), p. 052011. DOI: 10.1103/PhysRevD.104.052011. arXiv: 2104.13474 [hep-ex].

[220] Joel N. Butler and Tommaso Tabarelli de Fatis. "A MIP Timing Detector for the CMS Phase-2 Upgrade". In: (2019).

[221] Jia Liu, Zhen Liu, and Lian-Tao Wang. "Enhancing Long-Lived Particles Searches at the LHC with Precision Timing Information". In: *Phys. Rev. Lett.* 122 (13 Apr. 2019), p. 131801. DOI: 10.1103/PhysRevLett.122.131801. URL: https://link.aps.org/doi/10.1103/PhysRevLett.122.131801.

[222] Jia Liu et al. "Enhancing Sensitivities to Long-lived Particles with High Granularity Calorimeters at the LHC". In: *JHEP* 11 (2020), p. 066. DOI: 10.1007/JHEP11(2020)066. arXiv: 2005.10836 [hep-ph].

[223] Brent R. Yates. "A CMS Level-1 Track Finder for the HL-LHC". In: (Oct. 2021). arXiv: 2110.02826 [physics.ins-det].

[224] H. Aihara et al. *The Belle II Detector Upgrades Framework Conceptual Design Report*.

[225] Michael Duerr et al. "Long-lived dark Higgs and inelastic dark matter at Belle II". In: *Journal of High Energy Physics* 2021.4 (Apr. 2021). ISSN: 1029-8479. DOI: 10.1007/jhep04(2021)146. URL: http://dx.doi.org/10.1007/JHEP04(2021)146.

[226] David McKeen, John N. Ng, and Douglas Tuckler. *Higgs Portal Interpretation of the Belle II $B^+ \to K^+\nu\nu$ Measurement*. 2023. arXiv: 2312.00982 [hep-ph]. URL: https://arxiv.org/abs/2312.00982.

USC UNIVERSIDADE DE SANTIAGO DE COMPOSTELA

[227] I. Adachi et al. "Search for a Dark Higgs Boson Produced in Association with Inelastic Dark Matter at the Belle II Experiment". In: *Phys. Rev. Lett.* 135.13 (2025), p. 131801. DOI: 10.1103/37w5-glpp. arXiv: 2505.09705 [hep-ex].

[228] Henso FASER Collaboration: Abreu and Mansour et al. "The FASER detector". In: *Journal of Instrumentation* 19.05 (May 2024), P05066. ISSN: 1748-0221. DOI: 10.1088/1748-0221/19/05/p05066. URL: http://dx.doi.org/10.1088/1748-0221/19/05/P05066.

[229] Jae Hyeok Yoo. *The milliQan Experiment: Search for milli-charged Particles at the LHC*. 2018. arXiv: 1810.06733 [physics.ins-det]. URL: https://arxiv.org/abs/1810.06733.

[230] FASER Collaboration and Akitaka Ariga et al. *Technical Proposal for FASER: ForwArd Search ExpeRiment at the LHC*. 2018. arXiv: 1812.09139 [physics.ins-det]. URL: https://arxiv.org/abs/1812.09139.

[231] Saeid Foroughi-Abari, Felix Kling, and Yu-Dai Tsai. "Looking forward to millicharged dark sectors at the LHC". In: *Physical Review D* 104.3 (Aug. 2021). ISSN: 2470-0029. DOI: 10.1103/physrevd.104.035014. URL: http://dx.doi.org/10.1103/PhysRevD.104.035014.

[232] Branden Aitken, Cristiano Alpigiani, and Juan Carlos Arteaga-Velázquez et al. *MATHUSLA: An External Long-Lived Particle Detector to Maximize the Discovery Potential of the HL-LHC*. 2025. arXiv: 2504.01999 [physics.ins-det]. URL: https://arxiv.org/abs/2504.01999.

[233] Branden Aitken et al. "Conceptual Design Report for the MATHUSLA Long-Lived Particle Detector near CMS". In: (Mar. 2025). arXiv: 2503.20893 [physics.ins-det].

[234] Martin Bauer et al. "ANUBIS: Proposal to search for long-lived neutral particles in CERN service shafts". In: (Sept. 2019). arXiv: 1909.13022 [physics.ins-det].

[235] C. Ahdida et al. "The SHiP experiment at the proposed CERN SPS Beam Dump Facility". In: *Eur. Phys. J. C* 82.5 (2022), p. 486. DOI: 10.1140/epjc/s10052-022-10346-5. arXiv: 2112.01487 [physics.ins-det].

[236] P. Crivelli. "Status and prospects of the NA64 experiment at the CERN SPS". In: *Workshop on Feebly-Interacting Particles*. Jan. 2023. arXiv: 2301.09905 [hep-ex].

[237] James Pinfold et al. "Technical Design Report of the MoEDAL Experiment". In: (June 2009).

[238] A. Ball, J. Brooke, and C. et al Campagnari. "Sensitivity to millicharged particles in future proton-proton collisions at the LHC with the milliQan detector". In: *Physical Review D* 104.3 (Aug. 2021). ISSN: 2470-0029. DOI: 10.1103/physrevd.104.032002. URL: http://dx.doi.org/10.1103/PhysRevD.104.032002.

USC UNIVERSIDADE DE SANTIAGO DE COMPOSTELA

[239] B. Acharya et al. "Search for magnetic monopoles produced in 13 TeV proton-proton collisions with the MoEDAL detector". In: *Phys. Rev. D* (2025). DOI: 10.1103/PhysRevD.111.012003. arXiv: 2311.06509 [hep-ex].

[240] Vladimir V. Gligorov et al. "Searching for long-lived particles: A compact detector for exotics at LHCb". In: *Phys. Rev. D* 97 (1 2018), p. 015023. DOI: 10.1103/PhysRevD.97.015023. URL: https://link.aps.org/doi/10.1103/PhysRevD.97.015023.

[241] CODEX-b collaboration. *Technical design report for the CODEX-β demonstrator*. 2024. arXiv: 2406.12880 [physics.ins-det]. URL: https://arxiv.org/abs/2406.12880.

[242] Davide Boscherini. *The ATLAS RPC System for the LHC Run-3*. Tech. rep. Geneva: CERN, 2023. URL: https://cds.cern.ch/record/2850856.

[243] L. Pizzimento et al. "Development of a new Front End electronics in Silicon and Silicon-Germanium technology for the Resistive Plate Chamber detector for high rate experiments". In: *Journal of Instrumentation* 14.10 (Oct. 2019), pp. C10010–C10010. ISSN: 1748-0221. DOI: 10.1088/1748-0221/14/10/c10010. URL: http://dx.doi.org/10.1088/1748-0221/14/10/C10010.

[244] David Curtin and Michael E. Peskin. "Analysis of long-lived particle decays with the MATHUSLA detector". In: *Physical Review D* 97.1 (Jan. 2018). ISSN: 2470-0029. DOI: 10.1103/physrevd.97.015006. URL: http://dx.doi.org/10.1103/PhysRevD.97.015006.

[245] Giulio Aielli et al. *The Road Ahead for CODEX-b*. 2022. arXiv: 2203.07316 [hep-ex]. URL: https://arxiv.org/abs/2203.07316.

[246] R. Aaij et al. "Test of lepton universality in $b \to s\ell^+\ell^-$ decays". In: *Phys. Rev. Lett.* 131.5 (2023), p. 051803. DOI: 10.1103/PhysRevLett.131.051803. arXiv: 2212.09152 [hep-ex].

[247] Christian Bierlich *et al. A comprehensive guide to the physics and usage of PYTHIA 8.3*. 2022. arXiv: 2203.11601 [hep-ph]. URL: https://arxiv.org/abs/2203.11601.

[248] LHCb Collaboration. *LHCb VELO Upgrade Technical Design Report*. Tech. rep. CERN, 2013. DOI: 10.17181/CERN.4DGI.MZN4. URL: https://cds.cern.ch/record/1624070.

[249] LHCb Collaboration. *LHCb Tracker Upgrade Technical Design Report*. Tech. rep. CERN, 2014. DOI: 10.17181/CERN.OOOE.9O9T. URL: https://cds.cern.ch/record/1647400.

[250] I. Sanderswood. "One person's trash is another person's treasure: expanding physics reach with unused tracks". In: *Connecting the Dots 2022*. 2022.

USC UNIVERSIDADE DE SANTIAGO DE COMPOSTELA

[251] LHCb collaboration. "Measurement of J/ψ production in pp collisions at $\sqrt{s} = 7\ TeV$". In: *The European Physical Journal C* 71.5 (2011). ISSN: 1434-6052. DOI: 10.1140/epjc/s10052-011-1645-y. URL: http://dx.doi.org/10.1140/epjc/s10052-011-1645-y.

[252] Aaij et al. "Production of J/ψ and Υ mesons in pp collisions at $\sqrt{s} = 8$ TeV". In: *Journal of High Energy Physics* 2013.6 (June 2013). ISSN: 1029-8479. DOI: 10.1007/jhep06(2013)064. URL: http://dx.doi.org/10.1007/JHEP06(2013)064.

[253] Aaij et al. "Measurement of forward J/ψ production cross-sections in pp collision at $\sqrt{s} = 13\ TeV$". In: *Journal of High Energy Physics* 2015.10 (Oct. 2015). ISSN: 1029-8479. DOI: 10.1007/jhep10(2015)172. URL: http://dx.doi.org/10.1007/JHEP10(2015)172.

[254] Y. et al Amhis. "Averages of b-hadron, c-hadron, and τ-lepton properties as of 2018: Heavy Flavor Averaging Group (HFLAV)". In: *The European Physical Journal C* 81.3 (Mar. 2021). ISSN: 1434-6052. DOI: 10.1140/epjc/s10052-020-8156-7. URL: http://dx.doi.org/10.1140/epjc/s10052-020-8156-7.

[255] ROOT Development Team. *TGenPhaseSpace class reference in ROOT*. Doxygen-generated documentation. CERN. 2025. URL: https://root.cern.ch/doc/v636/classTGenPhaseSpace.html.

[256] Luc Devroye. *Non-Uniform Random Variate Generation*. See Chapter 2 for the inverse transform method. New York: Springer, 1986. ISBN: 9780387963053.

[257] SciPy Developers. *SciPy Interpolation Module*. Documentación de 'scipy.interpolate', incluyendo métodos como 'CubicSpline' y 'UnivariateSpline'. SciPy. 2025. URL: https://docs.scipy.org/doc/scipy/reference/interpolate.html.

[258] LHCb Collaboration. *LHCb PID Upgrade Technical Design Report*. Tech. rep. 2013. DOI: 10.17181/CERN.BD4G.I3VP. URL: https://cds.cern.ch/record/1624074.

[259] Wen Chen et al. "Four-lepton decays of neutral vector mesons". In: *Physical Review D* 104.9 (Nov. 2021). ISSN: 2470-0029. DOI: 10.1103/physrevd.104.094023. URL: http://dx.doi.org/10.1103/PhysRevD.104.094023.

[260] J et al Beringer. "Review of Particle Physics, 2012-2013". In: *Phys. Rev. D* 86.1 (2012). The 2012 edition of Review of Particle Physics is published for the Particle Data Group as article 010001 in volume 86 of Physical Review D. This edition should be cited as: J. Beringer et al. (Particle Data Group), Phys. Rev. D 86, 010001 (2012)., p. 010001. DOI: 10.1103/PhysRevD.86.010001. URL: https://cds.cern.ch/record/1481544.

USC UNIVERSIDADE DE SANTIAGO DE COMPOSTELA

[261] M. et al Alexander. "Mapping the material in the LHCb vertex locator using secondary hadronic interactions". In: *JINST* 13.06 (2018). All figures and tables are available at https://lhcbproject.web.cern.ch/lhcbproject/Publications/LHCbProjectPublic/LHCb-DP-2018-002.html, P06008. DOI: 10.1088/1748-0221/13/06/P06008. arXiv: 1803.07466. URL: https://cds.cern.ch/record/2309964.

[262] Luca Di Luzio et al. "ΛMs theory precision confronts flavour anomalies". In: *Journal of High Energy Physics* 2019.12 (Dec. 2019). ISSN: 1029-8479. DOI: 10.1007/jhep12(2019)009. URL: http://dx.doi.org/10.1007/JHEP12(2019)009.

[263] R. et al Aaij. "Precise determination of the B_s^0–$\overline{B}_s^0$ oscillation frequency". In: *Nature Physics* 18.1 (Jan. 2022), pp. 1–5. ISSN: 1745-2481. DOI: 10.1038/s41567-021-01394-x. URL: http://dx.doi.org/10.1038/s41567-021-01394-x.

[264] D. et al van Dyk. "EOS: a software for flavor physics phenomenology". In: *The European Physical Journal C* 82.6 (June 2022). ISSN: 1434-6052. DOI: 10.1140/epjc/s10052-022-10177-4. URL: http://dx.doi.org/10.1140/epjc/s10052-022-10177-4.

[265] R. et al Aaij. "Test of lepton universality in beauty-quark decays". In: *Nature Physics* 18.3 (Mar. 2022), pp. 277–282. ISSN: 1745-2481. DOI: 10.1038/s41567-021-01478-8. URL: http://dx.doi.org/10.1038/s41567-021-01478-8.

[266] R. et al Aaij. "Test of lepton universality with $B^0 \to K^{*0} l^+ l^-$ decays". In: *Journal of High Energy Physics* 2017.8 (Aug. 2017). ISSN: 1029-8479. DOI: 10.1007/jhep08(2017)055. URL: http://dx.doi.org/10.1007/JHEP08(2017)055.

[267] Anastasiia Filimonova, Ruth Schäfer, and Susanne Westhoff. "Probing dark sectors with long-lived particles at Belle II". In: *Physical Review D* 101.9 (May 2020). ISSN: 2470-0029. DOI: 10.1103/physrevd.101.095006. URL: http://dx.doi.org/10.1103/PhysRevD.101.095006.

[268] A. et al Tumasyan. "Search for long-lived particles decaying into muon pairs in proton-proton collisions at $\sqrt{s} = 13\ TeV$ collected with a dedicated high-rate data stream". In: *Journal of High Energy Physics* 2022.4 (Apr. 2022). ISSN: 1029-8479. DOI: 10.1007/jhep04(2022)062. URL: http://dx.doi.org/10.1007/JHEP04(2022)062.

[269] Giovanni Punzi. "Sensitivity of searches for new signals and its optimization". In: *eConf C030908* (2003). arXiv:physics/0308063, MODT002. URL: https://arxiv.org/abs/physics/0308063.

[270] Glen Cowan et al. "Asymptotic formulae for likelihood-based tests of new physics". In: *Eur. Phys. J. C* 71 (2011). [Erratum: Eur.Phys.J.C 73, 2501 (2013)], p. 1554. DOI: 10.1140/epjc/s10052-011-1554-0. arXiv: 1007.1727 [physics.data-an].

USC UNIVERSIDADE DE SANTIAGO DE COMPOSTELA

[271] LHCb Collaboration. *LHCb Online Operations Plots*. https://lbgroups.cern.ch/online/OperationsPlots/index.htm. Accessed: 13 Aug. 2025.

[272] Harry Victor Cliff, Valerie Gibson, and John Smeaton. "Tests of lepton universality using $B^0 \to K^0_S \ell^+ \ell^-$ and $B^+ \to K^{*+} \ell^+ \ell^-$ decays at the LHCb Experiment". In: *Physical Review Letters* (2020). arXiv: 2110.09501 [hep-ex]. URL: https://arxiv.org/pdf/2110.09501.

[273] Muriel Pivk and Francois R. Le Diberder. "SPlot: A Statistical tool to unfold data distributions". In: *Nucl. Instrum. Meth. A* 555 (2005), pp. 356–369. DOI: 10.1016/j.nima.2005.08.106. arXiv: physics/0402083.

[274] Lucio Anderlini et al. *The PIDCalib package*. Tech. rep. Geneva: CERN, 2016. URL: https://cds.cern.ch/record/2202412.

[275] Alex Rogozhnikov. *hep_ml: Machine Learning for High Energy Physics*. Version 0.8.0. 2025. URL: https://pypi.org/project/hep-ml/.

[276] Yoav Freund and Robert E. Schapire. "A Decision-Theoretic Generalization of On-Line Learning and an Application to Boosting". In: *Journal of Computer and System Sciences*. Vol. 55. 1. Elsevier, 1997, pp. 119–139.

[277] Jerome H. Friedman. "Greedy Function Approximation: A Gradient Boosting Machine". In: *Annals of Statistics* 29.5 (2001), pp. 1189–1232.

[278] Tianqi Chen and Carlos Guestrin. "XGBoost: A Scalable Tree Boosting System". In: *Proceedings of the 22nd ACM SIGKDD International Conference on Knowledge Discovery and Data Mining*. ACM. 2016, pp. 785–794. DOI: 10.1145/2939672.2939785.

[279] Kevin Jamieson and Ameet Talwalkar. "Non-stochastic Best Arm Identification and Hyperparameter Optimization". In: *Proceedings of the 19th International Conference on Artificial Intelligence and Statistics (AISTATS)*. Vol. 51. Proceedings of Machine Learning Research. Cadiz, Spain, 2016, pp. 240–248. URL: https://proceedings.mlr.press/v51/jamieson16.html.

[280] Nikolai V. Smirnov. "Table for estimating the goodness of fit of empirical distributions". In: *Annals of Mathematical Statistics* 19.2 (1948), pp. 279–281.

[281] Roel et al Aaij. "Precise measurement of the f_s/f_d ratio of fragmentation fractions and of B^0_s decay branching fractions". In: *Phys. Rev. D* 104.3 (2021), p. 032005. DOI: 10.1103/PhysRevD.104.032005. arXiv: 2103.06810 [hep-ex].

[282] F et al Archilli. "Performance of the Muon Identification at LHCb". In: *Journal of Instrumentation* 8.10 (Oct. 2013), P10020–P10020. ISSN: 1748-0221. DOI: 10.1088/1748-0221/8/10/p10020. URL: http://dx.doi.org/10.1088/1748-0221/8/10/P10020.

[283] Roland Waldi. *Efficiency estimation and errors*. LHCb Internal Note RW1902. Version 2. CERN GitLab, LHCb Internal Documentation. Institut für Physik, Universität Rostock, 2019.

[284] Zhu Wang. *Nonlinear Model Reduction Based On The Finite Element Method With Interpolated Coefficients: Semilinear Parabolic Equations*. 2013. arXiv: 1304.0279 [math.NA]. URL: https://arxiv.org/abs/1304.0279.

[285] ROOT Collaboration. *RooCrystalBall: Class Reference*. Documentation for RooFit's generalized asymmetrical double-sided Crystal Ball PDF. CERN ROOT. 2025. URL: https://root.cern.ch/doc/master/classRooCrystalBall.html.

[286] Glen Cowan et al. "Power-Constrained Limits". In: (May 2011). arXiv: 1105.3166 [physics.data-an].

[287] Matthew Kenzie et al. *GammaCombo: Framework para la combinación estadística de medidas*. https://gammacombo.github.io. Accedido: 2025-08-23. 2019. DOI: 10.5281/zenodo.3373613. URL: https://gammacombo.github.io.

[288] P. Dierckx. "An algorithm for smoothing, differentiation and integration of experimental data using spline functions". In: *Journal of Computational and Applied Mathematics* 1.1 (1975), pp. 165–184. DOI: 10.1016/0377-0427(75)90005-6.

[289] CAEN S.p.A. *SY4527 Universal Multichannel Power Supply System*. Mainframe high voltage power supply. Available at: https://www.caen.it/. CAEN S.p.A. Viareggio, Italy, 2015.

[290] R Guida and B Mandelli. "A portable gas recirculation unit for gaseous detectors". In: *JINST* 12.10 (2017), T10002. DOI: 10.1088/1748-0221/12/10/T10002. URL: https://cds.cern.ch/record/2307378.

[291] Paulo et al Moreira. *lpGBT documentation*. 2024. URL: https://cds.cern.ch/record/2809058.

[292] Thomas Gorordo et al. *Geometry Optimization for Long-lived Particle Detectors*. 2022. arXiv: 2211.08450 [hep-ph]. URL: https://arxiv.org/abs/2211.08450.

[293] Arne Brøndsted. *An Introduction to Convex Polytopes*. Vol. 90. Graduate Texts in Mathematics. New York, NY: Springer, 1983. ISBN: 9780387908390. DOI: 10.1007/978-1-4612-1148-8.

[294] ATLAS collaboration. "Measurement of the total and differential Higgs boson production cross-sections at $\sqrt{s} = 13\ TeV$ with the ATLAS detector by combining the $H^0 \to ZZ^* \to 4l$ and $H^0 \to \gamma\gamma$ decay channels". In: *Journal of High Energy Physics* 2023.5 (May 2023). ISSN: 1029-8479. DOI: 10.1007/jhep05(2023)028. URL: http://dx.doi.org/10.1007/JHEP05(2023)028.

[295] F. N. Fritsch and J. Butland. "A Method for Constructing Local Monotone Piecewise Cubic Interpolants". In: *SIAM Journal on Scientific and Statistical Computing* 5 (1984), pp. 300–304. DOI: 10.1137/0905021.

[296] Antonis PAPANESTIS. "The Ring Imaging Cherenkov Detectors for LHCb". In: Apr. 2007, p. 375. DOI: 10.22323/1.021.0375.





This thesis contributes to the search for Long-Lived Particles beyond the Standard Model in the LHCb and CODEX-b experiments. It presents an analysis of the rare B-meson decays into multi-muon final states predicted by non-minimal Composite Higgs models. Experimental data from LHCb corresponding to Run 2 are used to set limits in both the prompt and displaced regimes for Bs and Bu decay chains, with several reconstruction techniques explored to maximize the sensitivity reach. The work also describes contributions to the early development of
the future CODEX-b detector, including the installation of the CODEX-beta demonstrator during Run 3 and the creation of a fast-simulation framework.